

**Vertical-Cavity Surface-Emitting Lasers: Tailoring of Optical  
Admittances**

Kevin J. Knopp  
B.S., Boston University, 1994  
M.S., University of Colorado at Boulder, 1997

A thesis submitted to the  
Faculty of the Graduate School of the  
University of Colorado in partial fulfillment  
of the requirements for the degree of  
Doctor of Philosophy  
Department of Electrical Engineering  
1999

UMI Number: 9938828

---

**UMI Microform 9938828**  
**Copyright 1999, by UMI Company. All rights reserved.**

**This microform edition is protected against unauthorized  
copying under Title 17, United States Code.**

---

**UMI**  
**300 North Zeeb Road**  
**Ann Arbor, MI 48103**

This is an authorized facsimile, made from the microfilm master copy of the original dissertation or master thesis published by UMI.

The bibliographic information for this thesis is contained in UMI's Dissertation Abstracts database, the only central source for accessing almost every doctoral dissertation accepted in North America since 1861.

## UMI Dissertation Services

A Bell & Howell Company

300 North Zeeb Road  
P.O. Box 1346  
Ann Arbor, Michigan 48106-1346  
1-800-521-0600 734-761-4700  
<http://www.bellhowell.inforlearning.com>

Printed in 2000 by digital xerographic process  
on acid-free paper

DPGT

12

THIS PAGE BLANK (USPTO)

THIS PAGE BLANK (USPTO)

THIS PAGE BLANK (USPTO)



## INFORMATION TO USERS

This manuscript has been reproduced from the microfilm master. UMI films the text directly from the original or copy submitted. Thus, some thesis and dissertation copies are in typewriter face, while others may be from any type of computer printer.

**The quality of this reproduction is dependent upon the quality of the copy submitted.** Broken or indistinct print, colored or poor quality illustrations and photographs, print bleedthrough, substandard margins, and improper alignment can adversely affect reproduction.

In the unlikely event that the author did not send UMI a complete manuscript and there are missing pages, these will be noted. Also, if unauthorized copyright material had to be removed, a note will indicate the deletion.

Oversize materials (e.g., maps, drawings, charts) are reproduced by sectioning the original, beginning at the upper left-hand corner and continuing from left to right in equal sections with small overlaps. Each original is also photographed in one exposure and is included in reduced form at the back of the book.


Photographs included in the original manuscript have been reproduced xerographically in this copy. Higher quality 6" x 9" black and white photographic prints are available for any photographs or illustrations appearing in this copy for an additional charge. Contact UMI directly to order.

**UMI<sup>®</sup>**

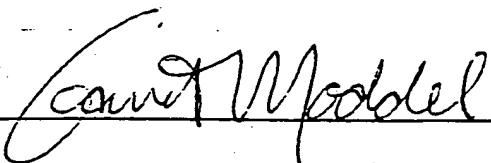
Bell & Howell Information and Learning  
300 North Zeeb Road, Ann Arbor, MI 48106-1346 USA  
800-521-0600

THIS PAGE BLANK (USPTO)

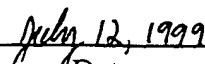
This thesis entitled:  
Vertical-Cavity Surface-Emitting Lasers: Tailoring of Optical Admittances  
written by Kevin J. Knopp  
has been approved for the Department of Electrical Engineering



Professor Adjunct David H. Christensen



Professor Garret Moddel

  
Date

The final copy of this thesis has been examined by  
the signatories, and we find that both the content and the form  
meet acceptable presentation standards of scholarly work in  
the above mentioned discipline.

## Abstract

Knopp, Kevin J. (Ph.D., Electrical Engineering)

Vertical-Cavity Surface-Emitting Lasers: Tailoring of Optical Admittances

Thesis directed by Professor Adjunct David H. Christensen

This dissertation focuses on tailoring the thin-film optical properties of vertical-cavity surface-emitting lasers (VCSELs) through the study and refinement of their optical admittance structure in the longitudinal and transverse dimensions. This tailoring allows control of laser radiation incident-on and emitted-from VCSELs.

I use admittance optimization in the longitudinal direction to fabricate VCSELs with wideband windows of constant reflectance amongst the typical interference fringe spectrum. These optimized devices offer improved stability in the coupling to a cw optical pump source and have significantly reduced the group velocity dispersion experienced by an incident ultrashort (sub-100 fs) optical pump pulse.

Additionally, I analyze the competition of transverse modes through an experimental study of their dynamics and spatio-spectral distributions using near-field scanning optical microscopy (NSOM). I show through experiment that spatially separated modes coexist by sharing the available gain, while spatially overlapping modes compete for the gain. The time-resolved data illustrates two dramatically different risetimes for orthogonal polarizations as the transverse mode families compete. To control the observed distributions, I propose a novel method

of tailoring the transverse admittance profile through the use of an out-of-phase reflection from a metal layer atop the semiconductor distributed Bragg reflector (DBR). I show through simulations that higher-order modes can be suppressed to a current of several times threshold in a 30  $\mu\text{m}$  diameter device using this method.

Further, I investigate the use of native-oxides layers and apertures in vertical-cavity devices. I present the optical dispersion and material properties of these oxide films. I apply conventional admittance matching techniques to create high-quality ( $<0.5\%$  reflectance), broad-bandwidth ( $<1\%$  over 250 nm) native-oxide antireflection (AR) coatings for integration on vertical-cavity devices. Lastly, I explore the operation of oxide apertures as intracavity lenses through derivation of their transverse phase profile and simulation of their diffraction loss.

To my family,  
for your unconditional support  
through the years.

## Acknowledgements

It is hard to believe nearly 5 years have passed since the day my wife (then girlfriend) and I pulled over at the Kansas border to Colorado and snapped a picture of the colorful welcome sign. The road has been very fruitful over the years due to the help of so many people. Foremost, I am indebted to my advisor, Dr. David H. Christensen, for providing me the opportunity for success. Dave gave me the laboratory instruction I needed in the early days, and the freedom I needed to grow in the later years. I am very grateful for all the support, respect, enthusiasm, and knowledge he has given to me. I also have to thank Dave for his understanding that graduate students are not simply temporary employees, but growing scientists.

Secondly, I thank Dr. Garret Moddel for his kind words of support, his willingness to serve as my committee chair, and his help in the preparation of this dissertation. I would also like to thank the rest of my committee for their willingness to wade through these pages: Dr. Leo Hollberg, Dr. Bart Van Zeghbroeck, and Dr. Kelvin Wagner.

Next, I need to express my gratitude to Dr. Richard P. Mirin at NIST. Rich has given me a tremendous amount of help and encouragement over the past two years. Rich has done countless growth runs for me, participated in numerous experiments (some wild and wacky), and has listened to a plethora of crazy ideas. Rich's "because you can" attitude is truly inspiring, however, his fear of flying does little to calm my own. I would also like to thank him for reading every word of this dissertation.

I also need to thank Dr. M. Selim Unlu of Boston University for the help and guidance he has provided me for the past 8 years throughout my undergraduate

and graduate work. I am very grateful to him and Dr.-to-be Greg Vander Rhodes for everything they have taught me about NSOM and for our collaboration.

Others that I would like to thank include: Dr. Michael Munroe, an NRC PostDoc who taught me how to be a little more like a physicist. Dr.-to-be Kevin L. Silverman for engaging in helpful discussions (many about motorcycles). Dr. Alexana Roshko for teaching me the in's and out's of AFM and SEM, and for taking the images within. Dr. Kris A. Bertness for providing numerous MBE growths.

Funding-wise, I thank Dave, Dr. Bob Hickernell, and NIST as a whole for providing me two years of fellowship funding, travel money, and five years of research dollars. I wouldn't have even made it to Colorado without the funding of NASA LaRC. They so graciously supported me as an undergraduate intern and then as an RA for three years. In particular, I am grateful to Dr. Jim Patterson who was instrumental in helping me sell to NASA a proposal that included funding of my education. I am equally as grateful to Dr. Alan Mickelson of CU and Dr. Keith Masterson of NIST for their willingness to work with me through all the paperwork of setting up an interaction between the university and two government agencies.

I also need to thank my loving and beautiful bride, Christina. Christina has served as a colleague, listener, advisor, motivator, friend, and true companion throughout these years. Her kindness shines so bright.

Finally, to all the others whose minds and cabinets I have rummaged, I thank you.



## Contents

List of Tables	xi
List of Figures	xii
1 Introduction	1
1.1 History of VCSELs	2
1.2 Dissertation Outline	5
2 VCSEL Design, Fabrication, and Characterization	8
2.1 Introduction	8
2.2 Design Methodology	12
2.3 NIST Electrically-Pumped Design	15
2.3.1 Minimize the Loss Current	16
2.3.2 Optimum Cavity Efficiency	21
2.3.3 Electrical and Thermal Properties	21
2.3.4 DBR Design	23
2.3.5 Design Schematic	27
2.4 Fabrication	29
2.4.1 Epitaxial Growth	29
2.4.2 Epitaxial Processing	30
2.5 Characterization	47
2.5.1 Wafer Level Testing	47
2.5.2 Device Level Testing	50
2.6 Summary	55
3 Optoelectronic Band Engineering	57
3.1 Introduction	57
3.2 Photonic Bandgap Properties of a Distributed Bragg Reflector	60
3.3 Thin-Film Optimization	63
3.3.1 Control Structure	63
3.3.2 Refinement	64
3.3.3 Simulation	68
3.4 Experimental Results	70
3.5 Thickness Deviations	75
3.6 Summary	79

<b>4</b>	<b>Transverse Mode Competition and Control in VCSELs</b>	<b>81</b>
4.1	Introduction	81
4.2	Temporal Characteristics	84
4.2.1	Large Signal Step-Response	84
4.2.2	Polarization Resolved Step-Response	86
4.3	Spatio-Spectral Mapping	89
4.3.1	The Near-Field Scanning Optical Microscope	89
4.3.2	Far-Field Characteristics	91
4.3.3	Near-Field Measurements	95
4.3.4	Discussion	103
4.4	Analysis of a Mode Control Technique	104
4.4.1	Plane Wave Calculations	104
4.4.2	Threshold Gain for "Ideal" Modes	111
4.4.3	Modal-Dependent Reflectivity and Threshold Gain	113
4.4.4	Discussion	118
4.5	Summary	121
<b>5</b>	<b>Native Oxide Technology</b>	<b>123</b>
5.1	Introduction	123
5.2	Formation	125
5.2.1	Oxide Chemistry	125
5.2.2	Oxide Fabrication	126
5.3	Optical Constants and Material Properties	135
5.3.1	Ellipsometry Analysis of Surface Oxide Films	135
5.3.2	Surface Morphology and Calculated Surface Scattering Loss	141
5.3.3	Discussion	143
5.4	Native-Oxide Antireflection Coatings	144
5.4.1	Background	144
5.4.2	Theory	145
5.4.3	Fabrication	158
5.4.4	Experiment	160
5.4.5	Discussion	166
5.5	Intracavity Lens Apertures	168
5.5.1	Abrupt Apertures	169
5.5.2	Linearly Tapered Apertures	171
5.5.3	Parabolic "Ideal" Apertures	172
5.5.4	Standing Wave Effects on Lens Power	173
5.5.5	Cavity Stability Analysis	173
5.5.6	Discussion on Confocal VCSEL Cavities	174
5.6	Optical Scattering from Intracavity Lenses / Current Apertures	176
5.6.1	Huygens' Integrals	177
5.6.2	Fox and Li Calculation	183
5.6.3	Discussion	191
5.7	Summary	192

<b>6</b>	<b>Ultrafast Implications of “Low-Ripple” VCSELs</b>	<b>194</b>
6.1	Problem with Ultrashort Pulse Excitation of VCSELs . . . . .	194
6.2	Pulse Interaction with the VCSEL Multilayer Structures . . . . .	195
6.2.1	Theory . . . . .	195
6.2.2	Modeling of the Dispersive Properties of VCSELs . . . . .	201
6.2.3	Calculated Pulse Profiles Through VCSEL Cavities . . . . .	212
6.3	Spectrally Resolved White-Light Interferometry . . . . .	219
6.3.1	Technique . . . . .	219
6.3.2	Dispersion Measurements . . . . .	225
6.4	Summary . . . . .	232
<b>7</b>	<b>Conclusion</b>	<b>234</b>
<b>A</b>	<b>Electrically Pumped VCSEL Process Sheets</b>	<b>249</b>
<b>B</b>	<b>A Proposal for Further Study – Ultrafast Photonics: Semiconductor Temporal Dynamics Enabling 10 GHz Passively Mode-Locked Solid-State Waveguide Lasers</b>	<b>254</b>
B.1	Objective . . . . .	254
B.2	Motivation . . . . .	255
B.3	Background . . . . .	256
B.3.1	Infrastructure & The State-of-the-Art . . . . .	256
B.3.2	Mode-Locking Mechanisms . . . . .	257
B.4	Problem Statement . . . . .	258
B.5	Proposed Research . . . . .	259
B.5.1	Saturation Recovery Dynamics . . . . .	260
B.5.2	Dispersion Compensating SESAMs . . . . .	262
B.6	Summary . . . . .	263

## List of Tables

2.1	The calculated enhancement factor for 10 nm thick GaAs wells with 10 nm thick $\text{Al}_{0.30}\text{Ga}_{0.70}\text{As}$ barriers. . . . .	18
4.1	Index of refraction at 980 nm for the gold, silver, and aluminum DBR terminations. . . . .	108
5.1	Summary of parameters and quantities for the three samples. . . . .	138
5.2	Summary of parameters of the VCSEL model used in the Fox and Li calculations. . . . .	187
5.3	A summary of the 2 micrometer radius Fox and Li results for infinite parabolic finite parabolic and abrupt oxide apertures. . . . .	191
6.1	Standard deviation of group delay and GVD measurements based on seven scans of the bare interferometer. . . . .	225

## List of Figures

2.1	A schematic of a generic VCSEL structure. . . . .	9
2.2	Illustration of some possible device geometries for VCSELs. . . . .	11
2.3	Diagram of the termination of a DBR to air (a) and to a substrate (b). In both cases the $A$ and $B$ ratios are the same and only $C$ differs. . . .	26
2.4	Schematic of the 1 <sup>st</sup> generation NIST VCSEL.. . . .	28
2.5	Illustration of the as grown NIST VCSEL structure in cross section. . .	31
2.6	Illustration of the desired outcome from the top DBR mesa etch. . . . .	32
2.7	A schematic of the photolithography mask used for patterning the square optical mesas. . . . .	33
2.8	A photograph of a sample after the top DBR has been etched down to the contact layer to form mesas. . . . .	34
2.9	A scanning electron microscope (SEM) image of an etched $5 \times 5 \mu\text{m}$ DBR mesa atop the contact layer. . . . .	34
2.10	Illustration of the desired outcome after completion of the current confinement mesa etch. . . . .	35
2.11	A schematic of the photolithography mask used for patterning the current confinement mesas. . . . .	37
2.12	A photograph illustrating the alignment of the circular photoresist pattern for the current confinement etch to the square DBR mesas. . . . .	37
2.13	Cross sectional illustration of the VCSEL sample after formation of the native-oxide aperture. . . . .	38
2.14	A photograph of a sample after 11 min of oxidation. . . . .	38
2.15	Cross sectional illustration of the VCSEL sample after deposition and lift-off of the $p$ -metals. . . . .	40
2.16	A schematic of the photolithography mask used for lift-off patterning of the $p$ -metal. . . . .	40
2.17	A photograph of the patterned photoresist prior to evaporation of the $p$ -contact metals. . . . .	41
2.18	A cross sectional illustration of a proposed $p$ -metallization layout for routing oxide-insulated wire traces. . . . .	42
2.19	Schematic of the photolithography mask used for the lift-off patterning of the wire-bond traces. . . . .	42
2.20	A photograph of a fully processed NIST $4 \times 4$ VCSEL array. . . . .	44

2.21	Schematic and photograph of the <i>in situ</i> wet-etch monitoring setup at NIST. . . . .	45
2.22	<i>In situ</i> reflectance signal obtained by etching through the entire VCSEL structure of Fig. 2.4. . . . .	48
2.23	Illustration of the optical pumping setup. . . . .	49
2.24	Pulsed L-I curves from $33\ \mu\text{m} \times 33\ \mu\text{m}$ native-oxide apertured NIST VCSELs. . . . .	52
2.25	Pulsed I-V curves from $33\ \mu\text{m} \times 33\ \mu\text{m}$ native-oxide apertured NIST VCSELs. . . . .	52
2.26	Picture of the $33\ \mu\text{m} \times 33\ \mu\text{m}$ lasing aperture of a NIST VCSEL imaged by a CCD camera. . . . .	53
3.1	Plot of the reflectance spectrum of an air-terminated 20-pair AlAs/GaAs DBR with the first three extended states labeled. . . . .	61
3.2	Plot of the calculated electric field intensity throughout a 20-pair AlAs/GaAs DBR for a wavelength at the center of the forbidden gap (relative wavelength of 1) . . . . .	62
3.3	Plot of the calculated electric field intensity throughout a 20-pair AlAs/GaAs DBR for a wavelength at the $N_{-1}$ and $N_{-2}$ extended states. . . . .	63
3.4	Simulated reflectance spectrum for a typical VCSEL structure illustrating the resonant wavelength and a possible pump wavelength amidst the DBR interference fringes. . . . .	64
3.5	Calculated reflectance spectrum for the optimized low-ripple structure. . . . .	67
3.6	Bar graph illustrating the low-ripple design's deviation from the typical quarter-wave thickness. . . . .	68
3.7	Simulated $\Gamma_{\text{pump}}(\lambda)$ and reflectance spectrum for the control structure. . . . .	69
3.8	Simulated $\Gamma_{\text{pump}}(\lambda)$ and reflectance spectrum for the control structure. . . . .	70
3.9	Measured (a) and simulated (b) reflectance of the control structure. . . . .	71
3.10	Measured (a) and simulated (b) reflectance of the low-ripple structure. . . . .	71
3.11	Optically pumped lasing spectrum of a $25\ \mu\text{m}$ square mesa-etched low-ripple device. . . . .	72
3.12	Filtered PLE emission and microspot reflectance versus pump wavelength for the control structure. . . . .	74
3.13	Filtered PLE emission and microspot reflectance versus pump wavelength for the optimized low-ripple structure. . . . .	74
3.14	Simulation results of a $\pm 1\%$ uniformly distributed random thickness variation in the control structure. . . . .	76
3.15	Simulation results of a $\pm 1\%$ uniformly distributed random thickness variation in the low-ripple structure. . . . .	76
3.16	The spectral response of the control structure to temperature changes over the range of 0 to $100\ ^\circ\text{C}$ . . . . .	78
3.17	The spectral response of the low-ripple structure to temperature changes over the range of 0 to $100\ ^\circ\text{C}$ . . . . .	79

4.1	Step response dynamics of index-guided VCSEL measured by exciting the sample to a few times threshold with a step function having a 43 ps risetime and 10 ns duration. . . . .	86
4.2	Polarization-resolved step-response dynamics of an index-guided VCSEL with 0 V prebias. . . . .	87
4.3	Polarization-resolved step-response dynamics of an index-guided VCSEL with 3.2 V prebias. . . . .	88
4.4	Schematic of the near-field microscope setup. . . . .	90
4.5	Far-field spectra illustrating the device's multi-transverse-mode characteristics for drive currents of: 7, 10, 15, and 17 mA. . . . .	92
4.6	Far-field spectrum at 17 mA showing the Lorentzian fits to each transverse mode of the far-field spectrum at 17 mA. . . . .	93
4.7	L-I behavior for each transverse mode illustrating competition or independent coexistence of various modes. . . . .	94
4.8	Representative shear force image acquired during a near-field scan of the topography of the VCSEL's p-contact. . . . .	95
4.9	Collected near-field images of the intensity distributions at: (a) 7 mA, (b) 10 mA, and (c) 15 mA. . . . .	97
4.10	Mapping of the NSOM measured optical emission onto the acquired shear-force data of the p-contact topography of a gain-guided VCSEL operating at 10 mA. . . . .	99
4.11	Composite images illustrating spectrally resolved near-field emission from a gain-guided VCSEL operating at: (a) 7 mA, (b) 10 mA, and (c) 15 mA. . . . .	101
4.12	Diagram (a) of a VCSEL top DBR with an even number of quarterwave layers, a phase matching layer of arbitrary thickness, and a metal termination. The lumped mirror model of the reflectance from the terminated DBR is shown in (b). . . . .	105
4.13	Plot of the magnitude of Eq. 4.6 versus the thickness of the phase matching layer for the metal terminations of Table 4.1. . . . .	108
4.14	Plot of the magnitude of Eq. 4.6 versus the thickness of the phase matching layer illustrating the minimum reflectance for the metal terminations of Table 4.1. . . . .	109
4.15	The simulated reflectance spectrum of a microcavity consisting of a 16.5-pair AlAs/GaAs bottom DBR, a $\lambda$ cavity spacer, and a 16-pair AlAs/GaAs top DBR where the layer thickness of the top most DBR layer has been adjusted according to the plot of Fig. 4.13 to create a destructive reflection when terminated with aluminum. . . . .	110
4.16	A plot of the threshold gain ratio versus thickness of the phase matching layer for the three metal terminations in the ideal case. . . . .	112
4.17	Calculated LP mode patterns for a 30 $\mu\text{m}$ diameter device with a wavelength of 1 $\mu\text{m}$ . . . . .	116
4.18	The spatial dependence of the metal termination used for modal-dependent reflectivity calculations. . . . .	117

4.19	The calculated modal-dependent reflectivity of a 16-pair AlAs/GaAs DBR at 1100 nm as a function of the radius of the opening in the Al terminator.	119
4.20	The threshold gain ratios as a function of the radius of the opening in the aluminum terminator.	119
4.21	A plot of the ratio for the threshold gain of the LP <sub>01</sub> mode to that of the ideal air-terminated mode.	120
5.1	Image of (a) a surface layer of Al <sub>0.90</sub> Ga <sub>0.10</sub> As after 1 year of ambient exposure and (b) an AFM image taken on the edge of a freshly cleaved AlAs/GaAs DBR.	127
5.2	A picture of the (a) apparatus for wet-thermal oxidation of AlGaAs and (b) its diagram.	128
5.3	Schematic (a) and images (b-d) of the lateral progression of the oxidation front across a buried high-Al containing layer of an etched mesa.	130
5.4	An AFM image of a 33 $\mu$ m diameter circular mesa after 2 min of oxidation.	131
5.5	Schematic (a) and images (b) of the lateral progression of the oxidation front outwards across a buried high-Al containing layer from an etched via hole.	132
5.6	A diagram of a taper consisting of a 25 nm grade from Al <sub>0.90</sub> Ga <sub>0.10</sub> As to AlAs, a 20 nm AlAs layer, and a 25 nm grade from AlAs back to Al <sub>0.90</sub> Ga <sub>0.10</sub> As.	133
5.7	The rate of oxidation for the via hole geometry of the buried 100 nm thick Al <sub>0.98</sub> Ga <sub>0.02</sub> As layer shown in Fig. 5.5. A fit to the data is also shown.	134
5.8	Dispersion curves measured for three different sample thicknesses of oxidized crystalline material. Error bars representative of third decimal place uncertainties are shown.	139
5.9	Dispersion curve measured for the oxidized crystalline (580 °C), LTG polycrystalline (350 °C), and LTG amorphous (250 °C) samples. The large variation (> 0.1) in the refractive index with sample crystallinity is illustrated.	141
5.10	AFM images of the oxide surface morphology for: (a) 164 nm thick, crystalline (580 °C), 10 nm z range, (b) ~400 nm thick, crystalline (580 °C), 100 nm z range, (c) 228 nm thick, LTG amorphous (250 °C), 25 nm z range, and (d) 418 nm thick, LTG polycrystalline (350 °C), 200 nm z range.	142
5.11	Plot illustrating the minimum reflectance achievable for a given matching-layer index of a single-layer AR coating on GaAs at a wavelength of 1 $\mu$ m.	146
5.12	The theoretical reflectance from a one-layer quarter-wave coating with $n_1=1.57$ (all wavelengths) on a GaAs substrate. The reflectance of uncoated GaAs is also shown.	147



5.13	The vector diagram for a two layer coating where $n_o$ , $n_1$ , $n_2$ , and $n_3$ are the indices of refraction of the incident medium, first matching film layer, second film layer, and substrate, respectively. $\delta_1$ and $\delta_2$ are the phase thicknesses of the film layers. The three material interfaces are labeled $a$ , $b$ , and $c$ .	148
5.14	Plot of the necessary matching layer index and equivalent composition for a given surface layer index to achieve zero-reflectance at $1\ \mu\text{m}$ with a quarter-quarter coating on GaAs.	149
5.15	A modified Schuster diagram for a two-layer AR coating. The solid black filled region represents the region of zero reflectance solutions given the constraints of the oxide index, available AlGaAs indexes for an incident medium of air and a GaAs substrate (at $1\ \mu\text{m}$ ).	151
5.16	Plot of the calculated reflectance minimum for a quarter-quarter coating versus aluminum composition of the matching layer for design wavelengths of 890 nm and 1550 nm.	153
5.17	A modified Schuster diagram for a buried-oxide AR coating. The rectangular solid black filled region indicates that an AR coating can be designed for zero reflectance using wet- oxidized AlGaAs and a matching layer of any Al composition for any substrate with an effective index between 2.5 and 3.5.	154
5.18	Summary of five native-oxide AR coatings designed and simulated. The sixth coating, $F$ , is a typical AR coating of ZnS/MgF <sub>2</sub> simulated for comparison.	156
5.19	The calculated reflectance of the six coatings summarized in Fig. 5.18. The broadband nature of each coating is illustrated.	157
5.20	The calculated reflectance of the six coatings summarized in Fig. 5.18. The minimum reflectance of each coating is illustrated.	157
5.21	The measured reflectance of a single-layer native-oxide AR coating. The measured reflectance of an uncoated substrate of GaAs is also shown.	161
5.22	The measured reflectance of the as-grown and oxidized samples of the oxide/Al <sub>0.80</sub> Ga <sub>0.20</sub> As two-layer coating.	162
5.23	The measured reflectance for the center and edge regions of a buried oxide coating on a $50\ \mu\text{m}$ pillar.	164
5.24	The measured reflectance of a semiconductor saturable absorber mirror with a two-layer native-oxide AR coating before and after 5 min of oxidation.	166
5.25	Depiction of (a) the confined optical mode in an oxide apertured VCSEL and (b) two-periods of the unfolded cavity lens-waveguide afforded by the intracavity oxide aperture.	169
5.26	The spherical wave fit for an (a) abrupt oxide aperture and (b) a linear tapered aperture.	171
5.27	A sketch of an intracavity contacted confocal VCSEL design.	176
5.28	Calculated near and far field diffraction patterns from a hard aperture of radius $a$ .	182

5.29	Pictorial illustration of the Fox and Li calculation. . . . .	183
5.30	Fox and Li calculation of a microresonator consisting of a circular 10 $\mu\text{m}$ diameter hard mirror separated by 3 $\mu\text{m}$ from another hard mirror of infinite extent. . . . .	184
5.31	Computed magnitude and phase after 500 iterations for a 5 $\mu\text{m}$ device with no intracavity lens. . . . .	188
5.32	Computed magnitude and phase after 500 iterations for a 5 $\mu\text{m}$ device with an infinite extent parabolic lens. . . . .	188
5.33	Computed magnitude and phase after 2000 iterations for a 5 $\mu\text{m}$ device with an abrupt oxide aperture. . . . .	189
5.34	The loss-per-pass calculated with each iteration for a 5 $\mu\text{m}$ device with an abrupt oxide aperture. . . . .	190
6.1	The reflectance and phase of a conventional VCSEL's cold cavity (without quantum wells). . . . .	202
6.2	The reflectance and phase of a low-ripple VCSEL's cold cavity (without quantum wells). . . . .	202
6.3	The calculated group delay for the conventional VCSEL cavity on reflectance. . . . .	204
6.4	The calculated group delay (solid line) for the low-ripple VCSEL cavity on reflectance. . . . .	204
6.5	Comparison of the group delay for the conventional and low-ripple VCSEL cavities on reflection. . . . .	205
6.6	The calculated group velocity dispersion (GVD) of the conventional VCSEL cavity on reflectance. . . . .	206
6.7	The calculated group velocity dispersion (GVD) of the low-ripple VCSEL cavity on reflectance. . . . .	207
6.8	The calculated group delay for the conventional VCSEL cavity on transmittance. . . . .	209
6.9	The calculated group delay for the low-ripple VCSEL cavity on transmittance. . . . .	209
6.10	The calculated group velocity dispersion (GVD) of the conventional VCSEL cavity on transmittance. . . . .	211
6.11	The calculated group velocity dispersion (GVD) of the low-ripple VCSEL cavity on transmittance. . . . .	211
6.12	The real electric field amplitude for the unchirped 40 fs Gaussian input pulse. . . . .	213
6.13	The intensity of $\tilde{E}_{in}^+(t)$ and its time dependent carrier frequency, $\omega(t)$ , for the 40 fs Gaussian input pulse. . . . .	214
6.14	Illustration of the overlap of the spectral intensity of the 40 fs input pulse, centered at a wavelength of 915 nm, with the interference ripple of the conventional cold-cavity VCSEL structure. . . . .	214
6.15	Illustration of the overlap of the spectral intensity of the 40 fs input pulse, centered at a wavelength of 915 nm, with the optical pumping window of the low-ripple cold-cavity VCSEL structure. . . . .	215

6.16	Plots of the electric field amplitude, intensity, and time dependent carrier frequency for a 40 fs pulse transmitted through the conventional structure at a center wavelength of (a) 915 nm, and (b) 940 nm. . . . .	216
6.17	Plots of the electric field amplitude, intensity, and time dependent carrier frequency for a 40 fs pulse transmitted through the low-ripple structure at a center wavelength of 915 nm with various chirp parameters: (a) $a=0$ , (b) $a=-0.5$ , (c) $a=-1.0$ , and (d) $a=-3.0$ . . . . .	218
6.18	The experimental setup for the spectrally resolved white-light interferometer. . . . .	221
6.19	Spectrally-resolved images recorded for the bare Michelson interferometer. . . . .	224
6.20	Spectrally-resolved interferogram images for the conventional cold-cavity VCSEL illustrating the variations in the reflected phase versus wavelength. . . . .	227
6.21	Fits to four representative vertical slices at various wavelengths across the 970 nm image of the conventional cavity. . . . .	228
6.22	Measured group delay upon reflection from the conventional VCSEL cavity. . . . .	229
6.23	Measured GVD upon reflection from the conventional VCSEL cavity. . . . .	229
6.24	Measured group delay upon reflection from the low-ripple VCSEL cavity. The dotted curve represents the sample's measured reflectance. . . . .	231
6.25	Measured GVD upon reflection from the low-ripple VCSEL cavity. The dotted curve represents the sample's measured reflectance. . . . .	231

## Chapter 1

### Introduction

Communication makes things work. Everything from personal relationships to automated teller transactions require it. Every second, 1.5 km of optical fiber is draped across the world to keep pace with it (Shiffman, 1999). Every day, communication as we know it is being revolutionized by the Internet and the birth of e-commerce. Vocal conversations now account for less than half of the total telecommunications traffic worldwide (Shiffman, 1999). Traffic on the Internet is doubling at a lightning rate of every 100 days (Shiffman, 1999). This brisk pace is extremely demanding on telecommunication technologies. The marketplace is willing to bear a seemingly endless quantity of high-speed sources and detectors.

One source being aggressively pursued for use in high-speed data-link transceivers is the vertical-cavity surface-emitting laser (VCSEL). VCSEL (pronounced "vic-sell") transceivers operating at a wavelength of 850 nm and a rate of 1 Gbit/s are now being shipped for use in short-haul data links. These 1000baseSX optical transceivers are intended to replace the 10baseT (10 Mbit/s) and 100baseT (100 Mbit/s) copper-wire modules currently used in the backbone of local-area-networks (LANs). The projected useful life of these optical transceivers is just 3 years. The product development of

short-haul 10 Gbit/s VCSEL transceivers has begun, and research efforts are underway for 1.3  $\mu\text{m}$  and 1.55  $\mu\text{m}$  long-haul VCSEL modules.

The tremendous promise of VCSELs arises from their cavity orientation. As their name suggests, a VCSEL's cavity is aligned perpendicular to the plane of the wafer on which they are grown. This orientation inherently dictates a short cavity length on the order of one optical wavelength. Lasing emission occurs normal to the wafer's surface and normal to their edge-emitting cousins. As a consequence of their short cavity and vertical orientation, VCSELs operate in a single longitudinal mode and can be made to have circularly symmetric beam profiles with low divergence. VCSELs avoid the complexities of longitudinal mode hops and can more efficiently couple to optical fiber than conventional edge-emitting lasers. VCSELs reduce fabrication costs through their compatibility with batch processing techniques. The ability to photolithographically define 2-dimensional (2D) arrays of coherent light sources and the possibility of integration with transistors opens a host of other applications beyond communications. VCSELs are being courted for use in head-up displays, print heads in laser printers, sensors, multi-track readout heads from data storage media, interconnects, scanning confocal microscopes, and a wealth of other novel applications.

## 1.1 History of VCSELs

In the early 1960s, researchers at IBM observed a narrowing of the spontaneous emission normal to the direction of a  $pn$  junction (Pankove, 1963). The lasing threshold in this direction was estimated to be 10 times larger than that in the direction along the junction. In March of 1963, Dr. Jacques I. Pankove at RCA Laboratories in Princeton

used this observation to conceive of a laser in which a circularly symmetric beam was emitted from a cavity oriented normal to the junction (Pankove, 1963). The notion of a vertical-cavity laser was born.

In 1964, and perhaps independently of Pankove's discovery, the vertical-cavity laser was first demonstrated in InSb at a wavelength of  $5.2\ \mu\text{m}$  by Dr. Ivars Melngailis at MIT Lincoln Laboratories (I. Melngailis, 1965). Coherent emission was obtained near 10 K with 50 nsec current pulses of 20 amps ( $60\ \text{kA}/\text{cm}^2$ ). Soon thereafter, the progress of vertical-cavity lasers gave way to the development of edge-emitting lasers.

Thirteen years later in 1977, Professor Kenichi Iga at the Tokyo Institute of Technology revisited<sup>1</sup> the idea of a vertical-cavity laser. His group's demonstration of a vertical-cavity laser came just two years later in 1979 (H. Soda, 1979). This device operated pulsed at 77 K with a wavelength of  $1.2\ \mu\text{m}$  and a threshold current density of  $44\ \text{kA}/\text{cm}^2$ . Metallic reflectors provided mirror reflectivities of  $\sim 85\%$ . To reduce the threshold current density, the volume of the active region had to be reduced. This required higher reflectance mirrors. Two amorphous quarter-wave dielectric mirrors were used by Iga's group to demonstrate the first continuous-wave operating GaAs vertical-cavity laser at room-temperature (F. Koyama, 1988 ; F. Koyama, 1989). Epitaxially grown mirrors were then pursued in an effort to reduce fabrication complexities by creating the laser cavity in a single epitaxial growth. The precision of epitaxial growth technologies was greatly taxed by this desire. The small refractive index contrast between semiconductor alloys demanded the growth of a large number of quarter-wave

---

<sup>1</sup>Dr. Iga is commonly (but mistakenly) considered to have been the first person to conceive of the vertical-cavity laser. The first reports mentioned in this dissertation have been overlooked by almost all VCSEL researchers.

layers. After the demonstration of a 20-pair GaAs/Al<sub>0.5</sub>Ga<sub>0.5</sub>As mirror with 94% reflectance by M. Ogura at the Electrotechnical Laboratory in Ibaraki, the Al<sub>x</sub>Ga<sub>1-x</sub>As material system fast became the system of choice for realizing high reflectance mirrors for GaAs based devices (M. Ogura, 1983).

The first structure incorporating such reflectors was a vertical distributed feedback laser (M. Ogura, 1987). The mirrors were demonstrated to be highly reflective and both electrically and thermally conductive. Numerous devices from Iga's group at the Tokyo Institute of Technology were then demonstrated using AlAs/GaAs mirrors. The most notable improvement in performance, however, came in March of 1989 by Dr. Jack Jewell *et. al.* at AT&T Bell Labs (J.L. Jewell, 1989). Their device used very high reflectance (99.9%) AlAs/GaAs mirrors and a single compressively-strained InGaAs quantum well active region for emission at 980 nm. The threshold current density of the device was only 1.8 kA/cm<sup>2</sup>. A 5 μm diameter device operated at currents of just over 1 mA. VCSELs were now viable.

Current injection through the epitaxial mirror is problematic as the band-edge offset between the AlAs and GaAs mirror layers creates barriers to current flow which increases the resistance and the needed drive voltage. In 1990 Randy Geels *et. al.* at the University of California, Santa Barbara (UCSB) demonstrated a reduction of the threshold voltage from 15 V to 4 V using compositional grading at the mirror interfaces (R.S. Geels, 1990). Their devices exhibited a threshold current density of 600 A/cm<sup>2</sup>. A selective doping scheme was later devised in 1992 by M. Sugimoto at the NEC Corporation to allow the creation of low resistance mirrors with minimal free-

carrier optical absorption (M. Sugimoto, 1992). This further reduced threshold current densities to  $450 \text{ A/cm}^2$ .

The most recent historic leap in VCSEL technology occurred in 1994 when Diana Huffaker *et. al.* at the University of Texas at Austin (UT Austin) used an oxide aperture to confine the injected current and simultaneously act as an intracavity lens for confinement of the optical mode (D.L. Huffaker<sup>a,b</sup>, 1994). A record low threshold current density of  $340 \text{ A/cm}^2$  was achieved in an  $8 \mu\text{m}$  square device. Also for the first time, cw lasers with sub-100  $\mu\text{A}$  threshold currents were demonstrated.

Today, mainstream efforts by powerhouse VCSEL research centers such as Hewlett Packard, Honeywell, Sandia National Laboratories, UCSB, and UT Austin are focused on further lowering threshold current densities, increasing modulation rates, and reaching the telecommunication wavelengths of  $1.3 \mu\text{m}$  and  $1.55 \mu\text{m}$ .

## 1.2 Dissertation Outline

The general theme of this dissertation is the thin-film optics of VCSELs. More specifically, this thesis encompasses the study and refinement of a VCSEL's optical admittance structure in the longitudinal and transverse dimensions. This facilitates control of laser radiation incident-on and emitted-from VCSELs.

In Chapter 2, I begin by introducing VCSELs and the requirements necessary to achieve lasing. I present the design methodology, device fabrication steps, and characterization results of VCSELs I have produced at the National Institute of Standards and Technology (NIST). The process sheets for these devices have been included as Appendix A. This chapter provides background while presenting experimental obser-



vations of some of the unique traits of VCSELs that will be explored later.

In Chapter 3, I present a thin-film optimization technique for matching optical admittances in a VCSEL along its longitudinal direction. This optimization tailors the coupling of an incident cw laser source used for optical pumping. Additionally, the optimized devices promote vertical integration and show promise for use in power-by-light applications, such as sensors.

In Chapter 4, I study the complex nature of the transverse modes in VCSELs both temporally and spatially. Spatio-spectral mapping of the mode distributions was performed using near-field scanning optical microscopy (NSOM). I discuss the collected data within the context of their effect on bit-error-rates in communication links. I then present a novel method of admittance optimization in the transverse direction for controlling the reflectance seen by each transverse mode.

Throughout Chapter 5, I investigate native-oxide technologies and their use in VCSELs. Specifically, I study the optical and material properties of the oxides. I apply conventional admittance matching techniques to create integrated antireflection coatings on vertical cavity devices. Further, I explore the operation of oxide apertures in VCSELs as intracavity lenses and quantify their associated diffraction loss.

In Chapter 6, I discuss the ramifications of the admittance optimization presented in Chapter 3 on the dispersion characteristics of the optimized structures. I explore the effect of these structures on an incident ultrashort (sub-100 fs) laser pulse through simulation and measurement.

Lastly, Chapter 7 serves to summarize and conclude the dissertation. In this

chapter, I evaluate the contributions of this work and its impact on the community. A proposal to the National Research Council (NRC) for future work has been included as Appendix B.

## Chapter 2

### VCSEL Design, Fabrication, and Characterization

#### 2.1 Introduction

A VCSEL is an etalon structure consisting of two mirrors centered around an optical gain medium to form a cavity. VCSELs are fabricated in a semiconductor thin-film deposition environment. The device's vertical orientation leads to a small gain volume. This small volume dictates the use of high-reflectance cavity mirrors in order for the round-trip gains to overcome the losses. Mirrors with greater than 99% reflectance are realizable using stacks of quarter-wavelength thick layers of alternating high and low index dielectric or semiconductor materials. These stacks form distributed Bragg reflectors (DBRs). The material of the mirror pairs is chosen by consideration of absorption, index of refraction, and in the case of semiconductor materials, lattice-matching. The VCSEL cavity consists of an active region centered between two passive cavity spacers and the DBRs. Figure 2.1 shows a schematic of this generic VCSEL structure. The active region is chosen to provide gain at the desired lasing wavelength and can be either bulk material, one or more quantum wells, or even layers of quantum dots. The passive spacers are used to adjust the total cavity length to match the

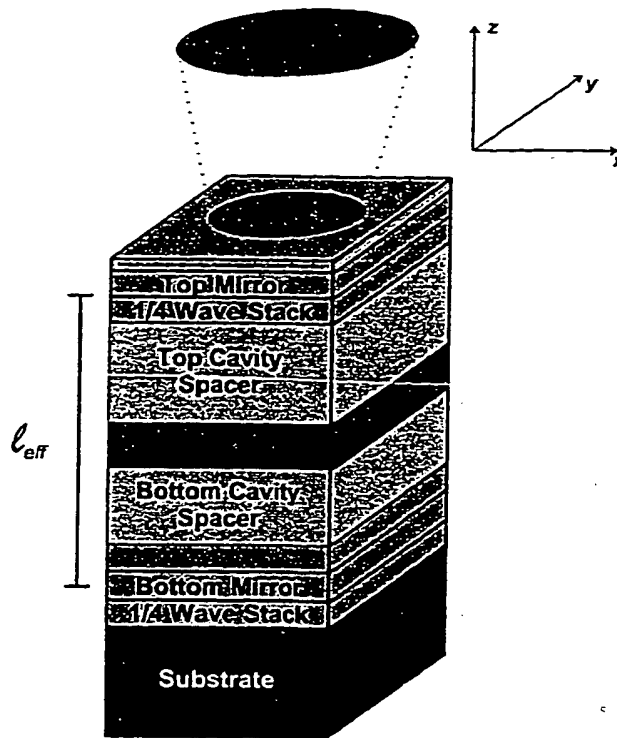


Figure 2.1: A schematic of a generic VCSEL structure.

resonance condition for the desired lasing wavelength. The spacer material is selected to avoid absorption at the lasing wavelength and to lattice-match with the active region and the surrounding mirrors. Laser emission will occur in the direction normal to the wafer surface.

Lasing can be stimulated in a VCSEL by two methods. When a semiconductor DBR is used, a  $p$ - $i$ - $n$  diode can be created by doping the top mirror  $p$ -type and the bottom mirror  $n$ -type during the growth. By applying ohmic contacts, an electrically pumped device is created. Alternatively, it is possible to stimulate lasing through optical excitation of the carriers. By shining photons on the active region with an

energy higher than the bandgap of the active region, electron-hole pairs are generated, and their radiative recombination across the gap results in spontaneous emission. If the material is pumped hard enough, a population inversion is created and lasing is achieved.

The geometry of a VCSEL has many possibilities. The geometry chosen for a particular device depends on the desired emission wavelength, the transparency of the substrate at that wavelength, the availability of high-quality epitaxial mirrors, the electrical conductivity of the mirrors, the current and optical mode confinement schemes, and the particular application. Figure 2.2 illustrates a few possible device geometries. Figure 2.2 (a) is a bottom-emitting mesa device. The top DBR is doped, and current is injected down through it to the active region. The top DBR is etched to form a mesa that confines the optical mode due to the index difference between the pillar and air. The output of the laser is passed through the substrate. For lasing wavelengths not transparent to the substrate, a top-emitting mesa device can be created by patterning a window in the top contact for output of the emission. Figure 2.2 (b) illustrates an ion-implanted device. Ions are used to bombard the crystal and create an insulating region to funnel the current. Optical mode confinement is provided through thermal lensing and gain guiding. This geometry is also applicable to both top and bottom emitting devices. An advantage to this geometry is its planarity. Figure 2.2 (c) is similar to the mesa structure of Fig. 2.2 (a). However, an insulating oxide layer is used to confine the optical mode and injected current away from the rough sidewalls of the mesa that can cause optical scattering and nonradiative recombination. This

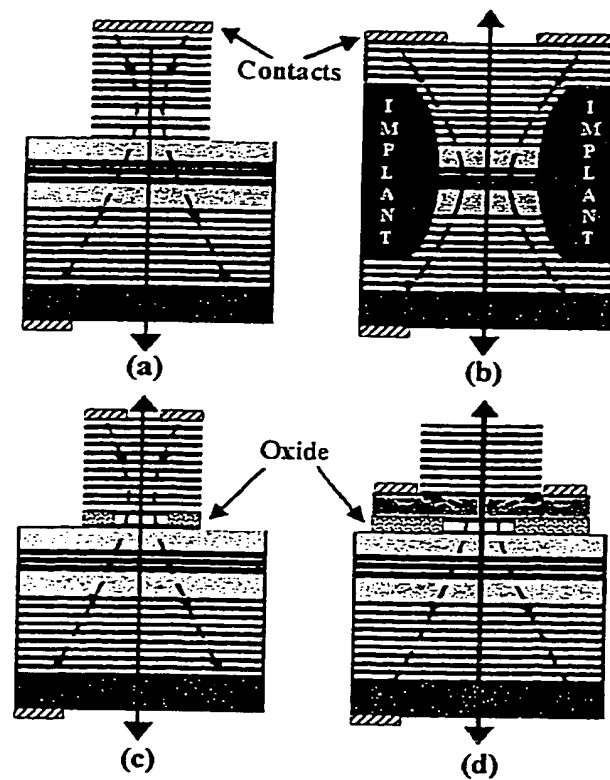


Figure 2.2: Illustration of some possible device geometries for VCSELs: (a) bottom-emitting mesa (b) ion-implanted (c) oxide-confined mesa (d) oxide-confined intracavity contacted. The dashed arrows indicate current flow and the solid arrows represent light.

geometry is again applicable to both top and bottom emitting devices. Figure 2.2 (d) is an oxide-confined structure with an intracavity top contact. In this geometry, the current is injected around the top DBR rather than through it. This allows the use of an undoped semiconductor or dielectric DBR. This device avoids the potentially large resistance of the epitaxial reflector thereby reducing ohmic heating.

In this chapter, I address the design and development of electrically-pumped VCSELs at NIST. In the first section, I introduce the basic design methodology. I then follow this general discussion with its specific application to the design of an intracavity contacted VCSEL for development at NIST. Section 2.4 then presents the fabrication process needed to realize this device. Results on the characterization of the devices are discussed in the last section.

## 2.2 Design Methodology

The design of an electrically-pumped VCSEL involves a plethora of engineering trade-offs. Many questions need to be addressed by the design: How many quantum wells are needed? How many top and bottom mirror pairs should be used? Should the top mirror have the same number of DBR pairs as the bottom mirror? What about the structure's resistance and resulting temperature? Will the cavity resonance and gain peak need to be shifted at room temperature? How is the optical absorption kept low? How will current be confined? What type of electrical contacts will be used? What are the process steps needed to fabricate it? One of the main objectives of a thesis by Corzine at the University of California Santa Barbara was to develop an algorithm for optimizing the design of a VCSEL (Corzine, 1993). This algorithm will be relied

upon as the foundation for my VCSEL designs. In this section, I will briefly introduce the algorithm methodology and present my calculations leading to the demonstration of the first electrically-pumped VCSEL at NIST.

The VCSEL design algorithm introduced by S. Corzine quite elegantly and extensively answers the question, "How do I design a laser which minimizes the total amount of current required to achieve a given output power?" (Corzine, 1993). The threshold condition for a VCSEL is,

$$G = T + A. \quad (2.1)$$

This equation states that the light generated ( $G$ ) must equal the light transmitted through the mirrors ( $T$ ) plus the light absorbed within cavity ( $A$ ). Following from the laser threshold equations in (Verdeyen, 1989 ; Yariv, 1991),

$$G = \Gamma_{enh} \Gamma_{xy} g_{mat} L_g, \quad (2.2)$$

$$T = \frac{1}{2} \ln \left[ \frac{1}{R_a R_b} \right], \quad (2.3)$$

$$A = \frac{1}{2} (A_a + A_b) + \sum \Gamma_{enh}^i \Gamma_{xy}^i \alpha_i L_i. \quad (2.4)$$

The light generated is equal to the product of the active region's material gain  $g_{mat}$ , the length of the gain region  $L_g$ , the lateral overlap of the optical mode with the gain medium  $\Gamma_{xy}$ , and the longitudinal overlap of the cavity mode with the gain medium  $\Gamma_{enh}$ . The transmitted light through the mirrors is simply related to the reflectance of the two cavity DBRs,  $R_a$  and  $R_b$ . The light absorbed is the sum of the light absorbed within the two cavity DBRs ( $A_a$  and  $A_b$ ) and elsewhere in the cavity. The absorption in the cavity (which includes diffraction loss) is written as the sum of various



contributions, each dependent on the lateral and longitudinal mode overlap ( $\Gamma_{enh}^i$  and  $\Gamma_{xy}^i$ ), the absorption coefficient of the material  $\alpha_i$ , and the length of the absorbing region  $L_i$ .

Another key quantity that needs to be introduced is the external quantum efficiency  $\eta_{ext}$  which defines the slope of the light versus current curve above threshold,

$$\eta_{ext} = \eta_i \eta_{cav}. \quad (2.5)$$

The external efficiency is the product of the internal quantum efficiency and the cavity efficiency. The internal quantum efficiency,  $\eta_i$ , is the fraction of current beyond threshold that contributes to stimulated emission. The cavity efficiency,  $\eta_{cav}$ , is the fraction of the photons generated that escape the cavity through the mirrors,

$$\eta_{cav} = \frac{T}{T + A}. \quad (2.6)$$

Next, an equation for the drive current needed to output a given power can be defined as the sum of the current needed to reach threshold and the current needed to get power out. This drive current is,

$$I = \frac{J_v V_{act}}{\eta_i} + \frac{q}{\hbar\omega} \frac{P}{\eta_{ext}}, \quad (2.7)$$

where  $J_v$  is the current per unit volume recombining in the active region at threshold,  $V_{act}$  is the volume of the active region,  $P$  is the operating power of the laser, and  $\eta_i$  is the quantum efficiency at threshold.<sup>1</sup> A normalized laser current equation can begin to be derived by multiplying the threshold current term (1st term) in Eq. 2.7 by  $G/G$

<sup>1</sup>The above threshold and at threshold quantum efficiencies are not necessarily equal due to the current dependencies of different leakage paths. See Appendix E of (Corzine, 1993 ) for a detailed discussion.

and then replacing the  $G$  in the numerator with  $G = A/(1 - \eta_{cav})$ , found from Eqs 2.1 and 2.6. Substituting in  $V_{act} = d_x d_y L_g$ , where  $d_x$  and  $d_y$  are the lateral dimensions of the active region, a normalized current equation can be written,

$$\frac{I}{I_o} = \frac{1}{1 - \eta_{cav}} + \frac{1}{\eta_{cav}} \frac{P}{P_o}, \quad (2.8)$$

where,

$$I_o = \frac{d_x d_y}{\Gamma_{enh} \Gamma_{xy}} \left( \frac{J_v}{g_{mat}} \right) \frac{1}{\eta_i} A, \quad (2.9)$$

$$P_o = I_o \eta_i \frac{\hbar \omega}{q}. \quad (2.10)$$

The laser current of Eq. 2.8 approaches the normalization parameter  $I_o$  as  $\eta_{cav}$  and  $P/P_o \rightarrow 0$ . Thus,  $I_o$  is the current needed to overcome the internal losses of the laser when the mean mirror reflectance approaches 100%. Accordingly,  $I_o$  is defined as the loss current of the laser.

The normalized current equation of Eq. 2.8 displays the beauty of this design algorithm. The loss current is essentially independent of the chosen mirror reflectivity ( $\eta_{cav}$ ) which implies the two can be optimized individually. Consequently, minimizing the laser current amounts to minimizing and evaluating the loss current and then determining the optimum value of  $\eta_{cav}$  for a given output power. The question of, "How do I design a laser which minimizes the total amount of current required to achieve a given output power?" has now been answered.

### 2.3 NIST Electrically-Pumped Design

I will now discuss the application of this methodology in the context of developing a device design for growth and fabrication using the facilities available at NIST. The

device skeleton chosen using these constraints is similar to that shown in Fig. 2.2 (d). It is a top emitting 850 nm device with an intracavity  $p$ -contact and a backside  $n$ -contact. A tapered native oxide aperture is used to confine the current and the optical mode away from the sidewalls of the top mirror mesa. A topside intracavity  $p$ -contact was chosen in an attempt to reduce series resistance and to allow for the optimization of the top mirror layer thicknesses (as will be discussed in Chp. 3) without affecting the device's electrical properties.

### 2.3.1 Minimize the Loss Current

The loss current of Eq. 2.8 can be minimized by considering each parameter individually. The first term of the equation stresses the importance of maximizing the confinement factor and minimizing the cross-sectional area of the cavity. The second term,  $J_v/g_{mat}$ , is the current-gain conversion factor. This factor is a measure of the performance of the active material. The last terms emphasize the importance of minimizing the internal losses of the cavity.

#### Minimize Current-Gain Conversion Factor

For 850 nm emission, 10 nm thick GaAs quantum wells (QWs) with AlGaAs barriers can be used as the active region. The below threshold quantum efficiency for the active region is difficult to quantify and will be assumed to be  $\sim 40\%$  (Corzine, 1993). The performance of the gain needs to be optimized by examining the current-gain conversion factor.

The current-gain conversion factor is just that; it describes how much gain can

be obtained for a given amount of injected current. For a GaAs QW, a plot of the delivered gain versus injected current is sub-linear. For low current densities, the QW has not yet reached transparency and is still absorbing. For high current densities, the QW begins to saturate and the curve rolls off. Thus, there is a maximum slope of  $g_{mat}$  versus  $J_v$  and a corresponding optimum value of gain. This optimum value for a single 10 nm GaAs QW is approximately  $1100 \text{ cm}^{-1}$ . At this value the  $J_v/g_{mat}$  ratio is minimized and is approximately  $300 \text{ mA}/(10 \text{ }\mu\text{m})^2$ . If the losses of the design dictate more gain than this optimum value, additional QWs are needed. This approach ensures that each QW is operating outside the regions of transparency and saturation. The number of quantum wells needed will be determined after all the losses have been estimated.

### Maximize Confinement Factors

In a native oxide confined device, the oxide aperture is used to simultaneously confine the current and the optical mode. This inherently maximizes their overlap. Consequently, the lateral confinement factor  $\Gamma_{xy}$  for the fundamental mode is  $\sim 1$ . The enhancement factor  $\Gamma_{enh}$  in the longitudinal direction, however, is adjustable. This factor is dependent on the spatial overlap of the QWs with the standing wave of the electric field created by the two counter-propagating waves in the cavity. When the length of the gain is much larger than the wavelength of light in the cavity, the nulls in the cosine squared oscillations of the electric field intensity overlap with the gain and the enhancement factor averages to 0.5. In the case of a QW active region, the thin slice of gain can be positioned about a peak of the standing wave to achieve a

# of Wells	$\Gamma_{enh}$
1	1.9896
3	1.6850
5	1.2446
7	0.89452
9	0.77580

Table 2.1: The calculated enhancement factor for 10 nm thick GaAs wells with 10 nm thick  $\text{Al}_{0.30}\text{Ga}_{0.70}\text{As}$  barriers.

maximum enhancement factor of 2 (S.W. Corzine, 1989). The enhancement factor for the NIST VCSEL has been calculated assuming 10 nm thick GaAs wells and 10 nm thick  $\text{Al}_{0.30}\text{Ga}_{0.70}\text{As}$  barriers centered symmetrically about the peak in the standing wave (Corzine, 1993). Table 2.1 shows the calculated values for a given number of wells. At this point, the design algorithm may appear slightly corrupted. The loss current is not truly independent of the mirror reflectivity because the number of QWs is not known until all the losses have been calculated. However, the tolerance on this parameter is not critical and 3 QWs can initially be assumed, yielding a midrange value of  $\Gamma_{enh} = 1.6850$ .

### Minimize Internal Cavity Losses

The internal cavity losses can be grouped into 3 categories: scattering loss, diffraction/coupling loss, and absorption loss.<sup>2</sup> Scattering loss comes as a result of the optical mode being incident on a rough surface. For the geometry of the NIST device, the native-oxide aperture confines the optical mode far from the etched sidewalls of the top mirror mesa. Scattering loss in this geometry then primarily occurs at the oxide

<sup>2</sup>It should be noted that the internal cavity loss does not include mirror transmission losses but does include their absorption.

aperture. In Chp. 5, I will discuss simulations of the scattering loss for a variety of aperture shapes. Until then, a value of  $0.1\%^3$  will be assumed (E.R. Hegblom, 1996). Diffraction loss in the resonator is dependent on the size of the waveguide as well as the length of the resonator, which in a VCSEL is on the order of the wavelength. The diffraction loss is estimated to be only  $0.02\%$  for the fundamental mode of an  $850\text{ nm}$  device that is  $10\text{ }\mu\text{m} \times 10\text{ }\mu\text{m}$  in size and has only one etched mirror (D.I. Babic, 1994).

Minimization of the absorption losses in a VCSEL requires trade-offs to be made between optical loss and electrical resistance. The most obvious method of reducing absorption of the QW emission is to ensure that the bandgaps of all the materials comprising the VCSEL are higher in energy than the energy of the desired emission. As a result, only AlGaAs alloys with Al compositions greater than about  $5\%$  can be used for an emission wavelength of  $850\text{ nm}$  ( $1.46\text{ eV}$ ). Free carrier absorption in the heavily-doped regions of the VCSEL cavity and mirrors, however, can also be a considerable source of loss. Doping is required to reduce electrical resistance and therefore minimize the generation of heat. The Be  $p$ -doping in the top intracavity layer causes a free carrier absorption of  $\sim 11.5\text{ cm}^{-1}$  per  $1 \times 10^{18}\text{ cm}^{-3}$  of dopant (H.C. Casey, 1975). The Si  $n$ -doping needed throughout the bottom DBR yields a free carrier absorption of  $\sim 5\text{ cm}^{-1}$  per  $1 \times 10^{18}\text{ cm}^{-3}$  of dopant (D.E. Hill, 1964).

The intracavity  $p$ -contact design reduces the free carrier absorption due to Be as the entire top DBR remains undoped, and only a thin doped layer is needed to provide an ohmic contact with the metal. The absorption loss for a  $5 \times 10^{18}\text{ cm}^{-3}$  Be-doped

---

<sup>3</sup>The values given for  $A$ , as well as  $T$  and  $G$ , are approximately per-pass values as they are much less than 1.

contacting layer 184 nm thick ( $3/4 \lambda$  at 850 nm) is about 0.1%. Without the use of a second intracavity contact (which greatly increases processing complexities), doping of the bottom mirror can not be avoided. The penetration of the QW emission into the doped distributed mirror can result in significant optical absorption. However, this absorption can be dramatically reduced by placing heavy doping only at every other material interface of the high and low index layers where there is a null in the electric field intensity.

At this point in the design, the number of mirror pairs needed has not yet been calculated, and a 38-pair  $\text{Al}_{0.15}\text{Ga}_{0.85}\text{As}/\text{Al}_{0.90}\text{Ga}_{0.10}\text{As}$  mirror will be assumed. For 20 nm thick  $5 \times 10^{18} \text{ cm}^{-3}$  Be-doped regions spaced by  $\lambda/2$  throughout this DBR, the optical absorption is essentially 0%! Adding Si doping of  $2 \times 10^{18} \text{ cm}^{-3}$  throughout the rest of the DBR further reduces the device's resistance at the expense of an extra 0.1% of loss. The electrical properties of the entire device will be discussed later in this section. Tallying all the loss contributions presented in this subsection yields a total estimated internal cavity loss of  $A = 0.31\%$  that must be overcome to achieve lasing.

#### Evaluate $I_o$ and $P_o$

All the parameters present in the loss current of Eq. 2.9 have now been estimated and the loss current can now be calculated. The loss current of the NIST design for a  $10 \mu\text{m} \times 10 \mu\text{m}$  device is 1.4 mA. Thus, over 1 mA of the drive current will be needed just to overcome the internal losses of the laser. The normalized power  $P_o$  is calculated using  $I_o$  to be 1.6 mW for an above threshold quantum efficiency of 80% (Corzine, 1993).

### 2.3.2 Optimum Cavity Efficiency

Now that the loss current has been minimized the cavity efficiency can be optimized. As  $\eta_{cav} \rightarrow 1$ , the threshold current term (1st term) of Eq. 2.8 goes to infinity while as  $\eta_{cav} \rightarrow 0$  the stimulated current term (2nd term) goes to infinity. As a result, there exists an optimum value. This optimum value is found by differentiating Eq. 2.8 with respect to  $\eta_{cav}$  and setting it to zero. The optimum cavity efficiency and corresponding minimum current are,

$$\eta_{cav} = \frac{\sqrt{P/P_o}}{1 + \sqrt{P/P_o}}, \quad (2.11)$$

and,

$$\frac{I}{I_o} = \left(1 + \sqrt{P/P_o}\right)^2. \quad (2.12)$$

For a desired output power of  $P = 1$  mW,  $\eta_{cav}$  evaluates to 44%. This cavity efficiency is related to the transmission through the mirrors by Eq. 2.6. This transmittance corresponds to a calculated mean reflectance of 99.756%.

The number of QWs needed can now be calculated by solving Eq. 2.1 for  $g_{mat}$  and dividing it by the optimum gain from a single QW,  $1100 \text{ cm}^{-1}$ . This evaluation shows that the NIST design requires 3 QWs to produce the needed  $3297 \text{ cm}^{-1}$  of gain.

### 2.3.3 Electrical and Thermal Properties

The above analysis has primarily focused on the optical aspects of the VCSEL design. The electrical aspects of the device are equally as important. The forward voltage drop across the device must be minimized to reduce resistive heating. Heating



of the device decreases the efficiency of the QWs and shifts the spectral position of the gain peak with respect to the cavity resonance and thereby potentially limits the maximum output power.

The threshold current and the drive current necessary to achieve an output of 1 mW from the NIST design can be calculated from Eq. 2.8 to be 2.5 mA and 4.4 mA for a  $10\text{ }\mu\text{m} \times 10\text{ }\mu\text{m}$  device. Assuming a current of 5 mA into a  $10\text{ }\mu\text{m} \times 10\text{ }\mu\text{m}$  device yields an injection current density of  $5\text{ kA/cm}^2$ .

The most significant voltages drops for the device occur across the *n*-doped bottom DBR, *p*-doped contact layer, and the diode. Voltage drops across the *p* and *n* ohmic contacts are relatively small (tenths of a volt) in comparison to these other drops as the contacting areas are large and the semiconductor doping levels are high. The ideal voltage drop across the diode is simply determined by the photon energy of the emission to be 1.46 V. The voltage drop across the *n*-mirror can be quite high due to the heterobarrier created at each layer interface in the mirror. As previously discussed, heavy doping throughout the mirror can reduce the resistance. However, it causes significant optical absorption. To avoid this, a modulation-doping scheme can be used to only place heavily doped regions at every other layer interface. Additionally, the heterobarriers can be reduced by using a compositional grade between mirror layers rather than an abrupt step.

The voltage drop across such a mirror has been extensively studied by M. Peters (Peters, 1995). Based on this study, a 2 V drop at a current density of  $5\text{ kA/cm}^2$  is estimated for a 38-pair  $\text{Al}_{0.15}\text{Ga}_{0.85}\text{As}/\text{Al}_{0.90}\text{Ga}_{0.10}\text{As}$  DBR with graded 20 nm thick

regions in which every other interface is Si-doped to  $5 \times 10^{18} \text{ cm}^{-3}$  and the rest of the DBR is uniformly doped to  $1 \times 10^{18} \text{ cm}^{-3}$ . The heterobarrier at the interface of the *p*-contact layer and the AlAs oxidation layer similarly causes a large voltage drop. The voltage drop across this barrier is estimated to be  $\sim 0.5 \text{ V}$  based on the drop across one pair of a similarly doped 18-pair AlAs/GaAs stack studied by M. Peters (Peters, 1995). Again, a composition grade can be used to reduce this heterobarrier.

The total drop across the device is estimated to be in the neighborhood of 4 V. At 5 mA, the dissipated power is then 20 mW. The optical emission accounts for only about 1 mW of this dissipated power. The remainder of the power results in an increase in the temperature of the active region of more than 30 °C using the thermal dissipation model found in (Coldren, 1995). This temperature rise translates into a red shift of the cavity resonance of 2.5 nm and a red shift of the gain peak by nearly 11 nm. Thus, the QW needs to be designed for a bluer emission wavelength at room-temperature so at the operating current for 1 mW the QW emission aligns to the cavity resonance. The emission wavelength is shifted to 845 nm by reducing the width of the QW to 9.3 nm. Additionally, the composition of the AlGaAs barriers must be selected to reduce leakage currents at the operating temperature. The rule of thumb of choosing the barrier Al composition to achieve a minimum of  $5kT$  confinement is satisfied using the chosen  $\text{Al}_{0.30}\text{Ga}_{0.70}\text{As}$  barriers (Corzine, 1993).

#### 2.3.4 DBR Design

The top and bottom mirrors need to be designed to achieve the calculated mean reflectance of 99.756%. This mean reflectance ( $= \sqrt{R_a R_b}$ ) does not dictate the

choice of either  $R_a$  or  $R_b$ , only their mean. Ideally, it is best to have all of the light emitted through one cavity mirror. For an 850 nm device, the light must be emitted through the top mirror as light emitted through the bottom mirror will be absorbed in the GaAs substrate. To have all of the light exit the top mirror would require an infinite number of pairs in the lower mirror. Since this is unfeasible, a fraction of light will always be lost. The law of diminishing returns quickly begins to limit the achievable fraction of light out of the top. The needed number of mirror pairs in the bottom mirror rises rapidly as the fraction of light out of the top mirror becomes greater than 90%. For this reason the fraction for the NIST design is chosen to be 90%.

In a VCSEL, the top and bottom DBRs usually comprise the same two alternating layers. A large index difference (or equivalently a large difference in composition) between the two layer materials is needed to reduce the number of mirror pairs required to achieve the desired reflectivity. However, to avoid absorption of the 850 nm laser emission only AlGaAs alloys with Al compositions of  $\gtrsim 5\%$  can be used. Further, the low index layers must be composed of a sufficiently low Al concentration to avoid oxidation during the formation of the native-oxide current aperture. For these reasons,  $\text{Al}_{0.90}\text{Ga}_{0.10}\text{As}$  is used as the low index layer and  $\text{Al}_{0.15}\text{Ga}_{0.85}\text{As}$  for the high index layer in the NIST design. The top DBR terminates on one side to the cavity and on the other side to air. The bottom DBR terminates on one side to the cavity and on the other to the substrate. Termination at the high index GaAs substrate requires an odd number of quarter-wave layers to maintain the high-low-high-low alternating sequence necessary to keep all interface reflections in phase. Termination to air similarly requires

an even number of quarter-wave layers to keep all the reflections in phase.

Now that the mirror layer compositions have been established and whether an odd or even number of pairs in each stack is needed, all that is left to determine is how many pairs are needed in each stack. The characteristic matrix method (Wolf, 1980) is an easy linear algebra technique that allows the reflectance properties of thin-film stacks to be quickly evaluated for many different wavelengths. This method will be used extensively throughout this dissertation via commercial thin-film software to simulate the reflectance spectrum of vertical-cavity devices. In this section, the primary interest is to determine the peak reflectance of a lossless multi-layer stack, not its entire spectral signature. As such, I will rely on a simple and elegant analytical technique devised by S.W. Corzine and R.H Yan that is based on relating the form of the common Fabry-Perot cavity equation to that of a tanh identity (S.W. Corzine, 1991). This technique is beneficial as it is able to determine the peak reflectance of graded DBRs through combining it with coupled-mode theory. Using this technique, the field reflectance from an  $N$  layer DBR is,

$$|r| = \frac{1 - AB^{N-1}C}{1 + AB^{N-1}C}. \quad (2.13)$$

Alternatively, the number of layers needed to achieve a desired reflectance is,

$$N = 1 + \frac{1}{\ln B} \ln \left[ \frac{1}{AC} \frac{1 - \sqrt{R}}{1 + \sqrt{R}} \right]. \quad (2.14)$$

For both equations,  $A$ ,  $B$ , and  $C$  are the low-to-high index ratios ( $A, B, C \leq 1$ ) for each interface in the stack as illustrated in Fig. 2.3. The ratio of  $C$  is dependant on the magnitudes of the input and output indices and are thus different for the top mirror

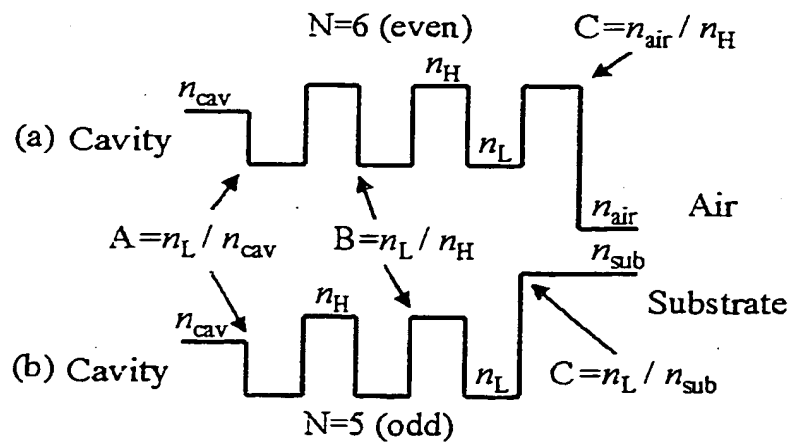


Figure 2.3: Diagram of the termination of a DBR to air (a) and to a substrate (b). In both cases the  $A$  and  $B$  ratios are the same and only  $C$  differs.

terminated to air (Fig. 2.3 (a) ) and the bottom mirror terminated to the substrate (Fig. 2.3 (b) ). It is useful to apply Eq. 2.14 in combination with the desired fraction of light out of the top mirror  $f_a$  to write two equations for calculating the needed number of layers in the top (subscript  $a$ ) and bottom (subscript  $b$ ) stacks of a VCSEL to achieve the desired mean reflectance  $R_{mean}$ . These two equations are:

$$N_a = 1 + \frac{1}{\ln B_a} \ln \left[ \frac{1}{A_a C_a} f_a (1 - R_{mean}) / 2 \right], \quad (2.15)$$

$$N_b = 1 + \frac{1}{\ln B_b} \ln \left[ \frac{1}{A_b C_b} (1 - f_a) (1 - R_{mean}) / 2 \right]. \quad (2.16)$$

In the NIST design,  $B_a = B_b = \frac{3.07}{3.46}$  for the  $\text{Al}_{0.15}\text{Ga}_{0.85}/\text{Al}_{0.90}\text{Ga}_{0.10}\text{As}$  interface,  $A_a = A_b = \frac{3.07}{3.24}$  for the  $\text{Al}_{0.30}\text{Ga}_{0.70}$  cavity-spacer /  $\text{Al}_{0.90}\text{Ga}_{0.10}\text{As}$  interface,  $C_a = \frac{1}{3.46}$  for the  $\text{Al}_{0.15}\text{Ga}_{0.85}/\text{air}$  termination, and  $C_b = \frac{3.07}{3.66}$  for the  $\text{Al}_{0.90}\text{Ga}_{0.10}\text{As}/\text{GaAs}$  substrate termination. The model by Terry was used for the  $\text{AlGaAs}$  optical indices in these ratios (F.L. Terry, 1991). Equations 2.15 and 2.16 yield  $N_a/2 = 23$  and

$N_b/2 = 37$  with the above index ratios,  $R_{mean} = 99.756\%$ , and  $f_a = 0.9$ . An additional layer is needed for the bottom mirror to keep all the interface reflections in phase for the substrate termination;  $N_b/2 = 37.5$ . The calculated reflectance of the top mirror is 99.520% and the reflectance of the bottom mirror is 99.956%. Grading in the lower  $n$ -doped DBR is needed to reduce resistance loss as previously discussed. This grade inevitably reduces the reflectance of the stack. Upon a full analysis, only one additional pair is needed to make up for this loss.

### 2.3.5 Design Schematic

Figure 2.4 illustrates the schematic for the NIST VCSEL design developed throughout this section. The device is designed to be grown on an  $n$ -doped GaAs substrate to facilitate a backside electrical contact. A “buffer” or smoothing layer of  $n$ -doped GaAs is then grown to prepare the surface. A 38.5-pair DBR consisting of  $n$ -doped  $\text{Al}_{0.90}\text{Ga}_{0.10}\text{As}/\text{Al}_{0.15}\text{Ga}_{0.85}\text{As}$  is then grown. The Al composition is graded and the doping level is increased over 20 nm at the material interfaces. The  $\text{Al}_{0.30}\text{Ga}_{0.70}\text{As}$  cavity spacers and GaAs QW active region are grown next. The remainder of the structure comprises the top 23-pair DBR. The graded quarter-wave AlAs layer above the top cavity spacer will be used to fabricate an oxide aperture. The three-quarter wave  $p$ -doped contacting layer is grown next. The contacting layer and AlAs aperture layer form one pair of the DBR. The other 22-pairs are deposited next. The growth is completed with the deposition of a thin GaAs capping layer to prevent oxidation of the top mirror layer.

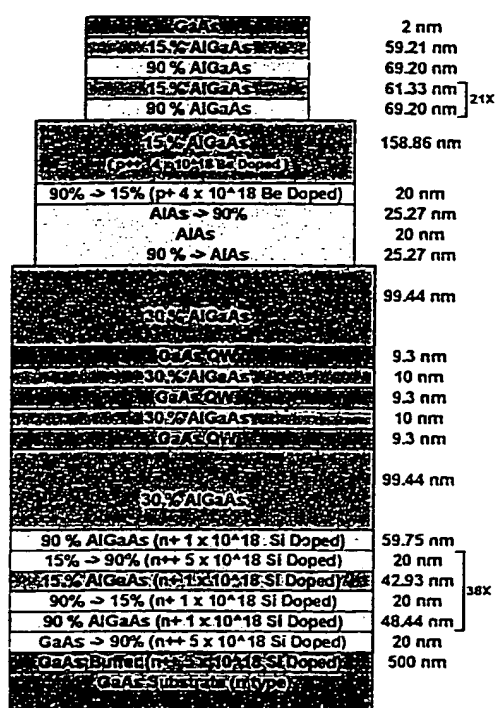


Figure 2.4: Schematic of the 1<sup>st</sup> generation NIST VCSEL..

## 2.4 Fabrication

### 2.4.1 Epitaxial Growth

The first step in fabricating a VCSEL is the growth of the structure's layers. The fabrication of these semiconductor heterostructures requires the growth of single-crystal lattice-matched layers with precisely controlled thicknesses and excellent uniformity. Three important classes of growth techniques used to achieve this are: liquid-phase-epitaxy (LPE), metal-organic chemical vapor deposition (MOCVD), and molecular beam epitaxy (MBE). While LPE and MOCVD are known for providing higher quality interfaces, MBE provides the ultimate in thickness control and uniformity (Coldren, 1995). MBE is the technique used at NIST.

MBE is performed under ultrahigh vacuum (UHV) conditions at about  $10^{-10}$  Torr. Elemental source material is contained in separate effusion cells. Each cell contains a crucible for holding a charge of material and an electric heater for melting it. Molecules evaporate from the melted charge and form a molecular beam which travels towards the heated substrate. Liquid nitrogen cryoshields line the walls of the reactor to condense any stray gases. The flux of the molecules is controlled by the cell temperatures, and cell shutters are used to select the species incident on the substrate. The stoichiometry for III-V compounds is controlled by use of the fact that group V elements are more volatile than group III elements. If the substrate is sufficiently hot,  $\sim 600$  °C, the group V atoms will re-evaporate. If a group V atom is in the presence of a group III atom, however, they will combine to form a compound. The substrate must also be sufficiently cool to allow the group III atoms to stick. Consequently, the



growth rate is determined by the group III flux and the group V flux is usually set several times higher. The typical growth rate of MBE is 1  $\mu\text{m/hr}$ .

An important aspect of the UHV environment of an MBE reactor is its compatibility with surface science tools that are based on electron scattering. This compatibility allows *in situ* measurements of the growth rate with monolayer precision. Additionally, MBE is compatible with other optical based *in situ* monitoring techniques that allow direct measurement of the optical properties of the sample (K. Bacher, 1992 ; Y.M. Houn, 1994 ; K.J. Knopp<sup>a</sup>, 1997). In VCSELs for instance, this allows thickness corrections to be made prior to the completion of the cavity and the deposition of the top DBR. These corrections help to ensure a particular resonance wavelength when the growth is complete.

#### 2.4.2 Epitaxial Processing

Once the VCSEL structure has been grown, individual devices must be defined and contacted. This is accomplished using photolithographic techniques (Williams, 1990). The processing of the NIST VCSEL design requires five main steps: an optical mesa etch, a current-confinement mesa etch, the formation of the native-oxide aperture, deposition of the top-side *p*-contact, and deposition of the backside *n*-contact. An overview of each of these fabrication steps will be given in this section. The details of each step can be found in the process sheet included as Appendix A.

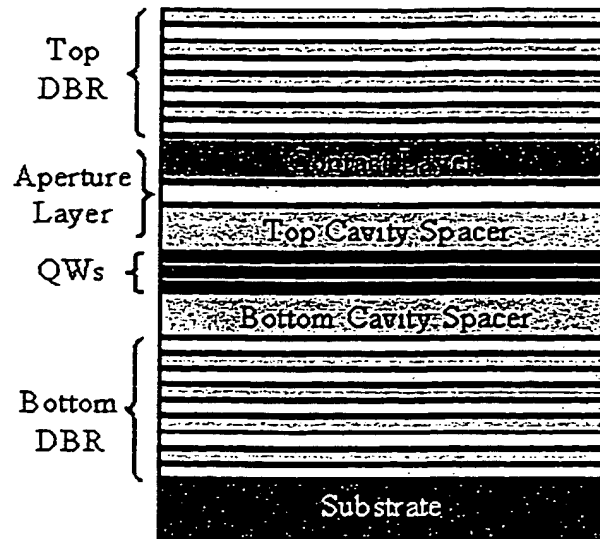


Figure 2.5: Illustration of the as grown NIST VCSEL structure in cross section.

### Optical Mesa Etch

This first process step is used to expose the heavily doped material of the intracavity contacting layer. This exposure allows the  $p$ -contact metal to be deposited onto the layer later in the process. Figure 2.5 illustrates in cross section the as-grown structure. Figure 2.6 illustrates the desired outcome from this process step. This is by far the most difficult processing step. The difficulty arises inherently from the intracavity contact geometry. The epitaxial layers of the top DBR must be etched down to the contacting layer and stopped. The lack of chlorine reactive-ion etching at NIST dictates a wet-chemical etching process. In order to precisely stop on the contacting layer, an "etch-stop" layer and a selective etchant or an *in situ* monitoring technique must be employed. Selective wet chemical etches in the AlGaAs material system either etch alloys with high gallium or high aluminum concentrations. Since the top DBR is

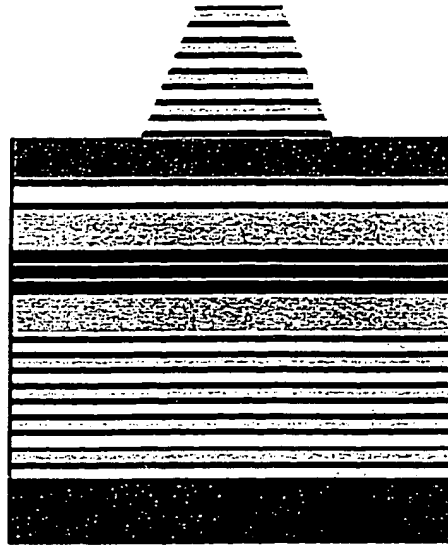


Figure 2.6: Illustration of the desired outcome from the top DBR mesa etch.

made up of alternating layers of  $\text{Al}_{0.15}\text{Ga}_{0.85}$  and  $\text{Al}_{0.90}\text{Ga}_{0.10}\text{As}$ , two selective etches can be used to remove a single layer of the top DBR at a time. This technique is quite tedious and the undercutting quickly becomes catastrophic. Alternatively, a setup was devised to allow the monitoring of the reflectance in time from a sample submersed in a nonselective chemical etchant of 1  $\text{H}_2\text{SO}_4$  (96%): 6  $\text{H}_2\text{O}_2$  (30%): 40  $\text{H}_2\text{O}$ . As the sample is etched the reflectance signal oscillates and the number of pairs removed can be determined. This *in situ* monitoring technique will be discussed in full at the end of this section.

Figure 2.7 shows a schematic of the photolithography mask used for patterning. The mask defines a  $4 \times 4$  array of devices on a  $150 \mu\text{m}$  pitch surrounded by alignment markers spaced by  $800 \mu\text{m}$ . The square mesas are aligned  $45^\circ$  with respect to the  $\langle 011 \rangle$  cleavage planes to yield more vertical sidewalls (Williams, 1990). The length of

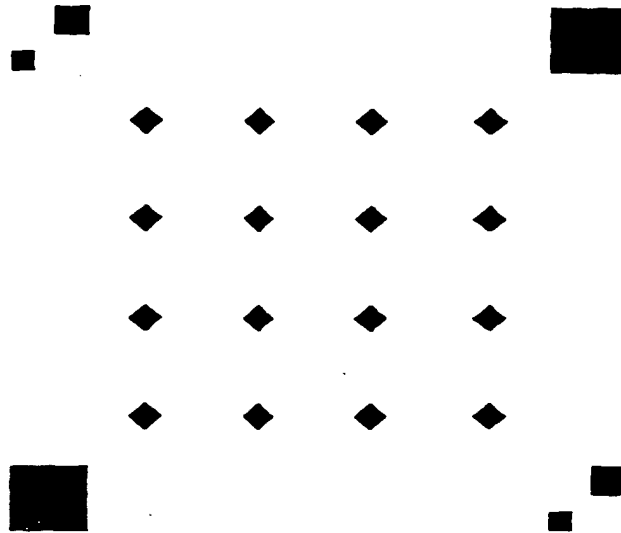


Figure 2.7: A schematic of the photolithography mask used for patterning the square optical mesas. The mask defines a  $4 \times 4$  array of devices on a  $150 \mu\text{m}$  pitch surrounded by alignment markers spaced by  $800 \mu\text{m}$ .

the squares set the approximate device size until further defined with a circular native-oxide aperture. This mask has fields of squares with 5, 10, 15, 20, 25, and  $30 \mu\text{m}$  sides. A photograph of a sample after completion of this process step is shown in Fig. 2.8. Etched mesas are observable which are  $20 \mu\text{m}$  on a side and  $\sim 3 \mu\text{m}$  tall. A scanning electron microscope (SEM) image is shown in Fig. 2.9 of an etched  $5 \times 5 \mu\text{m}$  DBR mesa atop the contact layer. The individual layers of the top mirror are observable.

### Current-Confinement Mesa Etch

The purpose of this second process step is to etch a circular mesa around the etched DBR mesa to expose the edges of the current aperture layer for oxidation and to define the lateral extent of the contacting layer for electrically isolating neighboring devices. A schematic of the desired outcome of this process step is shown in Fig. 2.10.

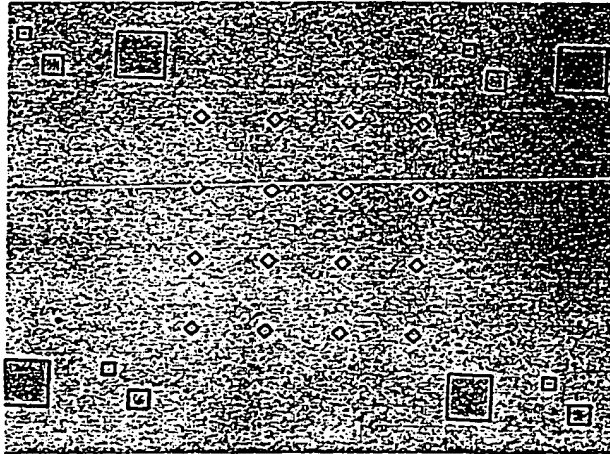


Figure 2.8: A photograph of a sample after the top DBR has been etched down to the contact layer to form mesas. The square mesas are  $20\text{ }\mu\text{m}$  on a side and  $\sim 3\text{ }\mu\text{m}$  tall.

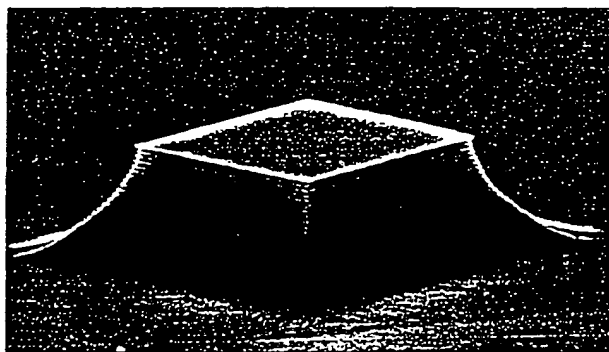


Figure 2.9: A scanning electron microscope (SEM) image of an etched  $5\times 5\text{ }\mu\text{m}$  DBR mesa atop the contact layer.

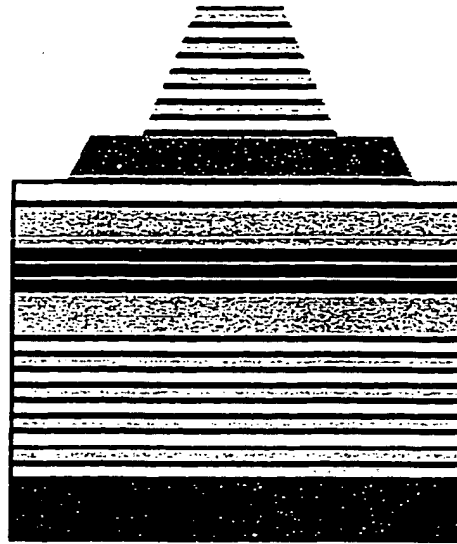


Figure 2.10: Illustration of the desired outcome after completion of the current confinement mesa etch.

A circular mask shape was chosen for this step to allow the formation of a circular current/optical confining aperture. The anisotropic nature of most wet chemical etchants of AlGaAs prevents a truly circular mesa from being replicated by the etchant into the semiconductor. This anisotropic effect is minimal as the desired etch depth is only 200 nm. In the previous process step, a square mesa was chosen as the etch depth was nearly 3  $\mu\text{m}$ . A selective etchant of citric acid (50% by weight) and hydrogen peroxide (30%) (10:1 by volume) was used to remove the  $\text{Al}_{0.15}\text{Ga}_{0.85}$  contacting layer between neighboring devices and stop on the high Al content current aperture layer beneath. The *in situ* reflectance monitoring technique can optionally be used to monitor the selectivity of the etchant and to minimize undercutting. To avoid atmospheric dehydrolyzation of the exposed layer the sample is kept submersed in fresh acetone until the next process step.

Figure 2.11 shows a schematic of the photolithography mask used for patterning. This mask has fields of circles with 50, 57, 64, 71, 78, and 85  $\mu\text{m}$  diameters for defining different contact areas. Compared to Fig. 2.7, this mask defines two additional devices in the center of the field. These additional devices are used as observation windows for monitoring the extent of the oxidation in the next process step. A photograph of the circular photoresist pattern aligned to the square mesas of the previous process step is shown in Fig. 2.12.

### Native-Oxide Aperture Formation

The high Al concentration layer exposed in the previous step oxidizes readily. A stable oxide can be formed by placing the sample into a three-zone tube furnace at 450°C under a 1 l/min flow of nitrogen gas bubbled through deionized water heated to 75°C. This allows the formation of an oxide on the exposed surfaces between neighboring devices. Additionally, the oxide front progresses laterally under the etched circular mesa to create a limiting aperture for the injected current and a lens for the optical mode. A schematic diagram of the desired outcome of this processing step is shown in Fig. 2.13. The formation, material properties, and implications of native-oxides will be discussed extensively in Chp. 5.

Figure 2.14 shows a photograph of the sample after 11 min of oxidation. The oxide between neighboring devices is visible as a dark grey (dark purple in color) region. The lateral extent of the oxide apertures is indicated by the change in reflectance observed across the circular mesas formed in the last process step that are not topped with a DBR (center mesa). This change in reflectance is due to the much lower optical

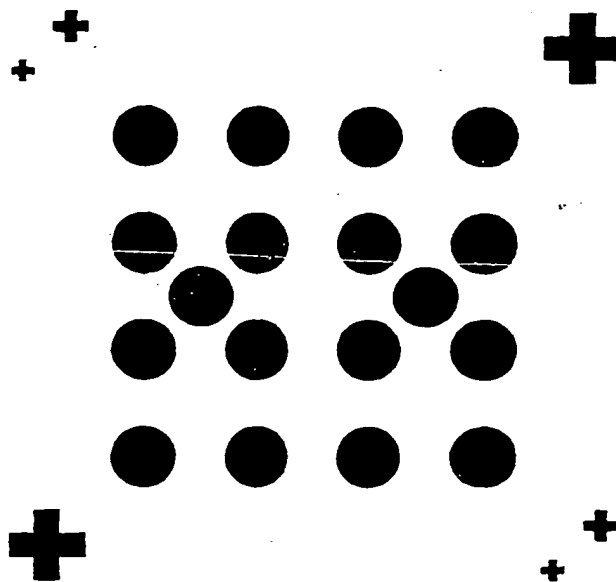


Figure 2.11: A schematic of the photolithography mask used for patterning the current confinement mesas.

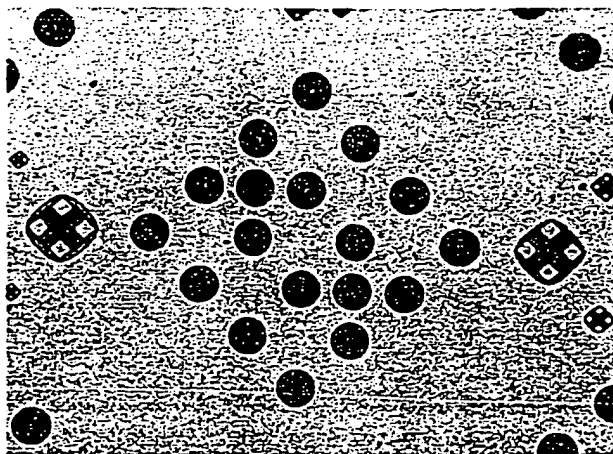


Figure 2.12: A photograph illustrating the alignment of the circular photoresist pattern for the current confinement etch to the square DBR mesas.



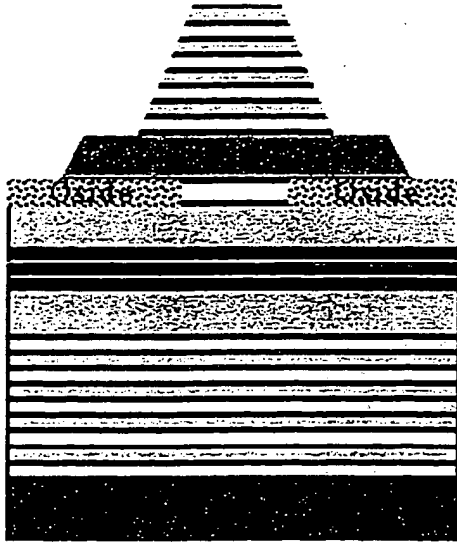


Figure 2.13: Cross sectional illustration of the VCSEL sample after formation of the native-oxide aperture.

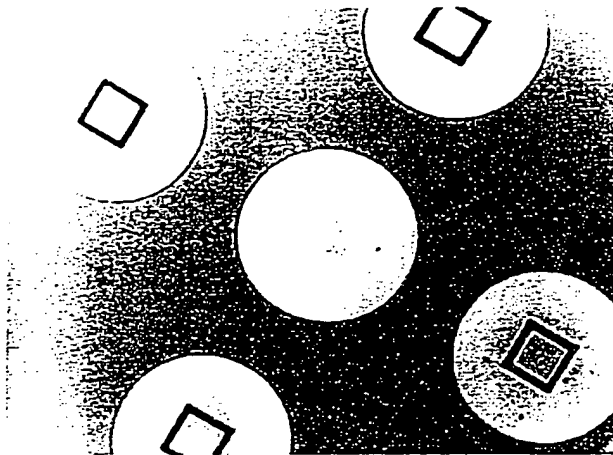


Figure 2.14: A photograph of a sample after 11 min of oxidation. The oxide between neighboring devices is visible as a dark grey colored region. The lateral extent of the oxide apertures is indicated by the change in reflectance observed across the circular mesas formed in the last process step that are not topped with a DBR (center mesa).

index of the oxide ( $\sim 1.5$ ) in comparison to the semiconductor ( $\sim 2.8$ ). The aperture is not visible in the mirror-topped mesas as the DBR is highly absorbing at the visible wavelengths. The oxide aperture observed in Fig. 2.14 is  $\sim 18 \mu\text{m}$  in diameter.

### Top-Side *p*-Contact

With the extent of the top-side contacting layer defined and the oxide aperture formed, the last process step needed on the top-side of the wafer is the deposition of the *p*-contact metal. It is desirable to have the completed contact (semiconductor and metal) exhibit linear current-voltage (IV) characteristics with minimal resistance. This type of contact is known as an ohmic contact. If the contacting layer of AlGaAs is doped highly enough, almost any metal deposited on its surface will result in an ohmic contact without having to be alloyed (Williams, 1990).

In this process step, a nonalloyed ohmic contact is formed by electron beam deposition of Ti (6 nm) and Au (200 nm) onto the  $5 \times 10^{18} \text{ cm}^{-3}$  Be doped contacting layer. The thin Ti layer wets the surface to help the Au adhere. Lift-off techniques are used for patterning of the metal (Williams, 1990). Before the metal is deposited, the sample is dipped in a solution of ammonium hydroxide and water (1:15) to remove any oxide build-up on the surface of the contacting layer resulting from the previous processing step and a UV/ozone cleaning step. The desired outcome of this processing step is illustrated in Fig. 2.15.

Figure 2.16 shows a schematic of the photolithography mask used for the lift-off patterning. Die numbering is visible in the center of the field. This mask has fields to mate with the circular and square mesas dimensions of the previous processing steps.

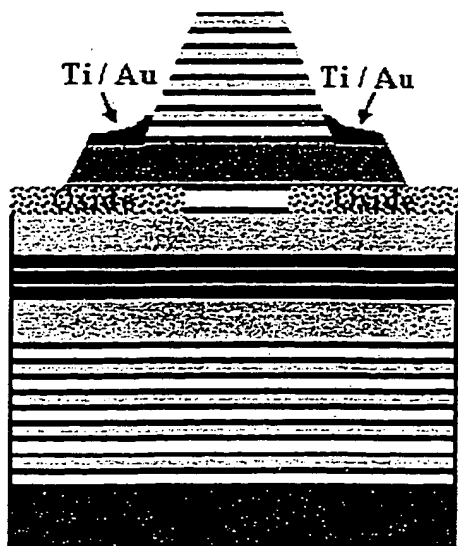


Figure 2.15: Cross sectional illustration of the VCSEL sample after deposition and lift-off of the  $p$ -metals.

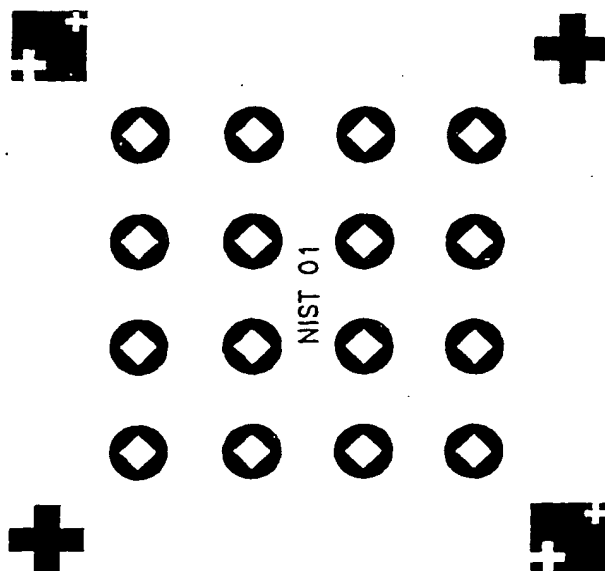


Figure 2.16: A schematic of the photolithography mask used for lift-off patterning of the  $p$ -metal.

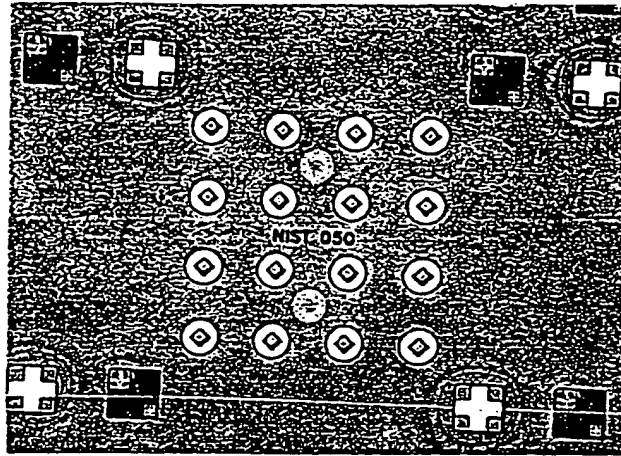


Figure 2.17: A photograph of the patterned photoresist prior to evaporation of the *p*-contact metals. The clear openings (light gray color) define the shape of the contact metal. The oxide aperture is also visible through the two mesas centered above and below the die labeling.

Figure 2.17 shows a photograph of the patterned photoresist prior to metal deposition. The white areas are openings in the resist where the metal will be deposited onto the semiconductor.

The lift-off pattern discussed above allows wafer-probe testing of individual devices. It does not facilitate manufacture of a packaged device. The oxidation step performed results in the creation of a layer of oxide atop the cavity of the VCSEL between neighboring devices. Wire traces can be routed in the contact metal out from individual devices to large  $100\ \mu\text{m} \times 100\ \mu\text{m}$  bond pads across the insulating oxide. The oxide insulates the wire trace from the undoped cavity and backside *n*-contact below. A cross sectional illustration of this layout is shown in Fig. 2.18. Figure 2.19 shows a schematic of the wire-bond lift-off mask. The most obvious concern with this layout is the capacitance of the oxide and its ability to isolate devices. This layout shows promise,

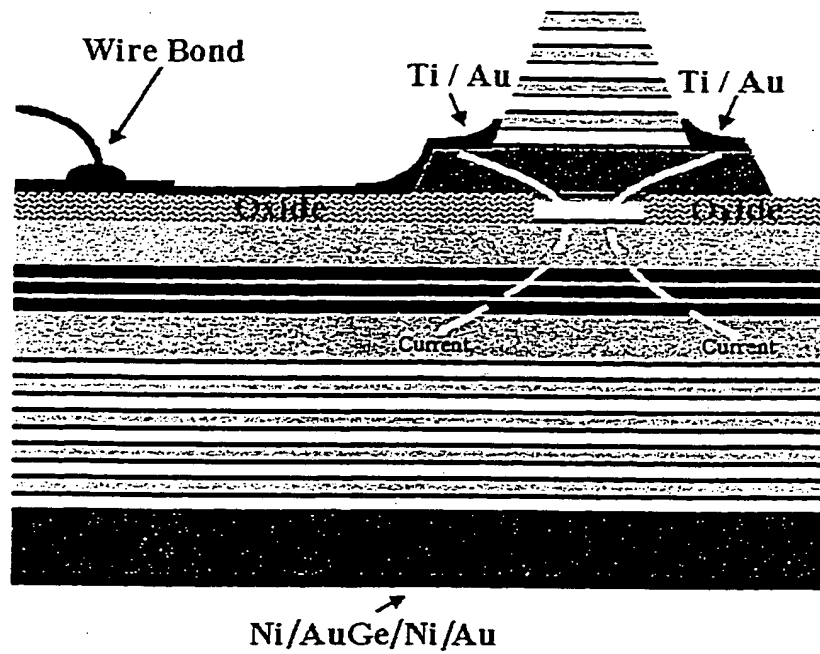


Figure 2.18: A cross sectional illustration of a proposed *p*-metallization layout for routing oxide-insulated wire traces.

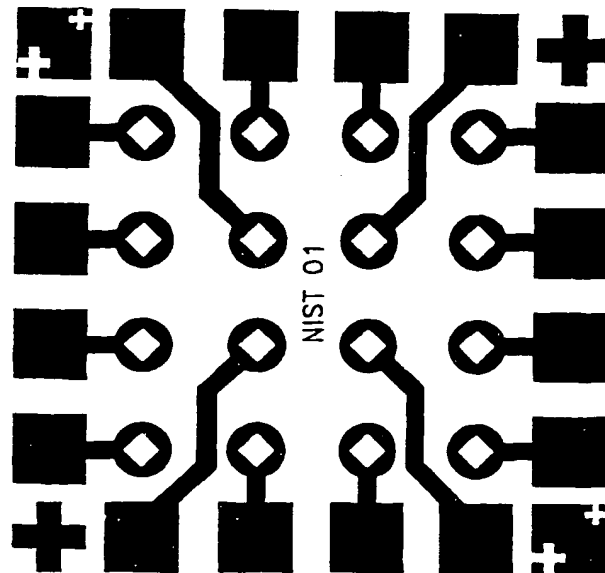


Figure 2.19: Schematic of the photolithography mask used for the lift-off patterning of the wire-bond traces.

however, as a different approach relying on a fully oxidized buried layer for isolating electrical traces has been demonstrated at speeds up to 1 Gbit/sec (G. Giaretta, 1997).

### Backside $n$ -Contact

The last process step is deposition of the  $n$ -contact metals onto the backside of the sample's substrate. This is a blanket deposition across the entire backside. Every device on the sample thus shares one common contact. The contact is formed by electron beam deposition of Ni (0.5 nm), AuGe (105 nm), Ni (25 nm), and Au (120 nm) onto the  $n$ -type GaAs substrate. This contact recipe is designed to be an ohmic contact when alloyed. The Ni serves to wet the surface and assist the infusion of Ge into the GaAs while the Au is an overlayer used to enhance the sheet conductivity and improve the surface morphology (Williams, 1990). Alloying the contact in the oxidation furnace results in destruction of the device due to peeling of the oxide aperture. The use of a rapid thermal annealer (RTA) may prevent this problem. The lack of access to an RTA forced the use of this contact without alloying. The high mobility of electrons and the large contact area (typical 1 cm  $\times$  1 cm), however, help to minimize the contact's resistance. While no photoresist patterning is required in this step, photoresist is commonly spun onto the topside of the sample to prevent abrasion of the processed device when mounted upside down in the evaporator.

### Complete Device

Figure 2.20 shows a photograph of a processed 4 $\times$ 4 VCSEL array. The dark regions are the surface oxide and the bright regions are the  $p$ -contact metal. A somewhat

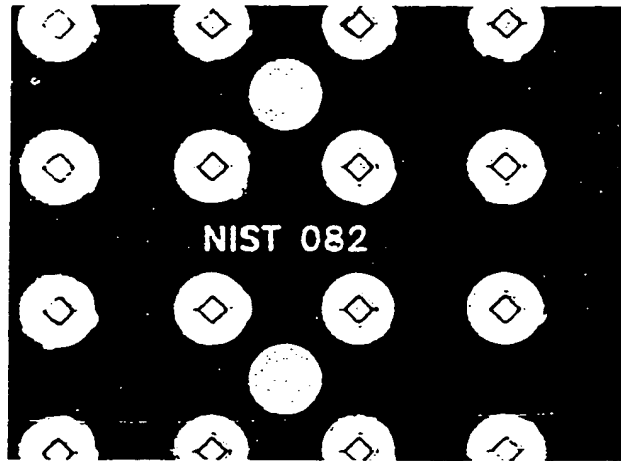


Figure 2.20: A photograph of a fully processed NIST 4×4 VCSEL array.

ragged edge is observed in the contacting metal on each device. This is a result of a nonideal edge profile on the photoresist which caused tearing as the excess metal lifted off.

#### *In situ* Wet-Etch Monitoring

A setup was devised to allow the real time monitoring of the etch depth (and hence control) for a sample submersed in a chemical etchant. This setup was inspired by the published work of N. Chand using bulk-optics (N. Chand, 1993). Figure 2.21 shows a schematic and photograph of the *in situ* wet-etch monitoring setup I have designed and implemented at NIST. The setup was designed to be operated inside a class 100 clean room exhaust hood due to the caustic nature of the chemical etchants and the cleanliness needed for VCSEL fabrication. A fiber-optic delivery approach was implemented to minimize the equipment needed under the fume hood. This allows

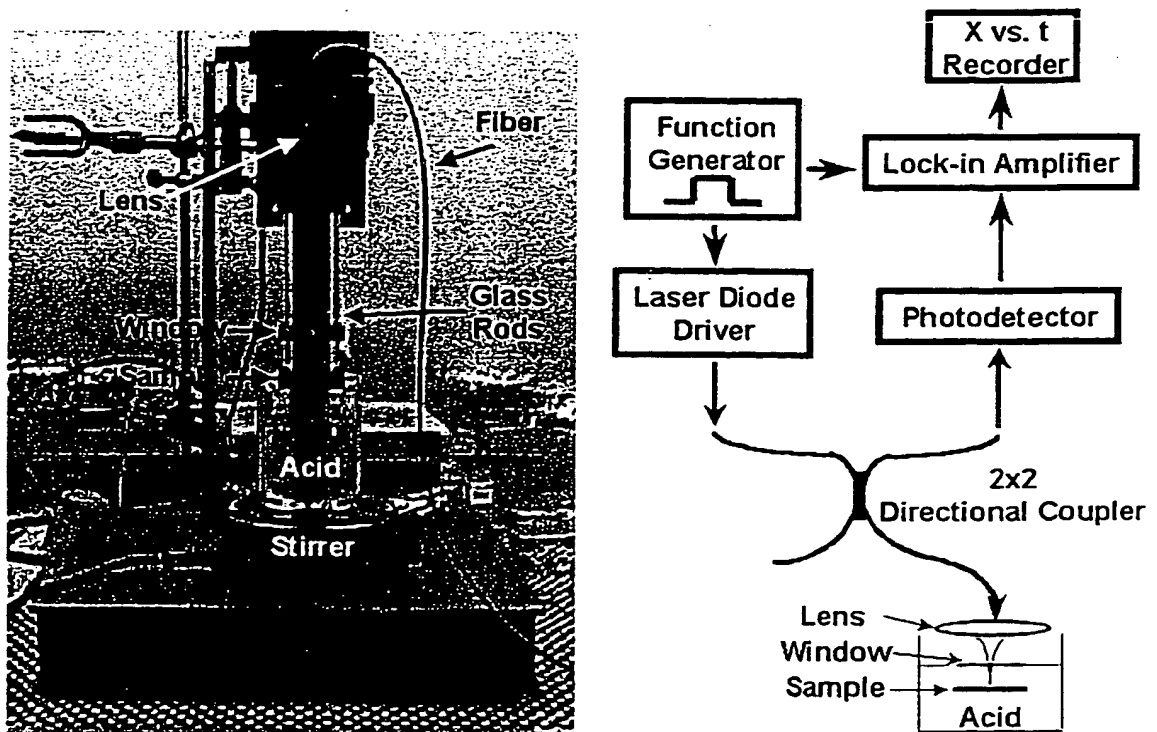


Figure 2.21: Schematic and photograph of the *in situ* wet-etch monitoring setup at NIST.



drive electronics, photodetectors, and data acquisition equipment to be placed outside the hood while requiring only a single fiber to pipe the source light to and from the sample.

The basic principle of operation for this setup is to illuminate the sample with laser light and monitor the oscillations of its reflectance in time. An 850 nm laser diode is used as the source to avoid absorption in the semiconductor and to be close to the Bragg wavelength of the VCSEL mirrors. A lock-in amplifier and photodetector are used for detection of the reflectance signal. The laser light is launched into one arm of a 2×2 directional coupler where it is split into 2 output legs. The output from one leg is focused with an aspheric lens through a fused silica window onto the sample while the output from the other leg is terminated. The fiber coupled lens is held above the acid on a translation stage in a kinematic mount. Four glass rods suspend a custom teflon cage-plate assembly housing the window and a second flat fused silica plate which serves as a sample holder. The sample is mounted with acetone soluble wax onto the second plate. The optics are aligned by maximizing the reflectance signal out of the fourth coupler leg through compensating for the change in focal length in water and the tilt of the sample imposed by the mounting wax. The reflectance signal is acquired using a lap-top computer and an A/D card. To begin etching the cage-plate assembly is lowered into the etchant until the window is in contact with the acid. The purpose of the window is to displace the water to create a stable exit surface for the reflected light. If the window is not used, the reflected light from the sample is refracted at the acid-air interface at a time varying angle due to the surface waves on the water caused

by mechanical vibrations in the room. This results in a time-dependent coupling loss that swamps the desired signal. To further isolate vibrations, the setup was built on top of a 1 ft×1 ft optical breadboard using a damped mounting rod.

The origin of the reflectance oscillations is a consequence of the interference of the reflectance from the layer being etched and the rest of the structure (which can be thought of as an equivalent substrate). The turning values of the oscillations correspond to the removal of a quarter-wave of material at the monitoring wavelength (Macleod, 1969). Analytical expressions can easily be derived for the oscillation frequency and contrast in the simplest case of a single layer atop a substrate (Yeh, 1988). For this work, the amplitude of the oscillations is described by a more complex relationship. However, the real interest here is the oscillation period. For every mirror pair removed ( $\lambda/2$ ), the reflectance oscillation will undergo one oscillation period. Figure 2.22 shows a measured signal obtained by etching the VCSEL structure of Fig. 2.4 in 1 H<sub>2</sub>SO<sub>4</sub> (96%): 6 H<sub>2</sub>O<sub>2</sub> (30%): 40 H<sub>2</sub>O. The measured etch rate is 0.5  $\mu\text{m}/\text{min}$ . Based on the time needed to flush the sample with H<sub>2</sub>O to stop the reaction, the etch depth can be controlled for this etchant solution to better than 30 nm.

## 2.5 Characterization

### 2.5.1 Wafer Level Testing

Various methods of characterization are necessary in all phases of fabrication to ensure a working device at the completion of the process. Once the sample is grown, the wafer is first characterized with a photoreflectometer for collection of the sample's

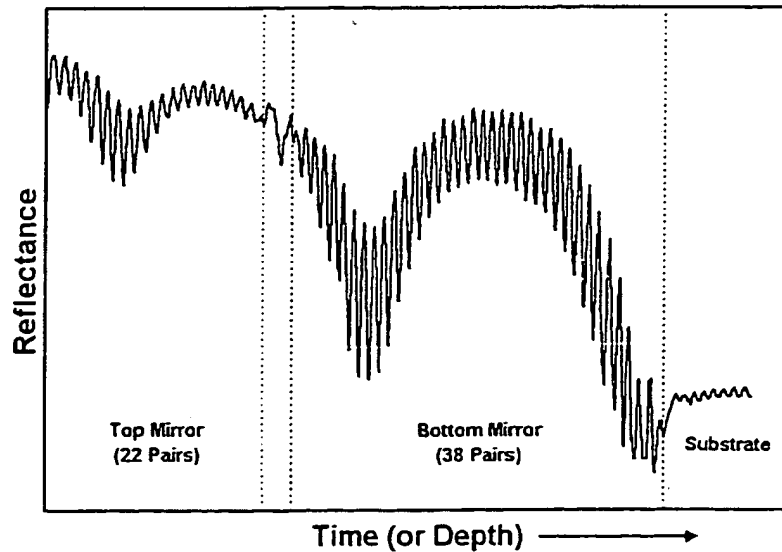


Figure 2.22: *In situ* reflectance signal obtained by etching through the entire VCSEL structure of Fig. 2.4.

reflectance signature and determination of the resonance wavelength. In fact, a great deal of information about the growth can be determined from this simple measurement (D.H. Christensen, 1992). Drifts and systematic error in the growth rates can be estimated through careful modeling of this data. Correlation of the model fit parameters with X-ray diffraction and photoluminescence measurements provides further information on the aluminum composition and physical thickness of the mirrors pairs (D.H. Christensen, 1992). Cross-sectional photoluminescence is also frequently used at NIST to allow excitation of the QW and collection of its emission via the side of the sample to avoid spectral filtering of the emission by the Fabry-Perot resonance of the cavity (D.T. Schaafsma, 1995). The offset between the QW emission peak at low injection levels can then be compared to the spectral position of the cavity resonance measured by the photoreflectometer. This provides valuable information on the likelihood of the

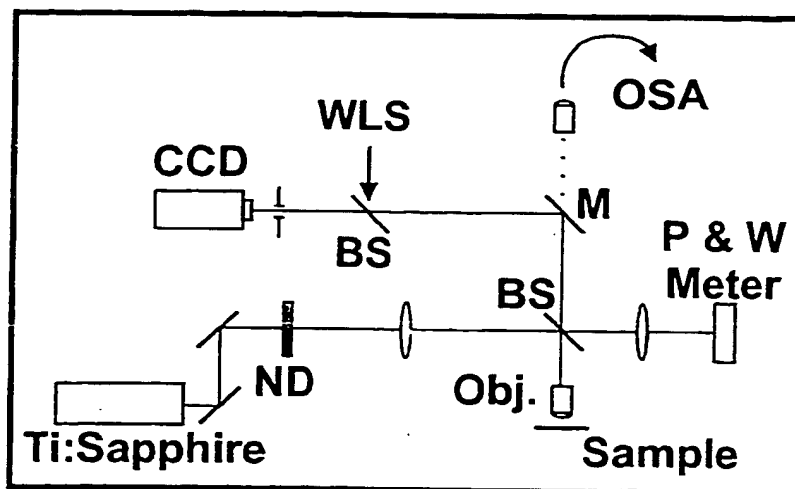


Figure 2.23: Illustration of the optical pumping setup. A tunable cw Ti:Sapphire laser is focused onto the sample using an objective. A CCD camera and white light source (WLS) are used for alignment of the beam. Removal of mirror M allows VCSEL output to be routed to a fiber-coupled optical spectrum analyzer (OSA). Incident pump power and wavelength are monitored (P&W Meter).

device to lase when the QWs become warmed through resistive heating.

In many cases, the as-grown electrically-pumped laser structure can be brought to lasing through excitation of the QWs with the light from a Ti:Sapphire laser. Laser light can be tuned to a minimum in the reflectance spectrum for transmission into the structure and absorption by the QWs. If enough confinement is achieved and gains exceed losses, lasing is stimulated. Figure 2.23 shows a schematic of the optical pumping setup I have developed at NIST. This setup consists of a tunable Ti:Sapphire pump laser, a focusing objective, a CCD camera, and an optical spectrum analyzer. Optical pumping of VCSELs will be further discussed and explored in Chp. 3.

The characterization methods discussed so far are all wafer level tests carried out on the as-grown sample. No processing of the wafer is necessary. This is a very

important point for a production environment. This allows an extensive amount of information regarding a growth to be obtained, if so desired, prior to the expensive and time-consuming tasks of processing and packaging.

### 2.5.2 Device Level Testing

The wafer level tests described above are concerned foremost with the optical properties of the sample. The electrical aspects of the sample are most easily evaluated by the performance of completed devices and processed test samples. The *p*-contact, for instance, in an intracavity contacted device can be a particularly troubling source of resistance. A test pattern for measuring the contact's resistance and the resistance of the  $5 \times 10^{18} \text{ cm}^{-3}$  doped contacting layer can be devised by creating a series of contacts separated by varying distances along an etched line (transmission line technique) (Williams, 1990). With this technique, nearly ohmic behavior was observed from the nonalloyed Ti/Au contact of the NIST VCSEL's *p*-contact structure. The contact resistance was extrapolated to be  $18 \text{ m}\Omega\cdot\text{cm}^2$  and the resistivity of the contacting layer was measured to be  $0.012 \text{ }\Omega\cdot\text{cm}$  (consistent with (Sze, 1981) for GaAs). Another useful test structure is created by performing the first mesa etch through the top DBR as a blanket (not patterned) etch. Performing the remaining process steps as specified for the VCSEL structure results in the creation of a light-emitting diode (LED). This structure provides identical electrical characteristics as the fully processed VCSEL while allowing observation of the QW emission at what would be lasing currents. This allows the current spreading characteristics of the device to be evaluated without the influence of spatial hole-burning effects.

An electrical/optical probing station was developed to characterize the performance of fabricated VCSEL devices and test structures. The sample is placed backside down onto a gold plated stage and a wafer probe is aligned using a microscope to the *p*-contact of the device under test. Current is driven with either a CW or pulsed driver. The driver provides the measurement of the forward voltage (*V*) and the current flow (*I*) through the device is measured with an inductive current probe. The voltage and current waveforms are then displayed on an oscilloscope. The optical emission from the sample is collected with the microscope and routed to an optical fiber for connection to an optical spectrum analyzer. Alternatively, the lasing aperture can be imaged onto a CCD camera or a large area Si detector can be slid in just above the sample to take light (*L*) versus current data.

The *L-I* curves taken on  $33\ \mu\text{m} \times 33\ \mu\text{m}^4$  native-oxide apertured devices are shown in Fig. 2.24. The corresponding *I-V* curves for these devices are shown in Fig. 2.25. The *L-I* and *I-V* data were taken under pulsed conditions using a  $2\ \mu\text{s}$  pulsewidth at a repetition rate of 1 kHz. The measured threshold current is 25 mA and the maximum output power is 4 mW. A captured image of the lasing aperture is shown in Fig. 2.26. Diffraction and interference effects are observable around the perimeter of the device.

### Lateral Resistance

CW lasing was not achievable in these devices due to the large forward voltages.

Inherently, the intracavity *p*-contact design forces current to flow laterally from the

---

<sup>4</sup>This device was processed in an identical manner as described in section 2.4. However, a square current confinement etch mask was used.

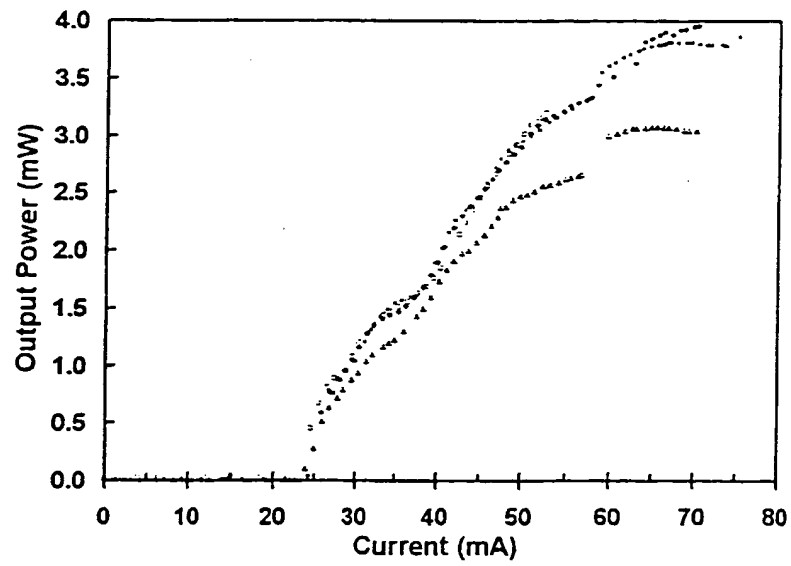


Figure 2.24: Pulsed L-I curves from  $33\ \mu\text{m} \times 33\ \mu\text{m}$  native-oxide apertured NIST VCSELs.

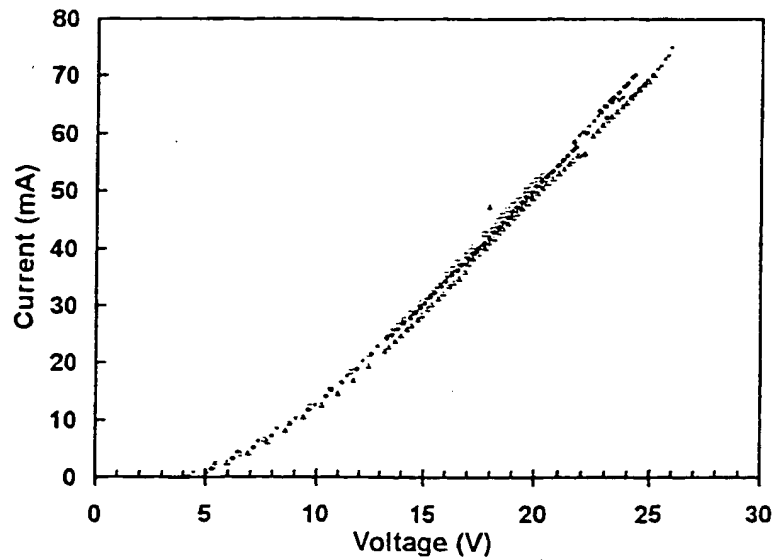


Figure 2.25: Pulsed I-V curves from  $33\ \mu\text{m} \times 33\ \mu\text{m}$  native-oxide apertured NIST VCSELs.

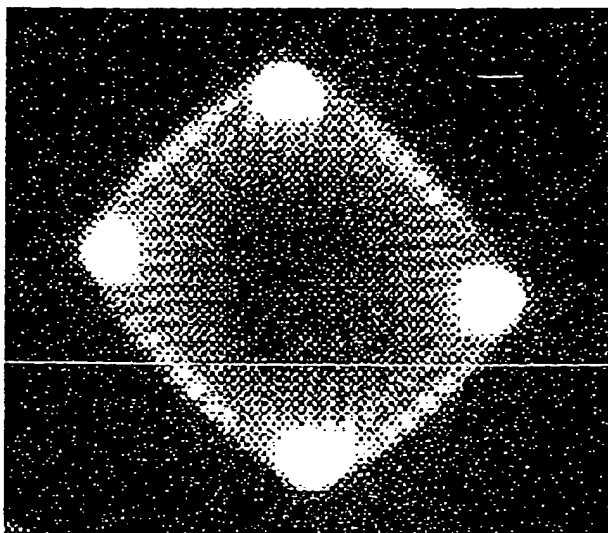


Figure 2.26: Picture of the  $33\text{ }\mu\text{m} \times 33\text{ }\mu\text{m}$  lasing aperture of a NIST VCSEL imaged by a CCD camera.

contact across the contacting layer and down through the opening in the oxide aperture into the diode. This lateral current flow across the thin contacting layer is quite resistive. Thus the distance the current must flow laterally along this layer must be minimized. The minimum distance is defined by the slope of the sidewalls of the etched DBR (See Fig. 2.15 page 40). However, it is desirable to have the oxide aperture smaller than the topmost layer of the etched DBR stack to ensure the optical mode is confined away from the etched sidewalls to minimize scattering losses. Consequently, the current at a minimum must flow laterally several micrometers from the contact to the edge of the oxide aperture. The device of Fig. 2.26 forced the current to flow laterally ten times this distance due to a lengthy oxidation. The series resistance of the diode is several hundred ohms. This resistance was reduced to about  $100\text{ }\Omega$  in a similarly processed sample having an oxide aperture diameter of  $18\text{ }\mu\text{m}$  within a mirror mesa having a



top layer width of  $20\text{ }\mu\text{m} \times 20\text{ }\mu\text{m}$ . The maximum power for this device, however, was limited to 0.6 mW by misalignment of the cavity resonance and QW emission peak.

### Discussion of Current Spreading

The image of Fig. 2.26 exhibits four separate lasing filaments each approximately  $5\text{ }\mu\text{m}$  in diameter. The presence of these filaments in the corners of the current aperture suggests that the lateral resistance across the device aperture is greater than the resistance longitudinally through the structure. This has been identified as a current crowding problem and as a major drawback to intracavity contacted devices (J.W. Scott, 1993). At low current levels, the device resistance is dominated by the diode resistance and the current injection is fairly uniform across the aperture. At higher current levels, the diode is being turned on harder and its dynamic resistance becomes low and the lateral currents in the contacting layer become shunted. Additional current is then only injected around the perimeter of the oxide aperture. This behavior is also observed in the emission from an LED processed from the VCSEL material.

By adding a resistive layer beneath the heavily doped contacting layer, the series resistance of the device can be increased and the laterally flowing current will travel further across the device aperture before turning down through the diode (J.W. Scott, 1993). This technique works to spread the current across the laser's aperture at the expense of increasing the ohmic heating of the device.

To model the current density versus radial device position of various two layer contacting designs, I have devised a simple one-dimensional resistor network model. This model was verified by comparing it to the published values in (J.W. Scott, 1993) obtained

using a two-dimensional finite-element model. Excellent agreement was observed for all radii with nearly exact agreement found in the region of interest, namely the device's center. Modeling of the device shown in Fig. 2.26 predicts a delta function of high current density at the perimeter of the oxide aperture and a voltage drop laterally across the contact layer of almost 10 V at 17 mA. A dramatic improvement in device performance is anticipated through the replacement of the contacting layer in Fig. 2.4 with a 357 nm thick  $5 \times 10^{18} \text{ cm}^{-3}$  Be-doped layer atop a 297 nm thick  $1 \times 10^{17} \text{ cm}^{-3}$  Be-doped layer. The resistor model predicts that for a 15  $\mu\text{m}$  diameter native-oxide apertured device, the majority of the aperture will be lasing for injection currents of three times threshold. Carrier diffusion is expected to further help to fill in the lasing aperture.

## 2.6 Summary

Throughout this chapter, I have presented the design, fabrication, and characterization of the first electrically-pumped VCSELs realized at NIST. I have given a brief overview of the design methodology used. I have applied this approach to the design of 850 nm VCSELs with intracavity *p*-contacts and native-oxide current confinement. The anticipated optical, electrical, and thermal properties were optimized through these calculations. I have discussed the clean room process for the fabrication of these devices. In this process, I have employed an *in situ* monitored wet etching technique for the precise and accurate control of etch depth. Additionally, I have characterized the performance of the fabricated VCSELs. A maximum output power of 4 mW was observed under pulsed drive conditions. Methods of reducing current crowding effects

through improving the spreading of current across the device aperture have also been discussed.

This chapter elucidates many traits unique to VCSELs that will be further explored in subsequent chapters. The effects of current spreading on the near-field modal pattern and diffraction losses from the oxide aperture are two such traits that will be explored. The device development work of this chapter is enabling a better understanding of the fundamental issues affecting device performance for the purpose of identifying and advancing the needed metrology tools and services at NIST.

## Chapter 3

### Optoelectronic Band Engineering

#### 3.1 Introduction

The concept of photonic crystals was first introduced in the separate works of E. Yablonovitch and S. John (S. John, 1987 ; E. Yablonovitch, 1987). A photonic crystal is a system with a dielectric function that is periodic along 1, 2, or 3 orthogonal directions. The dimensionality of the crystal is determined by the number of orthogonal periodic directions. Photonic crystals offer the possibility of building up photon density of states in a similar fashion as electronic density of states in solids. Photonic crystals have the ability to suppress electromagnetic wave propagation through the creation of a forbidden gap and to allow its propagation at frequencies above and below the gap. The first pioneering reports generated a host of enthusiasm as new classes of devices were proposed. Among them was the idea of placing a light emitter inside a three dimensional (3D) photonic crystal to inhibit or enhance spontaneous emission (E.M. Purcell, 1946 ; D.J. Heinzen, 1987) and to possibly create thresholdless microcavity lasers (M. Yamanishi, 1991).

VCSELs are the one-dimensional (1D) equivalent of 3D photonic crystal mi-

crolasers. VCSELs use two DBRs to form a cavity to confine light to 1D. As will be discussed in Chapter 5, native-oxide apertures can also be used as intracavity lenses to help laterally confine the optical mode. This confinement takes VCSELs one step further towards achieving true 3D photonic confinement. The recently reported achievement of omnidirectional reflectance from a 1D dielectric lattice (DBR) will potentially help VCSELs to achieve true 3D optical mode confinement (Y. Fink, 1998). It is foreseeable that in this pursuit researchers will tailor the photonic bandgap properties of these 1D omnireflectors to achieve desired 3D-like confinement properties for particular applications.

In this chapter and in the literature (K.J. Knopp<sup>a,b</sup>, 1996 ; K.J. Knopp<sup>a</sup>, 1997), I address the smoothing of the interference fringes in a VCSEL's reflectance spectrum through the use of commercial thin-film design software in an effort to reduce optical pump-coupling instabilities and eliminate the need for a tunable pump laser. A general technique for numerically optimizing the optical admittances in vertical-cavity structures is used to suppress the interference ripple in the typical reflectance/transmittance spectra. This technique is applicable to any vertical-cavity device whose photonic properties at various wavelengths requires modification for specific applications. This optimization is effectively tailoring the 1D photonic bandgap properties of a VCSEL to create a continuum of extended propagation states over a broad (50 nm) spectral region.

The interference fringes in the typical VCSEL reflectance spectrum arise from the use of quarter-wave DBRs as cavity mirrors. The mathematical derivation of the occurrence of the fringes in the reflectance spectrum of a quarter-wave stack is not trivial

(Macleod, 1969). Epstein has concluded that the fringes are a consequence of the mismatching of the equivalent admittances of the substrate, multilayer stack, and incident medium (L.I. Epstein, 1952). To smooth the interference fringes, better matching of admittances is needed. Methods for the reduction of the pass-band ripple in quarter-wave edge-filters have been discussed by Macleod (Macleod, 1969).

Previous optical pumping methods coupled pump light into VCSEL cavities through the short-wavelength interference fringes in the reflectance spectrum (K.J. Ebeling, 1991). The steep slopes and narrow widths of these fringes required a tunable pump laser to spectrally align the pump wavelength to a fringe minimum. Despite careful spectral alignment, the reflectance spectrum often shifted due to localized device heating from the pump beam. Therefore, the pump's coupling efficiency, as well as the VCSEL's output and lasing threshold, could change with device temperature. Viable optically pumped VCSEL applications have been limited by this coupling instability and the associated high cost of a tunable pump laser.

To date, optically pumped VCSELs have primarily served as stepping stones to their electrically pumped counterparts (M.A. Fisher, 1993 ; D.I. Babic, 1994 ; H. Jeon, 1995). Optical pumping has also provided a means of rapid material evaluation prior to costly device fabrication steps (Corzine, 1993). Stable optically pumped and hybrid optically/electrically pumped VCSELs, however, also hold promise in power-by-light applications, such as sensors.

I have modified the typical quarter-wave DBR interference fringes by applying thin-film design optimization techniques to semiconductor multilayers. I have created

devices with a wideband window of low reflectance while maintaining cavity-mode field overlap at the quantum wells. These devices allow for the thermally induced reflectance shift and eliminate the requirement of an expensive tunable pump laser. Further, they facilitate the use of inexpensive spectrally broad pump sources, such as LEDs.

The general approach of this work is to simulate, grow, and compare a typical VCSEL, as a control structure, to an optimized "low-ripple" VCSEL. I begin this chapter with a brief discussion of the photonic bandgap properties of DBRs to provide background for this chapter and Chapter 6. The presentation of this background material is an effort to further motivate the work of this chapter and elucidate its more general impact in the area of photonic band engineering. In section 3.3, I discuss the design of these low-ripple devices through presentation of the optimization scheme and modeled responses. Experimental measurements evaluating and comparing the grown devices are presented in section 3.4. Layer thickness variations through both physical and temperature-induced changes are considered in section 3.5, and section 3.6 serves to conclude.

## 3.2 Photonic Bandgap Properties of a Distributed Bragg Reflector

An infinite quarter-wave stack is a one-dimensional photonic crystal (E. Yablonovitch, 1987). The propagation of light through the stack is suppressed for wavelengths along the high reflecting stopband as the reflections from every material interface constructively add in phase so no wave can propagate. Thus, all incident wavelengths along the stop band fall within the forbidden gap. At the edges of the forbidden gap, in the reflectance nulls, are the first extended states that allow incident

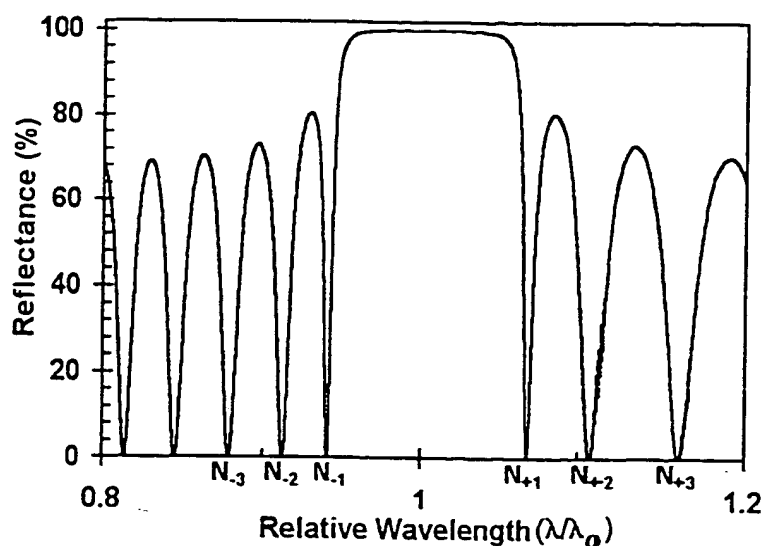


Figure 3.1: Plot of the reflectance spectrum of an air-terminated 20-pair AlAs/GaAs DBR with the first three extended states labeled.

light at that wavelength to propagate through the stack. There are an infinite number of extended states in the reflectance spectrum of an infinite quarter-wave stack. The infinite number of states forms a continuous band. In a finite quarter-wave stack, the number of extended states precisely equals the number of mirror layers in the stack. The first three extended states of a 20-pair AlAs/GaAs DBR are labeled in the plot of Fig. 3.1. Figure 3.2 shows the electric field intensity throughout the stack calculated for a wavelength at the center of the forbidden gap (relative wavelength of 1). The electric field intensity decays exponentially through the stack from a maximum at the incident-medium/stack interface. As a consequence of this decay, the reflected radiation appears to be coming from somewhere inside the stack. The  $1/e$  point of the decaying field is commonly used to define the penetration depth into the mirror. Figure 3.3 shows the electric field intensity throughout the stack calculated for a wavelength at the



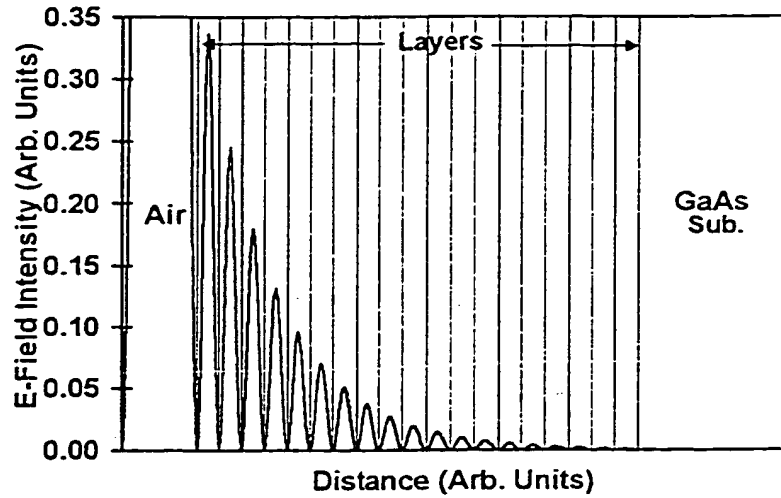


Figure 3.2: Plot of the calculated electric field intensity throughout a 20-pair AlAs/GaAs DBR for a wavelength at the center of the forbidden gap (relative wavelength of 1)

$N_{-1}$  and  $N_{-2}$  extended states. The electric field intensity propagates through the stack for both states without a reduction in amplitude. Resonant effects are seen through the observed build-up of the intensity within the structure. This build up is a storage of energy that effects the propagation time of light through the stack. These temporal effects will be discussed in Chapter 6. Calculating the electric field intensity throughout the stack for a wavelength at the  $N_{+1}$  and  $N_{+2}$  extended states shows identical distributions to those in Fig. 3.3, however, they are of opposite phase. This shift is a result of the  $\pi$  phase shift acquired across the stopband of this stack. Through a collaboration with Boston University, I have observed this shift in the intensity data of quantum well emission collected using near-field scanning optical microscopy along the cleaved edge of a VCSEL. This VCSEL contains quantum wells at every mirror layer interface to serve as probes of the electric field intensity at a given position (G.H. Vander Rhodes,

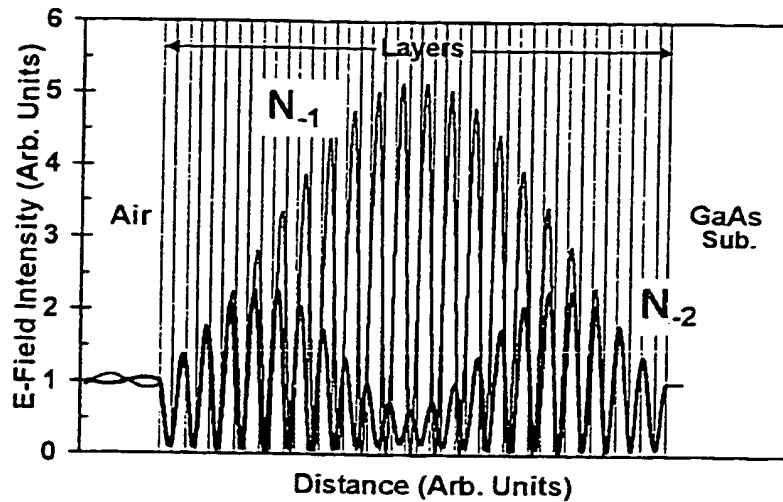


Figure 3.3: Plot of the calculated electric field intensity throughout a 20-pair AlAs/GaAs DBR for a wavelength at the  $N_{-1}$  and  $N_{-2}$  extended states.

1998).

### 3.3 Thin-Film Optimization

#### 3.3.1 Control Structure

The control structure chosen was a  $\lambda_o = 850$  nm resonant device consisting of a 19-pair,  $\lambda_o/4$ , AlAs/ $\text{Al}_{0.34}\text{Ga}_{0.66}\text{As}$  top mirror stack; a 27.5-pair,  $\lambda_o/4$ , AlAs/ $\text{Al}_{0.34}\text{Ga}_{0.66}\text{As}$  bottom mirror stack; and two  $\text{Al}_{0.34}\text{Ga}_{0.66}\text{As}$  cavity spacers to form a  $\lambda_o$  cavity with an active region of three 10 nm GaAs quantum wells with 10 nm wide  $\text{Al}_{0.34}\text{Ga}_{0.66}\text{As}$  barriers. The characteristic matrix approach was used to calculate the reflectance spectrum shown in Fig. 3.4 for this control device (Wolf, 1980). The typical interference fringes surrounding the high reflector band are illustrated. Dispersion and absorption were considered in this and all characteristic matrix calculations.

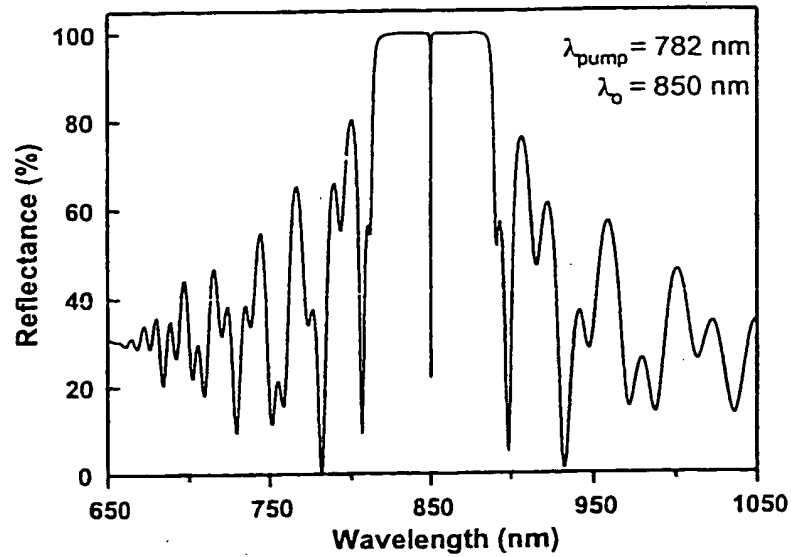


Figure 3.4: Simulated reflectance spectrum for a typical VCSEL structure illustrating the resonant wavelength and a possible pump wavelength amidst the DBR interference fringes.

A model of the complex dielectric function based on Terry's nine harmonic oscillator model was used for  $\text{Al}_{0.34}\text{Ga}_{0.66}\text{As}$  and GaAs (F.L. Terry, 1991). The Afromowitz model was used for ALAs (Afromovitz, 1974).

### 3.3.2 Refinement

Commercial thin-film optics software was used to refine the control design using specified targets to obtain an optimized design. The interference fringes within a 50 nm window on the high energy side of the 850 nm resonance were targeted for smoothing. While it was desired to produce a region of low constant reflectance across the window, cavity finesse and cavity-mode field overlap at the quantum wells could not be sacrificed. The window between 750 and 800 nm was chosen for optimization, and 100 target reflectance points of 5% were generated across the region. A least-

squares merit function was calculated to monitor the agreement between the refined design and the targeted design (W. Press, 1988). The merit function was minimized using the method of steepest descent, also known as the conjugate gradient method (W. Press, 1988). While other methods such as the variable metric method may locate a minimum with less computation time, the gradient method requires less computer memory (W. Press, 1988). This was of concern, because the control structure consisted of 118 layers including a 500 nm GaAs buffer layer and a 10 nm GaAs capping layer.

The complete optimization was performed on a PC platform by alternately running two individual 25-iteration gradient optimizations. The first gradient optimization used the 100 target values and was permitted to vary all of the layer thicknesses in both DBR stacks. The cavity spacers and the active region thicknesses were held fixed. While with each iteration the refined design approached the targets across the 50 nm window, the cavity finesse was reduced, and the resonant wavelength was red-shifted. This is a result of the optimized mirror layers deviating from the typical quarter-wave thickness. As the mirror layers deviate from quarter-wave, the reflections from some layers will destructively interfere, thus decreasing the overall reflectance. This results in a lower cavity finesse. Cavity finesse can be increased by adding additional DBR pairs before optimization. The two distributed mirror stacks bounding the cavity have a finite reflection delay that adds to the round-trip time of the cavity and increases the effective cavity length by a penetration depth (S.W. Corzine, 1992). As the two mirror stacks deviate away from quarter-wave thickness, increasing the penetration depth, the thickness of the cavity spacers needs to be adjusted to maintain the desired resonant

wavelength. The maximum increase in the optical path length of the cavity given in quarter-waves is,

$$\Delta l_{\max_{OPL}} = \frac{4}{\lambda_o} \left[ \sum_{i=0}^{N_{pairs_{B\&T}}} (n_L d_{i_{Lnp}} + n_H d_{i_{Hnp}}) - N_{pairs_{B\&T}} (n_L d_{Lqw} + n_H d_{Hqw}) \right], \quad (3.1)$$

where  $N_{pairs_{B\&T}}$  is the number of pairs in the bottom and top mirrors,  $n_L$  and  $n_H$  are the high and low indices of the mirror pairs,  $\lambda_o$  is the free space wavelength, and  $d$  is the thickness of the high and low mirror layers in the control (subscript  $qw$ ) and nonperiodic (subscript  $np$ ) structures. This is the maximum length increase as it does not take into account the electric field but rather only changes in layer thicknesses.

A better approximation for the increased cavity length is found from the group delay (phase penetration depth) of the light. The difference between the calculated group delay time for the nonperiodic structure and the control structure can be converted into a distance using the speed of light. The group delay effects of these structures will be discussed extensively in Chapter 6. The second gradient optimization holds the mirror stack layers and active region fixed while varying only the cavity spacers to make the cavity length adjustment. A single target reflectance of 0 at  $\lambda_o$  was used. The calculated length from Eq. 3.1 serves as a guide.

The optimized VCSEL design was a result of six iterations of the two-part optimization. Four additional DBR pairs were added to each mirror stack for increased cavity finesse. The effective finesse was calculated to be 290 for the optimized structure, as opposed to 562 for the control structure (R.P. Stanley, 1994). It should be noted that with an additional 6 DBR pairs added per stack prior to optimization, the effective

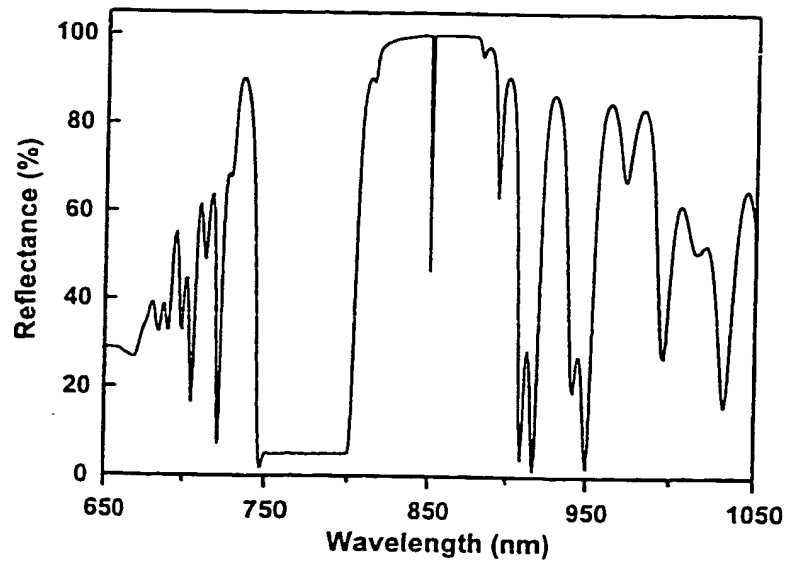


Figure 3.5: Calculated reflectance spectrum for the optimized low-ripple structure.

fineness of the optimized structure is greater than 1000. The 750-800 nm region for this low-ripple design has an average reflectance of 5%; the peak-to-peak amplitude of the ripple is 0.25%. Figure 3.5 shows the modeled reflectance. A bar graph illustrating the device's deviation from the typical quarter-wave thickness is shown in Fig. 3.6. One apparent feature of Fig. 3.6 is that only every other layer has been optimized. In fact every layer has been optimized, just some more than others. This stems from the effect each layer has on the merit function. To achieve the targeted reflectance, the thicknesses of layers that change the merit function the most are varied first. For a given change in physical thickness, the optical thickness of a high index layer changes more than a low index layer. Consequently, all the high index layers of the design are adjusted before their low index neighbor.

This optimization scheme can be readily applied to other material systems at

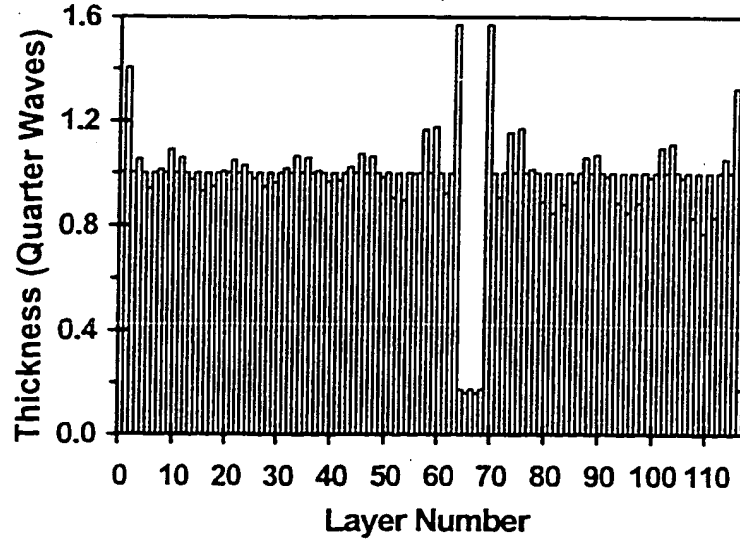


Figure 3.6: Bar graph illustrating the thicknesses of the low-ripple design. Layer 0 represents the bottom-most mirror layer while layer 116 is the topmost capping layer. Layers 63 and 69 are the cavity spacers surrounding the active region of layers 64-68.

other lasing wavelengths. Additionally, this scheme can be used to create a low-ripple transmission window on the long wavelength side of the DBR stop band to facilitate transmission through stacked vertical devices.

### 3.3.3 Simulation

In order to compare pump-coupling sensitivity for the control and low-ripple structures, a normalized pump field overlap factor  $\Gamma_{pump}$  must be defined,

$$\Gamma_{pump}(\lambda_{pump}) \equiv \frac{\int_{l_a} E^2(z, \lambda_{pump}) dz}{\int_{l_a} E^2(z, \lambda_o) dz} \quad (3.2)$$

where  $E^2$  is the electric-field intensity and  $\lambda_o$  and  $\lambda_{pump}$  are the resonant and pump wavelengths respectively. This equation yields a device-independent measure of pump-coupling sensitivity, that is, a measure of the dependence of  $\Gamma_{pump}$  on wavelength. It

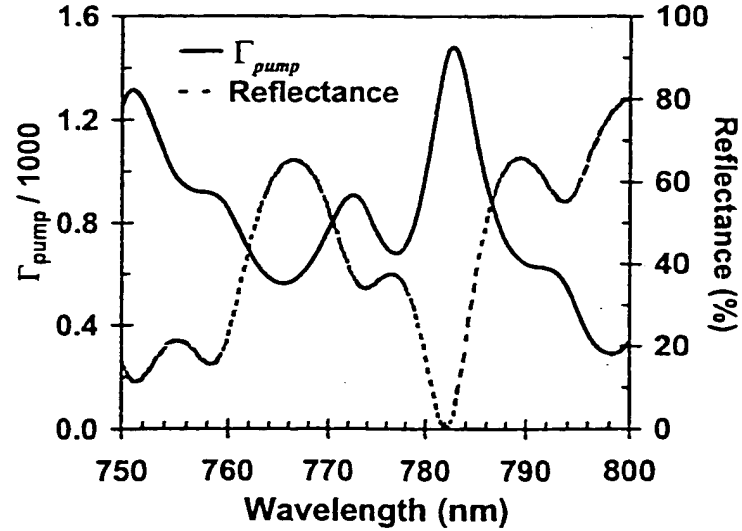


Figure 3.7: Simulated  $\Gamma_{pump}(\lambda)$  and reflectance spectrum for the control structure.

allows a meaningful one-to-one comparison of two devices with different cavity finesses and pump-absorption lengths  $l_a$ .

The response of the VCSEL's output to shifts of the reflectance spectrum was modeled by calculating  $\Gamma_{pump}$  as a function of wavelength. Equivalently, this is a measure of the output response of the VCSEL to different pump wavelengths. Figure 3.7 plots  $\Gamma_{pump}$  for the control design. The inverse relation between  $\Gamma_{pump}$  and the calculated reflectance is shown. The significant variation of  $\Gamma_{pump}$  with wavelength illustrates the described instability. The plot of  $\Gamma_{pump}$  for the optimized design shown in Fig. 3.8, however, shows a smooth negatively sloped dependence on wavelength. This smooth dependence indicates a substantial improvement in pump-coupling sensitivity.



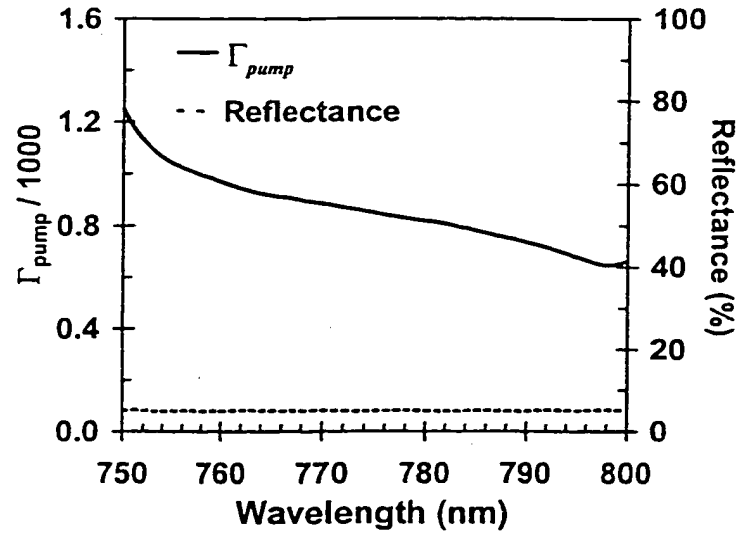


Figure 3.8: Simulated  $\Gamma_{pump}(\lambda)$  and reflectance spectrum for the control structure.

### 3.4 Experimental Results

Both the control and optimized structures were grown by MBE. The rotation of the substrate was paused over the topmost cavity spacer and the next two DBR pairs during the growths. This stop-rotation enabled a gradient of thickness to be achieved across the wafer, yielding a range of cavity resonances. Subsequent variation of detuning from the uniform QW emission wavelength is then possible. Reflectance and cross-sectional photoluminescence (D.H. Christensen, 1995) measurements show that a 12 nm range of cavity resonances was achieved relative to the uniform QW emission. The measured reflectance, with an uncertainty of 1%, of the control and optimized samples is shown in Figs. 3.9 (a) and 3.10 (a), respectively. The calculated reflectance of the control and optimized samples from Figs. 3.4 and 3.5 are replotted for comparison in Figs. 3.9 (b) and 3.10 (b). The data illustrate that the measured reflectance spectrum

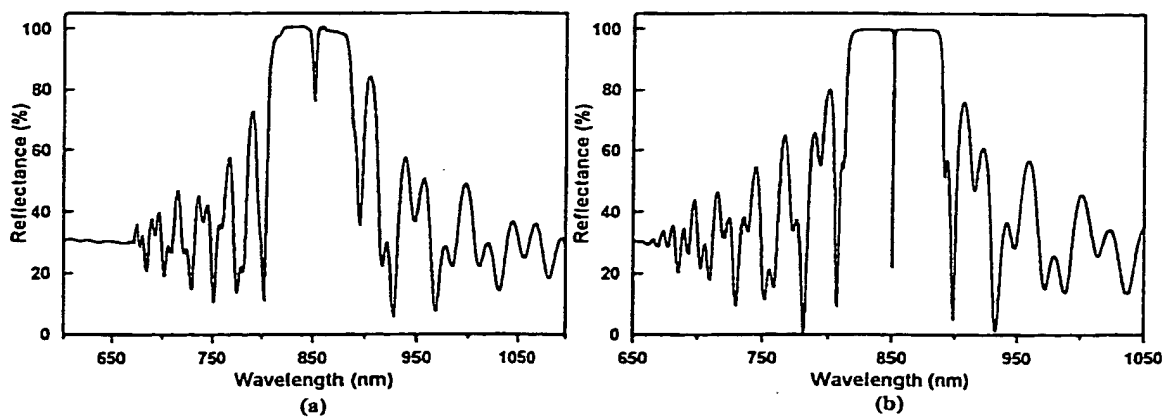


Figure 3.9: Measured (a) and simulated (b) reflectance of the control structure.

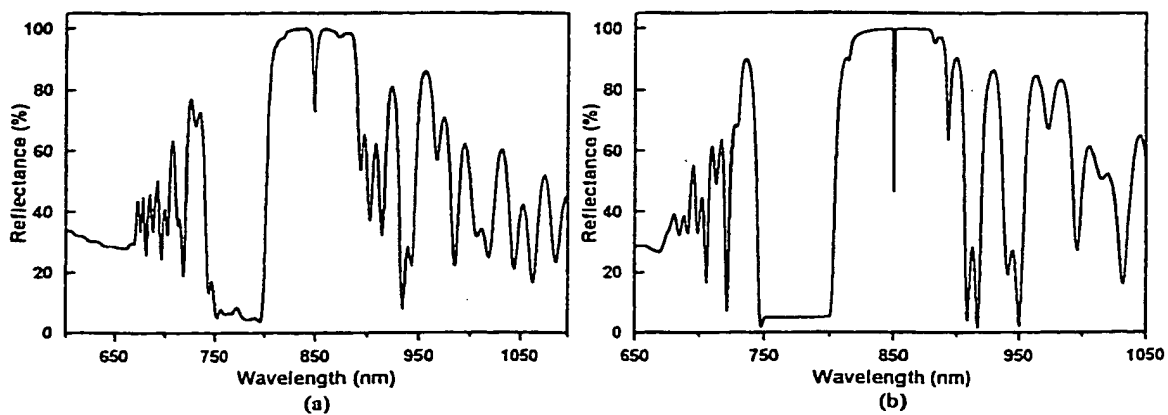


Figure 3.10: Measured (a) and simulated (b) reflectance of the low-ripple structure.

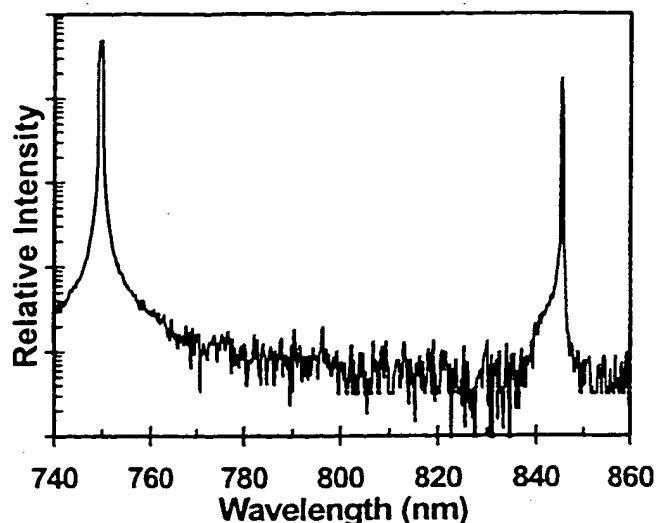


Figure 3.11: Optically pumped lasing spectrum of a 25  $\mu\text{m}$  square mesa-etched low-ripple device. Lasing is observed at 853 nm using a pump wavelength of 750 nm and an incident power of 60 mW.

of the grown specimens agree with the predicted value and that ripple control has been achieved in the optimized structure. The reflectance variations across the low-ripple window in the grown structure, however, are more significant than the designed  $\pm 0.25\%$ . The measured  $\pm 3\%$  variations of the low-ripple structure are a result of deviations in the growth as will be fully discussed in section 3.5. The resonances shown in Figs. 3.9 and 3.10 are also comparable, and thus the cavity properties of the control structure have been retained in the optimized structure. Comparison of the resonances of the grown devices to the calculated resonances is difficult due to the limited resolution of the measurement and the presence of quantum well absorption in the grown cavities.

Figure 3.11 shows the optically pumped lasing spectrum of this low-ripple VCSEL for a 25  $\mu\text{m}$ -square mesa-etched device. Lasing in this figure is shown at

843 nm and is achieved using a pump wavelength of 750 nm and an incident power of 60 mW into a 20-25  $\mu\text{m}$  spot. While this incident pump power is comparable to that of a typical VCSEL, further optimization of  $\Gamma_{\text{pump}}(\lambda)$  for increased pumping efficiency is foreseeable through the use of absorption targets in an attempt to increase the per pass absorption of the pump beam.

The experimental evaluation of  $\Gamma_{\text{pump}}(\lambda)$  for the two structures was performed by measuring their peak luminescence intensities coupled through the cavity resonance as a function of pump wavelength. This resulted in a filtered photoluminescence excitation (PLE) curve. The optical pumping setup used for this evaluation consists of a tunable Ti:Sapphire pump laser, a focusing objective, a CCD camera for alignment, and an optical spectrum analyzer (refer to Fig. 2.23, Pg. 49). The PLE emission of the control structure, as well as micro-spot reflectance of the illuminated region, is shown in Fig. 3.12. The inverse relation between  $\Gamma_{\text{pump}}$  and the device reflectance, and the significant variation of intensity with pump wavelength are apparent in this figure.

The plot for the optimized VCSEL in Fig. 3.13, however, shows  $\Gamma_{\text{pump}}$  to be a relatively smooth function of wavelength. The peak near 748 nm is a consequence of optimization of reflectance rather than  $\Gamma_{\text{pump}}(\lambda)$  directly. While optimization of the device's reflectance over the chosen pump window significantly flattens  $\Gamma_{\text{pump}}(\lambda)$ , the use of absorbance targets through incorporation of a quantum well absorption model will further optimize  $\Gamma_{\text{pump}}(\lambda)$  directly, allowing the 748 nm peak to be suppressed. A calculated fit to this emission is also shown in Fig. 3.13 through recalculation of  $\Gamma_{\text{pump}}(\lambda)$  with inclusion of the quantum well and cap layer absorption. The complex dielectric

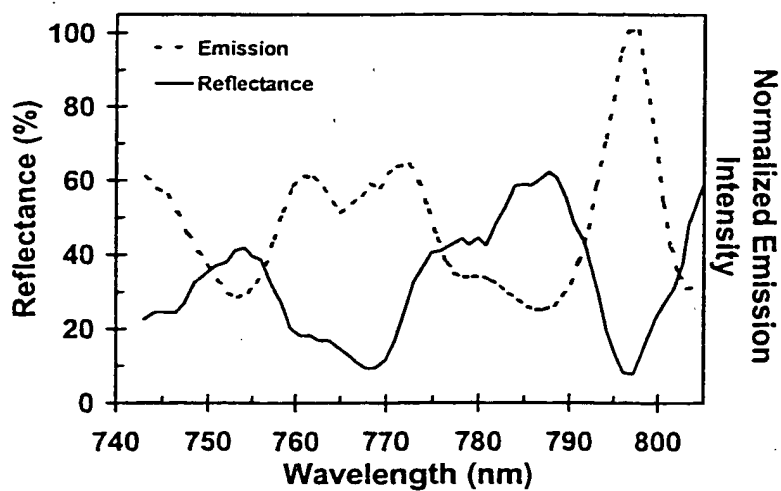


Figure 3.12: Filtered PLE emission and microspot reflectance versus pump wavelength for the control structure.

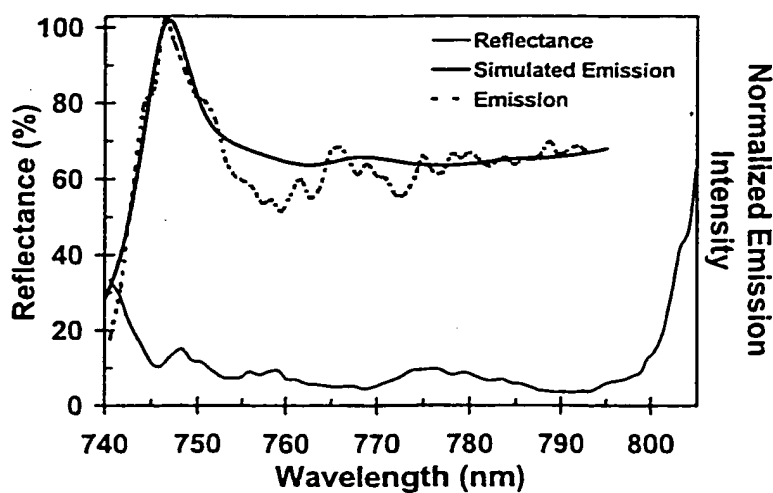


Figure 3.13: Filtered PLE emission and microspot reflectance versus pump wavelength for the optimized low-ripple structure. A calculated fit to the emission is also illustrated.

function model by Terry was again used for GaAs in a bulk material approximation for the quantum well and cap layer absorption. A linear dependence of quantum well gain on carrier density was assumed.

### 3.5 Thickness Deviations

Successful growth of VCSEL structures requires extremely high accuracy in layer thickness. Layer thickness must be controlled to better than 1% (J.L. Jewell, 1991). Several *in situ* techniques have been developed to meet the precision of growth control needed (V. Bardinal, 1995). For quarter-wave VCSEL structures, *in situ* techniques have been used to monitor and/or control the cavity's resonant wavelength and the full width at half-maximum (FWHM) of the reflectance stop band (K. Bacher, 1992 ; Y.M. Houng, 1994). For the optimized VCSEL structures presented here, the flatness of the pump window and its sensitivity to thickness variations is also of concern. Physical thickness variations during epitaxial growth and temperature induced optical thickness variations in fabricated devices are considered in this section.

For quarter-wave structures, small variations in layer thickness do not severely alter the reflectance spectrum across the high-reflecting region (O.S. Heavens, 1954). Reflectance simulations were calculated for 100 trials of a  $\pm 1\%$  uniformly distributed random thickness variation for both the control design and an optimized design. The simulation results for the control structure are shown in Fig. 3.14. The envelope of reflectance variation converges across the stop band. Minimal changes in the FWHM and average reflectance of the stop band are observable. Figure 3.15 shows the simulation results for a low-ripple VCSEL. Changes in the stop band are again minimal; however,

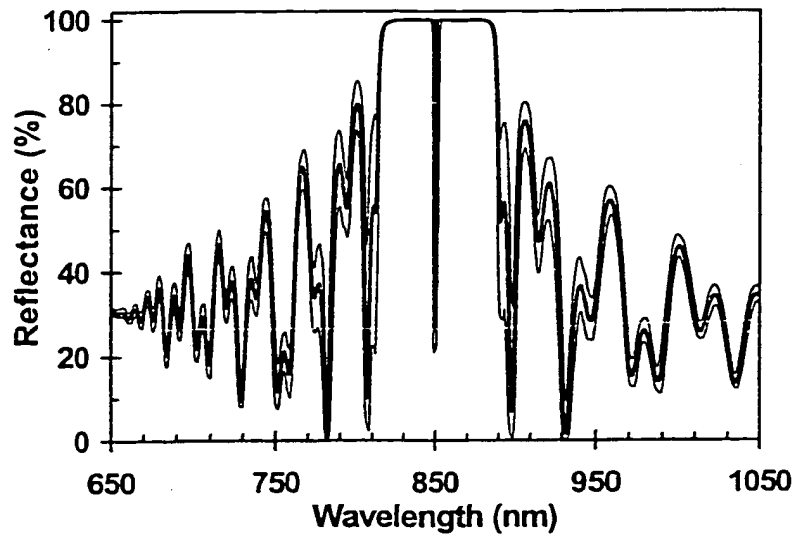


Figure 3.14: Simulation results of a  $\pm 1\%$  uniformly distributed random thickness variation in the control structure. The envelope of variation is shown by the two thin lines.

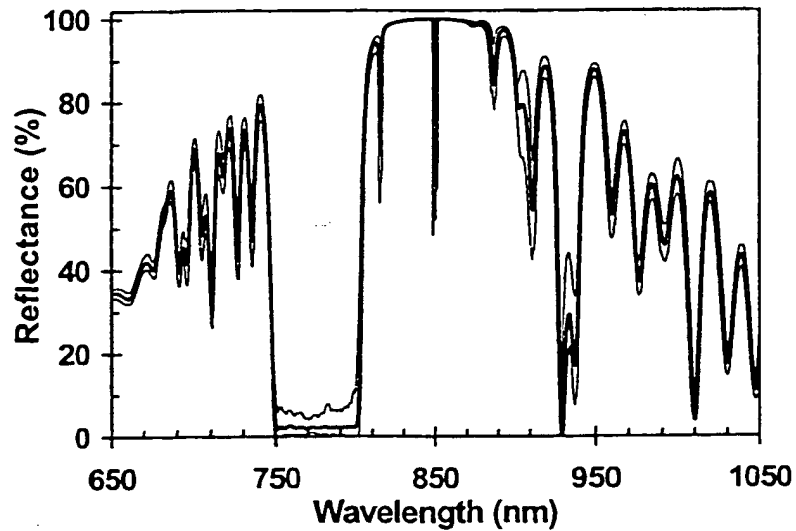


Figure 3.15: Simulation results of a  $\pm 1\%$  uniformly distributed random thickness variation in the low-ripple structure. The envelope of variation is shown by the two thin lines.

larger variations in the pump window are present. The nominal average reflectance across the pump window for this design is 2.17%. For the  $\pm 1\%$  thickness variation, the average reflectance of the window varied within an envelope of 0.39% to 6.35%. This envelope of variation is attributed to the small deviations from quarter-wave thickness that are responsible for creating the low-ripple window. Figure 3.6 illustrated that most layers are nearly a quarter-wavelength in thickness. Thus, a  $\pm 1\%$  change in thickness has a much more dramatic effect on the low-ripple window than on the highly reflecting stop band characteristic of quarter-wave layers. A similar simulation with a  $\pm 0.25\%$  thickness variation reduces the bounds of the envelope of average reflectance to 1.46% and 3.05%. Nonetheless, these tolerances are becoming achievable using state-of-the-art *in situ* monitored control and, as demonstrated here, functional devices are manufacturable without this control.

For a thin-film coating, a uniform shift of thickness in each of the structures layers results in a near proportional shift of the reflectance spectrum (Macleod, 1969). Two simulations were performed that simulated a  $\pm 1\%$  change in thickness uniformity across a sample, and the average reflectance of the pump window was monitored. The pump window's spectral position shifted proportionally to the thickness change, and the calculated average reflectances were 2.23% and 2.35% for a  $-1\%$  and  $+1\%$  change respectively. The change in average reflectance is attributed to the dielectric constants' dependence on wavelength.

The sensitivity of the low-ripple band to temperature variations was also measured for these devices. These are systematic variations in optical layer thickness. Ex-



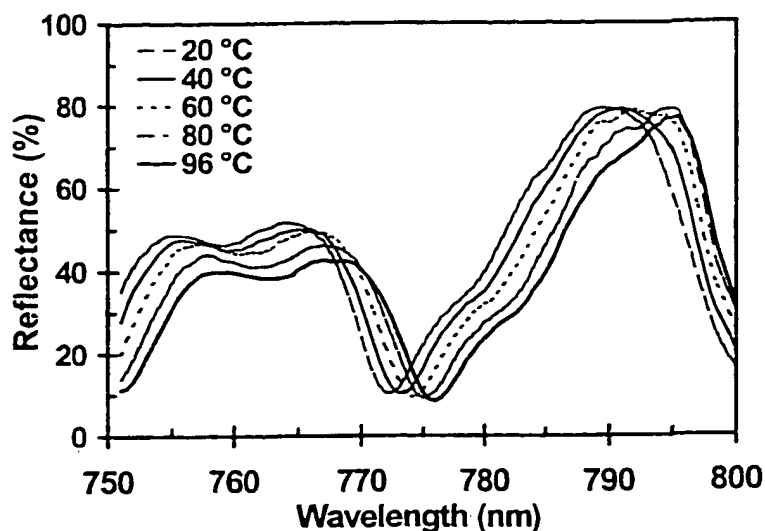


Figure 3.16: The spectral response of the control structure to temperature changes over the range of 0 to 100 °C.

perimental data were collected on the spectral response of both the control and low-ripple structures to temperature changes over the range of 0 to 100 °C. Figures 3.16 and 3.17 show plots of this data for the control and low-ripple devices, respectively. The low-ripple structure substantially reduces the variation of reflectance with temperature. The control device's reflectance spectrum shifts through the 100 °C range at a rate of 0.047 nm/°C, while the low-ripple pump window shifts at a rate of 0.036 nm/°C. The shift rate of the low-ripple window was measured by observing the shift of the short wavelength edge of the window. Simultaneously, the peak-to-peak ripple of the pump window varies less than 2%, and the pump bandwidth remains constant. This indicates a continuous range of flat pump-coupling sensitivity.

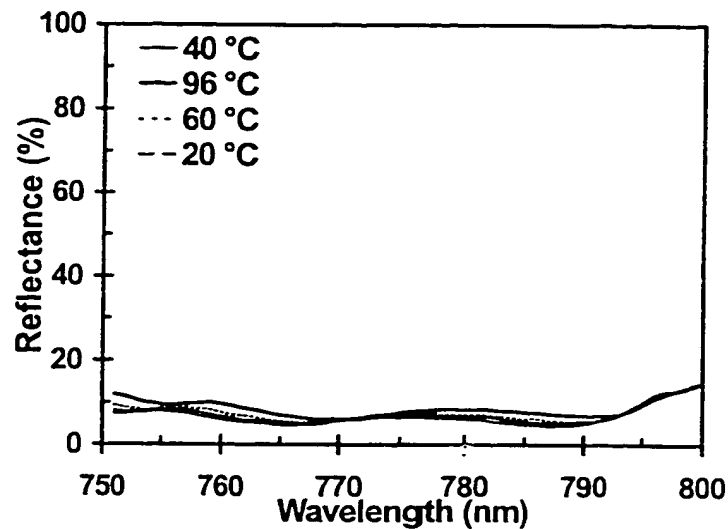


Figure 3.17: The spectral response of the low-ripple structure to temperature changes over the range of 0 to 100 °C.

### 3.6 Summary

I applied a general numerical technique for optimizing optical admittances to VCSELs. I have used this method to match the optical admittances to create a wideband window of low reflectance amongst the typical interference fringe spectrum. Through this modification of the reflectance signature, I have flattened the pump field overlap while maintaining adequate cavity finesse and cavity-mode field overlap at the quantum wells. I have demonstrated optically pumped lasing of these nonperiodic structures. The low-ripple structure substantially reduces the temperature and wavelength variation of the pump-field overlap by creating a window of nearly constant reflectance. The formation of this window, however, taxes the accuracy of MBE growth and requires additional mirror layers to maintain a high cavity finesse and a low lasing threshold.

Inclusion of the wavelength dependence of quantum well absorption and the use of *in situ* growth techniques will improve agreement between the presented simulations and measurements.

While these results have led to improved pump-coupling characteristics, further lateral bandgap engineering is needed to create ultra-low-threshold optically pumped VCSELs. Incorporation of the native-oxide technology of Chp. 5 for optical mode confinement should further reduce thresholds (D.L. Huffaker<sup>a,b</sup>, 1994). Additionally, optically pumped VCSELs substantially differ from their electrical pumped counterparts in that optically pumped devices do not utilize current confinement by their nature, and carrier outdiffusion is a dominant source of overall wall-plug efficiency reduction. Carrier confinement, as opposed to current confinement, should further reduce thresholds. Thus, I anticipate that suitable power-by-light devices will be achieved through combining a low-ripple reflectance window with an interdiffused carrier-confining radially symmetric potential step. Hybrid electrically/optically pumped low-ripple devices appear realizable, however, they will inevitably suffer from a slight increase in resistance (and thus degraded performance) due to the extra mirror pairs needed.

Furthermore, optimized low-ripple structures hold promise for use in resonant-cavity quantum-well detectors with integrated low-ripple pass-bands, and for facilitation of stacked vertical-cavity devices. Additionally, they are valuable for use in ultrafast sub-picosecond VCSEL characterization, as will be explored in Chp. 6. The method discussed is a general numerical technique for optimizing the optical admittances in vertical cavity structures using photonic band engineering.

## Chapter 4

### Transverse Mode Competition and Control in VCSELs

#### 4.1 Introduction

Vertical-cavity surface-emitting lasers hold tremendous promise in applications of optical interconnects, optical processing, and high-speed, short-haul optical communications. Their vertical orientation inherently dictates a short cavity length ( $\sim \lambda$ ) that causes lasing in a single longitudinal mode. The number of transverse lasing modes, however, is controlled in part by the device's lateral dimensions. The onset of higher-order modes at high injection currents can limit the maximum single-mode power and result in a decrease in spatial and temporal coherence (J. Chilla, 1995). These higher-order modes are a consequence of the interaction of the spatial distributions of the carriers and the optical field (V.N. Morozov, 1997). This interaction occurs through the complex dielectric constant.

Joule heating and the nonuniformity of the injected current initially cause the spatial dependence of the complex dielectric constant. The injected carriers produce a region of high gain near the contact and a lossy region far from the contact (see section 2.5.2 page 50). The lateral diffusion of carriers initially determines the spatial

dependence of the gain/loss between these two regions. The presence of the injected carriers also induces a decrease in the refractive index through plasma screening. The temperature profile across the device due to Joule heating not only affects the lateral diffusion of the carriers, but is also responsible for an increase in the refractive index. This increase leads to the creation of a "thermal lens". The interaction of these gain-guiding and index-guiding/antiguinding mechanisms with the optical field defines the transverse mode structure (V.N. Morozov, 1997). Specifically, these mechanisms result in spatial hole burning across the lasing aperture. Spatial hole burning has been identified as the dominant mode-selection mechanism in VCSELs (G.R. Hadley, 1996).

Every aspect of a VCSEL's optical and electrical design is intricately related to these transverse-mode-defining mechanisms. For example, whether or not a device injects current through the mirrors or via intracavity contacts affects the resistance (heating) and uniformity of the carriers. If a device uses a native oxide aperture for optical confinement, its index difference will come into play. Further, the device's diameter and cavity length affect the number of supported transverse modes and the diffraction loss experienced by each mode.

While it is often desirable for many applications to create devices which emit into a single transverse mode, this is not the case for short-haul data links. In short-haul data links, multimode fiber is preferred due to its lower cost and compatibility with existing links. The high coherence of single-transverse-mode VCSELs, in combination with the mode selective losses created by fiber-optic splitters and connectors, results in modal noise and high bit error rates (BERs). Large area multimode VCSELs have been

demonstrated as viable low coherence sources that can reduce modal noise and replace commonly used low-bandwidth ( $<1$  GHz) self-pulsating laser diodes and light-emitting diodes (K.H. Hahn, 1993). To achieve the needed reliability and low BERs in these high-speed data links, models and techniques for simulating and characterizing the dynamical, spectral and spatial properties of multimode VCSEL emission are needed to understand how their complex modal patterns affect system performance. A comprehensive numerical model has been reported in the literature that predicts the dynamic evolution of transverse modes in VCSELs (A. Valle, 1995). These calculations showed that spatially separated modes can coexist through sharing of the available gain while overlapping modes must compete. This competition determined whether single or multimode behavior was obtained in the steady state. The mode competition was also expected to influence how the steady-state optical output power of each modes varies with injected current. In section 4.2 of this chapter, I experimentally study the turn-on dynamics of a multimode VCSEL as a prelude to section 4.3 which characterizes the steady-state spectral and spatial properties of multimode VCSEL emission using the technique of near-field scanning optical microscopy (NSOM).

For many other applications, it is desirable to have a high-power output in a single high-quality transverse mode with a predefined polarization direction. The creation of a large-area single transverse-mode VCSEL has remained an elusive goal of many research groups. Numerous attempts have been made to achieve this goal ever since the early years of VCSEL research. The most obvious method of achieving single-mode emission is to reduce the lateral device dimensions to only a few micrometers

(< 5  $\mu\text{m}$ ) (C.J. Chang-Hasnain, 1990). These small sizes become difficult to fabricate, cause large voltage drops across the device, and limit the maximum output power to < 1 mW. Improved electrical performance of a single-mode device has been demonstrated using a reflector structure employing a 5  $\mu\text{m}$  diameter aperture for spatial filtering of the output beam from a large diameter device (R.A. Morgan, 1993). Complicated regrowth methods have been used to achieve better performance by creating a passive-antiguide buried-heterostructure that forces single-mode emission in an 8  $\mu\text{m}$  diameter device for currents up to 12 times that of threshold (Y.A. Wu, 1993). In section 4.4, I discuss a simple, elegant, and easy to implement method of mode control that creates a spatially dependent reflectivity using an out-of-phase reflection from a metal layer atop the semiconductor DBR.

## 4.2 Temporal Characteristics

In this section, I explore the multimode dynamics of VCSELs on a picosecond time-scale through polarization-resolved step-response measurements in the large signal regime. The dynamical redistribution of optical power among the various lasing modes is observed.

### 4.2.1 Large Signal Step-Response

The optical output of a VCSEL will ring sinusoidally in response to a sharp step in the applied current as the carrier and photon densities react. This ringing occurs at the relaxation oscillation frequency and damps to a steady-state value. In the small signal case where the laser is biased above threshold and the applied modulation is small,

the amount of damping in the relaxation oscillations is dependent on the applied DC bias (Peterman, 1988). The response moves from underdamped to critically damped as the output power (bias voltage) increases. When critically damped, the transient densities respond with exponential rise and fall times. When overdamped at higher output powers, the response slows and the time constants of the rise and fall times increase. For the large-signal (gain-switching) regime where the laser is modulated above and below threshold, solutions to the carrier and photon rate equations must be used for intuition (Peterman, 1988). With a zero bias and at the turn-on of the applied step ( $t = 0$ ), the carrier density increases as the active-region reservoir fills. The photon density remains small until the threshold carrier density is reached. Now, stimulated recombination limits the increase in carrier density as photon densities increase. The delay before the photon density is observed, through lasing emission, is appropriately called the turn-on delay. As the applied bias increases towards its threshold value, the turn-on delay is reduced. This turn-on delay is not beneficial in high speed communications links as it would cause timing jitter. The turn-on delay for small biases is proportional to the carrier lifetime ( $\sim 3 - 4$  ns) (Peterman, 1988).

The step response dynamics of index-guided VCSELs grown at Cornell University were measured by exciting the sample to two times threshold ( $\sim 15$  V) with a step function having a 43 ps risetime and 10 ns duration. The emission was detected over the course of the excitation pulse using a streak camera with 1 ps resolution. The Cornell VCSELs were designed to emit at  $1\text{ }\mu\text{m}$  and have top-side  $p$  and  $n$  contacts for mating with a  $50\text{ }\Omega$  ground-signal-ground (GSG) coplanar waveguide probe. The



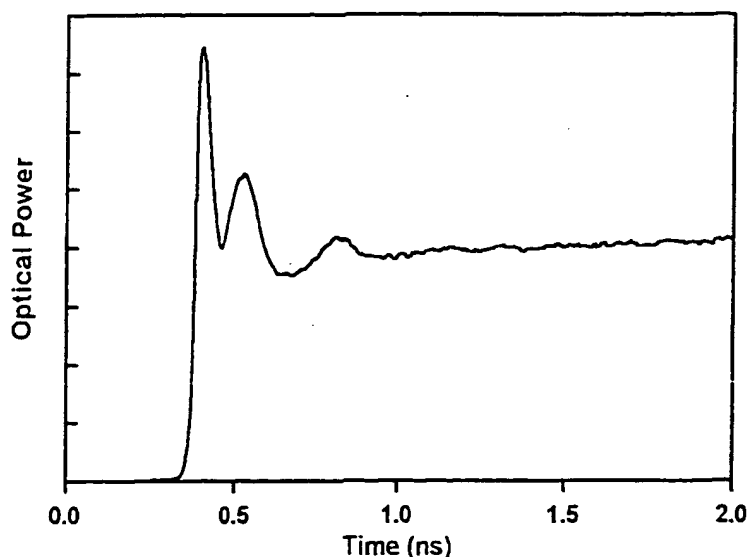


Figure 4.1: Step response dynamics of index-guided VCSEL measured by exciting the sample to a few times threshold with a step function having a 43 ps risetime and 10 ns duration.

diameter of the device's lasing aperture is 10  $\mu\text{m}$ . The VCSEL was prebiased through a bias tee. Figure 4.1 shows the measured step response under zero prebias. Damped relaxation oscillations at a frequency of  $\sim 12$  GHz are observed at the front of the pulse. As the prebias was increased to 3.2 V the turn-on delay was reduced by 140 ps. Adding prebias does not stimulate lasing because the devices do not lase cw as the wavelengths of the cavity resonance and the quantum well emission are misaligned.

#### 4.2.2 Polarization Resolved Step-Response

Although the optical power in Fig. 4.1 may appear to have reached a steady-state condition after  $< 1$  ns, the distribution of optical power between lasing transverse modes is varying with time as the individual modes compete for the available gain (A. Valle, 1995). The cylindrical symmetry and device geometry of a VCSEL causes

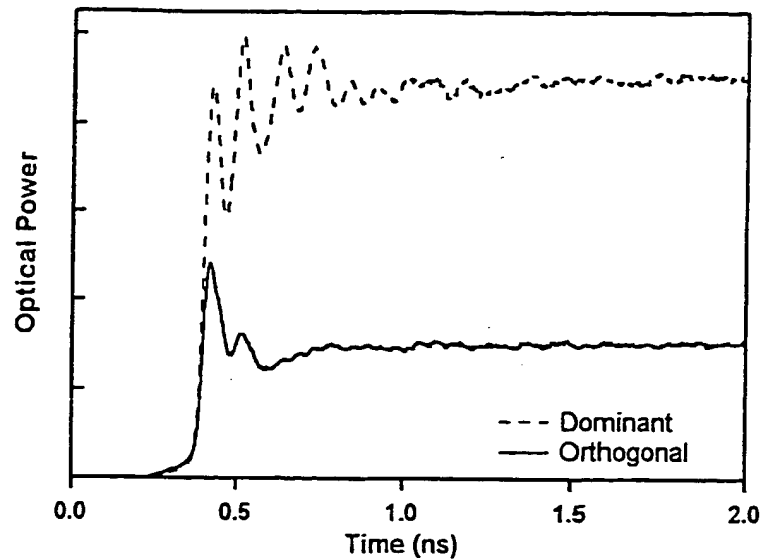


Figure 4.2: Polarization-resolved step-response dynamics of an index-guided VCSEL with 0 V prebias.

little polarization selectivity. In practice, inhomogeneities in the growth, nonuniformities in the injected carrier and photon densities, and temperature gradients, all cause the device to be linearly polarized to the crystal axes (D.V. Kuksenkov, 1995) with one dominant state during DC operation (O. Buccafusca, 1999). Both the dominant state and the orthogonal state can consist of families of transverse modes. Inserting a polarizer aligned to one polarization state before the streak camera allows the step response for that mode family to be measured. The step response of the dominant state mode family and the orthogonal state mode family were measured. For the Cornell devices, only two transverse modes were resolved in the collected spectrum of the emission; however, more modes may be present as the spectral resolution was limited to 0.2 nm. Figure 4.2 illustrates the collected data for both polarizations with a zero volt prebias. The plot shows that lasing of both mode families can be sustained with the

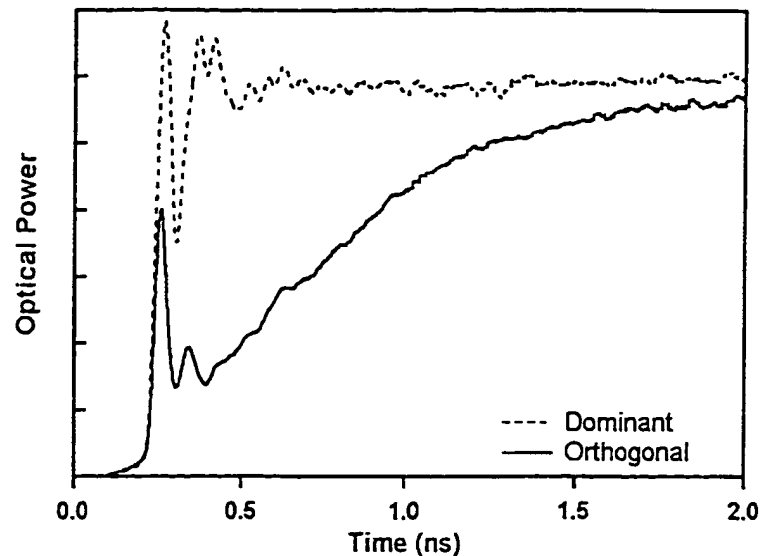


Figure 4.3: Polarization-resolved step-response dynamics of an index-guided VCSEL with 3.2 V prebias.

available gain. As the prebias is increased to 3.2 V, the collected emission spectrum indicates that the orthogonal state now includes an additional higher-order mode. Figure 4.3 illustrates the step response data for both polarizations with a prebias of 3.2 V. A slow turn on of the orthogonal mode family is evident. Initially, both mode families achieve lasing and exhibit relaxation oscillations. The photon density of the orthogonal mode family then quickly drops as there appears to be not enough gain to sustain lasing of both mode families. As the dominant mode reaches steady-state, however, the orthogonal mode begins to slowly rise as it is able to overcome the losses and reach a steady-state value.

The complex dynamical interplay observed between the two polarization-state mode families is a problem for high-speed data communication systems. Polarization dependent loss in these systems causes increased BER through turn-on jitter as two

dramatically different risetimes are observed (J.A. Tatum, 1997). In the next section, the spatial overlap of different transverse modes observed under static drive conditions will be explored.

### 4.3 Spatio-Spectral Mapping

In this section and in the literature (K.J. Knopp<sup>a,b</sup>, 1999), I report the use of near-field scanning optical microscopy (NSOM) for characterizing multi-transverse-mode proton-implanted 850 nm devices used in 2 Gbit/s multimode fiber-optic links. Specifically, I have used NSOM to study the steady-state spatial and spectral overlap of their transverse modes. I have correlated their measured overlap to oscillations in a spectrally resolved light-versus-current (L-I) curve captured in the far field. Overlapping modes are shown to compete for the available gain while spatially separated modes do not. I show that the high spatial and spectral resolution provided by near-field optical microscopy and spectroscopy makes this an ideal technique for characterizing these low-coherence VCSELs.

#### 4.3.1 The Near-Field Scanning Optical Microscope

NSOM is a useful tool for characterizing the electrical and optical properties of various semiconductor structures on a nanometer scale (B.B. Goldberg, 1995). NSOM is a technique in which a tapered optical fiber clad with metal is held atop a sample within a fraction of a wavelength and scanned across its surface (E. Betzig<sup>b</sup>, 1992). At each point in the scan the optical radiation emitted by the sample is collected from the near-field through the small metal aperture created at the tip of the tapered fiber. The spatial

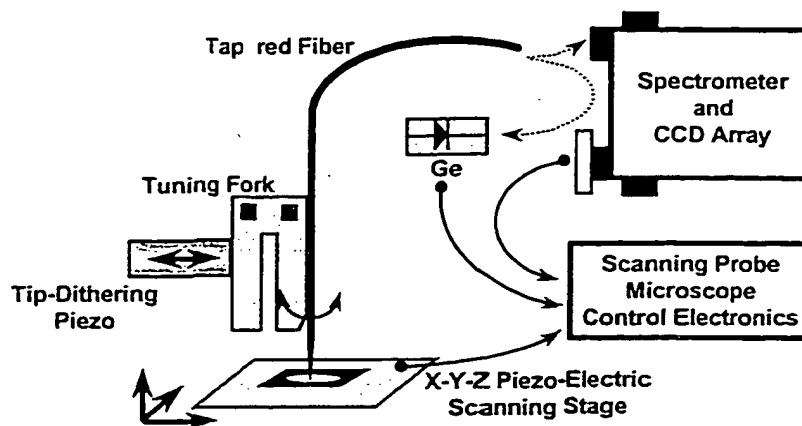


Figure 4.4: Schematic of the near-field microscope setup.

resolution of the scan is determined by the tip's aperture size and is approximately equal to the tip diameter ( $\sim 100$  nm).

The microscope used in this work is shown in Fig. 4.4. The sample is mounted to a piezo-electric stage and raster-scanned in the xy-plane under the fiber tip, which collects the emission from the sample and guides it directly to a detector to acquire a total intensity measurement or to a spectrometer to obtain localized spectral information. A charge-coupled device (CCD) array cooled by liquid nitrogen is used at the exit of a 0.64 m spectrometer with a 1200 groove/mm grating to yield spectral information with a resolution of 0.07 nm over a 25 nm band for each point of the scan. A commercial scanning probe microscope controller is used for data acquisition.

The tip must track the topography of the sample throughout the raster scan to maintain a fixed tip-to-sample distance of  $\sim 10$  nm. This tracking is achieved through simultaneous shear-force measurements (E. Betzig<sup>a</sup>, 1992). A low-cost, nonoptical method of shear-force detection is implemented by mounting the fiber tip onto one leg

of the tuning fork of a commercial quartz watch crystal (K. Karrai, 1995). The fiber tip and tuning fork are dithered by a piezo-electric tube at their resonance frequency, and tip-sample interactions are sensed by the tuning fork as a quenching of this resonance. Monitoring the resonance frequency allows a measurement of the tip-to-sample distance with nanometer resolution. Near-field microscopy thus provides a direct correlation of the emitted optical radiation pattern with topographical features of the sample.

#### 4.3.2 Far-Field Characteristics

The VCSEL devices studied were designed as high-reliability, multimode, gain-guided sources for use in commercial local-area networks (LAN) (J.K. Guenter, 1996). The devices were grown at Honeywell MicroSwitch by metal-organic chemical vapor deposition (MOCVD) and designed to emit at 850 nm. The structure consists of two AlAs/AlGaAs distributed Bragg reflectors (DBRs) centered around an active region of GaAs quantum wells to form a  $\lambda$  cavity. The devices have a 15  $\mu\text{m}$  diameter metal ring contact and a 20  $\mu\text{m}$  inner diameter, proton-implanted region to confine current. This geometry was chosen to provide the best compromise between threshold current, modulation bandwidth, series resistance, and spectral width (J.A. Tatum, 1997). High speed characteristics, reliability, device, and fabrication details for similar devices can be found in (R.A. Morgan, 1995 ; J.A. Tatum, 1997).

The multi-transverse-mode nature of these devices is evident in the lasing spectra collected in the far field and resolved by a spectrometer with 0.07 nm resolution. Figure 4.5 shows the far-field spectra at drive currents of 7, 10, 15, and 17 mA. As will be shown in section 4.3.3, the low-coherence VCSELs in this study do not emit into

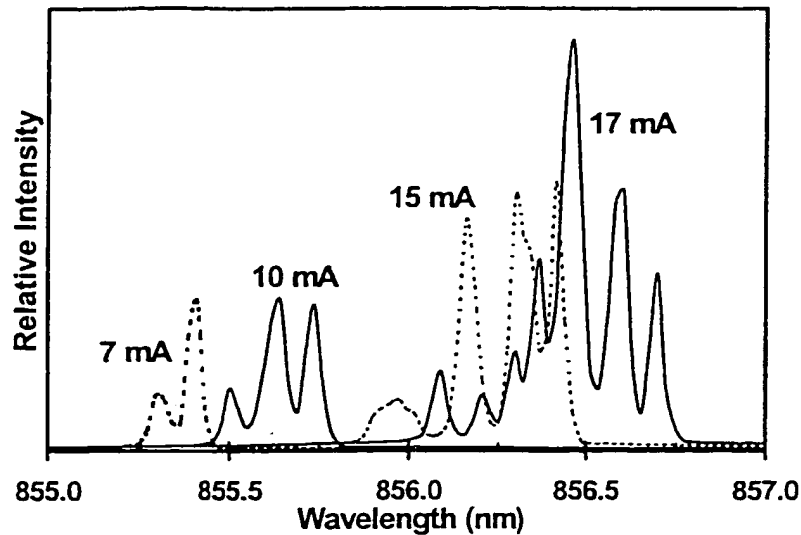


Figure 4.5: Far-field spectra illustrating the device's multi-transverse-mode characteristics for drive currents of: 7, 10, 15, and 17 mA.

identifiable mode patterns, but rather into multiple filaments. Consequently, each transverse mode will be identified by its energy. If present, degenerate modes in energy (or, in practice, “almost” degenerate modes) will not be resolved in the spectral data and thus will be lumped together and designated as one mode. The higher-order modes in confined systems occur at higher energies than the fundamental mode, denoted as mode 0. In a gain-guided VCSEL, lateral confinement is imposed by the spatially nonuniform distribution in the dielectric constant produced by gain guiding, thermally induced index guiding, and carrier-induced antiguiding (V.N. Morozov, 1997). In the spectra of Fig. 4.5 for each drive current, transverse-mode 0 occurs at the lowest energy (longest wavelength). Mode 1 occurs at the next highest energy and so forth. At a current (7 mA) just above threshold two transverse modes are supported with a wavelength separation of  $\sim 0.1$  nm. At higher injection currents, additional modes reach

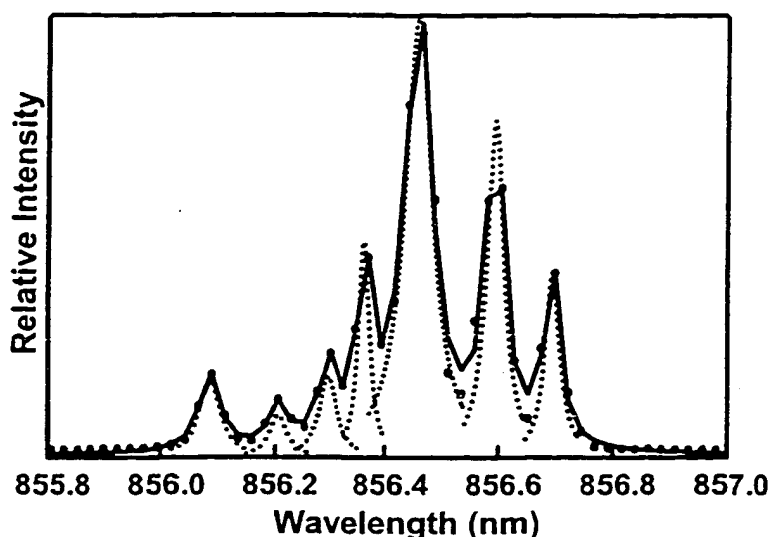


Figure 4.6: Far-field spectrum at 17 mA showing the Lorentzian fits (dotted lines) to each transverse mode of the far-field spectrum at 17 mA. The black dots show the collected data while the solid line shows the sum of all the Lorentzians.

threshold. At 17 mA, a total of 7 separate transverse modes are observed.

Spatially separated modes in VCSELs may theoretically coexist through sharing of the available gain (G.R. Hadley, 1996). For transverse modes with significant spatial overlap, modes must compete for the available gain (G.R. Hadley, 1996). It is possible to determine the L-I behavior of each resolved transverse mode by fitting each mode of the collected far-field spectra with a Lorentzian line. Taking the ratio of each Lorentzian's spectral area to the total area and scaling it to the device's total optical power yields an L-I curve for each transverse mode.

Figure 4.6 illustrates a fit to the collected spectra at a drive current of 17 mA. The dots shown are the collected data points while the solid line is the fit created by summing the contributions of the Lorentzians shown by the dotted lines. The L-I curves



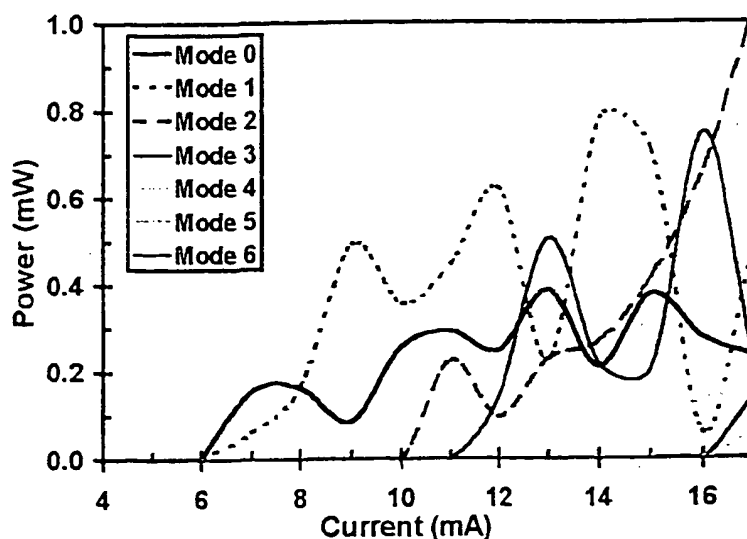


Figure 4.7: L-I behavior for each transverse mode illustrating competition or independent coexistence of various modes.

for each transverse mode are shown in Fig. 4.7. The most notable feature of this plot is the competition of modes 1 and 3. The power maxima of mode 1 clearly correlate with the power minima of mode 3 near the currents of 13, 14-15, and 16 mA. Competition between mode 0 and mode 1 is also apparent over the current range of 0 to 14 mA. This behavior indicates that these modes overlap spatially and compete for the same gain. The lack of features in mode 2 above 12 mA indicates that it is not in competition for gain and is thus spatially separate. I turn to NSOM to explore the spatial distributions of these transverse modes.

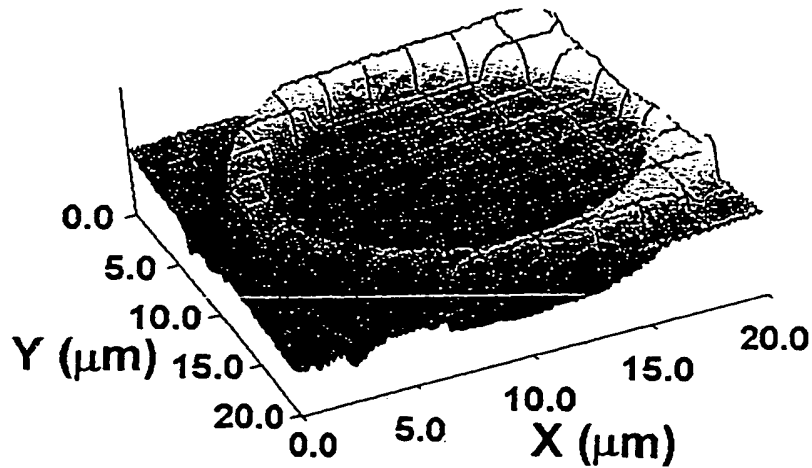


Figure 4.8: Representative shear force image acquired during a near-field scan of the topography of the VCSEL's p-contact. The z-axis is proportional to height and the height difference from the center of the aperture to the top of the contact is  $\sim 250$  nm.

### 4.3.3 Near-Field Measurements

#### Shear Force Images

NSOM measurements were taken at drive currents of 7, 10, and 15 mA over a  $20 \times 20 \mu\text{m}$  area with  $256 \times 128$  scan points. Several higher resolution images with  $512 \times 512$  pixels were also acquired to study the fine spatial structure observed in some modes. Simultaneously obtained shear-force measurements allowed correlation of the optical distributions to the topography of the VCSEL's top-mirror ring contact. A representative plot of the shear force data acquired during each scan is shown in Fig. 4.8, with height on the z-axis. The step height from the top of the contact to the center of the aperture is  $\sim 250$  nm.

## Intensity Images

Near-field images for three drive currents were obtained by guiding the collected light directly into a thermoelectrically cooled germanium detector. These images are shown in Fig. 4.9. At 7 mA drive current, I resolve two lasing regions with a  $10\text{ }\mu\text{m}$  separation located adjacent to the *p*-contact metal nearest the bond pad in the region of highest current density. The center of the most intense region is near ( $X\sim 16\text{ }\mu\text{m}$ ,  $Y\sim 14\text{ }\mu\text{m}$ ) while a second lower intensity lasing region is at ( $X\sim 16\text{ }\mu\text{m}$ ,  $Y\sim 4\text{ }\mu\text{m}$ ). The nonuniformity of the injected carrier density is apparent. At 10 mA, a third region and the remaining two lasing regions begin to fill along the perimeter of the ring contact. Index guiding through thermal lensing and spatial hole burning are responsible for the formation of a  $\sim 2.5\text{ }\mu\text{m}$  radius dark region that is centered at ( $X\sim 10\text{ }\mu\text{m}$ ,  $Y\sim 12\text{ }\mu\text{m}$ ) and does not lase. At 2.5 times threshold, additional lasing regions appear, and the non-lasing spot is reduced to  $\sim 1\text{ }\mu\text{m}$ . The aperture of the VCSEL now appears segmented into more than 6 smaller filaments of 2-3  $\mu\text{m}$  in diameter.

Fringes are observable in the intensity distributions in Fig. 4.9. Cross sections of higher resolution scans show that the fringes have a period on the order of half a wavelength. The fringes are not due to scanning artifacts, because they are not aligned with either scan direction and they are also present in the near-field image collected with conventional optics. Clipping of a Gaussian beam by an aperture can impose modulation onto the beam's intensity profile, however (Siegman, 1986). In these gain-guided devices, the proton-implanted region is larger than the aperture of the *p*-metal ring contact. Recombination and thus light is present under the metal

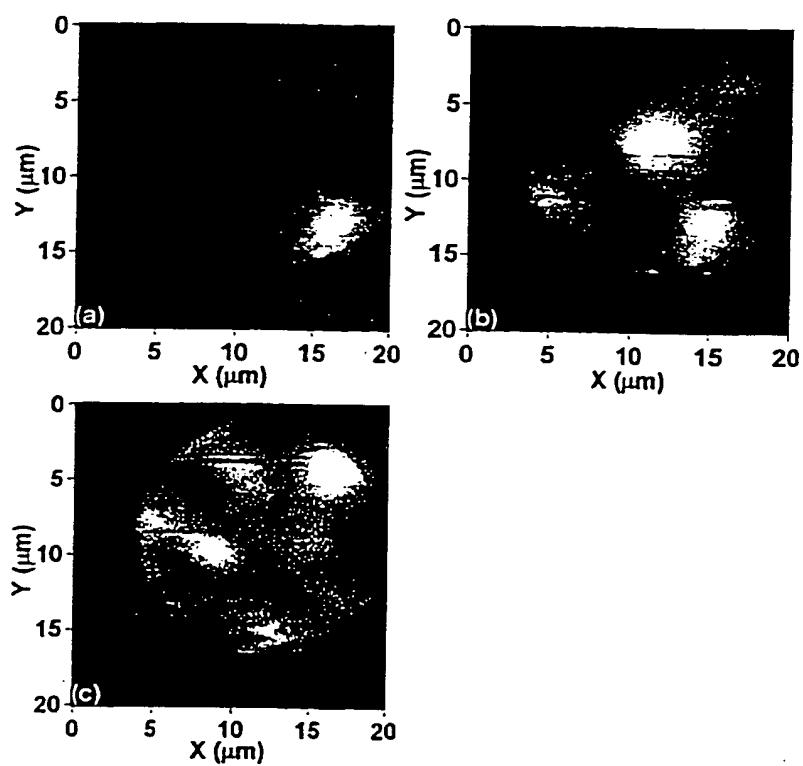


Figure 4.9: Collected near-field images of the intensity distributions at: (a) 7 mA, (b) 10 mA, and (c) 15 mA.

contact. The difference in the round-trip phase shift experienced by the light under the metal aperture and the light within the clear aperture due to termination of the DBR with metal rather than air creates an effective phase discontinuity that diffracts light. One plausible explanation is that the fringes are high-spatial frequency Fresnel ripples superimposed onto the mode within the near-field as a result of diffraction from this phase aperture. In the measurement plane, the Fresnel number is calculated to be large for micrometer diameter filaments and an assumed effective aperture residing several hundred nanometers below the sample surface. This gives rise to fringes having a period consistent with that observed.

An example of the correlation between the sample's optical distribution (at 10 mA) and topography is shown in Fig. 4.10. The shear force data are represented by the rendered three-dimensional (3D) object. The coloring of the 3D object represents increasing optical intensity through a color map that progresses from dark blue to purple, to orange, to yellow, to white-cyan. This figure illustrates the location of the three lasing regions relative to the *p*-contact metal.

### Spectrally Resolved Images

To obtain spectrally resolved images, the collected light from the NSOM tip was guided to a spectrometer. A total of 32x32 spectrally resolved scan points were acquired across the aperture. The intensity of each resolvable transverse mode was integrated and its wavelength range false-colored at each scan position. The resulting composite image displays relative intensity and spatial distribution information for each transverse mode. Bilinear interpolation was performed to smooth the pixellated images. An additive

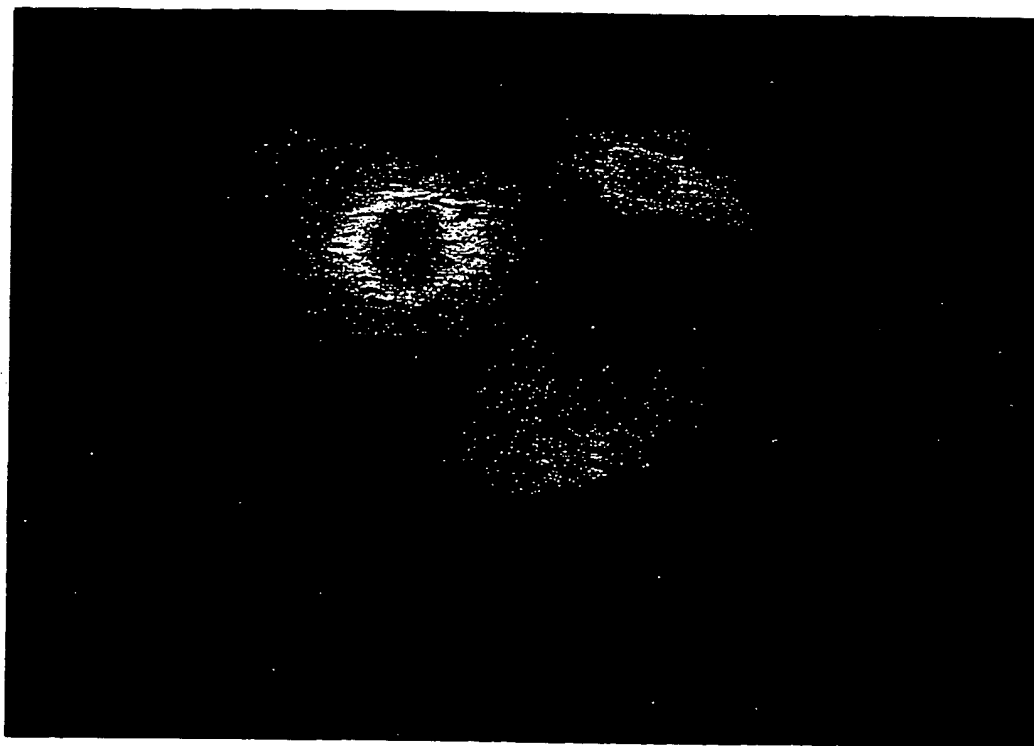


Figure 4.10: Mapping of the NSOM measured optical emission onto the acquired shear-force data of the  $p$ -contact topography of a gain-guided VCSEL operating at 10 mA. The shear-force data are represented by the rendered three-dimensional (3D) object. The coloring of the 3D object represents increasing optical intensity through a color map that progresses from dark blue to purple, to orange, to yellow, to white-cyan. (Courtesy of Greg Vander Rhodes)

color system with red, green, and blue primaries was used for false coloring. Mixing combinations of these primary colors in different proportions creates a spectrum of colors each with a different hue, saturation, and brightness (Agoston, 1987). The colors of the composite image thus relay information on the spatial overlap of the different transverse modes. For reference, if I combine equal proportions of any two primary colors, I get the secondary colors: red and blue create magenta, red and green create yellow, blue and green create cyan, while equal parts of red, green, and blue create white. These secondary colors are the primary colors of the subtractive color system. Overlaying contour lines, created by integrating the total intensity of all the modes, onto this composite image allows comparison of the intensity of one mode to that of another. The contour lines have been colored by an inverted grayscale to be visible on the image. High intensity is represented by dark contour lines.

Figure 4.11 shows three composite images for spectrally resolved near-field data at (a) 7 mA, (b) 10 mA, and (c) 15 mA. A key of the primary colors is shown in the upper-right corner of the images. As shown in Fig. 4.5, there are two transverse modes (modes 0 and 1) at 7 mA. Mode 0 has been colored with red, and the higher energy mode 1 has been colored with the higher energy false color of green. The strongest mode is mode 0 (red). The most intense portion of mode 0 is at the location ( $X \sim 14 \mu\text{m}$ ,  $Y \sim 2.5 \mu\text{m}$ ). The peak intensity of mode 1 (green) is near ( $X \sim 12 \mu\text{m}$ ,  $Y \sim 13 \mu\text{m}$ ). As suspected from the competition behavior observed in Fig. 4.11 for low current, there is spatial overlap between modes 0 and 1 as evident from the orange (reddish-yellow) and yellow-green colors (rather than pure red and green) in the image.

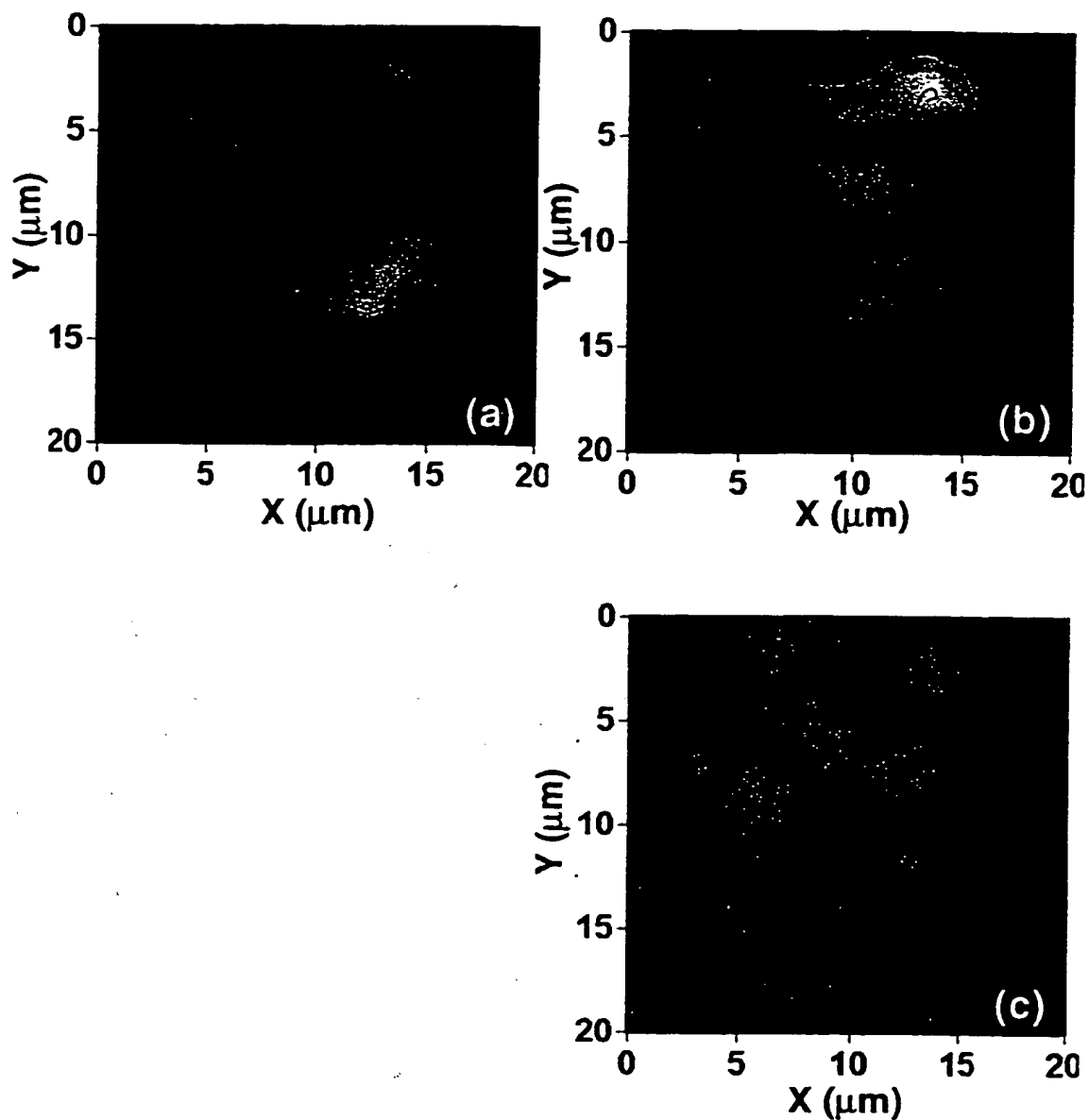


Figure 4.11: Composite images illustrating spectrally resolved near-field emission from a gain-guided VCSEL operating at: (a) 7 mA, (b) 10 mA, and (c) 15 mA. An additive color system with red, green, and blue primaries was used for false coloring the transverse modes in order of their energy. A key of the primary colors is shown in the upper right of each image. The various mixed colors relay information on the spatial overlap of the different transverse modes. The overlaid contour lines allow comparison of the intensity of one mode to another. High intensity is represented by dark contour lines.



At 10 mA, three transverse modes coexist. Each mode was again false-colored in order of energy (mode 0 is red, mode 1 is green, and mode 2 is blue), and the composite image is shown in Figure 4.11 (b). I see several nearly spectrally pure spatial regions of mode 0 (red). Almost all of mode 1 (green) overlaps mode 0, as there is little pure green in the image, but rather yellow. The peak intensity of mode 1 has now migrated to the lobe nearest the contact ring closest to the bonding pad at ( $X \sim 14 \mu\text{m}$ ,  $Y \sim 2.5 \mu\text{m}$ ). The contour lines indicate that the majority of the total device power is emitted by the three spectrally pure filaments of the fundamental mode and the large overlapping filament of modes 0 and 1. Mode 2 (blue) has just begun to turn on and begins filling between the stronger modes 0 and 1, with slight overlap.

One limitation of this visualization scheme is the number of transverse modes which can be colored. A maximum of three modes can be false-colored, because there are only three primary colors. At 15 mA, there are four transverse modes. For the image in Figure 4.11 (c), modes 0 and 1 were false-colored red, while modes 2 and 3 were colored green and blue, respectively. Separate plots (not shown) of the spatial distribution of modes 0 and 1 were used to identify each mode's contribution to the false color red in the composite image of Figure 4.11 (c). As indicated in Fig. 4.7, the most intense lobe of mode 2 (green) appears spatially separated from the other modes near ( $X \sim 14 \mu\text{m}$ ,  $Y \sim 2.5 \mu\text{m}$ ). A small contribution of mode 1 (red) overlaps with mode 2 (green), creating a yellow tint at the center of the ( $X \sim 14 \mu\text{m}$ ,  $Y \sim 2.5 \mu\text{m}$ ) location. Significant spatial overlap of modes 1 and 3 is evident by the magenta and pinkish-white colors as well as lack of intense locations of pure blue. These magenta and pinkish-white regions are the

most intense lasing filaments. There is one low intensity region of nearly pure white at ( $X \sim 6 \mu\text{m}$ ,  $Y \sim 9 \mu\text{m}$ ) indicating uniform overlap of all transverse modes.

#### 4.3.4 Discussion

Knowledge of the transverse mode characteristics of low-coherence VCSELs is important in the understanding of system reliability and BER in commercial LAN applications based on these devices. I have studied the transverse mode characteristics of gain-guided multimode VCSELs using the high spectral and spatial resolution afforded by near-field scanning optical microscopy and spectroscopy. Far-field spectra were used to calculate light-versus-current behavior for each transverse mode. I have reported the near-field spatial distributions of the emission intensity and lasing wavelengths of the transverse modes. Oscillations in the transverse-mode-resolved L-I curves indicated competition for gain among some modes as well as independent coexistence among others. Using the spectrally resolved near-field measurements, I have correlated these oscillations to their spatial overlap. I have experimentally verified that spatially separated transverse modes in VCSELs coexist by sharing the available gain, while spatially overlapping modes compete.

I have demonstrated that NSOM is a powerful tool for mapping and correlating the spectral, spatial, and topographical features of VCSELs within the near field. Unlike bulk-optic techniques that image the lasing aperture through a spectrometer onto a two-dimensional CCD array, spectrally resolved NSOM has no limitation on spectral resolution imposed by the spatial size of the aperture. I anticipate that further studies at various heights above the aperture will provide additional information on the angular

divergence of the separate lasing filaments. This information will be important in the determination of mode-coupling loss and consequently modal noise.

#### 4.4 Analysis of a Mode Control Technique

In this section, I discuss a simple and easy to implement transverse mode control technique that uses an out-of-phase reflection from a metal layer to spoil the high-Q of the VCSEL cavity in a localized lateral position to inhibit lasing in that region. Patterning of the metal across the VCSEL's DBR creates a spatially dependent reflectivity. Through analysis of the overlap integral between the supported waveguide modes and the metal pattern, the suppression of transverse modes can be evaluated and tailored.

##### 4.4.1 Plane Wave Calculations

The VCSEL cavity Q can be spoiled by reducing the reflectivity of one of the two DBRs. In a top emitting VCSEL the topmost DBR usually comprises an even number of quarter wavelength thick layers so as to have the reflectance from the uppermost semiconductor-air interface be in phase with the reflections from the other layers (refer to Chapter 2). For a bottom emitting device, the electrical contact is frequently placed atop the topmost DBR (see Fig. 2.2 (a) page 11). The thickness of the topmost semiconductor layer is adjusted to compensate for the phase shift upon reflection from the metal so this strong reflection is in phase with the reflections from the other layers (D.I. Babic, 1996). For mode control, I propose that the thickness of the topmost semiconductor layer be adjusted so this semiconductor-metal reflection is  $180^\circ$  out-of-

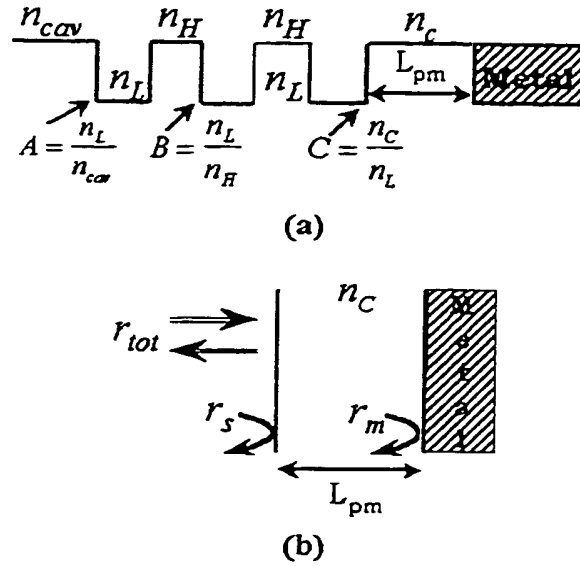


Figure 4.12: Diagram (a) of a VCSEL top DBR with an even number of quarterwave layers, a phase matching layer of arbitrary thickness, and a metal termination. The lumped mirror model of the reflectance from the terminated DBR is shown in (b).

phase with the other distributed reflections so as to substantially reduce the overall reflectance of the DBR. The deviation of this phase matching layer's thickness from a quarter wavelength will inevitably also reduce the reflectance of the air-terminated regions of the DBR.

As discussed in Chapter 2, the field reflectance from an  $N$  layer quarter wavelength thick DBR can be written as (Corzine, 1993),

$$|r| = \frac{1 - AB^{N-1}C}{1 + AB^{N-1}C}. \quad (4.1)$$

For the case of a VCSEL top mirror with an even number of pairs and a metal termination as shown in Fig. 4.12 (a), it is convenient to express the field reflectance and phase

as,

$$|r_s| = \frac{1 - AB^{N-2}C}{1 + AB^{N-2}C}, \quad \theta_s = \pi, \quad (4.2)$$

where  $A$ ,  $B$ , and  $C$  have modified to be,

$$A = \frac{n_L}{n_{cav}}, \quad B = \frac{n_L}{n_H}, \quad C = \frac{n_C}{n_L}. \quad (4.3)$$

The index of refraction of the low index layer is denoted with  $n_L$ , the high index layer with  $n_H$ , the cavity with  $n_{cav}$ , and the phase matching layer with  $n_C$ .<sup>1</sup> In this fashion, the field reflectance of the stack shown in Fig. 4.12 (a) has been written without the inclusion of the terminating metal-semiconductor reflection. This is needed to be able to examine the effect of a non-quarterwave matching layer on the overall reflectance of the DBR. The field reflectance from the phase matching layer-metal interface is,

$$r_m = \frac{n_C - (n_m + ik_m)}{n_C + (n_m + ik_m)}, \quad (4.4)$$

where  $n_m$  and  $k_m$  are the index and extinction coefficients of the terminating metal.

The interface reflectivity and phase are then,

$$R_m = \frac{(n_C - n_m)^2 + k^2}{(n_C + n_m)^2 + k^2}, \quad \theta_m = \frac{\pi}{2} + \tan^{-1} \left[ \frac{n_m^2 - n_C^2 + k^2}{2n_C k} \right]. \quad (4.5)$$

The reflectance from the metal-terminated DBR can be calculated by assuming a "lumped" mirror model (Babic, 1995) for the unterminated stack and applying the well known formula for the Fabry-Perot cavity (Fowles, 1975). This model is illustrated in Fig. 4.12 (b). The total field reflectance from the metal-terminated DBR as

---

<sup>1</sup>The index of the phase matching layer is denoted as  $n_C$ , as this layer is commonly referred to as the contact layer for the case of a VCSEL where current is injected through this layer.

a function of the phase matching layer thickness is,

$$r_{tot} = \frac{|r_s| e^{-i\theta_s} + \sqrt{R_m} e^{-i(\theta_m + \theta_{pm})}}{1 + |r_s| \sqrt{R_m} e^{-i(\theta_m + \theta_{pm} + \theta_s)}} \quad (4.6)$$

where the phase of the matching layer is,

$$\theta_{pm} = 2 \frac{2\pi L_{pm}}{\lambda} \quad (4.7)$$

The physical thickness of the matching layer is  $L_{pm}$  and  $\lambda$  is the wavelength of light in the layer. In practice the calculated value of  $L_{pm}$  needs to be adjusted by the penetration depth of the DBR, as a lumped mirror model was assumed.<sup>2</sup> If the metal is perfectly conducting ( $\theta_m = \pi$ ), a phase matching layer thickness of  $\lambda/2$  would be needed for the semiconductor-metal reflection to be in-phase and constructively add to the total reflectance of the mirror. Alternatively, a phase matching layer of  $\lambda/4$  would cause the semiconductor-metal reflection to out-of-phase and destructively interfere with the reflectance of the rest of the DBR stack. To grasp just how enormous the reflection from the semiconductor-metal interface is, it can be equated to an equivalent number,  $N_{equ}$ , of DBR layers (Corzine, 1993),

$$\frac{1 - \sqrt{R_m}}{1 + \sqrt{R_m}} = B^{N_{equ}} \Rightarrow N_{equ} = \frac{\ln \left[ \frac{1 - \sqrt{R_m}}{1 + \sqrt{R_m}} \right]}{\ln \left[ \frac{n_L}{n_H} \right]} \quad (4.8)$$

For the index and extinction coefficient of aluminum, silver, or gold, the number of equivalent mirror pairs ( $N_{equ}/2$ ) is  $\sim 12$ . In other words, an out-of-phase reflection is equivalent to the removal of 12 mirror pairs!

Figure 4.13 illustrates the magnitude of Eq. 4.6 versus the thickness of the phase matching layer for the metal terminations of Table 4.1. The value of  $|r_s|$  used

Termination	$n$	$k$
Perfect Conductor	0	$\infty$
Gold (Au)	0.174	5.69
Silver (Ag)	0.110	6.56
Aluminum (Al)	1.75	8.50

Table 4.1: Index of refraction at 980 nm for the gold, silver, and aluminum DBR terminations.

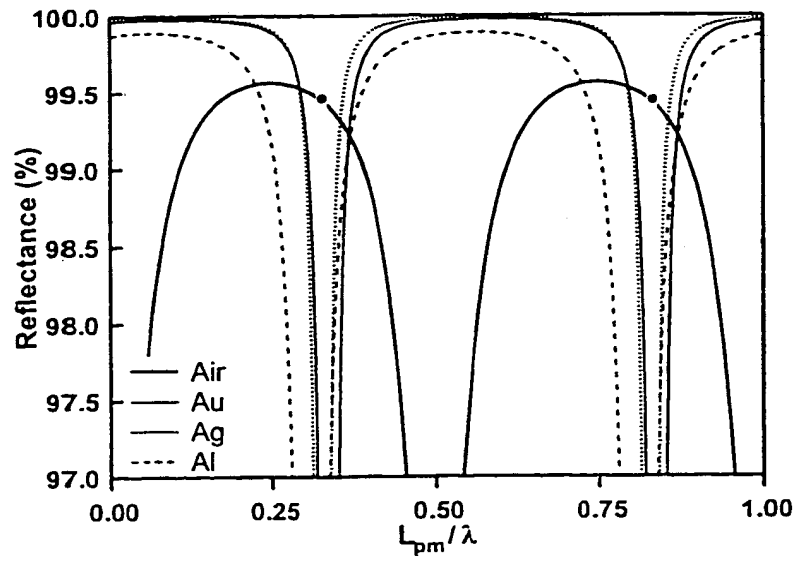


Figure 4.13: Plot of the magnitude of Eq. 4.6 versus the thickness of the phase matching layer for the metal terminations of Table 4.1.

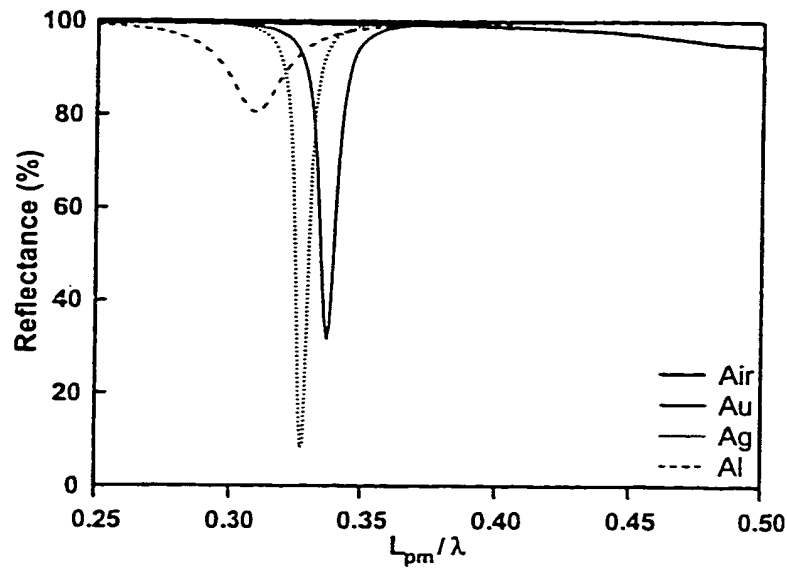


Figure 4.14: Plot of the magnitude of Eq. 4.6 versus the thickness of the phase matching layer illustrating the minimum reflectance for the metal terminations of Table 4.1.

in this plot comes from the reflectance of a 16-pair AlAs/GaAs DBR at 980 nm. The metal terminations used need only be slightly thicker than the penetration depth of the metal (15 nm). An in-phase reflection from the metals occurs at a thickness slightly greater than  $\lambda/2$ , as the metals are not perfect conductors. As expected, the maximum reflectance for an air-terminated reflector comes for a matching layer thickness of  $\lambda/4$ . With a slight increase in the matching layer thickness beyond  $\lambda/4$  (to near the dot in the figure), the reflectance of the air-terminated DBR is only slightly reduced, as the semiconductor-air interface is only equivalent to about 3 mirror pairs. The reflectance of the metal-terminated DBRs, however, are drastically reduced. Figure 4.14 shows the minimum reflectance values achievable with the different terminations. With the

<sup>2</sup>The lumped mirror approximation was used to allow meaningful analytical equations to be derived and discussed. The characteristic matrix should be used to refine the calculations prior to growth of the structure.



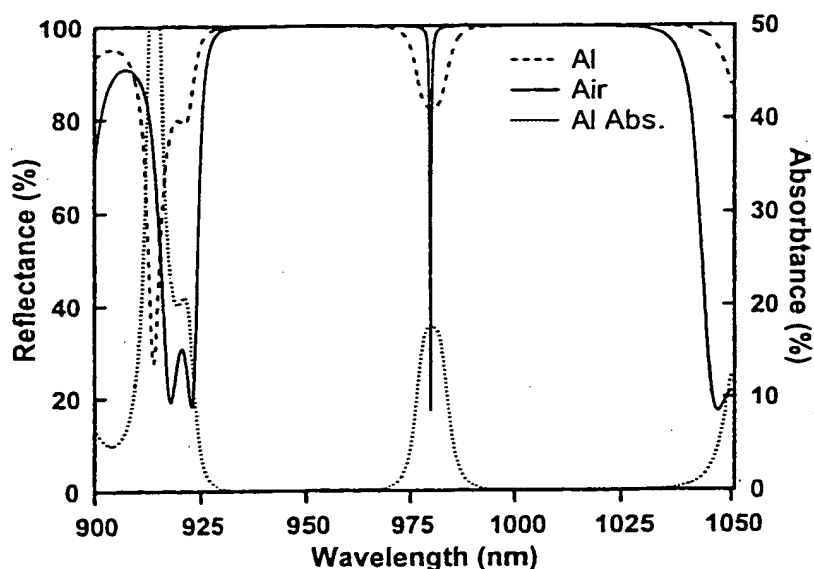


Figure 4.15: The simulated reflectance spectrum of a microcavity consisting of a 16.5-pair AlAs/GaAs bottom DBR, a  $\lambda$  cavity spacer, and a 16-pair AlAs/GaAs top DBR where the layer thickness of the top most DBR layer has been adjusted according to the plot of Fig. 4.13 to create a destructive reflection when terminated with aluminum.

aluminum termination the reflectance is reduced to a minimum of 80% while gold and silver further reduce the minimum to 32% and 8%, respectively. The lower reflectance minima of gold and silver come with the penalty of having a more critical dependence on the matching layer thickness. All the metal terminations shown would more than sufficiently reduce the finesse of the VCSEL cavity below that needed to achieve lasing. Figure 4.15 shows the simulated reflectance spectrum of a microcavity consisting of a 16.5-pair AlAs/GaAs bottom DBR, a  $\lambda$  cavity spacer, and a 16-pair AlAs/GaAs top DBR where the layer thickness of the top most DBR layer has been adjusted according to the plot of Fig. 4.13 to create a destructive reflection when terminated with aluminum. The solid line shows the simulated reflectance observed from within the substrate for the air-terminated cavity. The thick dashed line shows the reflectance of the metal-

terminated cavity. Substantial broadening of the cavity resonance is observed in the metal-terminated case, as the aluminum layer absorbs a portion of the incident light (thin dashed line) and reflects the rest out-of-phase. An inherent limitation to this type of mode control is that the field amplitude that “sees” the metal terminator decreases as the number of mirror pairs is increased due to the exponential decay of the field within the mirror. This results in a given metal terminator having less of an effect on the cavity finesse as DBR pairs are added. Thus, the ratio of the threshold gain between modes solely under the air-terminated region to the modes under the metal-terminated region is increased. This ratio increases to one for an infinite number of DBR pairs.

#### 4.4.2 Threshold Gain for “Ideal” Modes

The different reflectivities for a mode solely under the air-terminated region versus the metal-terminated region gives rise to two different threshold gains. The threshold gain equations for the air and metal-terminated regions are,

$$\Gamma g_{th,Air} = \langle \alpha_i \rangle + \frac{1}{L} \ln \left( \frac{1}{r_B r_{T_{Air}}} \right), \quad (4.9)$$

and,

$$\Gamma g_{th,Met} = \langle \alpha_i \rangle + \frac{1}{L} \ln \left( \frac{1}{r_B r_{T_{Met}}} \right), \quad (4.10)$$

where  $\Gamma$  is the optical confinement factor,  $g_{th}$  is the gain needed to reach threshold,  $\langle \alpha_i \rangle$  is a distributed loss factor,  $L$  is the cavity length, and  $r_B$  and  $r_T$  are the field reflectances of the bottom and top mirrors.<sup>3</sup> The amount of mode suppression can be

---

<sup>3</sup>Refer to Chapter 2 for a more detailed explanation of these variables and their effect on a VCSEL's performance.

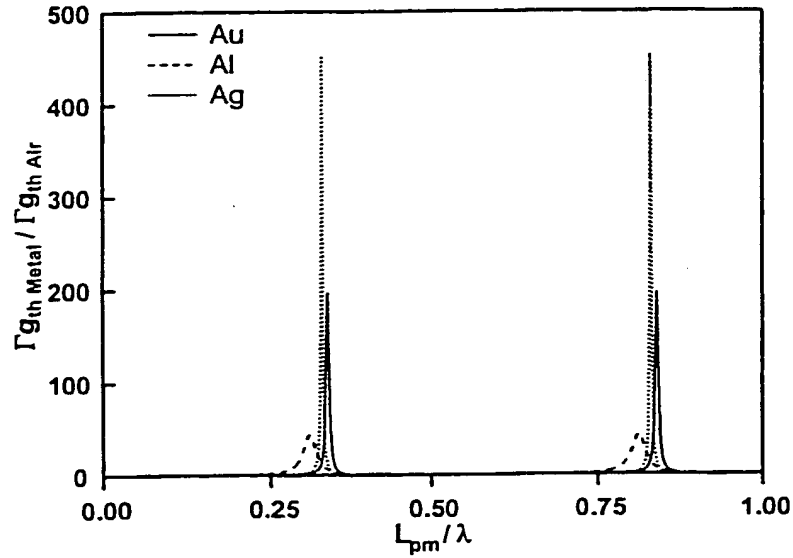


Figure 4.16: A plot of the threshold gain ratio versus thickness of the phase matching layer for the three metal terminations in the ideal case.

evaluated in the ideal case by taking the ratio of the threshold gains for the metal and air regions. The ideal case is where the higher-order modes completely overlap the low-Q metal region and the low-order mode completely overlaps the high-Q air-terminated region. Assuming the internal losses are small in comparison to the mirror losses and that bottom mirror reflectivity is approximately unity, the threshold gain ratio is simply,

$$\frac{\Gamma g_{th_{Met}}}{\Gamma g_{th_{Air}}} = \frac{\ln(r_{T_{Met}})}{\ln(r_{T_{Air}})}. \quad (4.11)$$

A plot of this ratio versus thickness of the phase matching layer for the three metal terminations is shown in Fig. 4.16. The threshold gain of the low-Q mode is more than 450 times that of the high-Q mode for termination with silver! The threshold gain ratios for gold and aluminum terminations are broader while still being significant at nearly 200 and 45 times, respectively. These high ratios show promise for dealing with

the nonideal case where the higher and lower order modes overlap with both the air and metal-terminated regions to some degree.

#### 4.4.3 Modal-Dependent Reflectivity and Threshold Gain

In the nonideal case an effective reflectivity of the top mirror must be derived that is dependent on a given transverse mode's overlap with the metal and air-terminated regions. Consequently, the guided modes of a VCSEL must be approximated. Linearly polarized (LP) modes are a good approximation for the guided modes in most optical fibers whose core refractive index is only slightly higher than that of the cladding medium (Yariv, 1991). The guided transverse modes of a gain-guided VCSEL, and in some cases an oxide confined VCSEL,<sup>4</sup> can also be approximated using LP modes. The injected carriers in a gain-guided VCSEL produce a region of high gain with a decreased refractive index. Additionally, spreading of the injected current across the device aperture raises the temperature of the active region and subsequently increases the refractive index. This increase in refractive index is often larger than the decrease induced by the injected carriers. For a typical 30  $\mu\text{m}$  diameter gain-guided device operating at 1.5 times the threshold current, the index difference between the "core" and "cladding" has been modeled to be  $\sim 0.003$  (Y.G. Zhao, 1996).

The electric-field form derived in (Yariv, 1991) that describes LP modes is,

$$\begin{aligned} E &= AJ_l(hr) e^{i\phi_l} \exp[i(\omega t - \beta z)], \quad r < a \text{ (Core)} \\ E &= BK_l(qr) e^{i\phi_l} \exp[i(\omega t - \beta z)], \quad r > a \text{ (Cladding)} \end{aligned} \quad (4.12)$$

---

<sup>4</sup>Depending on the position of the oxide lens in the standing wave,  $\Delta n$  for an oxide-confined device can be an order of magnitude less than 1. This index difference is discussed in Chapter 4.

where  $A$  and  $B$  are constants,  $\beta$  is the propagation constant,  $a$  is the radius at which the index step from core to cladding occurs,  $h$  and  $q$  are the transverse wave numbers,  $\omega$  and  $t$  are the angular frequency and time, and  $r, \phi$ , and  $z$  are the cylindrical coordinates. The circular symmetry of the device yields solutions of this form for both  $x$  and  $y$  polarizations. For continuity at ( $r = a$ ),

$$B = \frac{AJ_l(ha)}{K_l(qa)}, \quad (4.13)$$

where  $A$  is determined by normalization. Considering the continuity of  $E_z$  at ( $r = a$ ) and that continuity must hold for all  $\phi$  yields the mode conditions,

$$h \frac{J_{l+1}(ha)}{J_l(ha)} = q \frac{K_{l+1}(qa)}{K_l(qa)}, \quad (4.14)$$

and

$$h \frac{J_{l-1}(ha)}{J_l(ha)} = -q \frac{K_{l-1}(qa)}{K_l(qa)}. \quad (4.15)$$

The transverse wave numbers are related through  $\beta$  via,

$$h^2 = n_{core}^2 \left( \frac{\omega}{c} \right)^2 - \beta^2, \quad (4.16)$$

and,

$$q^2 = \beta^2 - n_{clad}^2 \left( \frac{\omega}{c} \right)^2, \quad (4.17)$$

where  $n_{core}$  and  $n_{clad}$  are the index of refraction of the core and cladding, and  $c$  is the speed of light in a vacuum. Solving Eqs. 4.16 and 4.17 for either of the transverse wave number variables and substituting into Eq. 4.14 yields solutions for the variable as a function of  $l$  and  $m$ . The root of the transcendental equation is indicated by

$m$  and  $l = 1, 2, 3, \dots$ . The modes calculated with these transverse wave numbers are designated by  $LP_{lm}$ . Figure 4.17 shows several LP modes. The patterns shown were calculated for a 30  $\mu\text{m}$  diameter device with a wavelength of 1  $\mu\text{m}$  using  $n_{\text{core}} = 3.4195$  and  $n_{\text{clad}} = 3.4165$ . The cladding index chosen is the average refractive index of GaAs and AlAs. The core index is equal to the cladding index plus the index difference modeled for a 30  $\mu\text{m}$  diameter gain-guided device by (Y.G. Zhao, 1996).

A modal-dependent reflectivity needs to be derived to evaluate the threshold gain of each LP mode. This is accomplished by calculating the spatial overlap integral of the metal termination with the LP mode. The spatial dependence of the metal termination is shown in Fig. 4.18. This is the simplest of all the patterns able to be used as it is independent of  $\phi$ . The modal-dependent reflectivity is,

$$R_{l,m} = \int_0^\infty R(r) |U_{l,m}(r)|^2 dr, \quad (4.18)$$

where  $R(r)$  is the radial dependent reflectivity for the termination shown in Fig. 4.18 and  $U_{l,m}(r)$  is the electric field mode function. Substituting in  $R(r)$ ,

$$R_{l,m} = \int_0^{a_m} R_{\text{air-stack}} |U_{l,m}(r)|^2 dr + \int_{a_m}^\infty R_{\text{m-stack}} |U_{l,m}(r)|^2 dr, \quad (4.19)$$

where  $a_m$  is the radius of the opening in the metal terminator, and  $R_{\text{air-stack}}$  and  $R_{\text{m-stack}}$  are the total reflectances of the air-terminated and metal-terminated stacks of Fig. 4.13 for a given matching layer thickness. Knowing that,

$$\int_0^\infty |U_{l,m}(r)|^2 dr = 1 \quad (4.20)$$

then,

$$\int_{a_m}^\infty R_{\text{m-stack}} |U_{l,m}(r)|^2 dr = 1 - \int_0^{a_m} R_{\text{m-stack}} |U_{l,m}(r)|^2 dr. \quad (4.21)$$

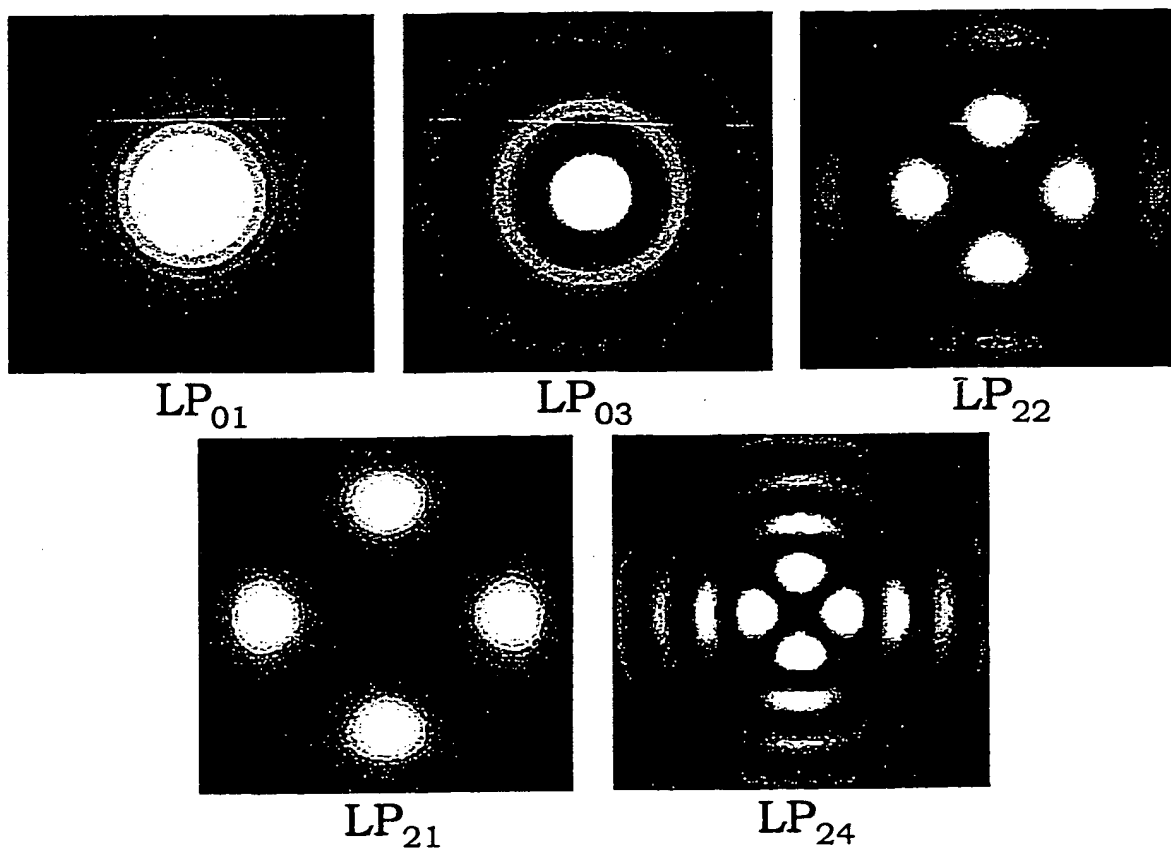


Figure 4.17: Calculated LP mode patterns for a 30  $\mu\text{m}$  diameter device with a wavelength of 1  $\mu\text{m}$ . The refractive indices used were  $n_{\text{core}} = 3.4195$  and  $n_{\text{clad}} = 3.4165$ .

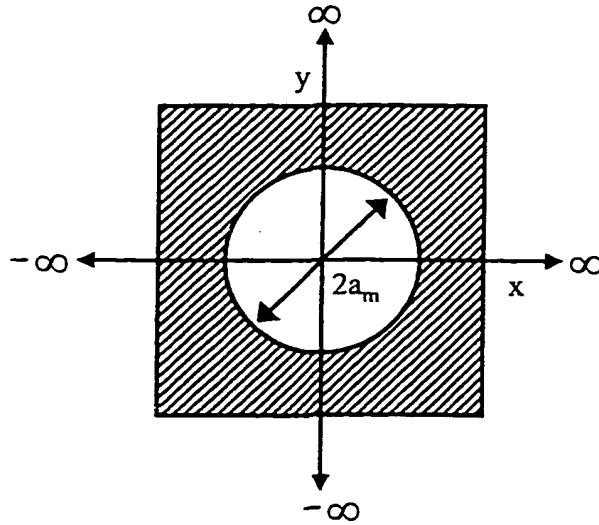


Figure 4.18: The spatial dependence of the metal termination used for modal-dependent reflectivity calculations.

The modal-dependent reflectivity can now be rewritten as,

$$R_{l,m} = (R_{air-stack} - R_{m-stack}) \int_0^{a_m} |U_{l,m}(r)|^2 dr + R_{m-stack}. \quad (4.22)$$

As  $a_m \rightarrow \infty$ ,  $R_{l,m} \rightarrow R_{air-stack}$  for all modes. Conversely as  $a_m \rightarrow 0$ ,  $R_{l,m} \rightarrow R_{m-stack}$  for all modes. A characteristic matrix calculation of a 16-pair AlAs/GaAs DBR at 1100 nm shows that the peak reflectance is 99.3%. Adjusting the thickness of the topmost layer of the stack to an antiresonant condition for an Al terminator results in reducing the air-terminated reflectance ( $R_{air-stack}$ ) to 99.27%. Termination of the adjusted stack with Al results in  $R_{m-stack} = 70\%$ . The modal-dependent reflectivity calculated is shown in Fig. 4.19 for this stack with various LP modes of a 30  $\mu\text{m}$  diameter device. As the opening in the termination metal is closed the reflectance for all modes goes to that of the metal termination. Conversely, if it is opened the reflectance for all modes approaches that of the air termination. Creating an Al termination with



an opening whose radius is a few micrometers smaller than the device radius causes the reflectance of higher-order modes to be reduced by up to several percent without significantly reducing the reflectance of the fundamental mode,  $R_{01}$ . The ratio of the threshold gain of a  $LP_{lm}$  mode to the fundamental  $LP_{01}$  mode is calculated using the modal-dependent reflectivities in Fig. 4.19 and the ratio in Eq. 4.11. Figure 4.20 shows the calculated gain ratios. This plot shows that the threshold gain for the  $LP_{24}$  mode can be increased by 7.25 times using an Al terminator with an opening radius of  $14\ \mu\text{m}$ . Simultaneously, the threshold gain of the  $LP_{14}$  mode is increased to 4 times, the  $LP_{21}$  to 2 times, and the  $LP_{02}$  and  $LP_{14}$  modes to nearly 1.5 times. This calculation indicates that significant higher-order mode suppression can be achieved in a large-aperture ( $30\ \mu\text{m}$  diameter). It is important to realize that this suppression of the higher-order modes comes at the penalty of increasing the needed gain for the fundamental mode to reach threshold. Figure 4.21 shows the ratio of the threshold gain for the  $LP_{01}$  mode to that of the ideal air-terminated mode. This plot shows that the needed threshold gain increases as the opening in the metal terminator gets smaller and more of the mode experiences the loss from the destructive semiconductor-metal reflection. For an Al terminator with an opening radius of  $14\ \mu\text{m}$ , the threshold gain of the fundamental mode is increased slightly to 1.1 times threshold.

#### 4.4.4 Discussion

In this section, a novel transverse mode control technique for VCSELs has been introduced. I have shown that high-order transverse modes can be suppressed to a current of several times threshold in a  $30\ \mu\text{m}$  diameter device using an out-of-phase

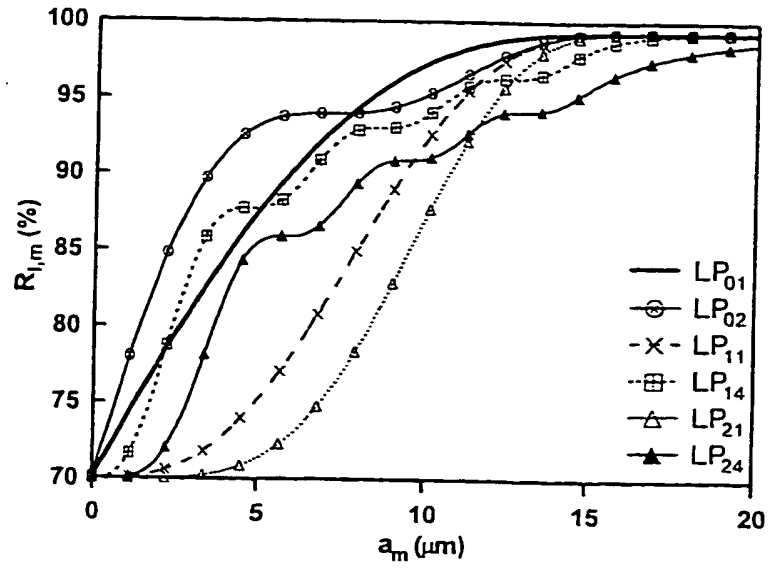


Figure 4.19: The calculated modal-dependent reflectivity of a 16-pair AlAs/GaAs DBR at 1100 nm as a function of the radius of the opening in the Al terminator.

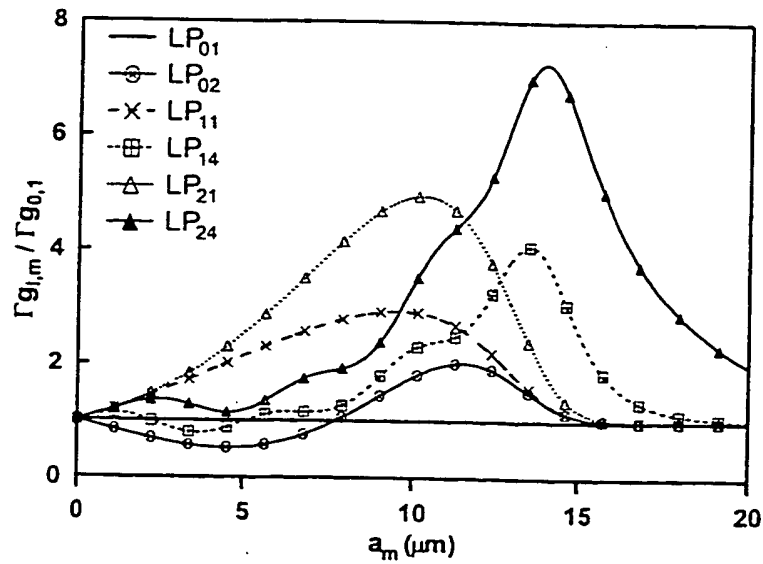


Figure 4.20: The threshold gain ratios as a function of the radius of the opening in the aluminum terminator. The modal-dependent reflectivities in Fig. 4.19 and the ratio in Eq. 4.11 were used.

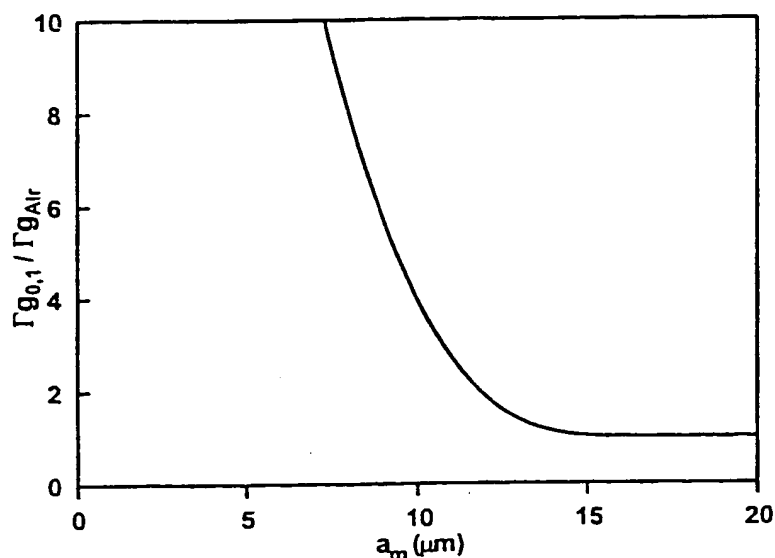


Figure 4.21: A plot of the ratio for the threshold gain of the  $\text{LP}_{01}$  mode to that of the ideal air-terminated mode.

reflection from an aluminum layer atop the semiconductor DBR. Increased suppression is expected through the use of other terminator metals and pattern geometries. While further more detailed simulations are warranted, the complex modal patterns observed in practical devices may make an experimental approach more fruitful. It is anticipated that higher-power single mode VCSELs could be created using this technique. Two similar concepts have been reported more recently than this work. The first method relies on adjustment of the topmost mirror layer's thickness to create a small out-of-phase reflection from the semiconductor-air interface (P. Dowd, 1997). Lasing is achieved after the laser aperture is defined by etching the top mirror layer to a precise thickness in post growth processing. The second method reported is a brute force approach that uses an etch to remove mirror layers from the center of the device aperture and force lasing only in a single higher-order mode (T. Milster, 1998). I believe the method of

mode control presented in this section is a simpler and more elegant alternative to the reported methods. The ability to process and achieve lasing in the as-grown material makes it possible for the mode patterns of a particular device to be analyzed prior to suppression and the choice of the metal pattern. In addition, the use of metal terminators with short optical penetration depths inherently means the thickness of the deposited metal is not critical, unlike the etches of the reported methods. Further, increased loss to the fundamental mode from etching the lasing aperture will not be experienced.

#### 4.5 Summary

Throughout this chapter, I have discussed experimental results on the competition of transverse modes in VCSELs. I have explored the dynamical evolution of these modes through polarization-resolved step response measurements. I have shown that under certain drive conditions multiple transverse mode families can be sustained with the available gain while under other drive conditions one family experiences a slow turn-on as the two sets of modes struggle to coexist. This slow turn-on gives rise to increased BERs in multimode fiber links through the introduction of timing jitter. I have further explored the influence of mode competition on the steady-state L-I behavior of transverse modes in proton-implanted 850 nm devices using near-field scanning optical microscopy. I have reported the near-field spatial distributions of the emission intensity and lasing wavelengths of the transverse modes. Oscillations in the transverse-mode-resolved L-I curves indicate competition for gain among some modes as well as independent coexistence among others. Using the spectrally resolved near-field

measurements, I have correlated these oscillations to their spatial overlap. I have thus experimentally verified that spatially separated transverse modes in VCSELs coexist by sharing the available gain, while spatially overlapping modes compete. The outcome of this work is anticipated to motivate the advancement of the state-of-the-art in VCSEL characterization through inspiring the combination of the high spectral and spatial resolution afforded by NSOM with time-resolved collection techniques.

Additionally in this chapter, I have introduced a novel transverse-mode control technique and have shown through simulations that high-order transverse modes can be suppressed to a current of several times threshold in a  $30\text{ }\mu\text{m}$  diameter device using an out-of-phase reflection from an aluminum layer atop the semiconductor DBR. Increased suppression is expected through the use of other terminator metals and pattern geometries. It is anticipated that higher-power large-area single-mode VCSELs could be created using this technique. Ultimately, NSOM could be used in a research environment to analyze the spatio-spectral characteristics of particular devices after initial laser fabrication to provide feedback for the selection of the metal pattern needed to suppress the observed higher-order modes.

## Chapter 5

### Native Oxide Technology

#### 5.1 Introduction

The wet thermal oxidation of aluminum-rich III-V compound semiconductors creates a dense and stable "native-oxide" film with tremendous versatility (J.M. Dallesasse<sup>a</sup>, 1990). This electrically-insulating and low refractive index oxide material has been used in fabricating innovative and higher performance optoelectronic devices. Apertures formed with this oxide have been used for current and optical-mode confinement in both edge-emitting (J.M. Dallesasse, 1991) and vertical-cavity surface-emitting lasers (VCSELs) (D.L. Huffaker<sup>a,b</sup>, 1994). The discovery of this oxide is said to be enabling the "next generation" of VCSELs. Lasing threshold currents for these new generation devices are dramatically decreasing while output powers and efficiencies are rapidly rising. Industrial research efforts are moving swiftly into this new arena of research with the goal of being first to market with a reliable higher performance vertical-cavity laser. Many questions remain to be answered in this pursuit, with perhaps one of the most disconcerting being: Can these devices be manufactured reproducibly and reliably?

The most obvious place to turn for this answer is to the oxide itself. While the chemistry and microstructure of the oxidation have been the subject of extensive study, the literature has been lacking reports of its optical properties. In this chapter and in the literature (K.J. Knopp<sup>a,b</sup>, 1998), I report the optical constants of oxidized crystalline and low-temperature-grown  $\text{Al}_{0.98}\text{Ga}_{0.02}\text{As}$  over 240 – 1700 nm. More recent publications have confirmed portions of this work through the report of similar results (A. Bek, 1999 ; Hall, 1999).

Native oxides have also been receiving much interest for their use in the formation of low-loss and broad-bandwidth  $\text{Al}_x\text{O}_y\text{-GaAs}$  distributed Bragg reflectors for VCSELs, spatial light modulators, solar cells, and light-emitting diodes (M.H. MacDougal, 1997). Many of these optoelectronic devices and others, such as photodetectors and saturable Bragg reflectors, benefit from broad-bandwidth antireflection (AR) coatings. In this chapter I report the development of high quality, broad-bandwidth, native-oxide antireflection coatings. These coatings reduce manufacturing complexities while promoting integration with other native-oxide technologies.

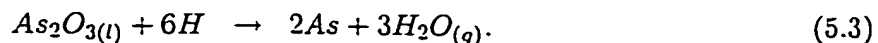
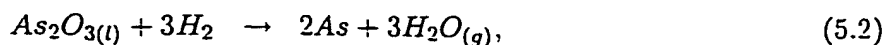
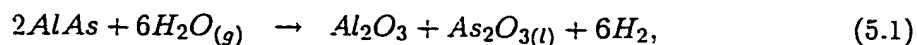
The small gain volume of a VCSEL requires > 99% reflectivity mirrors to stimulate lasing. All sources of loss in the device's microcavity must be minimized for optimal performance. In the last two sections of this chapter, I derive phase distributions of oxide intracavity lenses and use them in Fox and Li resonant mode calculations to estimate scattering losses for various lens shapes.

## 5.2 Formation

### 5.2.1 Oxide Chemistry

Aluminum is an extremely reactive element that tends to form oxygen rich compounds. At room temperature and atmospheric pressure the oxide formed on AlGaAs is unstable and readily corrodes the surface. The formation of this unstable oxide on the facets of edge emitting lasers causes device degradation. In 1990 during a study of the lifetime of AlGaAs quantum well heterostructures, devices were exposed to water vapor at an elevated temperature to accelerate their aging. It was soon discovered that this intended destructive hydrolyzation procedure resulted in the formation of a highly stable phase of AlAs-oxide (J.M. Dallesasse<sup>b</sup>, 1990).

The exact reactions involved in forming this stable AlAs-oxide are unknown. The reactions most likely involve the formation of several different compounds and quite possibly include electrochemical reactions which depend on the potential differences between layers (J.M. Dallesasse<sup>a</sup>, 1990). Three thermodynamically favorable reactions at 425° C are (C.I.H. Ashby, 1997):



The first reaction is responsible for the formation of the aluminum oxide while the later two are responsible for the conversion of arsenic oxide to elemental arsenic which escapes from the oxidized film. The resulting oxide consists primarily of an amorphous solid



solution of  $(\text{Al}_x\text{Ga}_{1-x})_2\text{O}_3$  (K.D. Choquette, 1997). The reduction of the arsenic oxide by the hydrogen at the elevated temperature is believed to be responsible for the oxide's stability. If the Al in Eq. 5.1 is replaced with Ga, the heat of formation of the reaction is increased. Consequently, the oxidation rate of  $\text{Al}_x\text{Ga}_{1-x}\text{As}$  is retarded as the Ga mole fraction is increased (C.I.H. Ashby, 1997).

### 5.2.2 Oxide Fabrication

#### Dry Oxidation

Exposure to the atmosphere causes "dry" oxidation of  $\text{Al}_x\text{Ga}_{1-x}\text{As}$ <sup>1</sup>. Dry oxidation leads to corrosion of the layer and eventually its complete demise as it turns into a powder containing various compounds from the Al-As-O-H phase diagram. This corrosion is evident in the images of Fig. 5.1. Fig. 5.1 (a) shows a picture of a surface layer of  $\text{Al}_{0.90}\text{Ga}_{0.10}\text{As}$  after 1 year of ambient exposure. The surface has not yet degraded to a powder but it appears "rusty". Fig. 5.1 (b) shows an AFM image taken on the edge of a freshly cleaved  $\text{AlAs}/\text{Al}_{0.3}\text{Ga}_{0.7}\text{As}$  DBR. Measurable oxidation of the AlAs layers begins in a matter of minutes. The light shades in Fig. 5.1 (b) represent the AlAs layers. The measured height difference between these oxidized AlAs layers and GaAs layers (darker shades) is  $\sim 20$  nm after 10–20 min of exposure to the atmosphere.

#### Wet Thermal Oxidation

In contrast, the wet thermal oxidation of  $\text{Al}_x\text{Ga}_{1-x}\text{As}$  leads to the formation of a dense and stable oxide. The wet thermal oxidation process is relatively simple.

---

<sup>1</sup>The term "dry" is intended to show contrast to the wet thermal environment used to form stable oxide films. The residual water vapor in air is most likely responsible for the oxidation.

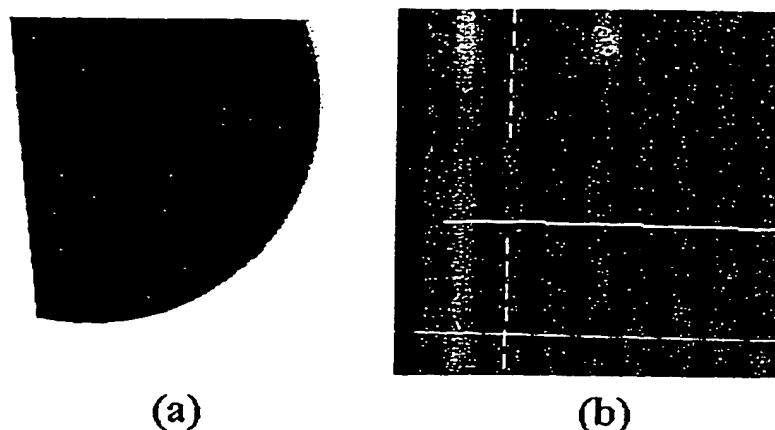
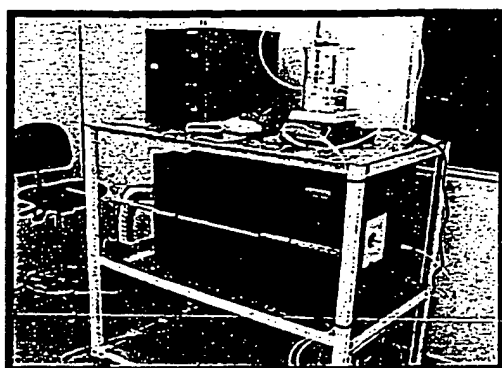
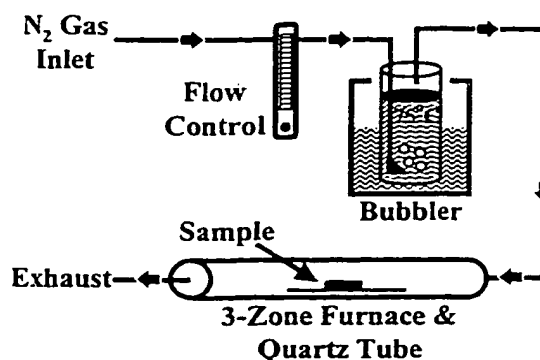


Figure 5.1: Image of (a) a surface layer of  $\text{Al}_{0.90}\text{Ga}_{0.10}\text{As}$  after 1 year of ambient exposure and (b) an AFM image taken on the edge of a freshly cleaved  $\text{AlAs}/\text{Al}_{0.3}\text{Ga}_{0.7}\text{As}$  DBR. The surface in (a) has not yet degraded to a powder but it appears "rusty". Measurable oxidation of the  $\text{AlAs}$  layers in (b) begins in a matter of minutes. The light shades in (b) represent the  $\text{AlAs}$  layers.

The sample to be oxidized is heated to  $\sim 450^\circ\text{C}$  and exposed for a length of time to a flow of water vapor transported by a gas. Careful control of the process parameters is needed, however, to establish a reliable and reproducible process. A picture and schematic of the oxidation setup I have installed at NIST is shown in Fig. 5.2. High-purity nitrogen gas from the boil-off of  $\text{LN}_2$  is used for a carrier of the water vapor. The gas flow rate is set by a needle-valve on the flow meter to 1 L/min. The gas flows into a bubbler filled with deionized water and suspended inside an outer bath which is heated by a hot plate. The large volume of the outer bath maintains the bubbler water at the constant temperature of  $75^\circ\text{C}$ . The steam from the bubbler is then routed into a three temperature-zone furnace housing a 3" diameter quartz tube containing a sample boat at  $450^\circ\text{C}$ . A flexible duct is connected loosely to the endcap of the furnace tube for venting the reaction by-products to an exhaust stack. Mapping the temperature



(a)



(b)

Figure 5.2: A picture of the (a) apparatus for wet-thermal oxidation of AlGaAs and (b) its diagram. The apparatus employs a constant temperature bath for the bubbler and 3 temperature zone furnace for reproducibility.

gradient along the long axis of the tube shows that the three zone furnace provides excellent temperature uniformity over more than twice the length of the sample boat (6"). These parameters have been used for all oxidations in this work.

Samples are oxidized by placing them on a boat and sliding them into the furnace for a specified length of time using a push-rod. Native oxide is created across the surface of a high aluminium containing epitaxial layer by placing them into the furnace immediately after they are removed from the ultrahigh vacuum of the MBE reactor. Alternatively, the epitaxial layers can be capped with a sacrificial layer of GaAs which is selectively etched off immediately before oxidation. A 100 nm thick surface oxide can be formed uniformly across an entire 2" wafer in several minutes.

To create a layer of oxide beneath the sample surface, a multilayer stack of AlGaAs layers must be grown. Using the dependence of the oxidation rate on Al composition, the Al composition of each layer in the stack is chosen to either promote

or inhibit oxidation. Small changes (few percent) in the aluminum composition from layer-to-layer result in dramatic changes in the oxidation rate as the rate exhibits an exponential dependence on Al composition (K.D. Choquette, 1997). Prior to oxidation, the sample is patterned and etched to create mesas or via holes (C.L. Chua, 1997) that expose portions of the buried layers to the flow of steam. The oxidation progresses laterally across each exposed buried layer from the sidewalls towards the center of an etched mesa or outwards from an etched via hole. In this fashion, a buried oxide layer can be incorporated into the multilayer structures of DBRs and VCSELs. Buried oxide layers which do not completely close in across the VCSEL aperture are used for current confinement and the creation of intracavity lenses as will be discussed in section 5.5.

### Mesa Oxidation

Figure 5.3 (a) shows a drawing of a typical etched mesa in which the oxidation is progressing laterally into the center of the pillar. The distance the oxide front has progressed into the pillar depends on the oxidation rate of each layer. The images of Fig. 5.3 (b-d) show the lateral progression of the oxidation front across a buried high Al containing layer in etched  $25 \times 25 \mu\text{m}$  square and  $30 \mu\text{m}$  diameter circular mesas. An optical microscope was used to observe these images. The oxidized region appears in each image as a white band concentric to the outer perimeter of the mesa. The oxidation rate is somewhat dependent on crystallographic orientation of the semiconductor. Figure 5.4 shows an AFM image of a  $33 \mu\text{m}$  diameter circular mesa after 2 min of oxidation. The oxide front perimeter forms a rounded rectangle rather than a circle. The rectangle has a  $14 \mu\text{m}$  diagonal with a  $12 \mu\text{m}$  side. This AFM detects a height

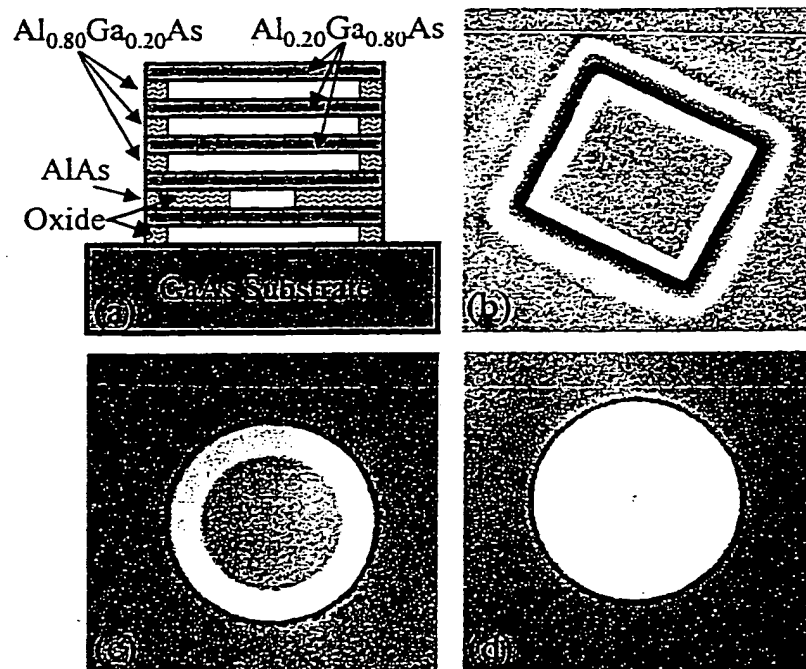


Figure 5.3: Schematic (a) and images (b-d) of the lateral progression of the oxidation front across a buried high-Al containing layer of an etched mesa. The oxidation of the  $\text{Al}_{0.90}\text{Ga}_{0.10}\text{As}$  layers of a VSEL's top DBR is shown in (b). The circular mesas of (c) and (d) illustrate the 8 min and 20 min oxidations of a buried AR coating containing an  $\text{Al}_{0.98}\text{Ga}_{0.02}\text{As}$  layer. The size of the square mesa is  $25 \times 25 \mu\text{m}$  and the diameter of the circular mesas is  $50 \mu\text{m}$ .

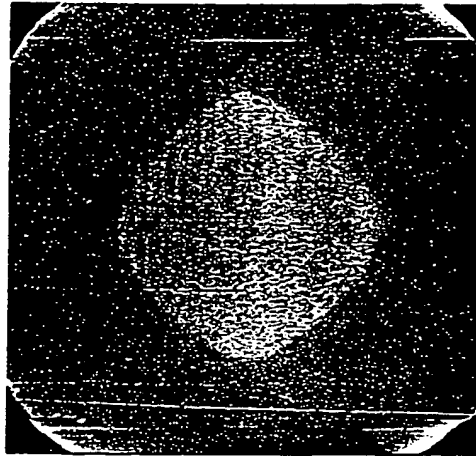


Figure 5.4: An AFM image of a  $33\text{ }\mu\text{m}$  diameter circular mesa after 2 min of oxidation. The oxide front perimeter forms a rounded rectangle rather than a circle. The rectangle has a  $14\text{ }\mu\text{m}$  diagonal with a  $12\text{ }\mu\text{m}$  side. The buried layer oxidized is the graded layer design to be shown and discussed in Fig. 5.6.

difference of 2 nm between the oxidized and unoxidized regions. This height step is a result of the contraction of the layer thickness upon oxidation. The contraction (and expansion) of various oxides will be further discussed in the next section.

### Via Hole Oxidation

Figure 5.5 (a) shows a drawing of the via hole oxidation geometry where the oxidation is progressing laterally outwards from the via holes. The images of Fig. 5.5 (b) show the observed progression of the oxidation front outwards across a buried high Al containing layer with time. The oxide, shown by the light gray, is progressing outwards from each via hole in a concentric circle after 1.5 hours. The oxide circles then begin to merge and form star-shaped unoxidized regions until finally at 2 hours the layer is completely oxidized.

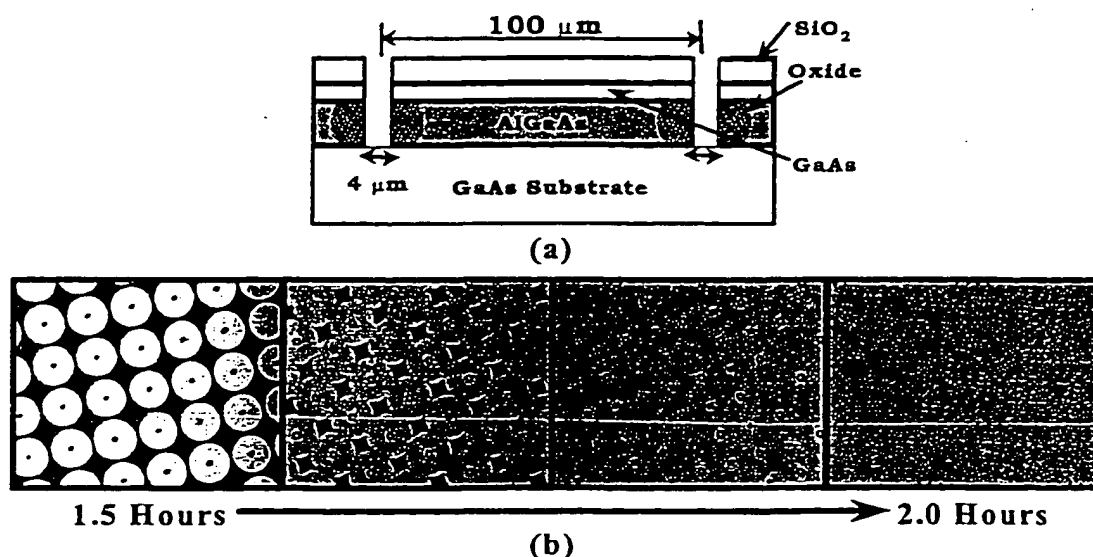


Figure 5.5: Schematic (a) and images (b) of the lateral progression of the oxidation front outwards across a buried high-Al containing layer from an etched via hole. The SiO<sub>2</sub> layer of (a) is used to help prevent consumption and peeling of the thin (13 nm) GaAs capping layer due to surface oxidation.

### Graded Layer Oxidation

Rather than growing a single  $\sim 100$  nm thick layer with a single high-Al composition for oxidation, the layer's composition can be graded over its thickness. This grading allows the oxidation front to be tapered. The exact taper profile formed is a complex diffusion problem dependent on the compositions of the cladding and grading layers as well as their ability to transport reactants to and from the reaction front. The taper allows the creation of an intracavity lens that varies in thickness across the aperture of a device. This will be shown to be beneficial from the point of view of optical scattering losses in sections 5.5 and 5.6. A typical taper used in the multilayer structures of this work consists of a 25 nm grade from Al<sub>0.90</sub>Ga<sub>0.10</sub>As to AlAs, a 20 nm AlAs

layer, and a 25 nm grade from AlAs back to  $\text{Al}_{0.90}\text{Ga}_{0.10}\text{As}$ . A diagram of this grading layer and a sketch of the anticipated taper profile is shown in Fig. 5.6. This layer is a

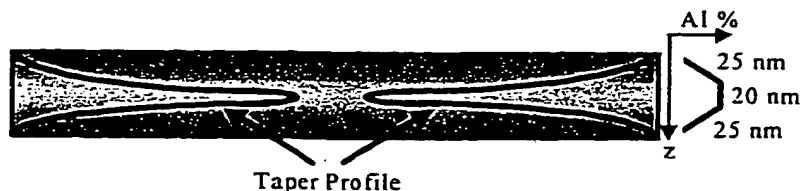


Figure 5.6: A diagram of a taper consisting of a 25 nm grade from  $\text{Al}_{0.90}\text{Ga}_{0.10}\text{As}$  to AlAs, a 20 nm AlAs layer, and a 25 nm grade from AlAs back to  $\text{Al}_{0.90}\text{Ga}_{0.10}\text{As}$ . An outline of the anticipated taper profile is shown.

quarter wavelength thick at 850 nm and is inserted into the top DBR of VCSELs for current and optical mode confinement

### Oxidation Rates

The oxidation rate of a layer is very dependent on the layer composition, oxidation geometry (surface, buried mesa, buried via), composition grading, neighboring layers, layer thicknesses, and of course the furnace parameters: temperature, humidity and flow-rate. For surface oxides, the reaction front progresses longitudinally through the thin  $\text{Al}_x\text{Ga}_{1-x}\text{As}$  layer. The reaction front does not need to travel transversely as the entire transverse dimension of the layer is exposed to the water vapor simultaneously. Characterization of the oxidation rate is difficult as the entire layer is oxidized within minutes. The oxidation rate of an  $\text{Al}_x\text{Ga}_{1-x}\text{As}$  surface layer has been estimated to be 50 nm/min based upon fits to reflectance measurements. *In situ* monitoring techniques are needed for a more quantitative analysis. The oxidation of a single 70 nm thick



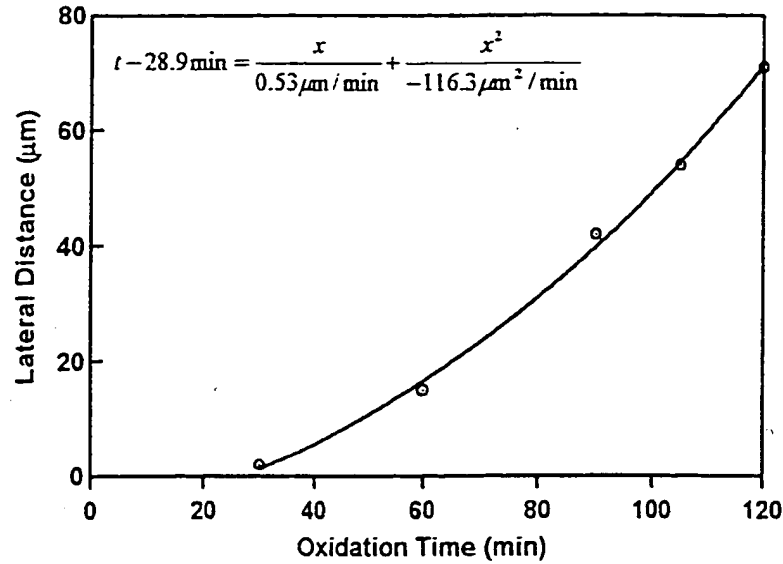


Figure 5.7: The rate of oxidation for the via hole geometry of the buried 100 nm thick  $\text{Al}_{0.98}\text{Ga}_{0.02}\text{As}$  layer shown in Fig. 5.5. A fit to the data is also shown.

$\text{Al}_{0.90}\text{Ga}_{0.10}\text{As}$  buried layer clad by  $\text{Al}_{0.15}\text{Ga}_{0.85}\text{As}$  has been measured to be linear at a rate of  $0.2 \mu\text{m}/\text{min}$  over a  $5 \mu\text{m}$  distance.

Figure 5.7 shows the rate of oxidation for the via hole geometry of the buried 100 nm thick  $\text{Al}_{0.98}\text{Ga}_{0.02}\text{As}$  layer shown in Fig. 5.5. A fit of the data points is also shown. A turn on time of nearly 30 min is evident. Presumably the oxidation rate becomes faster with increasing time because the oxidation fronts are becoming closer and transport of reactants is able to occur through multiple via holes. Strain may also be playing a large role. The oxidation rate of the graded layer of Fig. 5.6 for the mesa geometry and 100 nm  $\text{Al}_{0.80}\text{Ga}_{0.20}\text{As}$  cladding layers is  $1 \mu\text{m}/\text{min}$ . The rate is linear over the measured oxidation length of  $25 \mu\text{m}$ .

### 5.3 Optical Constants and Material Properties

While the kinetics (M. Ochiai, 1996 ; R.L. Naone, 1997) and microstructure (R.D. Twisten, 1996) of the oxidation reaction and resulting oxide have been studied, reports of the oxide's optical constants are lacking. The few refractive index values reported in the literature have been measured either by single-wavelength ellipsometry at 633 nm (A.R. Sugg, 1993 ; E.F. Schubert, 1994) or by extrapolating from the spectral shift in the peak reflectance of an oxidized  $(\text{Al}_{0.98}\text{Ga}_{0.02})_x\text{O}_y$ -GaAs DBR (M.H. MacDougall, 1994).

In this section, I report the optical constants of oxidized crystalline and low-temperature-grown (LTG)  $\text{Al}_{0.98}\text{Ga}_{0.02}\text{As}$  films over the wavelength range of 240-1700 nm, as determined by variable angle spectroscopic ellipsometry.<sup>2</sup> I additionally report the expansion / contraction coefficients and atomic force microscopy (AFM) analysis of the surface morphology of these oxide films. Lastly, I calculate optical scattering loss based on AFM measurements of surface roughness.

#### 5.3.1 Ellipsometry Analysis of Surface Oxide Films

The samples consisted of a single  $\text{Al}_{0.98}\text{Ga}_{0.02}\text{As}$  layer nominally 100 – 300 nm thick grown by molecular beam epitaxy (MBE) as a digital alloy with a 6 nm (5.5 nm AlAs, 0.5 nm  $\text{Al}_{0.50}\text{Ga}_{0.50}\text{As}$ ) period. The samples were grown at temperatures of 580 °C, 350 °C, and 250 °C, respectively yielding crystalline, polycrystalline, and amor-

<sup>2</sup>All samples were characterized with the J.A. Woollam Company Variable Angle Spectroscopic Ellipsometer (VASE®) system. The data were acquired and analyzed using WVASE32 analysis software version 3.012. Trade name is to aid in duplicating the measurement and does not imply endorsement by the National Institute of Standards and Technology.

phous layers, as determined by reflection high-energy electron diffraction (RHEED) measurements. The polycrystalline and amorphous layers incorporate excess arsenic, resulting in nonstoichiometric layers. All samples were oxidized at 450 °C in the three-zone tube furnace under a 1 L/min flow of nitrogen gas bubbled through deionized water at 75 °C. To limit atmospheric hydrolization, all samples were oxidized immediately upon removal from the reactor. The oxidation rate for the crystalline sample was determined by reflectance fits to be  $\approx 35$  nm/min. The oxidation rates for both LTG samples were significantly greater and will require *in situ* monitoring for a quantitative characterization of these thin surface layers.

Ellipsometry measures the polarization state ( $\Psi$  and  $\Delta$ ) of a reflected monochromatic, polarized, collimated beam of light incident at a given angle to the sample normal (J.A. Woollam, 1992). In contrast to single-wavelength ellipsometry, variable angle spectroscopic ellipsometry measures the polarization state at multiple wavelengths and angles of incidence and thus minimizes the possibility of correlated variables in the regression analysis fit. This technique thereby allows the unique determination of optical constants, film thickness, and additional microstructural properties. The optical model used in our experiments was an oxide layer clad on top by a surface roughness layer and on the bottom by a thin interfacial layer. The fitting parameters of the model were the surface roughness thickness, the thickness of the oxide layer, the thickness of an interface layer between the substrate and oxide, three Cauchy coefficients describing the refractive index, and one parameter fitting a small thickness nonuniformity across the illumination spot of the ellipsometer. The optical constants of crystalline GaAs

were collected from published literature (J.B. Theeten, 1978 ; Palik, 1985 ; D.S. Gerber, 1993). A Herzinger-Johs parameterized dispersion model (B. Johs, 1998) was fit to the reference data to extract one set of optical constants for GaAs over the entire measured spectral range. These substrate optical constants were not permitted to vary during the fit. The refractive index  $n$  of the oxide layer was modeled over the entire measured wavelength  $\lambda$  range using a Cauchy dispersion function of the form,

$$n(\lambda) = A + \frac{B}{\lambda^2} + \frac{C}{\lambda^4}. \quad (5.4)$$

The thin interface or "intermix" layer between the oxide and the substrate was modeled as 50% GaAs and 50% oxide using a Bruggeman effective medium approximation (D.E. Aspnes, 1979). Similarly, the surface roughness layer was modeled as a 50/50 mixture of oxide and void. Data were acquired at three angles of incidence (65°, 70°, and 75°) over the spectral range of 240-1700 nm in steps of 10 nm. All angles and wavelengths were fit simultaneously to maximize sensitivity to the model fitting parameters. Model fitting parameters and other quantities discussed are tabulated in Table 5.1 to serve as a reference throughout this section.

For the oxidized crystalline (580 °C) sample, excellent fits to the measured  $\Psi$  and  $\Delta$  polarization functions were obtained without the addition of a surface roughness layer and with the inclusion of a thin 1.9 nm interfacial layer. The thin interface layer illustrates the atomic abruptness of the  $(\text{Al}_{0.98}\text{Ga}_{0.02})_x\text{O}_y$ -GaAs interface and is consistent with reported high-resolution transmission electron-microscopy (TEM) measurements (T. Takamori, 1996). The complex refractive index determined for the 164 nm thick sample indicates no measurable absorption over the entire spectral range

Crystallinity	Crystalline	Polycrystalline	Amorphous
$T_{Growth}(^{\circ}C)$	580	350	250
$t_{Intermix}(nm)$	1.9	24	4.5
$t_{Oxide}(nm)$	164	418	228
$t_{SR}(nm)$	0	33	7
$A$	1.5713	1.4297	1.4485
$B$	$4.83 \times 10^{-3}$	$1.14 \times 10^{-2}$	$4.41 \times 10^{-3}$
$C$	$9.67 \times 10^{-5}$	0	$5.15 \times 10^{-5}$
$\%_{Exp}$	$> -2\%$	$\sim 13\%$	$> 25\%$
$\alpha_{Scatter}$	$2.1 \times 10^{-4}\%$	$> 1.6\%$	$6.6 \times 10^{-4}\%$

Table 5.1: Summary of parameters and quantities for the three samples.

from 240 – 1700 nm. The upper bound on the absorption is given by the noise in the measurement, and thus the extinction coefficient  $k$  is  $< 0.0015$  at 240 nm. The Cauchy fitting coefficients for the real part of the refractive index are:  $A = 1.5713$ ,  $B = 4.83 \times 10^{-3}$ , and  $C = 9.67 \times 10^{-5}$ , using  $\lambda$  in micrometers. The uncertainties in the  $n(\lambda)$  functions reported in this section are sample dependent and are in the third decimal place, based on measured uncertainties in the  $\Psi$  and  $\Delta$  measurement.

I have observed variations in the refractive index of up to 0.015 across several similarly grown and oxidized samples of different thicknesses. Figure 5.8 shows the index for three different sample thicknesses and error bars representative of third decimal place uncertainties. I observe a variation in the real index of  $\pm 0.5\%$  for layer thickness variations of  $\pm 6\%$ . For these three samples, I observe a decrease in refractive index with increasing film thickness. The shape of the dispersion curves (Cauchy  $B$  &  $C$  coefficients) are similar, indicating that all three films are of the same material but different densities.

To obtain a measurement of the expansion or contraction of the oxide films, the

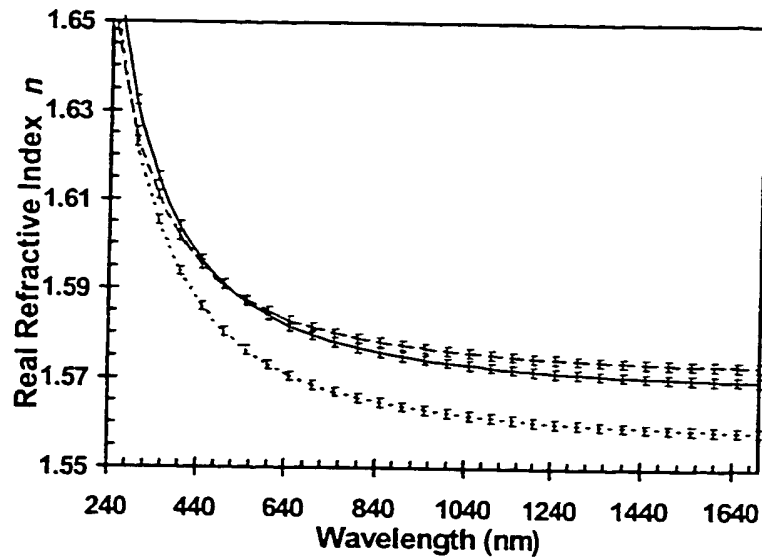


Figure 5.8: Dispersion curves measured for three different sample thicknesses of oxidized crystalline material. Error bars representative of third decimal place uncertainties are shown.

reflectance of one quarter of the “as-grown” sample was measured using a spectrophotometer while another quarter was simultaneously oxidized. The as-grown sample’s reflectance spectrum was fit using Terry’s nine harmonic oscillator model (F.L. Terry, 1991) for the optical constants of  $\text{Al}_{0.98}\text{Ga}_{0.02}\text{As}$  and GaAs, with the addition of a thin dry-oxidized cap layer whose index was approximated using the measured ellipsometric index data obtained for wet thermal oxidation. Comparison of the determined as-grown thickness to the oxide thickness measured by ellipsometry showed a  $< 2\%$  contraction of the film.

For the oxidized LTG amorphous ( $250\text{ }^{\circ}\text{C}$ ) sample, fits to the measured  $\Psi$  and  $\Delta$  polarization functions were obtained with a 7 nm surface roughness layer and a 4.5 nm interfacial layer. The Cauchy fitting coefficients for the refractive index are:

$A = 1.4485$ ,  $B = 4.41 \times 10^{-3}$ , and  $C = 5.15 \times 10^{-5}$ , using  $\lambda$  in micrometers. The absorption of this 228 nm thick layer is again below instrumental sensitivity. The shape of the dispersion curves for the crystalline and amorphous samples are similar; however, the index of the amorphous sample is offset due to a lower  $A$  coefficient. This characteristic is again indicative of a lower density film of the same material. Comparing the as-grown thickness to the thickness of the oxide layer reveals a  $> 25\%$  expansion of the oxide layer. One explanation for this large expansion is the large quantity ( $\sim 10\%$ ) of excess arsenic incorporated into the layer at low growth temperatures (D.P. Docter, 1998 ; Ibbetson, 1998). When the arsenic-rich layer is oxidized, the arsenic escapes (A.R. Sugg, 1993), leaving voids that decrease the density of the oxide and lower the value of the  $A$  coefficient in the Cauchy fit. The reduced density is consistent with the observed increased oxidation rate as gas transport of reactants through the layer to the oxidation front is facilitated (R.D. Twisten, 1996).

For the oxidized LTG polycrystalline (350 °C) sample, fits to the measured  $\Psi$  and  $\Delta$  polarization functions were obtained with a 33 nm surface roughness layer and a 24 nm interfacial layer over the wavelength range of 900 – 1700 nm. The limited spectral range of a good fit suggests that the oxidation had not entirely consumed the LTG- $\text{Al}_{0.98}\text{Ga}_{0.02}\text{As}$  and a thin unoxidized, arsenic-rich layer remains below the oxide. The Cauchy fitting coefficients for the refractive index over the 900 – 1700 nm spectral range are:  $A = 1.4297$ ,  $B = 1.14 \times 10^{-2}$ , and  $C = 0$ , using  $\lambda$  in micrometers. The extinction coefficient for this 419 nm sample is again below the noise limit of the measurement. An oxide layer expansion of  $\sim 13\%$  was measured. Figure 5.9 displays

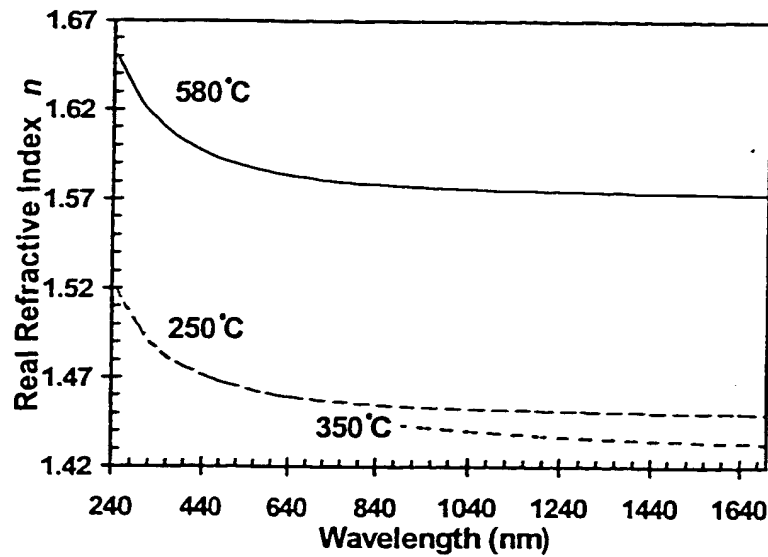


Figure 5.9: Dispersion curve measured for the oxidized crystalline (580 °C), LTG polycrystalline (350 °C), and LTG amorphous (250 °C) samples. The large variation ( $> 0.1$ ) in the refractive index with sample crystallinity is illustrated.

the dispersion curves for the three samples grown at different temperatures. The large variation ( $> 0.1$ ) in the refractive index with sample crystallinity is illustrated.

### 5.3.2 Surface Morphology and Calculated Surface Scattering Loss

The surface morphologies of the oxide films were studied by AFM, and representative images are shown in Fig. 5.10. Figure 5.10 (a) is an image of the 164 nm thick oxidized crystalline layer. The image shows elongated  $1 - 1.5 \mu\text{m}$  features aligned with the  $[01\bar{1}]$  direction atop a flat and uniform underlayer. Figure 5.10 (b) shows an image of a  $\sim 400$  nm thick oxidized crystalline layer. The elongated features are no longer visible, and cracking of the film is evident. The variation in the surface morphology suggests variations in the complex microstructure of the oxide and its dependence on thickness, as also suggested by our refractive index measurements. The 228 nm thick, oxidized



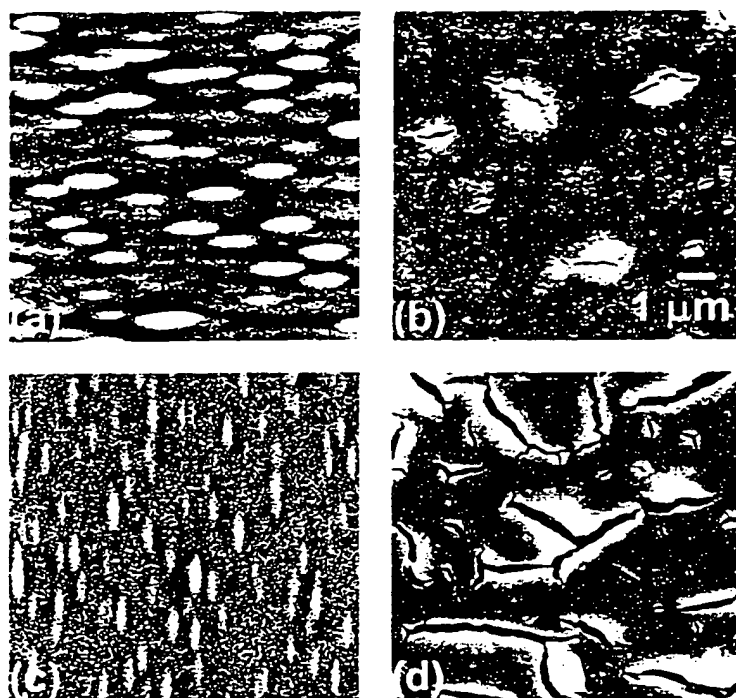


Figure 5.10: AFM images of the oxide surface morphology for: (a) 164 nm thick, crystalline (580 °C), 10 nm z range, (b) ~400 nm thick, crystalline (580 °C), 100 nm z range, (c) 228 nm thick, LTG amorphous (250 °C), 25 nm z range, and (d) 418 nm thick, LTG polycrystalline (350 °C), 200 nm z range.

LTG, amorphous (250 °C) sample is shown in Fig. 5.10 (c). Elongated features are again observed, but are oriented along the [011] direction and atop a grainy underlayer. Alignment of these features to a crystal axis in the amorphous sample suggests that the orientation is imposed by the crystalline substrate. Severe cracking is observed for the oxidized, 418 nm thick, LTG polycrystalline (350 °C) sample shown in Fig. 5.10 (d). The cracks range in width from 50 to 300 nm and are several micrometers long. The severity of the cracking in the LTG sample as compared to an oxidized crystalline film of similar thickness (Fig. 3(b) ) indicates regions of higher stress resulting from the larger volume change of the oxidized polycrystalline material.

Optical scattering loss for the first surface can be calculated for the four samples of Fig. 5.10 using the rms roughness from the AFM data, assuming a Gaussian distribution of heights and normally incident illumination with a wavelength of 1  $\mu\text{m}$  (H.E. Bennett, 1961). For the four samples in Fig. 5.10 (a-d), the calculated optical scattering loss per pass is  $2.1 \times 10^{-4}\%$ ,  $5.3 \times 10^{-2}\%$ ,  $6.6 \times 10^{-4}\%$ , and  $> 1.6\%$  respectively. The rms roughness of the 164 nm thick, oxidized crystalline layer is 0.5 nm, comparable to a plasma-enhanced chemical-vapor-deposited coating.

### 5.3.3 Discussion

I have reported the optical constants of oxidized crystalline and LTG  $\text{Al}_{0.98}\text{Ga}_{0.02}\text{As}$  over the wavelength range of 240 – 1700 nm. For oxidized crystalline material, I observe a variation in the real index of  $\pm 0.5\%$  for layer thickness variations of  $\pm 6\%$ . I have shown that upon oxidation, LTG material expands, while crystalline material contracts. Furthermore, I calculate a low optical scattering loss for oxidized

crystalline material based on analysis of AFM measurements. Knowledge of the dispersion characteristics of native-oxide films will aid device design and prove useful in the development of the broad bandwidth, native-oxide antireflection coatings of the next section.

## 5.4 Native-Oxide Antireflection Coatings

### 5.4.1 Background

Native oxides have been used in the formation of low-loss and broad-bandwidth  $\text{Al}_x\text{O}_y$ -GaAs distributed Bragg reflectors (DBRs) for VCSELs, spatial light modulators, solar cells, and light-emitting diodes (M.H. MacDougal, 1997). Many of these optoelectronic devices and others, such as photodetectors and saturable Bragg reflectors, benefit from broad-bandwidth antireflection (AR) coatings.

Traditionally, device designs in need of passivation layers, insulating layers, broad-bandwidth DBRs and AR coatings have used evaporated or sputtered dielectrics (for example, silicon dioxide, silicon nitride, or aluminum oxide). Native-oxide technology is now allowing innovative and higher performance all-epitaxially grown optoelectronic devices to be fabricated without the need for any additional deposition techniques beyond the semiconductor epitaxy.

In this section and in (K.J. Knopp<sup>a</sup>, 1998 ; K.J. Knopp<sup>c</sup>, 1999), I report the development of high quality ( $< 0.5\%$  reflectance), broad-bandwidth ( $< 1\%$  over 250 nm), antireflection coatings using the low index provided by native-oxide films. These native-oxide AR coatings reduce manufacturing complexities and promote inte-

gration with other native-oxide technologies. Furthermore, since these coatings are simple to manufacture and can be selectively etched from GaAs, they are suitable as *in situ* AR coatings for optical microlithography (W.A. Loong, 1991). Throughout this section, I address the design criteria, fabrication, and characterizations of AR coatings composed of surface and buried oxide layers on GaAs. I consider manufacturing and device integration issues and demonstrate their application to the multilayer structure of a saturable absorber mirror.

### 5.4.2 Theory

#### Single-Layer AR Coating

The simplest AR coating uses a single film on top of a substrate to match the admittance of the incident medium to that of the substrate. The condition for proper matching of the substrate is well known (Macleod, 1969). To achieve zero reflectance at one wavelength with this coating, the sum of the two wave vectors reflected from the medium interfaces must be 0. This is accomplished if they are 180° out of phase (quarter wavelength layers) and if the two reflection coefficients are equal. Setting the reflection coefficients equal sets the relationship between the optical index of the substrate ( $n_2$ ), film ( $n_1$ ), and incident medium ( $n_0$ ),

$$n_1^2 = n_0 n_2. \quad (5.5)$$

Using an incident medium of air and an index of refraction of 3.46 for GaAs at a wavelength of 1  $\mu\text{m}$ , the calculated index for the matching film is 1.86. The index of wet-oxidized  $\text{Al}_x\text{Ga}_{1-x}\text{As}$  is  $\approx 1.57$  while electron-beam-deposited  $\text{Al}_2\text{O}_3$  has a higher

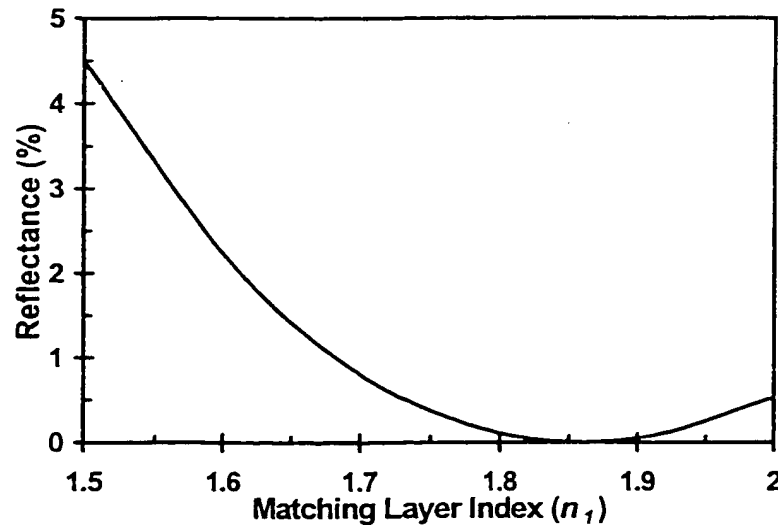


Figure 5.11: Plot illustrating the minimum reflectance achievable for a given matching-layer index of a single-layer AR coating on GaAs at a wavelength of  $1\ \mu\text{m}$ .

index, near 1.77 (A.K. Chin, 1983). Unless the index of the oxide exactly matches the square root of the substrate index, there will not be a point of zero reflectance, but rather a point of minimum reflectance. For a matching layer index of 1.57, the calculated minimum reflectance is 2.8%. For electron beam deposited  $\text{Al}_2\text{O}_3$ , the calculated minimum reflectance is 0.25%. Figure 5.11 shows the effect of the matching-layer index on the minimum reflectance. Figure 5.12 illustrates the reflectance from a one-layer quarter-wave coating on a GaAs substrate with  $n_1 = 1.57$  (for all wavelengths). The reflectance of uncoated GaAs is also shown for comparison. The reflectance is substantially reduced over the entire region. The coating exhibits less than 5% reflectance over a 295 nm range centered around the design wavelength of  $1\ \mu\text{m}$ . To broaden the region of low reflectance and further reduce the reflectance below that of a matching layer of wet-oxidized  $\text{Al}_x\text{Ga}_{1-x}\text{As}$  on GaAs, more layers must be added to the design.

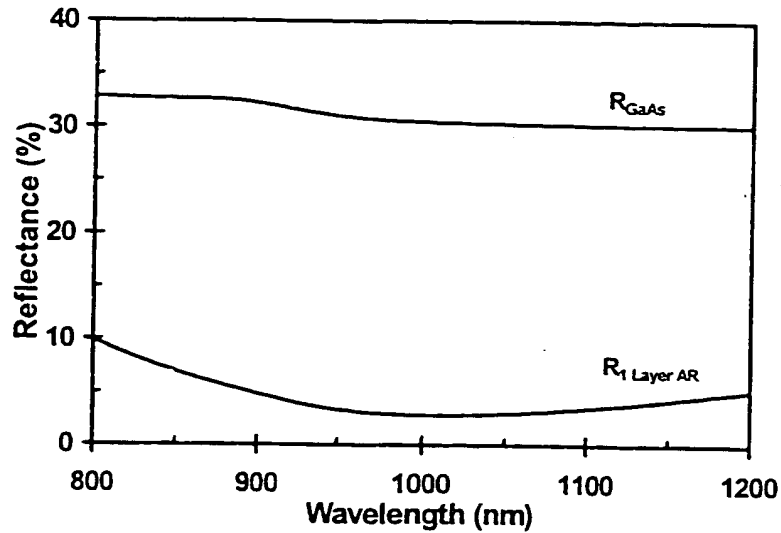


Figure 5.12: The theoretical reflectance from a one-layer quarter-wave coating with  $n_1=1.57$  (all wavelengths) on a GaAs substrate. The reflectance of uncoated GaAs is also shown.

### Two-Layer AR Coating (Quarter-Quarter)

The disadvantage of the single-layer coating is the limited number of adjustable parameters (i.e., the matching layer index and thickness are fixed). Usually, in AR-coating design the index of refraction of the films is not a variable parameter. More layers are thus needed to obtain proper admittance matching with the available indices of refraction. In the  $\text{Al}_x\text{Ga}_{1-x}\text{As}$ /native-oxide material system, the index of refraction of the oxide layer is also not widely variable. However, the index of the semiconductor can be continuously varied between  $\approx 2.9$  (AlAs) and  $\approx 3.5$  (GaAs). Having this available toolbox of indices greatly increases the flexibility of the coating design. A lower reflectance value can be achieved by using a second semiconductor layer of variable index to match between the oxide layer and the substrate. A second layer also broadens

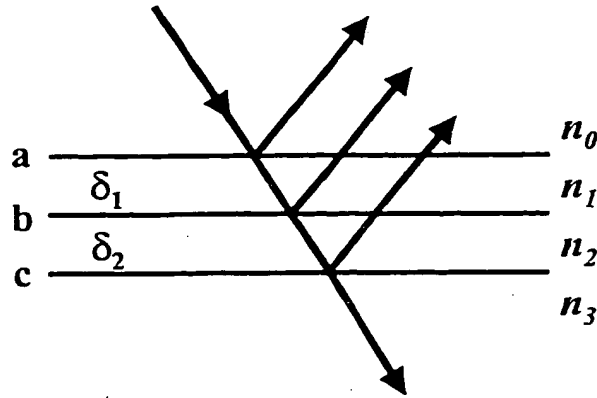


Figure 5.13: The vector diagram for a two layer coating where  $n_o$ ,  $n_1$ ,  $n_2$ , and  $n_3$  are the indices of refraction of the incident medium, first matching film layer, second film layer, and substrate, respectively.  $\delta_1$  and  $\delta_2$  are the phase thicknesses of the film layers. The three material interfaces are labeled  $a$ ,  $b$ , and  $c$ .

the low reflectance region. The design of a two-layer AR coating in which the optical thickness of the oxide and matching layers are fixed at a quarter-wavelength and the index is calculated to exactly match admittances is straightforward (Macleod, 1969). Fixing the thickness and calculating the index assures reasonably thick layers and has historically aided in optical monitoring during deposition. The calculation of the needed index involves equating the admittance of the incident medium with the equivalent admittance of the coating. The result is

$$n_o = \frac{n_1^2 n_3}{n_2}. \quad (5.6)$$

The variables of Eq. 5.6 are defined in the vector diagram shown in Fig. 5.13, where  $n_2$  now represents the index of the second film layer and  $n_3$  represents the index of the substrate. The phase thicknesses of the two film layers are denoted by  $\delta_1$  and  $\delta_2$ . The three material interfaces are labeled  $a$ ,  $b$ , and  $c$ .

Solving for  $n_2$  using the indices of electron-beam-deposited  $\text{Al}_2\text{O}_3$ , GaAs (at

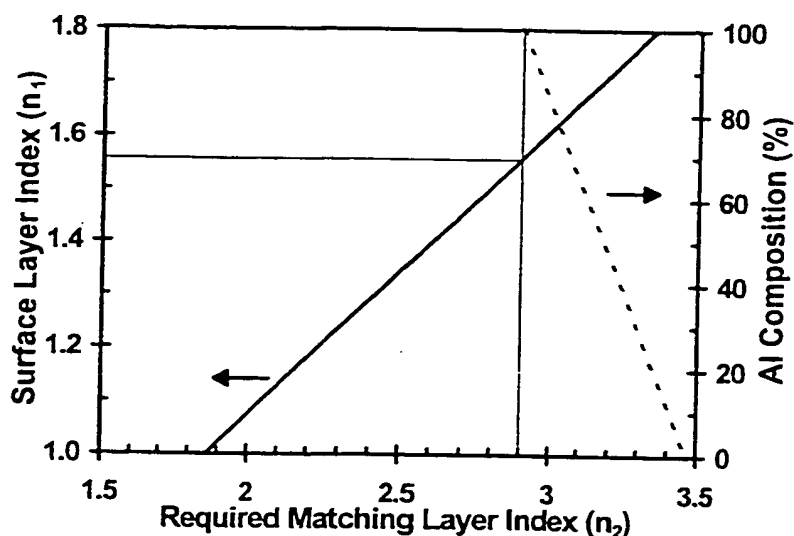


Figure 5.14: Plot of the necessary matching layer index and equivalent composition for a given surface layer index to achieve zero-reflectance at  $1\ \mu\text{m}$  with a quarter-quarter coating on GaAs.

$1\ \mu\text{m}$ ), and air yields a value of 3.29. This corresponds to an  $\text{Al}_x\text{Ga}_{1-x}\text{As}$  layer with an Al composition of 39%. However, for an assumed oxide index of 1.57, the needed matching index ( $n_2$ ) is 2.92, very near the lowest achievable index in the  $\text{Al}_x\text{Ga}_{1-x}\text{As}$  material system. Additionally, the higher the aluminum composition, the harder it will be to accurately control the thickness of the surface oxide layer as the oxidation selectivity is reduced (K.D. Choquette, 1997). Figure 5.14 illustrates the needed matching layer index and equivalent composition for a given surface layer index. Alternatively, a device may require matching between air and an equivalent index less than that of GaAs. The index of the oxide layer and the available range of  $\text{Al}_x\text{Ga}_{1-x}\text{As}$  indices limit the range of substrate compositions which can be exactly matched. Parallel lines to the left of the solid line of Fig. 5.14 can be drawn to represent lower equivalent substrate



indices. The x-intercept is the square root of the substrate index. A quarter-quarter AR coating of ( $n_1 = 1.57$ ) / AlAs on GaAs has a calculated reflectance minimum of  $1.6 \times 10^{-3}\%$  and exhibits a reflectance of  $< 1\%$  over a 400 nm range about its design wavelength of 1  $\mu\text{m}$ .

### Two-Layer AR Coating (Arbitrary Thickness)

**Surface Oxide** A problem with the two-layer coating above is the limited range of substrate indices that can be matched for a given oxide index because of the available  $\text{Al}_x\text{Ga}_{1-x}\text{As}$  index values. Additionally, the necessarily high Al composition of the matching layer makes manufacturing more difficult. For a coating that is not forced to be constructed of layers a quarter-wavelength thick, the layer materials can be chosen from a range of indices and the coating thickness adjusted to suit. This allows flexibility in choosing oxidation selectivity and layer thicknesses.

A set of equations for the phase thicknesses of the two layers can be obtained by writing out the characteristic matrix for the assembly and equating the real and imaginary parts of the layers' admittance, separately, to the admittance of the incident medium (Macleod, 1969). The equations for the phase thickness of the two layers are

$$\tan^2 \delta_1 = \frac{(n_3 - n_0)(n_2^2 - n_0 n_3) n_1^2}{(n_1^2 n_3 - n_0 n_2^2)(n_0 n_3 - n_1^2)}, \quad (5.7)$$

$$\tan \delta_1 \tan \delta_2 = \frac{n_1 n_2 (n_3 - n_0)}{n_1^2 n_3 - n_0 n_2^2}. \quad (5.8)$$

The phase thickness is then related to the physical thickness by

$$\delta = \frac{2\pi n d}{\lambda}, \quad (5.9)$$

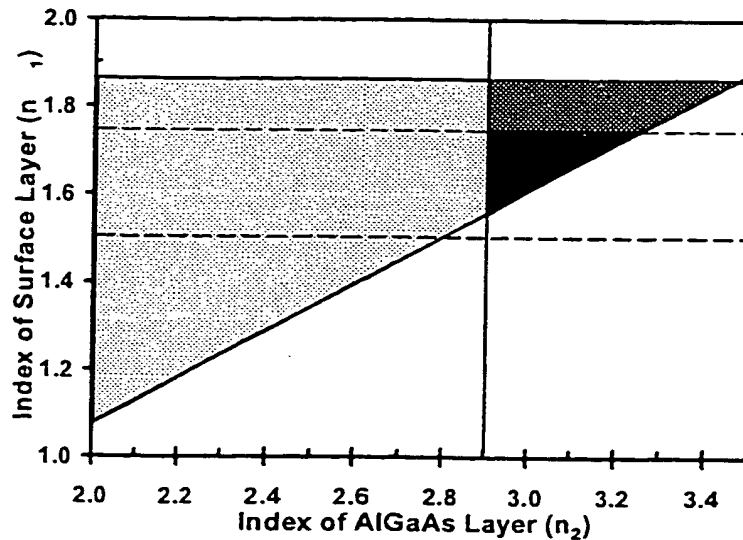


Figure 5.15: A modified Schuster diagram for a two-layer AR coating. The solid black filled region represents the region of zero reflectance solutions given the constraints of the oxide index, available AlGaAs indexes for an incident medium of air and a GaAs substrate (at  $1\ \mu\text{m}$ ).

where  $n$  is the index of the layer,  $d$  is its physical thickness,  $\lambda$  is the wavelength of the design and normal incidence has been assumed.

A Schuster diagram is a useful way to represent pairs of real solutions to Eqs. 5.7 and 5.8 (Macleod, 1969 ; K. Schuster, 1949). A modified form of the Schuster diagram is shown in Fig. 5.15. Again taking  $n_0$  as air,  $n_1$  as oxide,  $n_2$  as  $\text{Al}_x\text{Ga}_{1-x}\text{As}$ , and  $n_3$  as the GaAs substrate, the region satisfying the equations for zero reflectance are filled with a light hashing. Dotted horizontal lines at  $n_1 = 1.5$  and  $1.75$  bound the range of indices between wet-oxidized AlGaAs and electron-beam-deposited  $\text{Al}_2\text{O}_3$ . A vertical line indicating the lowest achievable  $\text{Al}_x\text{Ga}_{1-x}\text{As}$  index ( $\approx 2.9$ ) for layer 2 is also shown. The triangular dark checkered region represents the real solutions for  $n_2$  indices achievable in the  $\text{Al}_x\text{Ga}_{1-x}\text{As}$  material system. The solid black fill shows the

subset region obtained by logically ANDing the constraints of the oxide index, available  $\text{Al}_x\text{Ga}_{1-x}\text{As}$  indexes, and the region satisfying the mathematics for zero reflectance for an incident medium of air and a GaAs substrate. While this coating scheme yields a range of possible indices for  $n_2$  for a given  $n_1$  index, the overall region is limited. For an oxide index of 1.57, a real solution is achievable only with an AlAs matching layer. Additionally, this solid black filled region shrinks as the substrate index is lowered.

The Schuster diagram displays solutions that yield zero reflectance. It provides little information regarding solutions with minimum reflectance when a zero reflectance solution does not exist. To aid in the coating's manufacture, I generally want to use a lower Al composition and thus higher  $n_2$ . This is the region in Fig. 5.15 to the right of the diagonal line. By minimizing the equations for the reflectance of the assembly, I find that the lowest reflectance in this situation is achieved for quarter-quarter coatings. Quarter-quarter coatings, represented by Eq. 5.6, are illustrated on the Schuster diagram by the diagonal line. Figure 5.16 shows the calculated reflectance minimum for a quarter-quarter coating versus Al composition of the matching layer for 890 nm and 1550 nm. Figure 5.16 uses an oxide index of 1.57, a substrate of GaAs, and an incident medium of air. Despite the nonexistence of a zero solution, reflectance minima of a few tenths of one percent can be achieved for matching layers with aluminum compositions as low as 70%.

**Buried Oxide** In (5.4.2), the topmost layer of the coating was oxide. By expanding the axis range of the Schuster diagram, real solutions exist when  $n_1$  is greater than  $n_2$ . Thus, by switching to a buried oxide layer rather than a surface oxide layer, the region

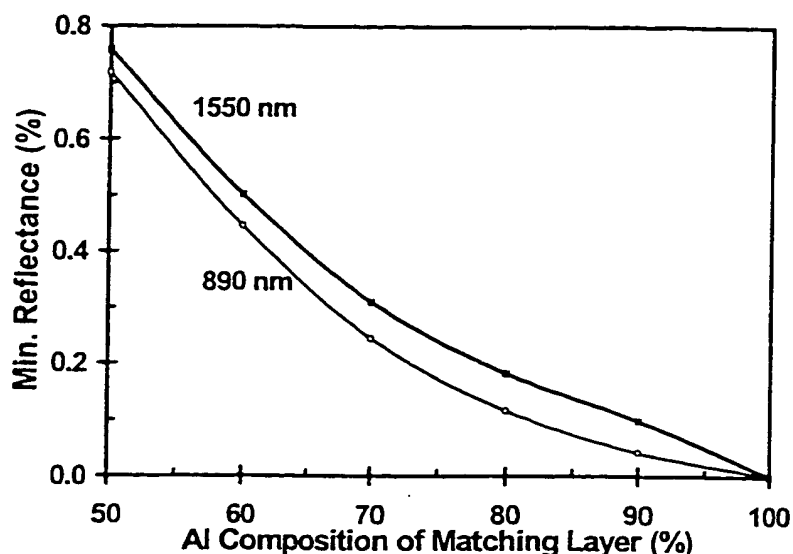


Figure 5.16: Plot of the calculated reflectance minimum for a quarter-quarter coating versus aluminum composition of the matching layer for design wavelengths of 890 nm and 1550 nm. An oxide index of 1.57, a substrate of GaAs and an incident medium of air are used.

of real solutions is substantially increased. Figure 5.17 illustrates this. Two dotted vertical lines at  $n_2 = 1.5$  and  $1.75$  bound the range of indices between wet-oxidized AlGaAs and electron-beam-deposited  $\text{Al}_2\text{O}_3$  for reference. The solid black filled region is now a rectangle rather than a triangle. This rectangle indicates that an AR coating can be designed for zero reflectance using a matching layer of any Al composition and a buried layer with any index from near wet thermally oxidized AlGaAs to even higher than that for electron-beam-deposited  $\text{Al}_2\text{O}_3$ . The thicknesses of the coating layers are adjusted to match admittances. Additionally, any effective substrate index between 2.5 and 3.5 can be properly matched with a buried layer of native oxide and an  $\text{Al}_x\text{Ga}_{1-x}\text{As}$  matching layer of any Al composition.

Further, the thickness of the cap layer can be increased independently of the

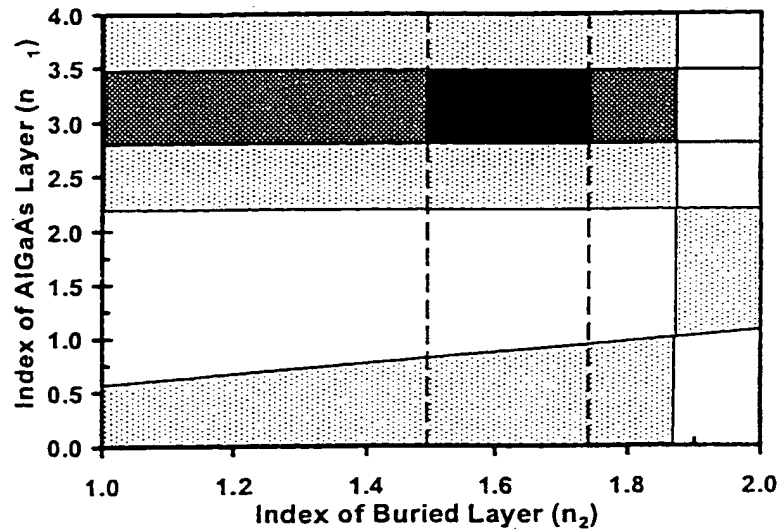


Figure 5.17: A modified Schuster diagram for a buried-oxide AR coating. The rectangular solid black filled region indicates that an AR coating can be designed for zero reflectance using wet-oxidized AlGaAs and a matching layer of any Al composition for any substrate with an effective index between 2.5 and 3.5.

oxide thickness by shifting the tangent solution by  $\pi$  (see Eqs. 5.7 and 5.8). This allows the capping layer thickness to be increased from tens to hundreds of nanometers at the expense of reduced bandwidth. I have had difficulty fabricating thin capping layer designs using a planar laterally oxidized structure (C.L. Chua, 1997) over large hole spacings ( $\approx 150 \mu\text{m}$ ). The long oxidation time required (1 – 2 hours) causes significant surface oxidation and delamination of the cap layer.

The two-layer buried geometry provides the most flexibility in the coating's design. Trade-offs in thickness and Al composition can easily be made for a given oxide index, effective substrate index, and design wavelength.

## Native-Oxide AR Coating Performance

I have designed and simulated five different coatings to serve as examples of the performance anticipated from native-oxide AR coatings. I have also simulated a typical AR coating of ZnS/MgF<sub>2</sub> for comparison. Due to the broad spectral bandwidth of these coatings (hundreds of nanometers), careful consideration of the dispersion in the semiconductor and native oxide is important. I have used Terry's nine-harmonic oscillator model (F.L. Terry, 1991) for the index of all compositions of Al<sub>x</sub>Ga<sub>1-x</sub>As with the exception of AlAs, where I have used the Afromovitz model (M.A. Afromovitz, 1974). Previously in section 5.3, I have reported the index of refraction of surface native-oxide layers analyzed by variable-angle spectroscopic ellipsometry over the wavelength range of 240 – 1700 nm. This data was fit with a Cauchy dispersion formula and used for the simulations of this section. The dispersion formula and parameters used are given by

$$n(\lambda) = 1.5713 + \frac{4.83 \times 10^{-3}}{\lambda^2} + \frac{9.67 \times 10^{-5}}{\lambda^4}, \quad (5.10)$$

where  $\lambda$  is in micrometers. The center wavelength of the five coating designs is 1  $\mu\text{m}$ . The characteristic matrix method (Wolf, 1980) was used for the calculation of the reflectance spectra via a commercial thin-film program.

Coating *A* is simply a quarter-wave thick (159 nm) layer of native oxide on a substrate of GaAs. Coating *B* is a quarter-wavelength of surface oxide on a quarter-wave thick AlAs layer (85 nm) on top of a GaAs substrate. Coating *C* is a quarter-quarter, surface-oxide coating of native oxide on Al<sub>0.8</sub>Ga<sub>0.20</sub>As (81 nm) on top of a substrate of GaAs. Coating *D* is an 87 nm thick, buried oxide layer, sandwiched between a GaAs substrate and a 13 nm capping layer of GaAs. Coating *E* is an 87 nm thick, buried

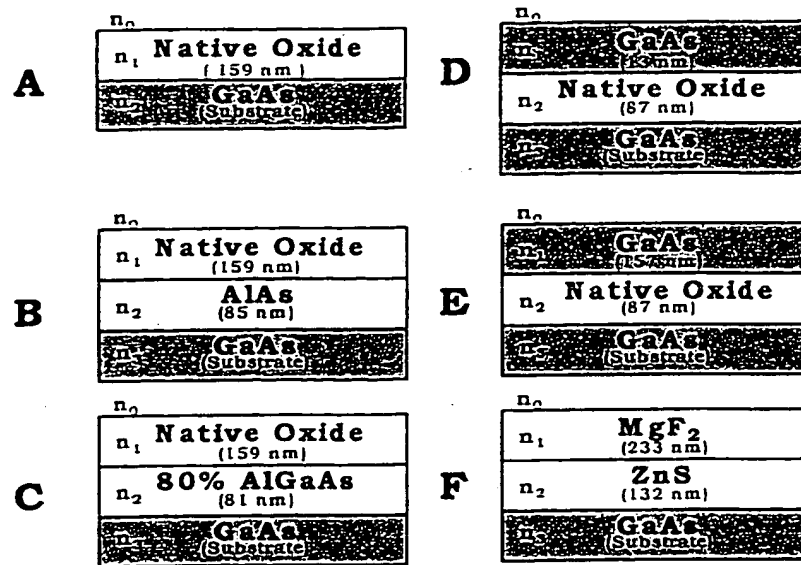


Figure 5.18: Summary of five native-oxide AR coatings designed and simulated. The sixth coating, *F*, is a typical AR coating of ZnS/MgF<sub>2</sub> simulated for comparison.

oxide layer, sandwiched between a GaAs substrate and a 157 nm thick, “ $\pi$ -shifted”, capping layer of GaAs. Coating *F* is a layer of MgF<sub>2</sub> ( $n = 1.38$ , 233 nm) on ZnS ( $n = 2.3$ , 132 nm) on top a substrate of GaAs. These six coatings are summarized in Fig. 5.18. The calculated reflectance spectrum of each coating is shown in Figs. 5.19 and 5.20. As discussed in section 5.4.2, the achievable reflectance minimum of coating *A* is fundamentally limited to several percent due to the admittance mismatch. The two-layer surface-oxide coating, *B*, exhibits a very near theoretical zero solution of  $1.6 \times 10^{-3}\%$ . Coating *B* has a reflectance of less than 1% over 400 nm. If the center wavelength of the design is shifted further past the absorption edge of the GaAs substrate to 1300 nm, this range is extended to slightly over 500 nm. Coating *C* consists of a surface oxide with a matching layer that does not provide a zero reflectance solution. The calculated minimum reflectance of this coating is 0.21%. The reflectance is less

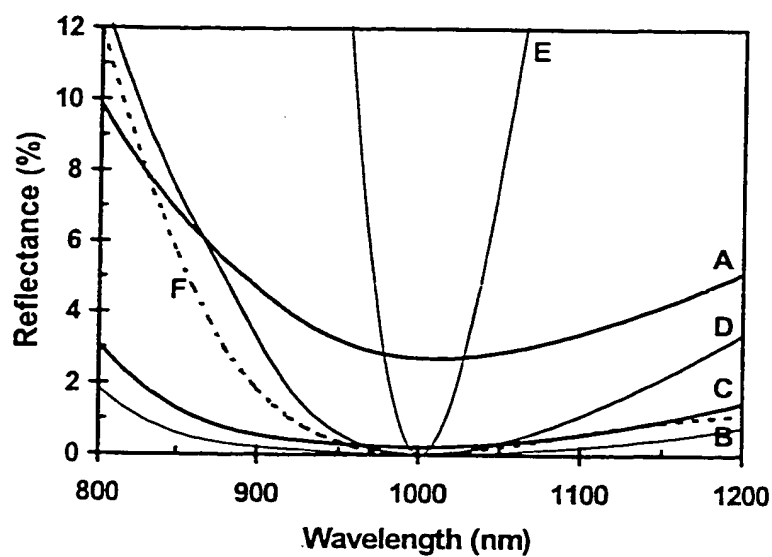


Figure 5.19: The calculated reflectance of the six coatings summarized in Fig. 5.18. The broadband nature of each coating is illustrated.

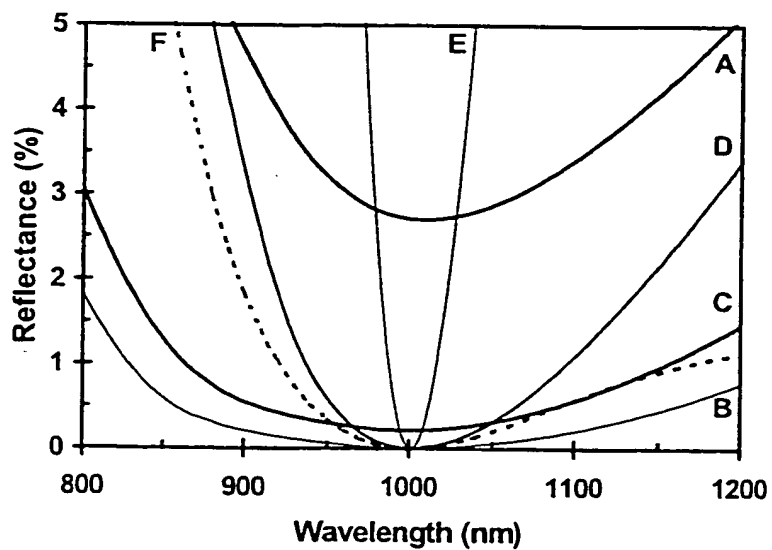


Figure 5.20: The calculated reflectance of the six coatings summarized in Fig. 5.18. The minimum reflectance of each coating is illustrated.



than 1% over 290 nm. Coatings *D* and *E* are buried oxide coatings. While both have a theoretical minimum reflectance of 0, the region of low reflectance for buried coatings is significantly less than surface oxide coatings. Coating *D* has a reflectance of less than 1% over 158 nm. The  $\pi$ -shifted cap of coating *E* further reduces this region to 30 nm.

Excellent broad-bandwidth response is achieved for both surface and buried geometries. Comparing their performance to coating *F*, a conventional ZnS/MgF<sub>2</sub> coating (dashed line in Figs. 5.19 and 5.20), shows that surface-oxide AR coatings offer broader bandwidths with slightly higher reflectance minima. Buried oxides provide zero-reflectance solutions with a narrower spectral bandwidth. Choice of the coating geometry primarily depends on the device design (aperture size and effective substrate index).

### 5.4.3 Fabrication

A conventional antireflection coating used on semiconductor devices is ZnS/MgF<sub>2</sub>. Such a coating is typically deposited by evaporation. Before deposition, the sample must be scrupulously cleaned to remove any small particles present on the wafer. This cleaning step is very important since pinholes in the deposited film are easily formed. The complete evaporation setup consists of a vacuum chamber, cryogenic pumps, power supplies for the crucible heaters, thickness monitoring equipment, and a substrate heater. Additionally, process gases are needed to control the film's stoichiometry.

In this work, antireflection coatings are fabricated using buried or surface layer native-oxide films produced by wet thermal oxidation at atmospheric pressure of AlGaAs

layers of high Al content. Since oxidation depends highly on Al composition, no thickness monitoring equipment is needed (K.D. Choquette, 1997). The simplicity of wet thermal oxidation significantly reduces the manufacturing complexities associated with conventional AR coating deposition on semiconductor devices.

All samples were grown by molecular beam epitaxy (MBE) at a substrate temperature of 580 °C. The layers to be oxidized were  $\text{Al}_{0.98}\text{Ga}_{0.02}\text{As}$ , grown as a digital alloy with a 6 nm (5.5 nm AlAs, 0.5 nm  $\text{Al}_{0.50}\text{Ga}_{0.50}\text{As}$ ) period. All oxidations were carried out at 450 °C in the three-zone tube furnace under a 1 L/min flow of nitrogen gas bubbled through deionized water heated to 75 °C. A solvent cleaning was performed immediately before loading each sample into the furnace. A root-mean-square (rms) roughness of 0.5 nm for the surface oxides was measured by atomic force microscopy (AFM) (see section 5.3). Pinholes in the coatings were not observed.

The surface oxide growths were either terminated on the high Al containing layer or capped with a sacrificial 10 nm layer of GaAs. Uncapped samples were oxidized immediately upon removal from the ultrahigh vacuum of the reactor to limit atmospheric hydrolization. For the capped samples, an etching solution of citric acid (50% by mass) and hydrogen peroxide (30%) (10:1 by volume) was used to remove the cap layer immediately before wet oxidation. The oxidation time for the surface oxide samples was several minutes.

The buried oxide epitaxial material was etched down to the substrate in 50  $\mu\text{m}$  diameter pillars using a 1:6:40 solution of  $\text{H}_2\text{SO}_4\text{:H}_2\text{O}_2\text{:H}_2\text{O}$ . An optical microscope was used to determine the position of the oxide front. A linear oxidation rate of  $\approx 1 \mu\text{m}/\text{min}$

was observed. The buried coating samples were oxidized 24 min.

The surface and buried geometries inherently lend themselves to different device applications. The surface geometry is useful for devices with optical apertures anywhere from a few micrometers to a full wafer. This is because the reaction front progresses longitudinally through the thin  $\text{Al}_{0.98}\text{Ga}_{0.02}\text{As}$  layer. The reaction front does not need to travel transversely across the optical aperture as in the case of the buried geometry. The buried geometry is therefore limited to device apertures smaller than  $\approx 100\text{ }\mu\text{m}$ . Native-oxide AR coatings can be integrated with current-confining oxide apertures in both geometries. Since the surface oxidation will progress significantly faster than the transverse oxidation needed to form the aperture, the formation of a surface AR coating does not impose limits on the aperture size. In the buried geometry, oxidation selectivity can be used to allow the AR coating to fully close across the optical aperture as the current aperture arrives at the correct diameter.

#### 5.4.4 Experiment

##### Surface-Oxide AR Coating

**Single Layer Coating** To demonstrate the simplest native-oxide AR coating, a single layer of  $\text{Al}_{0.98}\text{Ga}_{0.02}\text{As}$  was grown, and a quarter-wafer sample was oxidized for 12 min. A 164 nm thick layer of oxide was produced on top of a GaAs substrate. Variable angle spectroscopic ellipsometry was used to determine the index of refraction and physical thickness. A layer contraction of  $< 2\%$  was determined by comparing reflectance fits of the unoxidized sample with the measured oxide thickness. Ellipsometry indicated

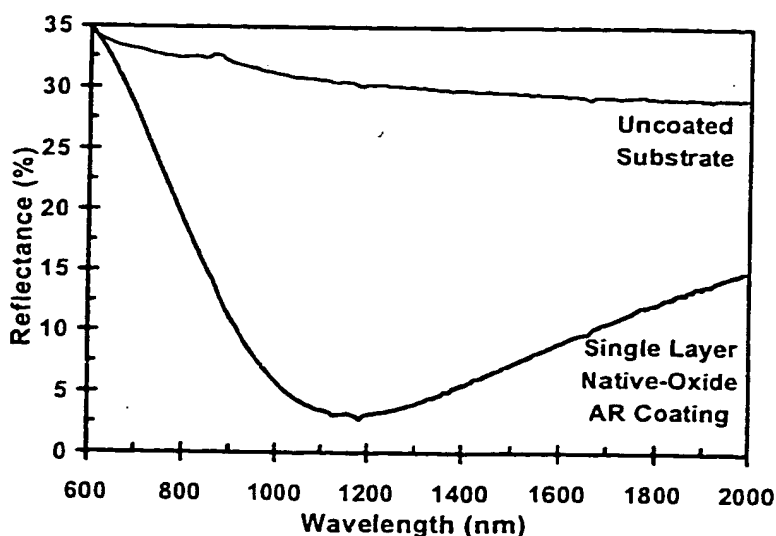


Figure 5.21: The measured reflectance of a single-layer native-oxide AR coating. The measured reflectance of an uncoated substrate of GaAs is also shown.

an abrupt interface between the oxide and substrate and a small surface roughness as confirmed with AFM (see section 5.3). The reflectance of this sample (and all surface oxide samples) was measured with a spectrophotometer from 0.6 to 2  $\mu\text{m}$  having an uncertainty of 0.05%. The measured reflectance was calibrated to a NIST traceable standard with a stated uncertainty of 0.005%. The sample's reflectance is shown in Fig. 5.21. The sample has a minimum reflectance of  $\approx 2.9\%$  and a reflectance of less than 5% over 330 nm. I observed excellent thickness uniformity across the entire quarter-wafer. The measured reflectance of an uncoated GaAs substrate is also shown in Fig. 5.21 for comparison.

**Two Layer Coating** To lower and broaden the reflectance minimum I have fabricated two layer surface-oxide coatings. I have designed a coating with a matching layer

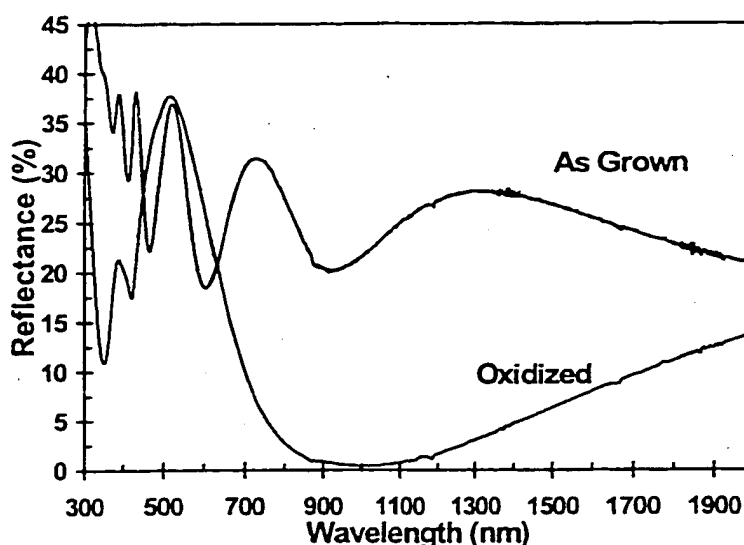


Figure 5.22: The measured reflectance of the as-grown and oxidized samples of the oxide/ $\text{Al}_{0.80}\text{Ga}_{0.20}\text{As}$  two-layer coating.

of  $\text{Al}_{0.80}\text{Ga}_{0.20}\text{As}$  to yield an oxidation selectivity of 100:1 (K.D. Choquette, 1997) at the expense of increasing the minimum reflectance. The design is coating *C* shown in Fig. 5.18. A quarter-wafer sample was placed in the furnace for 6 min. Simultaneously, the reflectance of another quarter-wafer sample was also measured for the oxidized sample. The reflectance spectrum of the as-grown and oxidized samples are shown in Fig. 5.22. A reflectance minimum of  $0.41 \pm 0.06\%$  at  $1 \mu\text{m}$  was measured by fitting a third-order polynomial around the minimum ( $\approx \pm 125 \text{ nm}$ ) and calculating the standard deviation of the fit. The reflectance of the sample is less than 1% over  $> 250 \text{ nm}$ . The calculated minimum reflectance for the design as discussed in section 5.4.2 is 0.21%. Variable angle spectroscopic ellipsometry of the fabricated coating has determined that the oxide thickness is 176 nm and the  $\text{Al}_{0.80}\text{Ga}_{0.20}\text{As}$  matching layer is 74 nm thick. A reduction in the index by  $\approx 0.04$  (at  $1 \mu\text{m}$ ) from that given in

Eq. 5.10 was also determined. Calculation of the coating's minimum reflectance with these adjusted parameters yields a reflectance minimum of 0.36%, which is close to the measured minimum.

Optical scattering loss from the first surface can be calculated for the surface oxide samples using the rms roughness from the AFM data (0.5 nm), assuming a Gaussian distribution of heights and normally incident illumination with a wavelength of 1  $\mu\text{m}$  (H.E. Bennett, 1961). The calculated optical scattering loss per pass is  $2.1 \times 10^{-4}\%$ . This scattering loss indicates the order of magnitude of the anticipated transmittance ultimately achievable through surface oxide AR coatings.

### Buried-Oxide AR Coating

I have fabricated coating *E* shown in Fig. 5.18. Coating *E* is a  $\pi$ -shifted design. Compositional grading was used over 20 nm at the GaAs-Al<sub>0.98</sub>Ga<sub>0.02</sub>As interfaces to avoid delamination after oxidation (M.H. MacDougal, 1997).

In order to measure the reflectance of the etched 50  $\mu\text{m}$  pillars, a Ti:sapphire laser beam was focused using a microscope objective to a  $\approx 2 \mu\text{m}$  diameter spot with an incident half-angle cone of  $\approx 25^\circ$  and scanned in wavelength from 900 to 1000 nm. An InGaAs detector collected the reflected light and the higher intensity transmitted light was trapped by a beam dump. Irises were used to block the scattered light from the unpolished back of the substrate. The measured sample's reflectance was calibrated to the front surface reflection off a fused-quartz optical flat (W.S. Rodney, 1954). Care was taken to ensure that the sample and flat were measured in the same focal plane. Lock-in detection at 2 kHz was used to obtain a high signal-noise ratio. A measurement

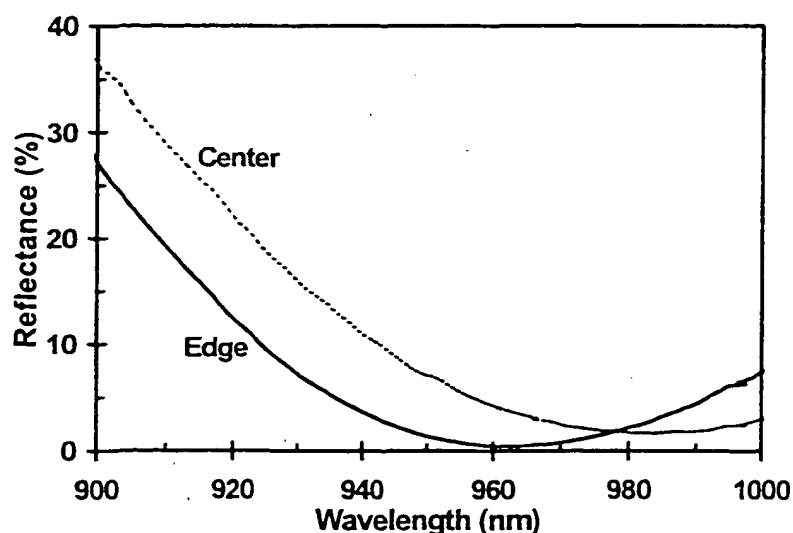


Figure 5.23: The measured reflectance for the center and edge regions of a buried oxide coating on a  $50\text{ }\mu\text{m}$  pillar. The center exhibits a higher minimum of reflectance as it is not fully oxidized, that is, the oxide aperture has not fully closed in across the pillar.

uncertainty of 0.2% was estimated.

Gradations in oxide thickness due to incomplete oxidation were seen by imaging the sample pillars with the monochromatic laser light and observing the contrast of the image. When the laser was tuned to near the designed wavelength of minimum reflectance, the outermost regions of the pillar appeared as a dark ring while the center and substrate appeared brighter.

Figure 5.23 shows the measured reflectance for the center and edge regions of the pillar. The fully oxidized edge has a minimum reflectance at 960 nm of 0.4% and a reflectance of  $< 1\%$  over 21 nm. The minimum reflectance of the partially oxidized center region has shifted to near 980 nm and has increased to 1.6%. The nonzero minimum of reflectance measured at the edge is attributed to the semiconductor layers

being thinner than designed. A small index variation, as discussed in section 5.4.4, can also lead to a few tenths of one percent increase in the minimum reflectance.

### Integration with a Saturable Absorbing Mirror

Intracavity semiconductor saturable absorber mirrors (SESAMs) are important for compact mode-locked or Q-switched solid-state laser systems. I have integrated a native-oxide AR coating with an antiresonant Fabry-Perot SESAM (U. Keller, 1996) to demonstrate application to a multilayer device. An AR coating is required on this device to avoid Fabry-Perot resonance effects. The elimination of this resonance broadens the region of high reflectivity and low group velocity dispersion (GVD) to enable the generation of shorter optical pulses (U. Keller, 1996). Additionally, an AR coating on an antiresonant Fabry-Perot SESAM is used to increase the intensity entering the semiconductor saturable absorber to reduce the effective saturation intensity. The AR coating must be broadband and introduce minimal GVD.  $\text{Al}_2\text{O}_3$  is typically used for these needs (U. Keller, 1996). Native-oxide AR coatings also satisfy these requirements.

The antiresonant SESAM design for 1020 nm consists of nine  $\text{In}_{0.25}\text{Ga}_{0.75}\text{As}$  quantum wells with GaAs barriers on top of a 20-pair AlAs/GaAs bottom DBR. An equivalent index for the structure was determined by first calculating the optical penetration distance into the bottom DBR and adding the optical path length of the rest of the structure assuming a constant field intensity. Dividing by the sum of the effective bottom mirror thickness and the physical thickness of the rest of the structure yields an effective index of 3.34.

A surface-oxide coating was designed to minimize the reflectance from this



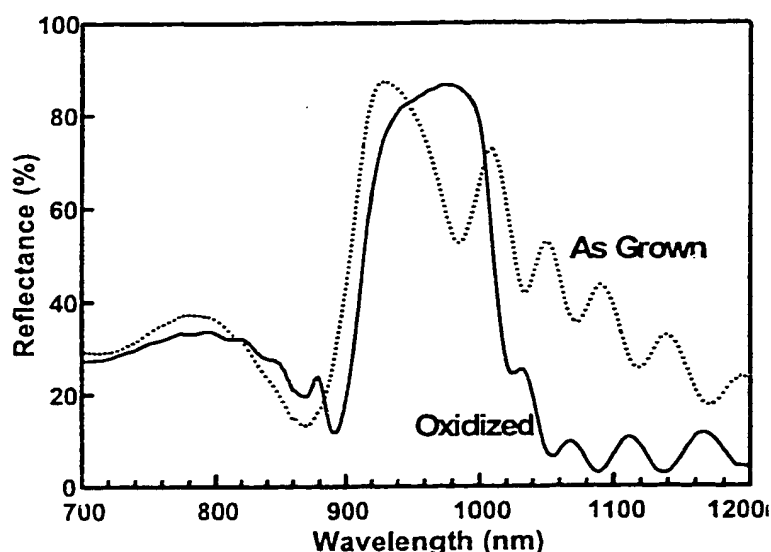


Figure 5.24: The measured reflectance of a semiconductor saturable absorber mirror with a two-layer native-oxide AR coating before and after 5 min of oxidation. The Fabry-Perot resonance near 980 nm is eliminated after oxidation.

effective substrate using a matching layer of  $\text{Al}_{0.80}\text{Ga}_{0.20}\text{As}$ . A zero reflectance solution does not exist for this coating; a minimum of 0.45% was calculated for a quarter-quarter coating. Figure 5.24 shows the reflectance spectrum of the SESAM before (dashed line) and after 5 min of oxidation (solid line). The Fabry-Perot resonance present in the as-grown spectrum, due to the reflection from the semiconductor-air interface, disappears after oxidation.

#### 5.4.5 Discussion

In summary, I have developed two-layer native-oxide antireflection coatings in two geometries: buried and surface. I have studied and reported the design criteria surrounding each of these two geometries. I have mathematically shown that surface oxide coatings can offer a nearly zero minimum of reflectance and a reflectance of  $< 1\%$

over a bandwidth of 500 nm for the case of an AlAs matching layer. Reducing the Al composition in the AlGaAs matching layer to 80% yields a coating with a reflectance minimum of 0.2% and a reflectance of  $< 1\%$  over a bandwidth of nearly 300 nm. Buried oxide coatings can be designed to exactly match the admittance of any substrate with effective index between 2.5 and 3.5 using a matching layer of any Al composition and a buried layer with any index near that of wet thermally oxidized  $\text{Al}_x\text{Ga}_{1-x}\text{As}$ . Buried coatings with a zero reflectance minimum and a  $< 1\%$  reflectance bandwidth of  $> 150$  nm have been designed and simulated.

I have experimentally demonstrated a surface coating having a reflectance minimum of 0.4% and a reflectance of  $< 1\%$  over a bandwidth of  $> 250$  nm. I have additionally developed a  $\pi$ -shifted buried-oxide coating having a reflectance minimum of 0.4% and a reflectance of  $< 1\%$  over a bandwidth of 21 nm. I have also shown integration of a native-oxide AR coating with the multilayer structure of a semiconductor saturable absorber mirror in order to remove the Fabry-Perot resonance and thus reduce the effective saturation intensity. The calculated optical scattering loss from measured roughness data indicates that reflectance minima as low as  $10^{-4}\%$  are ultimately achievable with native-oxide antireflection coatings.

Native-oxide AR coatings reduce manufacturing complexity and cost while promoting integration with other developing native-oxide technologies and rivaling the performance of traditionally deposited coatings.

## 5.5 Intracavity Lens Apertures

Many methods of optical mode and current confinement have been explored to reduce the lasing threshold in VCSELs. The use of oxide apertures to simultaneously provide optical and current confinement has become an active area of research in recent years. These dielectric apertures provide periodic lens waveguiding with lower optical loss than that experienced for an etched waveguide. Simultaneously, the insulating properties of the oxide are exploited to aperture the current.

A lateral variation in index across the device aperture of a VCSEL is created through oxidation of a buried AlGaAs layer with high Al composition as described in section 5.2. This large lateral index difference of  $\sim 1.3$  between the oxidized and unoxidized AlAs layer creates an intracavity lens which leads to periodic lens waveguiding in the cavity (P.D. Floyd, 1996). Essentially, the aperture acts as a low-order Fresnel lens. Figure 5.25 depicts the confined optical mode in an oxide apertured VCSEL and two-periods of the unfolded cavity lens-waveguide afforded by the intracavity oxide aperture.  $M_1$  and  $M_2$  denote the top and bottom mirrors for a VCSEL with a device radius of  $a$ . The mirrors are separated by the effective cavity length,  $L_{eff}$ . The lateral phase discontinuity across the device aperture, shown in Fig. 5.25 (a), scatters light from the lowest order mode into higher order modes. In the case of an ideal lens, the lateral index profile is parabolic (continuous) and the lens is able to exactly compensate for the diffraction of the mode. If such an ideal lens could be achieved across the device aperture, the diffraction loss would be zero. Grading of the aluminium composition as discussed in section 5.2 can be employed to create a tapered index profile in an effort to

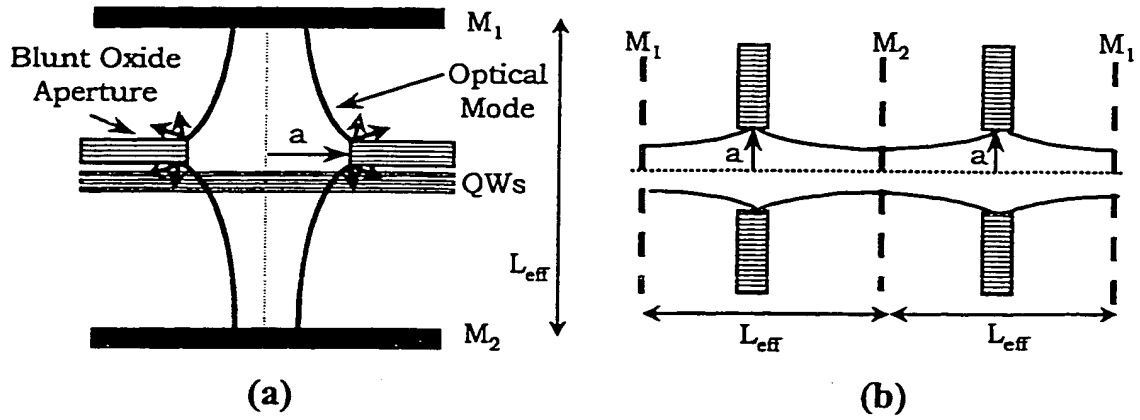


Figure 5.25: Depiction of (a) the confined optical mode in an oxide apertured VCSEL and (b) two-periods of the unfolded cavity lens-waveguide afforded by the intracavity oxide aperture.

reduce the phase discontinuities across the aperture and achieve more of an ideal lens. In this section, the phase distribution of various oxide aperture profiles is formalized and the focal length of the lenses are estimated. The effect of the intracavity lens on the cavity's stability is also considered. The phase distributions derived here will then be used to discuss diffraction effects in the next section.

### 5.5.1 Abrupt Apertures

For the case of a thin lens where the entrance,  $P_1(x, y)$ , and exit,  $P_2(x, y)$ , planes are equal, the phase dependence on  $x$  and  $y$  can be written as,

$$\phi_{P_2-P_1}(x, y) = kn_{ox}t(x, y) + kn_{AlAs}[t_o - t(x, y)], \quad (5.11)$$

where  $k$  is the propagation constant in air,  $n_{ox}$  and  $n_{AlAs}$  are the index of the oxidized and unoxidized AlAs,  $t_o$  is the thickness of the fully oxidized layer, and  $t(x, y)$  is the transverse dependence of the oxide aperture's thickness. For the case of the abrupt

aperture in one dimension,  $t(x)$  is a step function whose value changes from 0 to  $t_o$  at the device radius of  $a$ . Ignoring the constant on axis phase term for the blunt aperture,<sup>3</sup> the phase dependence can be written as,

$$\phi(x) = \begin{cases} k\Delta n t_o, & |x| < a \\ 0, & |x| \geq a \end{cases}, \quad (5.12)$$

where  $\Delta n$  is the index difference between unoxidized and oxidized AIs. From Fourier optics, the phase impinged on a plane wave by a lens which causes the wave to focus at a distance  $f$  is,

$$p_l = \exp \left[ \frac{-ik(x^2 + y^2)}{2f} \right]. \quad (5.13)$$

By fitting the phase distribution of the blunt aperture to an ideal spherical wave distribution and simply equating the phase of the lens to the fitted phase of the oxide aperture, the focal length can be estimated to be,

$$f = \frac{a^2}{\Delta n t_o}. \quad (5.14)$$

Note that this formula does not account for standing wave effects and this discussion is deferred until later in this section. The spherical wave fit is illustrated in Fig. 5.26 (a). Using an index difference of 1.3, an oxide thickness of 80 nm, and a device radius of 5  $\mu\text{m}$ , the calculated focal length is 240  $\mu\text{m}$ .

<sup>3</sup>A constant phase shift added or subtracted across the aperture does not change the lens power or diffraction effects.

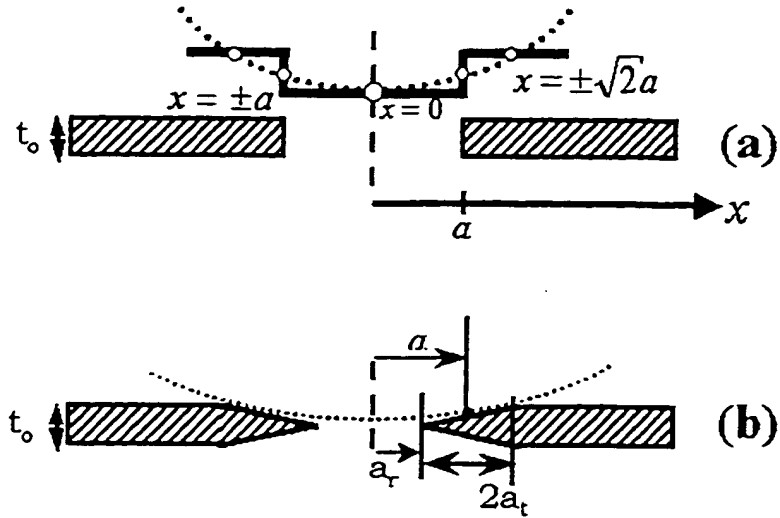


Figure 5.26: The spherical wave fit for an (a) abrupt oxide aperture and (b) a linear tapered aperture.

### 5.5.2 Linearly Tapered Apertures

In a similar manner as presented for the abrupt taper, the phase distribution of the linear taper in Fig. 5.26 (b) can be described as,

$$\phi(x) = \begin{cases} 0, & |x| \geq a + a_t \\ \frac{k\Delta nt_o}{2a_t} (a + a_t - |x|), & a - a_t < |x| < a + a_t \\ k\Delta nt_o, & |x| \leq a - a_t \end{cases} \quad (5.15)$$

where  $a_r$  is the open aperture radius,  $a_t$  is the taper length, and  $a = a_r + a_t$  as expressed in Fig. 5.26 (b). By matching this phase distribution to a spherical wave, the focal length,  $f$ , is estimated to be,

$$f = \frac{(a_r + a_t)^2}{\Delta nt_o}. \quad (5.16)$$

It can be easily seen from Fig. 5.26 (b) that such a taper is expected to significantly reduce the diffraction loss as it much better approximates a spherical wave. The oxidation kinetics and grading profile control the taper length and hence the focal length and diffraction loss. Due to the exponential dependence of the oxidation rate on aluminum composition as well as the oxidation rate dependence on cladding layer composition, an epitaxial layer with a nonlinear grade in aluminum composition is needed to achieve a linear taper when oxidized. In most practical cases, a linear grade in the aluminium composition will suffice. In fact, the oxidized profile is curved and most likely fits a spherical wave somewhat better. Thus, the formalism of the linear tapered aperture is mostly for the analytical convenience of providing a taper profile somewhere between an abrupt aperture and an ideal lens.

### 5.5.3 Parabolic "Ideal" Apertures

The phase variation across the aperture of a device with a parabolic grade is simply,

$$\phi(x) = k\Delta nt_o \left(\frac{x}{a}\right)^2, \quad (5.17)$$

Since a parabolic grade perfectly fits a spherical wave the focal length is exactly,

$$f = \frac{a^2}{2\Delta nt_o}. \quad (5.18)$$

As an example of a slightly non-ideal grading profile, some of the simulations to be discussed in section 5.6 make use of a parabolic lens with a finite lateral extent within

a bulk layer of oxide. The phase dependence of such a lens is written as,

$$\phi(x) = \begin{cases} k\Delta n t_o, & |x| > a \\ k\Delta n t_o \left(\frac{x}{a}\right)^2, & |x| \leq a \end{cases} \quad (5.19)$$

#### 5.5.4 Standing Wave Effects on Lens Power

The periodic lens waveguide picture shown in Fig. 5.25 (b) neglects reflections from the DBRs and the aperture which setup a standing wave in the optical cavity. Since VCSEL cavities are on the order of a wavelength and oxide apertures are only a quarter-wavelength or less thick, the position of the lens in the cavity effects its power. A lens overlapped with a standing-wave peak has a different effective phase than a lens overlapping a standing-wave null. As specified in (G.R. Hadley, 1995) a single-pass phase can be determined for the lens by determining the index difference based on the change in the cavity's resonance wavelength with and without a fully oxidized aperture. For a typical VCSEL with a quarter-wave thick AlAs layer that forms the first top mirror layer to be oxidized,  $\Delta n$  in the previous equations of this section should be replaced by a distributed index difference of only  $\sim 0.06$ . This value has been shown to correctly predict the transverse mode spacing found experimentally (K.L. Lear, 1995).

#### 5.5.5 Cavity Stability Analysis

It is interesting to look at the effect of placing such a long focal length (hundreds of micrometers) lens inside a cavity with an effective length of  $1 - 2 \mu\text{m}$ . For a VCSEL cavity without an oxide aperture and with a pillar diameter much greater than the injected current diameter (so as to neglect waveguiding effects), the VCSEL cavity



is marginally stable according to the stability criterion of Gaussian resonator theory (Verdeyen, 1989). Thus, any slight deviation in the parallelism of the top and bottom mirrors results in the optical mode spreading towards the sidewalls of the device into a larger mode diameter. For such a VCSEL with the addition of an intracavity lens, the ABCD unit cell of the equivalent lens waveguide is,

$$T = \begin{bmatrix} 1 - \frac{x_l}{f} & L_{eff} \left(2 - \frac{x_l}{f}\right) \\ -\frac{1}{f} \left[1 + \left(1 - \frac{x_l}{f}\right)\right] & 1 - \frac{1}{f} \left[4L_{eff} - x_l + \frac{1}{f} (x_l^2 - 2x_l L_{eff})\right] \end{bmatrix}, \quad (5.20)$$

where  $f$  is the focal length of the intracavity lens,  $L_{eff}$  is the effective cavity length, and  $x_l$  is the distance of the aperture from the equivalent top mirror,  $M_1$ . Analyzing the stability equation (Verdeyen, 1989),

$$0 \leq \frac{A + D + 2}{4} \leq 1, \quad (5.21)$$

for the unit cell of Eq. 5.20 yields,

$$0 \leq \left(1 - \frac{L_{eff}}{f} - \frac{1}{4f^2} [x_l^2 - 2L_{eff}x_l]\right) \leq 1. \quad (5.22)$$

This criterion shows that regardless of the position of the lens and so long as it has a positive power, the resulting cavity forms a stable periodic focusing system for rays. Thus, VCSEL cavities with intracavity oxide lenses can confine the optical mode to a region far from the sidewalls of the device and into a smaller mode diameter.

### 5.5.6 Discussion on Confocal VCSEL Cavities

Confocal laser cavities are desirable as they offer a degeneracy in transverse-mode resonant frequencies, reduced mode volumes, and reduced diffraction loss for

higher-order transverse modes than planar mirror cavities (Siegman, 1986). Confocal VCSEL cavities have been demonstrated using external mirror and therefore large (centimeter) cavity lengths. A confocal VCSEL microcavity with "internal" mirrors has not yet been achieved. Recently, there has been one report of a device which is clearly reaching towards this goal using a curved micromachined top mirror (P. Tayebati, 1998). Limits on the machineable curvature of the top mirror prevent the cavity from becoming truly confocal. I propose that confocal VCSEL microcavities can be created through the integration of multiple native-oxide apertures within the DBRs.

A confocal laser cavity can be formed with one planar mirror and a second concave mirror whose radius of curvature,  $R$ , is equal to the effective cavity length. The needed radius of curvature of the second mirror can then be translated into an equivalent focal length of a needed intracavity oxide lens using,

$$f_{equ} = \frac{R}{2} = \frac{L_{eff}}{2}. \quad (5.23)$$

Setting this equivalent focal length equal to the focal length of an abrupt oxide aperture given in Eq. 5.14 and solving for the oxide thickness yields,

$$t_o = \frac{2a^2}{\Delta n L_{eff} n_{ave}}, \quad (5.24)$$

where  $a$  is again the device radius,  $\Delta n$  is the index difference of the unoxidized and oxidized AlAs,  $L_{eff}$  is the effective cavity length, and  $n_{ave}$  is the average index of the semiconductor cavity. For small device radii,  $t_o$  is approximately 1-3  $\mu\text{m}$ . This is a rather thick oxide lens, however, it is conceivable that it could be distributed throughout the entire top mirror. For a 30-pair AlAs/GaAs mirror, with 80 nm of oxide per AlAs

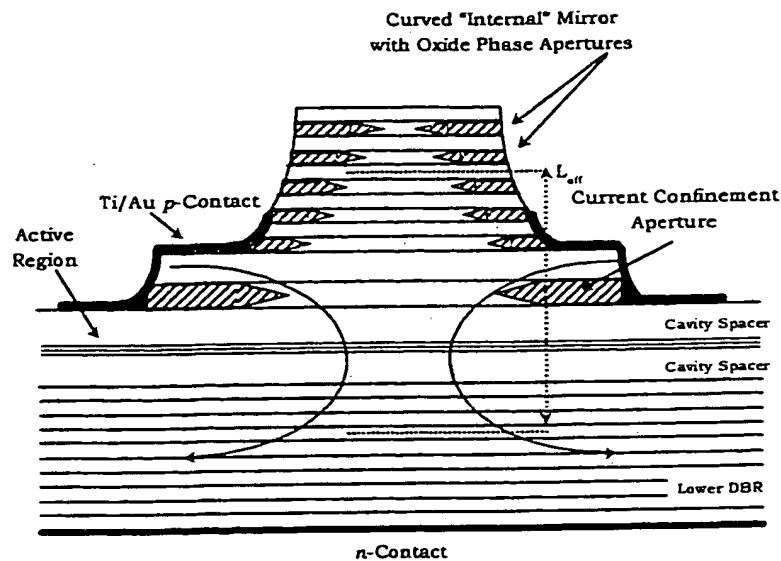


Figure 5.27: A sketch of an intracavity contacted confocal VCSEL design.

layer, over  $1\ \mu\text{m}$  of oxide material could be incorporated. When the lens is distributed some amount of  $z$  dependence of the lateral oxidation distance is needed. This is achievable through variations in the aluminium composition from aperture-to-aperture or through sloping of the sidewalls by wet chemically etching. A sketch of an intracavity contacted confocal VCSEL design is shown in Fig. 5.27. The most obvious challenge in making such a device lase is the potentially high scattering loss from the oxide apertures. Further study of the equivalent optical power of an assembly of apertures and an analysis of the loss from oxide apertures is needed prior to the realization of this design.

## 5.6 Optical Scattering from Intracavity Lenses / Current Apertures

Due to the discrete nature of intracavity lenses there is some associated scattering loss for the lowest order mode unless the index profile of the aperture is parabolic

as in the case for a perfect lens. Fabrication of these nanometer thick intracavity elements inevitably results in non-ideal lateral index profiles. In this section, theory and computer algorithms are developed for modeling scattering losses in oxide apertured VCSELs based on the classic calculations of Fox and Li (A.G. Fox, 1961) with the inclusion of "soft/hard translucent" apertures. The theory presented in this section is based around the treatment found in (Siegman, 1986).

### 5.6.1 Huygens' Integrals

#### Huygens' Integral in the Fresnel Approximation

Huygens' qualitative ideas concerning diffraction were centered around viewing an incident electric field distribution over a closed surface  $S_o$  as a collection of Huygens' wavelets radiating from each point on the surface. Fresnel and Kirchoff later developed a mathematically rigorous form expressing these intuitive ideas. The general form of Huygens' integral equation developed is,

$$\tilde{E}(s, z) = \frac{i}{\lambda} \iint_{S_o} \tilde{E}_o(s_o, z_o) \frac{\exp[-ik\rho(r, r_o)]}{\rho(r, r_o)} \cos\theta(r, r_o) dS_o, \quad (5.25)$$

where  $\rho(r, r_o)$  is the distance between source and observation points,  $dS_o$  is an incremental element of surface area at the point  $(s_o, z_o)$  on the surface  $S_o$  and the cosine factor is an obliquity factor which depends on the angle between the line element  $\rho(r, r_o)$  and the normal to the surface area element.

If all points on the source and observation planes are close to the z-axis ("paraxial"), the Fresnel approximation to diffraction theory states that the distance  $\rho(r, r_o)$

expressed as,

$$\rho(r, r_o) \equiv \sqrt{(x - x_o)^2 + (y - y_o)^2 + (z - z_o)^2} \quad (5.26)$$

can be written as a power series in the form,

$$\rho(r, r_o) = z - z_o + \frac{(x - x_o)^2 + (y - y_o)^2}{2(z - z_o)} + \dots \quad (5.27)$$

According to Fresnel diffraction theory, all terms higher than quadratic can be dropped within the phase shift factor of Huygens' integral and even the quadratic terms can be dropped in the  $1/\rho$  term. Plugging these approximations into Huygens' integral and assuming the distance  $(z - z_o)$  between source and observation planes is large enough so the cosine term can be set to unity results in,

$$\tilde{E}(x, y, z) \approx \frac{ie^{-ik(z-z_o)}}{\lambda(z-z_o)} \iint \tilde{E}_o(x_o, y_o, z_o) \exp \left[ -ik \frac{(x - x_o)^2 + (y - y_o)^2}{2(z - z_o)} \right] dx_o dy_o. \quad (5.28)$$

This equation is known as the Huygen's integral within the Fresnel approximation.

### Validity of the Fresnel approximation

Looking at the Fresnel approximation to Huygens' integral one can see that it is equivalent to replacing the spherical wave in the general Huygens' integral expression with a so called "paraxial-spherical wave" of the form

$$\tilde{E}(x, y, z) \approx \frac{e^{-ik(z-z_o)}}{(z - z_o)} \exp \left[ -ik \frac{(x - x_o)^2 + (y - y_o)^2}{2(z - z_o)} \right]. \quad (5.29)$$

This "paraxial-spherical wave" exactly satisfies the paraxial wave equation. Therefore, any field expression which solves Huygens' integral in the Fresnel approximation also satisfies the paraxial wave equation.

However, the consequences of dropping the quadratic and higher terms in the phase term of the integrand must still be understood. By dropping these terms it is assumed that they contribute a negligible amount to the complex exponent compared to  $\pi/2$ . Looking at the magnitude of the next higher-order term in the power series expansion for one of the transverse coordinates requires that

$$\left| k \frac{(x_1 - x_o)^4}{4L^3} \right| \leq \frac{\pi}{2}, \quad (5.30)$$

where  $L = (z - z_o)$ . If the beam is confined within a width  $2a$  this criterion can be rewritten as,

$$\left| \frac{2\pi}{\lambda} \frac{(2a)^4}{4L^3} \right| \leq \frac{\pi}{2} \text{ or } \frac{L}{2a} \geq \left( \frac{2a}{\lambda} \right)^{\frac{1}{3}}. \quad (5.31)$$

While this criterion may seem to place further restrictions on the use of the paraxial wave equation, its physical interpretation is as follows. Physically, the Fresnel approximation to Huygens' integral can be used to calculate forward beam propagation over arbitrarily short distances as the source points for the beam being propagated are far behind (or ahead) of the start and end planes of the propagation. This is only true if there are no sharp discontinuities at or near the start and end planes. Sharp discontinuities give rise to Sommerfeld "edge-waves" propagating at angles outside the paraxial approximation. In the cases of a hard opaque aperture or a discontinuous phase aperture the Fresnel approximation to Huygen's integral can not be used unless the above criterion is satisfied. Compliance to the above criterion assures that the edge-waves have become paraxial.

### Fresnel Approximation of Huygens' Integral in Cylindrical Coordinates

For modeling the diffraction effects in cylindrically symmetric VCSELs, it is obviously advantageous to work in cylindrical coordinates. Fresnel's approximation to Huygens' integral can be written in cylindrical coordinates as

$$\tilde{u}(r, \theta) = \frac{i}{L\lambda} \int_0^\infty r_o dr_o \int_0^{2\pi} \tilde{u}_o(r_o, \theta_o) \exp \left[ -i \left( \frac{\pi}{L\lambda} \right) [r^2 + r_o^2 - 2rr_o \cos(\theta - \theta_o)] \right] d\theta_o. \quad (5.32)$$

This formulation has been written using the reduced wavefunction,  $\tilde{u}(r, \theta)$ , as the on-axis phase shift  $\exp(-jkL)$  is omitted because the total phase shift is not needed. The transverse variation of the wavefunction is the desirable quantity.

If the wavefunction has m-th order azimuthal symmetry then separation of variables of the form

$$\tilde{u}(r, \theta) = \tilde{u}_m(r) e^{\pm im\theta}, \quad (5.33)$$

can be used. Huygens' integral then can be shown to reduce to the form of a Fourier-Bessel transform (Hankel transform). This reduced form is written as,

$$\tilde{u}_m(r) = \frac{2\pi i^{m+1}}{L\lambda} \int_0^\infty r_o \tilde{u}_o(r_o) \exp \left[ -i \left( \frac{\pi}{L\lambda} \right) (r^2 + r_o^2) \right] J_m \left( \frac{2\pi r_o r}{L\lambda} \right) dr_o. \quad (5.34)$$

This Hankel transform is the backbone equation for the recursive Fox and Li mode calculation to be carried out in section 5.6.2.

### Verification of the FHT Computer Form of Fresnel Huygens' Integral

The recursive application of this function hundreds of times demands an efficient method of calculation. Naively setting out to do this calculation by brut force

means, such as trapezoidal integration, leaves the user with code that will run until the next millennium. In this work I followed and implemented the fast Hankel transform (FHT) routine outlined in (A.E. Siegman, 1977). The FHT computer form of Fresnel-Huygens' integral was coded into Mathematica and verified prior to use in the Fox and Li calculations by simulating the diffraction from an opaque circular aperture in the near and far-fields. These simulations also serve as reference for analysis of the VCSEL results.

It is convenient in these calculations to define a quantity called the Fresnel number,  $N$ . The Fresnel number is the number of Fresnel zones contained within the aperture as seen from an observation point. Each Fresnel zone is simply a bright or dark annular ring of intensity seen in the diffraction pattern from a circular aperture as formally described by Huygens' integrals. The Fresnel number for a circular aperture is

$$N = \frac{a^2}{L\lambda}, \quad (5.35)$$

where  $a$  is the radius of the aperture. Through relating to the Rayleigh range,  $N$  is  $\geq 1$  within the near-field and  $\ll 1$  within the far-field.

Calculated near-field intensity patterns for a uniformly illuminated circular aperture are shown in Fig. 5.28 (a-c). It is immediately apparent in these intensity patterns that there are  $N$  large amplitude fringes across the diameter of the beam and that they are modulated by a high-frequency ripple. There also exists a center most dip for even Fresnel numbers and a center most peak for odd Fresnel numbers. All of these observations exactly coincide with the simulations and experiments illustrated



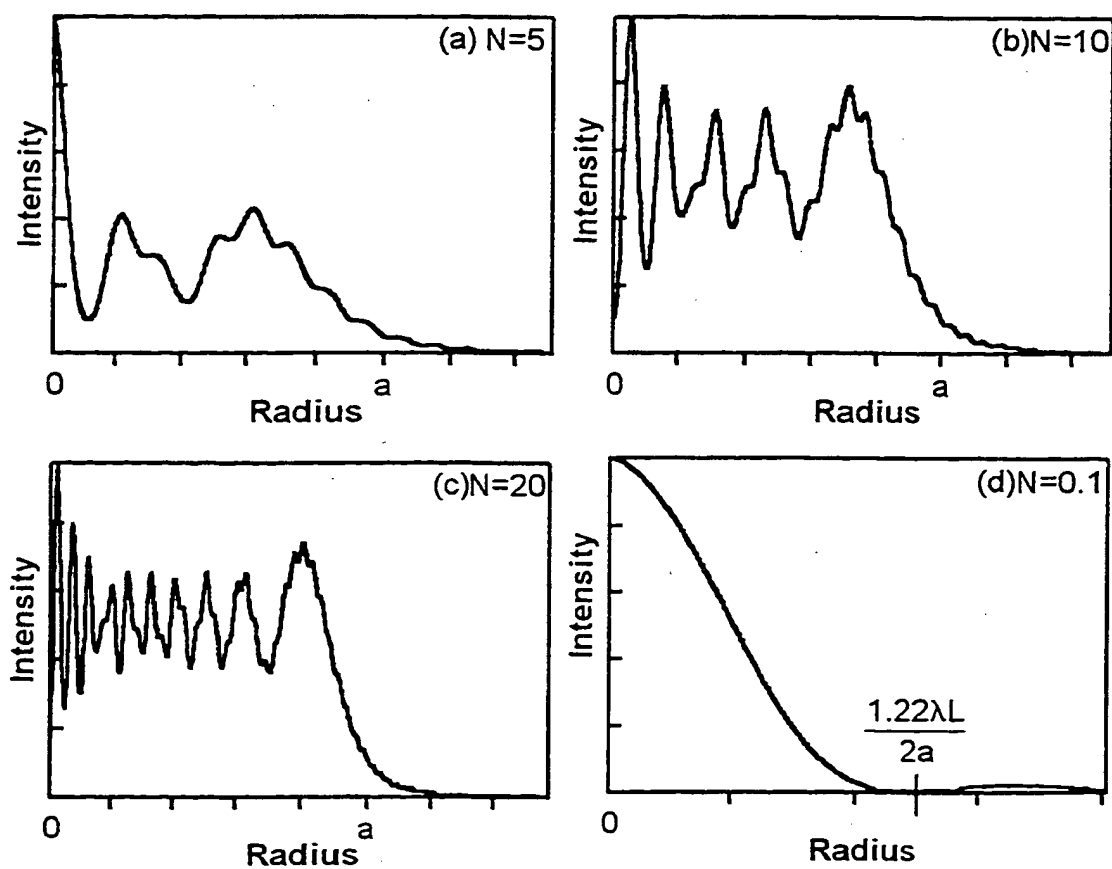


Figure 5.28: Calculated near and far field diffraction patterns from a hard aperture of radius  $a$ : (a) Near field pattern for  $N = 5$ , (b) Near field pattern for  $N = 10$ , (c) Near field pattern for  $N = 20$ , (d) Far field pattern for  $N = 0.1$

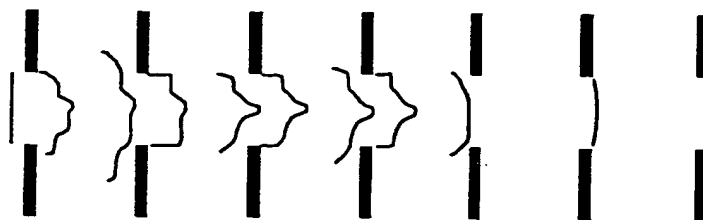


Figure 5.29: Pictorial illustration of the Fox and Li calculation for a mode propagating from left to right through a series of hard apertures.

in (Siegman, 1986). A far-field intensity pattern for a uniformly illuminated circular aperture is shown in Fig. 5.28 (d). As shown analytically for  $N \ll 1$  in (Siegman, 1986), the pattern is the magnitude squared of a “jinc” function where the first null is positioned at  $1.22\lambda L/2a$ .

### 5.6.2 Fox and Li Calculation

Open resonators have been extensively studied due to the introduction of the Fabry-Perot laser in 1958. The most important issue is the determination of the lowest-order mode of the cavity. Even for simple geometries this solution is difficult to arrive at analytically so most published work relies on numeric methods. One of the simplest and earliest works was done by Fox and Li in 1961 (A.G. Fox, 1961). In that work, the solution of the oscillating modes of a resonator with circular finite mirrors is obtained through recursive use of the Fresnel-Huygens’ integral. An initial mode distribution with a normalized area of 1 is assumed and is then propagated from one aperture to the next through application of Fresnel-Huygens’ integral as illustrated pictorially in Fig. 5.29. With each pass through the unfolded resonator, the beam diffracts and some of its energy strikes the opaque apertures and exits the resonator. By integrating

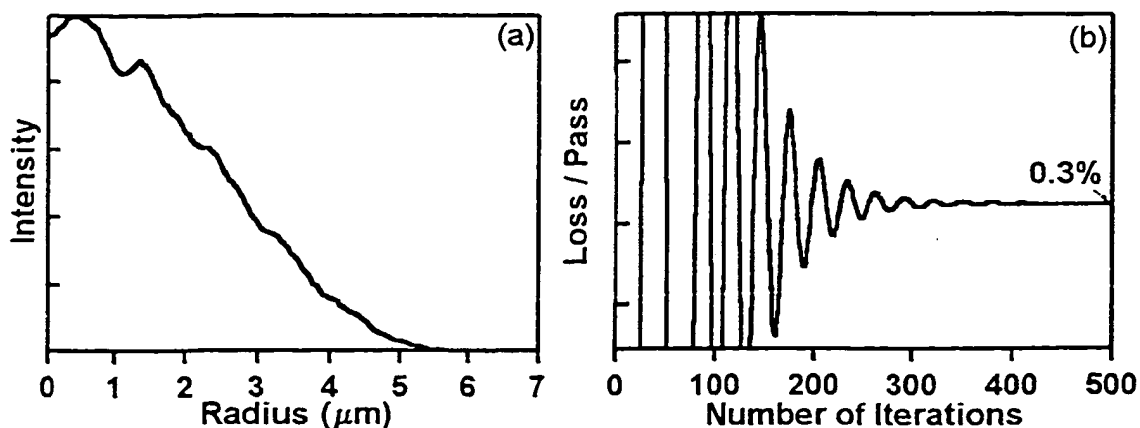


Figure 5.30: Fox and Li calculation of a microresonator consisting of a circular  $10\ \mu\text{m}$  diameter hard mirror separated by  $3\ \mu\text{m}$  from another hard mirror of infinite extent. A normalized wavelength of  $(1.55\ \mu\text{m}/3.2)$  was used and 500 iterations were performed. The computed magnitude is shown in (a) and (b) illustrates the damping of the loss with increasing iterations.

over the intensity that strikes the aperture a loss-per-pass value can be calculated. The area is then re-normalized and the distribution is sent through the next aperture. After repeated iteration through the apertures a steady state mode solution is reached and the loss-per-pass becomes constant.

Using the FHT form of Fresnel-Huygens' integral of Eq. 5.34, Mathematica code was developed to carry out this iterative technique. The code was verified on a published micro-resonator (Babic, 1995) structure. This resonator consists of a circular  $10\ \mu\text{m}$  diameter hard mirror separated by  $3\ \mu\text{m}$  from another hard mirror of infinite extent. A normalized wavelength of  $(1.55\ \mu\text{m}/3.2)$  was used and 500 iterations were performed. Figure 5.30 (a) shows the computed magnitude. Figure 5.30 (b) illustrates the damping of the loss with increasing iterations which serves as an indicator of convergence. The computed magnitude agrees well with the published values. Figure 5.30 (a)

shows that the intensity is non-zero at the edge of the mirror as expected for a non-zero value of the loss-per-pass. The discontinuity upon reflection from the finite mirror gives rise to the ripple in intensity plots. It has been shown that this iterative solution for loss matches that calculated using the scalar beam propagation method (BPM) and scalar plane wave expansion method (Babic, 1995).

Determining the oscillating modes in practical VCSELs is quite difficult. Non-linear effects such as non-uniform current injection, spatial hole burning, and gain-guiding play important roles as discussed in Chapter 4. Device geometry is also important. Often a dominant method of mode selection can be assumed to simplify the problem. The mode defining mechanism relevant to oxide confined VCSELs is aperturing (Babic, 1995).

The calculated near and far-field patterns shown in Fig. 5.28 are for "hard opaque" apertures. This means the light can not penetrate the aperture (opaque) and the aperture is blunt (hard). This type of aperture is used in the classic Fox and Li calculations (A.G. Fox, 1961). For the calculation of diffraction losses from oxide apertured VCSELs, it is necessary to consider apertures that allow light to be transmitted and have both blunt and tapered edge profiles. These types of apertures will be referred to as translucent hard and soft apertures. Only two types of translucent apertures will be considered. As discussed in section 5.5, any taper shape which reduces the phase discontinuities across the aperture will reduce optical scattering loss. Only abrupt and parabolic apertures which represent the worst and best cases will be considered.

The resonant mode in an aperture dominated device is selected by the spatial

and angular filtering of the aperture. The apertures involved in native-oxide confined VCSELs are the lateral extent of the DBR mirrors, the angular dependence of the DBR's stopband, and the oxide-aperture. The model used in this section for calculations is an open resonator where the DBR mirrors have been replaced by equivalent hard reflectors (Corzine, 1993) and the cavity length has been adjusted to include the DBRs penetration depth. The limiting aperture in the model is taken as the native-oxide aperture. This is easily justified because in practical oxide-confined VCSELs the oxide aperture confines the injected current, hence gain, to a small transverse region far from the sidewalls of the top mirror mesa (refer to Fig. 2.2 (c and d) on page 11). The bottom mirror remains unetched in the processing so it is of infinite extent.

The position of the oxide lens in the cavity is taken to be at the equivalent top mirror so the distance between lenses in the unfolded cavity is the effective cavity length,  $L_{eff}$ . This is done because the oxide lens usually resides within the last mirror layer of the top DBR. Standing wave effects on the effective power of the lens have been included through the use of an adjusted index difference,  $\Delta n_{oxide}$ , as discussed in section 5.5.4. A summary of the parameters of the VCSEL model used is given in Table 5.2.

Unlike opaque apertured resonators, the loss-per-pass value for translucent apertured resonators can not be calculated by simply integrating the light outside the clear aperture and comparing it to its normalized value of one. Instead, the spatial frequency of the mode needs to be analyzed immediately after the position dependent phase of the lens is applied. All spatial frequencies above a given cutoff frequency,  $k_c$ , are

Parameter	Value
$\lambda$	$0.98 \mu m$
$n_{ave}$	3.4
$\lambda/n_{ave}$	$0.285 \mu m$
$\Delta n_{oxide}$	0.06
$t_{oxide}$	$0.08 \mu m$
$L_{eff}$	$4 \mu m$
$N_{pts}$	512

Table 5.2: Summary of parameters of the VCSEL model used in the Fox and Li calculations.

considered to be lost out of the resonator due to the angular dependence of the DBR's reflectance (E.R. Hegblom, 1996). All frequencies above this cutoff are integrated and a loss factor can be calculated. The cutoff frequency used in the simulations is  $\sim 7$  cycles/ $\mu m$ . This cutoff has been determined in (E.R. Hegblom, 1996) based on scatter calculations of various propagation models.

The first simulations performed used infinite transverse-extent parabolic oxide tapers. The effect of an intracavity lens in confining the optical mode can easily be seen by comparing the results to a simulation where the focal length of the lens is set to infinity ( $\Delta n_{oxide} = 0$ ). Figure 5.31 shows the magnitude and phase after 500 iterations for the infinite focal length oxide lens and resonator parameters given in Table 5.2. Figure 5.32 shows the magnitude and phase after 500 iterations for a similar but finite focal length lens cavity. The lensed resonator clearly is confining the mode to the diameter of the lens. The mode of the non-lensed resonator is being confined by the mathematically imposed aperture at  $7.5 \mu m$ . As this mathematical aperture is opened the mode continues to spread out. The observed ripple in the magnitude and phase is due to the abruptness of the mathematical aperture.

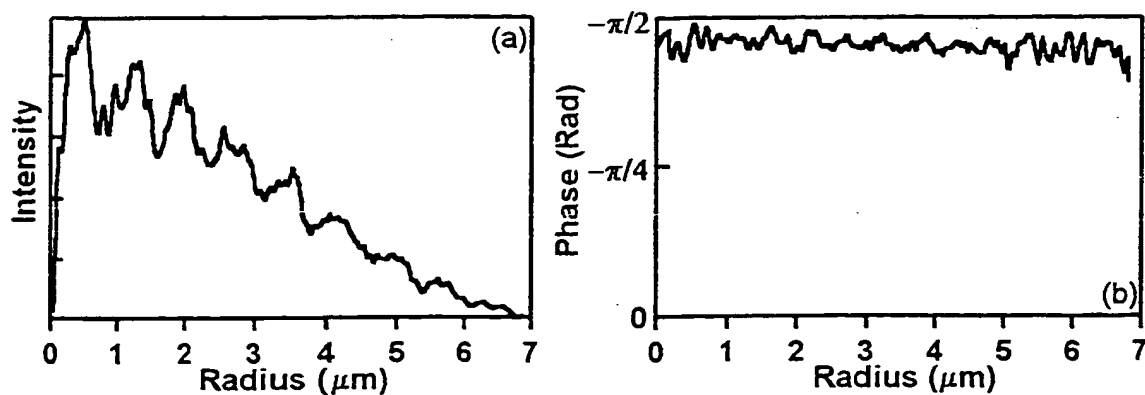


Figure 5.31: Computed magnitude and phase after 500 iterations for a 5  $\mu\text{m}$  device with no intracavity lens.

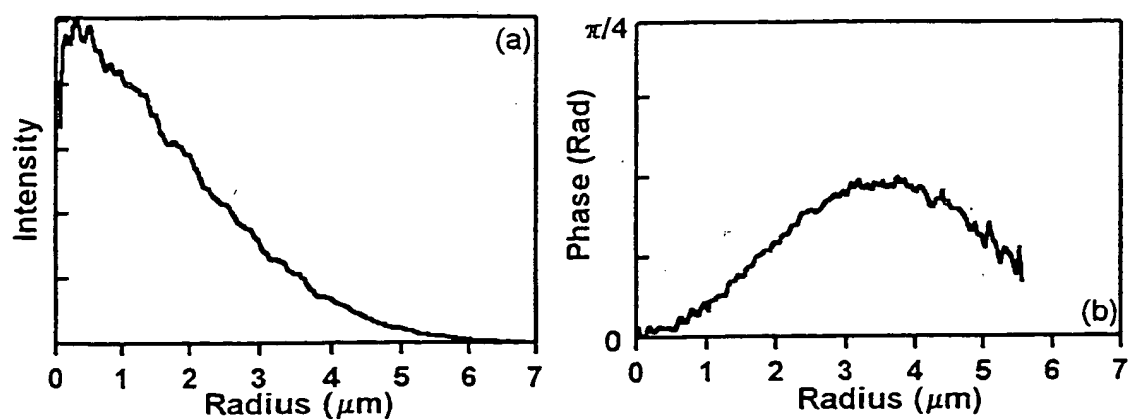


Figure 5.32: Computed magnitude and phase after 500 iterations for a 5  $\mu\text{m}$  device with an infinite extent parabolic lens.

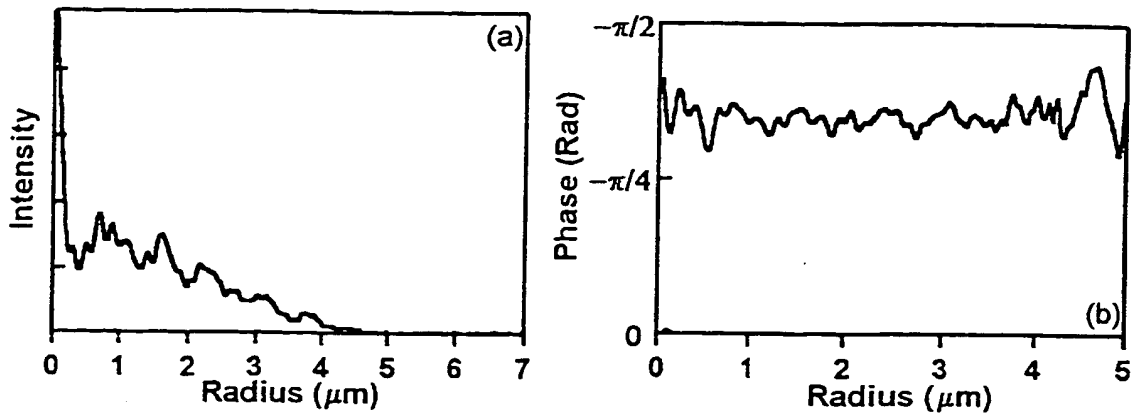


Figure 5.33: Computed magnitude and phase after 2000 iterations for a  $5\ \mu\text{m}$  device with an abrupt oxide aperture.

The loss in a resonator with a parabolic tapered oxide lens of infinite extent should be zero as this perfect lens is able to exactly compensate for the diffraction of the mode. For the simulation of Fig. 5.32, the loss was seen to oscillate chaotically for the first hundred iterations and then periodically oscillate around zero after a few hundred iterations. This indicates that the rounding errors in the calculation make the loss-per-pass values at best accurate to  $\pm 0.0005\%$ .

The second series of simulations performed were on abrupt oxide apertures. The computed magnitude and phase after 2000 iterations for a  $5\ \mu\text{m}$  radius aperture are shown in Fig. 5.33. The loss-per-pass calculated with each iteration is shown in Fig. 5.34. Ripple is obvious in both the magnitude and phase plots of Fig. 5.33 due to the discontinuous phase step of the abrupt aperture. It is also apparent that the simulation is converging slower to a steady state solution. After 2000 iterations the steady-state loss-per-pass has not converged but can be extrapolated to be  $\approx 0.007\%$ . This loss is about an order of magnitude higher than the rounding error seen for the



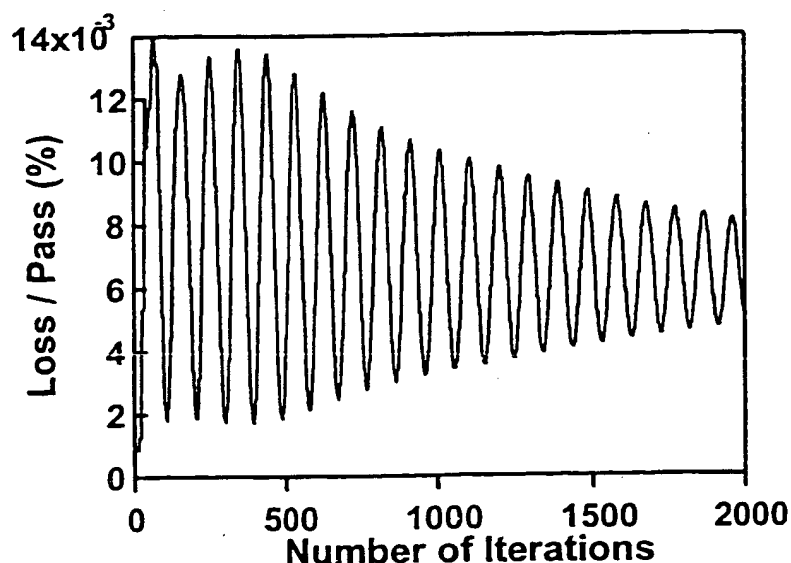


Figure 5.34: The loss-per-pass calculated with each iteration for a 5  $\mu\text{m}$  device with an abrupt oxide aperture.

parabolic taper. It is important to remember that this is a loss-per-pass value. In the high finesse cavities of a VCSEL (lots of passes), these losses may become a significant fraction of the overall losses for small device diameters. This value is in agreement with the published data of (E.R. Hegblom, 1996).

Simulations of the scattering loss were performed in the same manner as discussed above for 2  $\mu\text{m}$  radius devices using the three different oxide taper geometries discussed: parabolic, finite parabolic, and abrupt. Infinite extent parabolic simulations were performed merely to insure the software was within check. From these simulations, the finite parabolic taper has less loss than the abrupt aperture and the ideal parabolic lens loss goes to zero as expected. Losses for the non-ideal tapers also go up with reduced device size. A summary of the 2  $\mu\text{m}$  and 5  $\mu\text{m}$  radius results is given in Table 5.3.

Device Radius	Parabolic	Parabolic Finite	Abrupt
5 $\mu\text{m}$	0%	0.003%	0.007%
2 $\mu\text{m}$	$\rightarrow$ 0%	0.008%	0.01%

Table 5.3: A summary of the 2 micrometer radius Fox and Li results for infinite parabolic finite parabolic and abrupt oxide apertures.

### 5.6.3 Discussion

It should be realized that historically laser cavities were large compared to a wavelength, both longitudinally and laterally. It was therefore completely valid to employ scalar diffraction theory and the Fresnel approximation to find the cavity modes. In VCSELs, where all dimensions are of the size of a wavelength, the rigorousness of the solution is a concern. In fact, during the first passes of the Fox and Li calculations presented here, the constraint presented in Eq. 5.31 could be violated. This criterion states that the observation plane must be far enough away from an abrupt aperture so that the edge waves will have become paraxial. With increasing iterations the mode is diffracting less and less from the edges of the aperture so edge waves effects become less of a concern. Reasonable results for diffraction loss have been achieved when compared to other techniques for microcavities of these small dimensions, as discussed earlier.

In this section, theory and computer algorithms were developed for modeling scattering losses in oxide apertured VCSELs based on the classical calculations of Fox and Li. Results on calculated scatter loss and intensity mode profiles for resonators with various taper geometries were determined. Simulation of abrupt apertures showed substantial ripple in their magnitude and phase while parabolic tapered apertures do not. The current computer code performs a 1000 iteration simulation in approximately

45 min on a Silicon Graphics Octane platform. For calculations with higher numbers of iterations and with wider mathematical apertures, the computation time needs to be reduced through optimization of the FHT algorithm. Diffraction loss from oxide apertures is most important for long-wavelength and/or single transverse-mode devices. For devices with radial dimensions greater than 5  $\mu\text{m}$  the scatter loss from abrupt apertures becomes almost negligible.

## 5.7 Summary

In this chapter I have reported the optical constants of oxidized crystalline and LTG  $\text{Al}_{0.98}\text{Ga}_{0.02}\text{As}$  over the wavelength range of 240 – 1700 nm. I calculate a low optical scattering loss for oxidized crystalline material based on analysis of AFM surface roughness measurements. The measured optical constants have been used to develop two-layer native-oxide antireflection coatings in two geometries: buried and surface. I have studied and reported the design criteria surrounding each of these two geometries. I have experimentally demonstrated a surface coating having a reflectance minimum of 0.4% and a reflectance of < 1% over a bandwidth of > 250 nm. I have additionally developed a buried-oxide coating having a reflectance minimum of 0.4% and a reflectance of < 1% over a bandwidth of 21 nm. From the AFM surface roughness measurements, the calculated optical scattering loss indicates that reflectance minima as low as  $10^{-4}\%$  are ultimately achievable with these coatings.

Additionally in this chapter, I have developed the phase distributions of intracavity oxide lenses and the necessary theory and computer algorithms for modeling scattering losses in oxide apertured VCSELs based on the resonant mode calculations of

Fox and Li. Simulation of oxide confined resonators clearly shows substantial confinement of the optical mode. Abrupt oxide apertures showed substantial ripple in their magnitude and phase while parabolic tapered apertures did not.

The new field of native-oxide technologies is advancing rapidly. The results presented in this chapter are important to the community as they contribute to a better understanding of the properties and applications of this new material. Research on tailoring the oxide index and taper profiles through the addition of dopants to the bubbler water, and the development of alternative oxidation methods such as UV exposure, will further push on the frontier of this up and coming technology.

## Chapter 6

### Ultrafast Implications of "Low-Ripple" VCSELs

#### 6.1 Problem with Ultrashort Pulse Excitation of VCSELs

The tremendous interest in vertical-cavity surface-emitting lasers extends beyond their obvious commercial applications. The physics community views these devices as ideal systems for the study of quantum optical effects. The coupling between the device's microcavity and gain medium is known to modify carrier relaxation processes and dynamics. The dynamics of these devices are difficult to study as they occur on subpicosecond time-scales. The coupled cavity and gain system of an optically pumped VCSEL exhibits Rabi oscillations (picosecond oscillations) in its output intensity due to this coupling (C. Weisbuch, 1992 ; J. Jacobson, 1994 ; T. B Norris, 1994 ; R. Houdre, 1995). While these measurements are necessarily made by optically pumping the VCSEL on resonance, there have been other reports on the modification in the spontaneous emission rate in VCSELs pumped at higher energies off resonance. This modification is attributed to the thermalization of free carriers to the energy supported by the cavity. The time needed for the free carriers to thermalize is on the order of 100 fs. Thus, to observe such spontaneous emission rate modifying effects, free car-

riers must be generated with an ultrashort (10's of fs) pump pulse and the VCSEL emission detected with a time-scale resolution of  $<100$  fs. Such detection is feasible using a technique like optical homodyne detection (U. Leonhardt, 1996). However, direct excitation of VCSELs with these ultrashort pulse durations has fundamentally been limited by the temporal broadening (spectral narrowing) caused by the filtering of the pulse spectrum by the cavity interference ripple. By eliminating (or tailoring) the Fabry-Perot interference fringes, as in the case for the previously discussed "low-ripple" device, I can modify the cavity's influence on an impinging ultrashort optical pulse.

The intent of this chapter is not to delve into the vast world of quantum optical effects in VCSELs, but rather to discuss the dispersion characteristics of conventional and thin-film optimized devices with the above physics as motivation. In the next section, I will present the mathematics needed to consider ultrashort pulse propagation in multilayer structures along with simulations of the temporal profiles of the propagated pulses. Spectrally-resolved white-light interferometry will be used in section 6.3 to directly measure the dispersion characteristics of passive VCSEL cavities. Section 6.4 will summarize and conclude the chapter.

## 6.2 Pulse Interaction with the VCSEL Multilayer Structures

### 6.2.1 Theory

This section gives a brief review of the properties of light in the time and frequency domains with conventions tailored to femtosecond optical pulses. The theory presented is by no means a complete treatment and is merely an introduction for devel-

oping an intuitive understanding of the effects of multilayer structures on femtosecond pulses. This discussion is a subset of the full and rigorous treatment on ultrashort pulse phenomena found throughout (Diels, 1996).

Light as an electromagnetic wave is fully described by an electric field with space and time dependence. The interaction of light and matter is then governed semiclassically by Maxwell's equations. The electric field can be completely described in either the time or the frequency domain with measured quantities that are real. Nevertheless, it is mathematically convenient to express the electric field as a complex quantity. Starting with the real electric field  $E(t)$ , whose spatial dependence has been neglected, the complex spectrum of the field strength  $\tilde{E}(\Omega)$  can be defined via a Fourier transformation (FT):

$$\tilde{E}(\Omega) = \mathcal{F}\{E(t)\} = \int_{-\infty}^{+\infty} E(t) e^{-i\Omega t} dt = |\tilde{E}(\Omega)| e^{i\Phi(\Omega)}. \quad (6.1)$$

The spectral amplitude and phase are denoted by  $|\tilde{E}(\Omega)|$  and  $\Phi(\Omega)$ , respectively. Given  $\tilde{E}(\Omega)$ , the time-dependent electric field can be determined through a corresponding inverse Fourier transformation (IFT). It is often desirable to have a complex representation of the electric field not only in the frequency domain but also in the time domain. Additionally, it is convenient to use only functions with positive frequency components. These desires are satisfied by expressing the real physical electric field  $E(t)$  as,

$$E(t) = \tilde{E}^+(t) + \tilde{E}^-(t), \quad (6.2)$$

where  $\tilde{E}^+(t)$  is the IFT of the positive frequencies of  $\tilde{E}(\Omega)$  and  $\tilde{E}^-(t)$  is the IFT of the negative frequencies, or equivalently the complex conjugate of  $\tilde{E}^+(t)$  as  $E(t)$  is a

real function.<sup>1</sup> The electric field's complex FT can be represented similarly as,

$$\tilde{E}(\Omega) = \tilde{E}^+(\Omega) + \tilde{E}^-(\Omega), \quad (6.3)$$

where the superscript plus denotes the positive frequencies and the superscript minus represents the negative frequencies of  $\tilde{E}(\Omega)$ . Usually, the complex electric field  $\tilde{E}^+(t)$  is represented as the product of an amplitude function and a phase term. In most cases with femtosecond optical pulses, the spectral amplitude will only have appreciable values in a small frequency interval centered around a mean frequency,  $\omega_l$ . Thus,  $\omega_l$  can be thought of as a carrier frequency and  $\tilde{E}^+(t)$  can be expressed as the product of a time dependent phase term  $\phi(t)$ , carrier frequency term, and a field envelope  $\varepsilon(t)$ :

$$\tilde{E}^+(t) = \frac{1}{2}\varepsilon(t)e^{i\phi(t)}e^{i\omega_l t}. \quad (6.4)$$

The result of Eq. 6.4 is useful in the case when the bandwidth of the pulse is a small fraction of the carrier frequency. This condition is satisfied for the pulse durations of interest in this work; however, this may not hold when dealing with today's record setting pulses containing only a few optical cycles.

By looking at the derivative of the total phase factor  $(\phi(t) + \omega_l t)$  in Eq. 6.4, an instantaneous frequency  $\omega(t)$  can be determined:

$$\omega(t) = \omega_l + \frac{d}{dt}\phi(t). \quad (6.5)$$

The carrier frequency should be chosen to minimize the variation of the phase  $\phi(t)$  and is commonly taken to be the frequency at the peak of the pulse. If the derivative of the time dependent phase,  $\frac{d}{dt}\phi(t)$ , evaluates to a constant, the instantaneous frequency

---

<sup>1</sup>For a real function of  $E(t)$ ,  $\tilde{E}(\Omega) = \tilde{E}^*(-\Omega)$ .



does not vary with time and is equal to the carrier frequency plus the constant. If the derivative is equal to a function of time, the carrier frequency varies across the pulse, and the pulse is said to be frequency modulated or "chirped". If the second derivative is positive, the pulse is "up" chirped as the carrier frequency increases across the pulse. If the second derivative of  $\phi(t)$  is negative, the pulse is said to be "down" chirped as the carrier frequency decreases across the pulse. Thus, for a downward chirped pulse the front of the pulse (in time) consists of the higher frequencies (blue wavelengths) while the back of the pulse consists of the lower frequencies (red wavelengths). The converse is true for an upward chirped pulse.

Since the temporal and spectral characteristics of the electric field are related through Fourier transformations, one can not vary independently from the other. This relationship leads to an uncertainty principle relating the temporal and spectral widths of a given pulse. A transform limited (unchirped) pulse has the minimum time-bandwidth product possible. A chirped pulse has a larger time-bandwidth product.

The propagation of femtosecond pulses is governed by a wave equation derived out of Maxwell's equations (see e.g. (Jackson, 1975) ). The characteristic matrix method uses the general solution to Maxwell's equations for a single slab of material to turn linear propagation through a multilayer structure into a simple linear algebra problem (Mickelson, 1992). As a result, the spectral and temporal changes that a pulse experiences upon reflection (or transmission) through a linear multilayer stack can be determined through the simple application of a complex optical transfer function,  $\tilde{H}(\Omega)$ , obtained by the characteristic matrix method. The optical transfer function contains

the phase delay,  $\Psi(\Omega)$ , and amplitude scaling,  $R(\Omega)$ , information for each frequency component of the incident pulse. The field reflected at the sample's surface is related to the incident field spectrum by,

$$\tilde{E}_{out}(\Omega) = R(\Omega) e^{-i\Psi(\Omega)} \tilde{E}_{in}(\Omega) = \tilde{H}(\Omega) \tilde{E}_{in}(\Omega). \quad (6.6)$$

The complex reflection from the mirror may not only cause intensity loss but may also lead to modification of the temporal pulse shape. To gain an understanding of the effect of  $\Psi(\Omega)$  on the pulse,  $\Psi(\Omega)$  can be rewritten as a Taylor series expansion around the carrier frequency:

$$\Psi(\Omega) = \sum_{n=0}^{\infty} b_n (\Omega - \omega_l)^n, \quad (6.7)$$

where,

$$b_n = \frac{1}{n!} \left. \frac{d^n \Psi(\Omega)}{d\Omega^n} \right|_{\omega_l}. \quad (6.8)$$

Transforming to the time domain with  $\Psi(\Omega)$  expanded and holding the reflectivity constant across the pulse yields,

$$\tilde{E}_{out}(t) = \frac{R}{2\pi} e^{-ib_0} e^{i\omega_l t} \int_{-\infty}^{+\infty} \tilde{E}_{in}(\Omega) e^{i(\Omega - \omega_l)(t - b_1)} \exp \left\{ -i \sum_{n=2}^{\infty} b_n (\Omega - \omega_l)^n \right\} d\Omega. \quad (6.9)$$

The effect of the various expansion coefficients is now apparent. The  $b_0$  term is merely a constant phase shift which has no effect on the pulse. The  $b_1$  term just shifts the time axis of the pulse and is analogous<sup>2</sup> to *group delay*. The higher-order coefficients ( $n \geq 2$ )

<sup>2</sup>Group delay and GVD are defined through the expansion of the propagation constant,  $k(\Omega)$ , for transparent media. However, taking  $\Psi(\Omega) = k(\Omega)d$  we see that they are related by a penetration depth into the sample,  $d$ , which is actually frequency dependent. Thus, I call it analogous because the effects of  $d$  can't be separated out from the group delay  $\left. \frac{dk}{d\Omega} \right|_{\omega_l}$  and GVD  $\left. \frac{d^2k}{d\Omega^2} \right|_{\omega_l}$  coefficients and furthermore the end result on the pulse is equivalent.

result in nonlinear changes to the pulse's phase. The second order  $b_2$  term is analogous to *group velocity dispersion* (GVD). A reduced form of the wave equation shows that a transform-limited pulse (no chirp) propagates unchanged in space and time through a loss-free medium whose propagation constant contains only constant phase shifts and group delay terms. When GVD is added to the medium, the initially unchirped pulse acquires a quadratic phase dependence as it propagates. This chirps the pulse and increases the time-bandwidth product by either increasing its spectral or temporal width. The solution to the reduced wave equation, for linear optical processes, also shows that the spectrum of the pulse must remain constant as it propagates. Consequently, the pulse must broaden in time.

If the phase response of a multilayer structure  $\Psi(\Omega)$  could be tailored in such a way that it is a nonzero constant or a linear function of frequency (see Eq. 6.5), the incident pulse will be reflected (or transmitted) unchanged. If the difference in the phase of the multilayer structure and incident pulse is zero, a chirped pulse can actually be compressed to a transform-limited pulse with a shorter duration.

In Eqs. 6.6 - 6.9 the reflectance was assumed to be constant with frequency. This represents a situation where the carrier frequency of the pulse is near that of the center frequency of a DBR, for example. Away from the center frequency, the reflectance is varying quite rapidly compared to the spectral width of the pulse. The variations in phase and amplitude of the reflectance are intimately related via the Kramers-Kronig relation, and both must be considered for proper analysis (Jackson, 1975).

### 6.2.2 Modeling of the Dispersive Properties of VCSELs

The group delay and GVD of two VCSEL cavity designs have been numerically calculated and compared in both transmission and reflection. The first structure is a conventional VCSEL cavity consisting of a 15-pair AlAs/GaAs top mirror, a one-wavelength cavity spacer, and a 15.5-pair AlAs/GaAs bottom mirror. The second structure is a thin-film optimized low-ripple device designed as explained in Chp. 3 using this conventional structure as a starting design. The resonance wavelength of both cavities is  $1\text{ }\mu\text{m}$ , and both designs are “cold” cavities as they do not contain any absorbing quantum wells. The complex reflectances of the conventional and low-ripple passive designs are shown in Figs. 6.1 and 6.2, respectively.

#### Group Delay Upon Reflection

As evident from Eq. 6.9, group delay results in a shifting of the time axis. Since the entire wave packet travels at the group velocity, the group delay merely represents the delay experienced by an entire pulse of a given center wavelength. In the simplest picture, the group delay can be thought of as being proportional to the penetration depth of the light into the multilayer structure. For example, consider a “simple” chirped mirror where the quarter-wavelength thick layers have a Bragg wavelength for individual pairs that increases linearly approaching the substrate. For such a mirror, the longer wavelengths penetrate deeper than the shorter wavelengths that are reflected by the topmost pairs. It is expected using this picture that the group delay will vary linearly with wavelength. While it has been shown that the simulated group delay

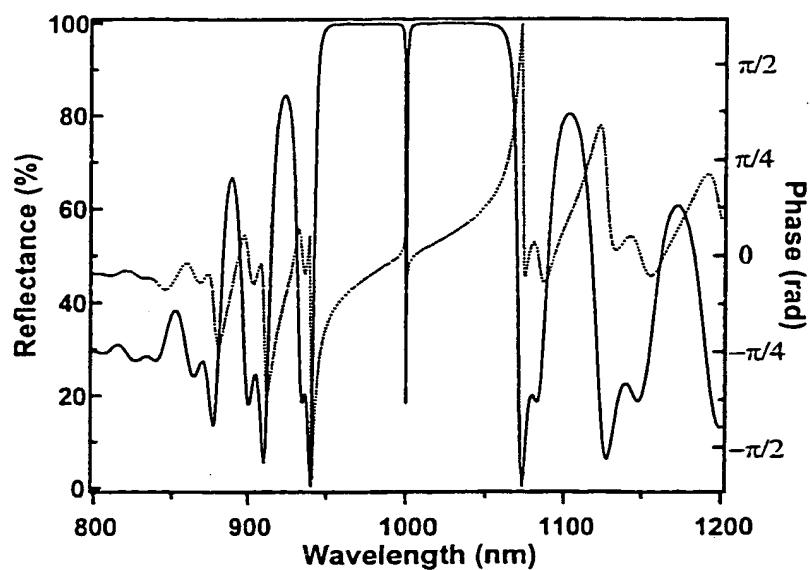


Figure 6.1: The reflectance and phase of a conventional VCSEL's cold cavity (without quantum wells). The dotted lines illustrates the phase.

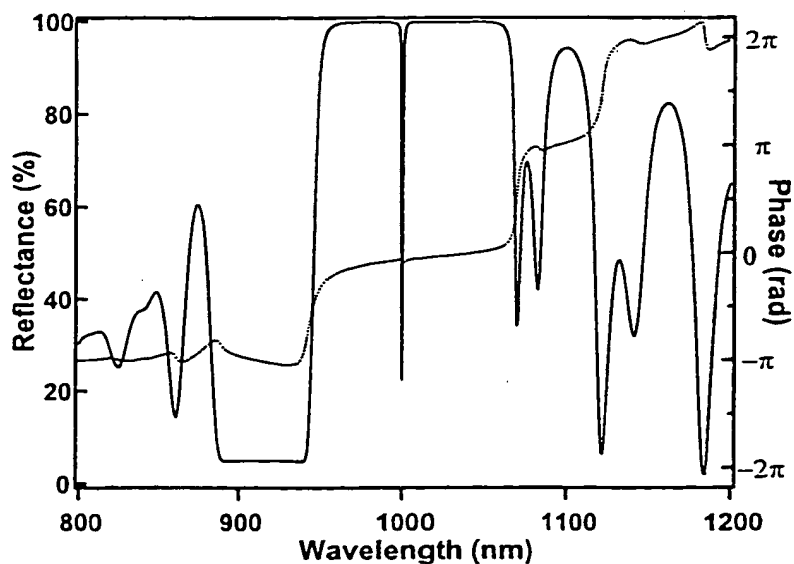


Figure 6.2: The reflectance and phase of a low-ripple VCSEL's cold cavity (without quantum wells). The dotted lines illustrates the phase.

from such a mirror does have a linear trend, it also exhibits large oscillations along the way (N. Matuschek, 1998). These oscillations are a result of the interference between the large reflections off the pairs of the correct thickness and the small reflections from the thinner pairs above it. This picture must be used with caution because these interference effects are not taken into account!

The group delay has been calculated for each structure by directly taking the first derivative of the simulated phase (see Eq. 6.7). The calculation results are shown in Fig. 6.3 for the conventional structure and in Fig. 6.4 for the low-ripple structure. Their reflectance spectra are shown for reference.

The penetration depth picture can be used fairly successfully to explain the group delay behavior in Figs. 6.3 and 6.4 in the region of high reflectivity away from the cavity resonance. In this region, the vast majority of the light is reflected from the top mirror stack. The optimized layers in the low-ripple design allow light to penetrate further into this stack. It is then expected that the group delay of the optimized structure would be higher than that of the conventional structure. This is in fact true, and is illustrated in the plot of Fig. 6.5. The group delay for both designs across the region of high reflectivity is shown. Near the wavelength of 1025 nm, the low-ripple structure has approximately 1-2 fs more of delay. On the shorter wavelength side of the cavity resonance at 975 nm, the low-ripple has an additional delay of 5 fs. For the shorter wavelengths in Fig. 6.5, the reflectance of the low-ripple structure decreases, allowing light to penetrate further into the mirror resulting in an increase in the group delay.

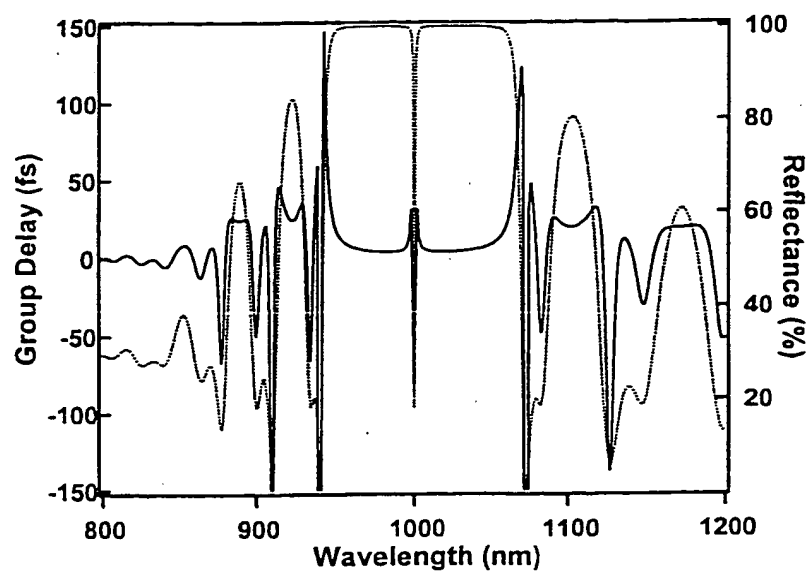


Figure 6.3: The calculated group delay (solid line) for the conventional VCSEL cavity on reflectance.

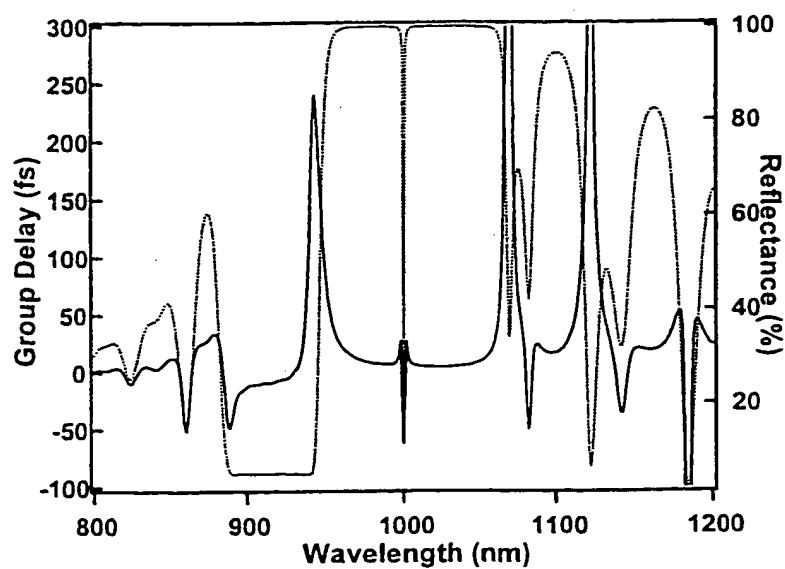


Figure 6.4: The calculated group delay (solid line) for the low-ripple VCSEL cavity on reflectance.

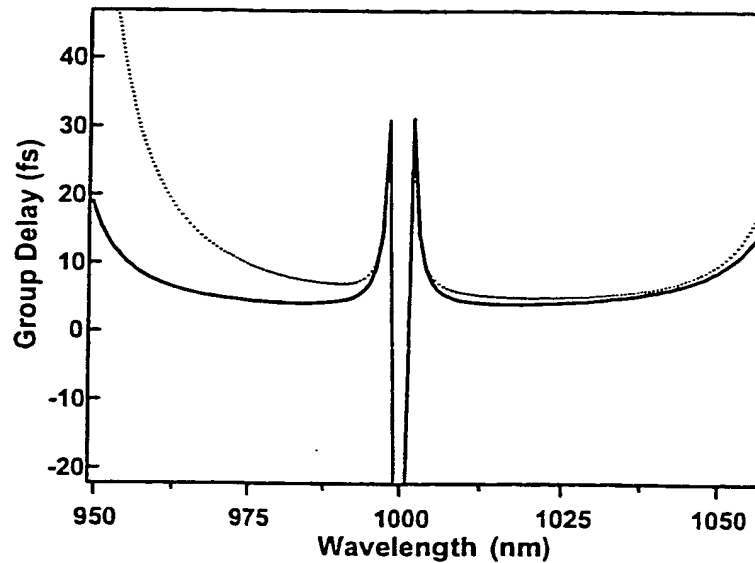


Figure 6.5: Comparison of the group delay for the conventional (solid) and low-ripple VCSEL cavities on reflection.

For all other regions of the spectrum shown in Figs. 6.3 and 6.4, the use of this intuitive penetration depth picture is questionable. In particular, this picture does not explain the negative group delay values occurring near the propagation modes (reflectance nulls) in Fig. 6.3, for instance. These regions are a result of interference that modifies the phase of the reflection in such a way that the pulse appears to be advanced in time.

Lastly, the most important observation shown in Fig. 6.4 is the presence of a region where the group delay is varying slowly over a 30 nm section of the optical pumping window near 915 nm. To obtain an understanding of the dispersive effects of these structures on the reflected pulse shape, the derivative of the group delay (a.k.a. GVD) needs to be analyzed.



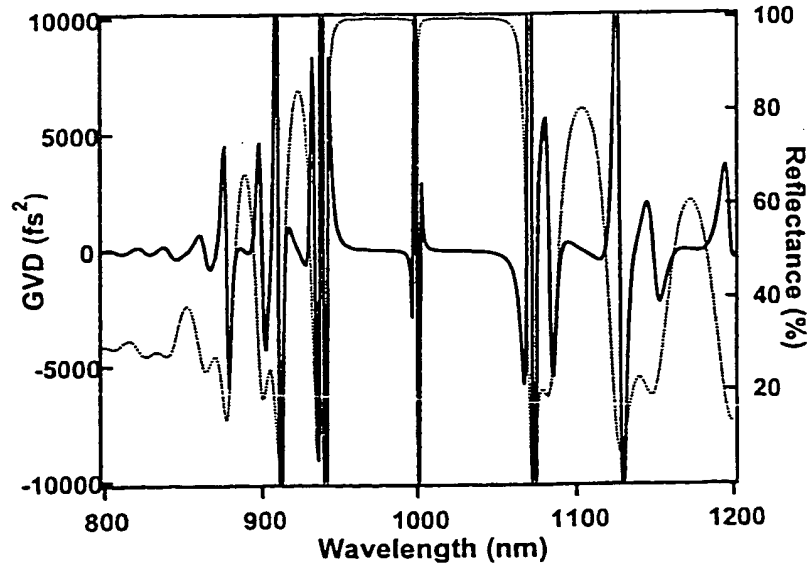


Figure 6.6: The calculated group velocity dispersion (GVD) of the conventional VCSEL cavity on reflectance. The reflectance is illustrated by the dotted curve.

### GVD Upon Reflection

The GVD has been calculated for both structures by evaluating the  $b_2$  expansion term of Eq. 6.8 from the simulated phase. The GVD of the conventional structure is shown in Fig. 6.6. Extremely large oscillations in the GVD are observable near the desired pump wavelengths surrounding 915 nm. These large oscillations signify that the cubic and higher terms in the Taylor expansion of the phase are indeed appreciable and must be considered when determining the characteristics of pulses with carrier wavelengths in this region. To understand the severity of these oscillations it is interesting to compare a value of  $5000 \text{ fs}^2$  obtainable in these structures with a penetration depth on the order of  $1 \mu\text{m}$ , to that obtainable in a length of glass. In fused silica<sup>3</sup>, for

<sup>3</sup>This value was obtained for a wavelength of 800 nm from the 1997/1998 Newport Corporation optics catalog, page 8-3.

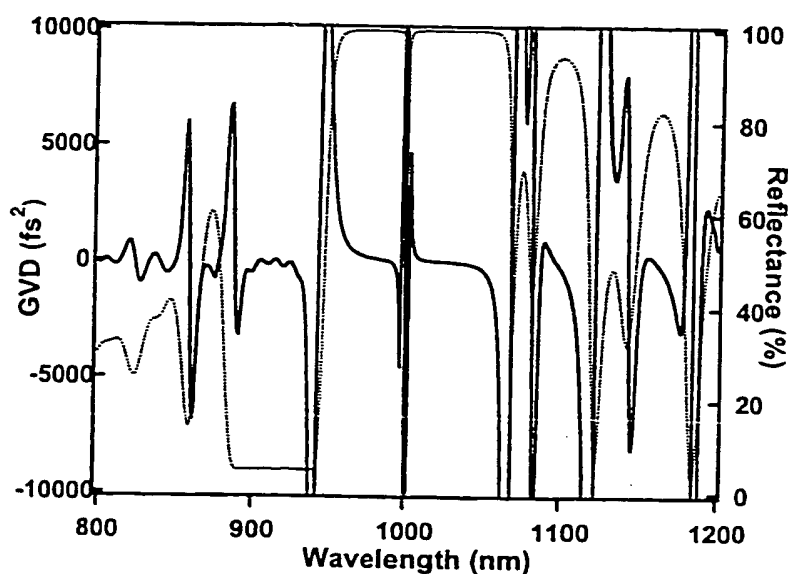


Figure 6.7: The calculated group velocity dispersion (GVD) of the low-ripple VCSEL cavity on reflectance. The reflectance is illustrated by the dotted curve.

example, the GVD is  $360 \text{ fs}^2/\text{cm}$ . This means  $5000 \text{ fs}^2$  is equivalent to roughly 14 cm of glass! These values are not entirely unreasonable, however, when compared to the values three orders of magnitude larger that are achievable with dielectric Gires-Tournois interferometers (J. Heppner, 1985).

The calculated GVD upon reflectance from the low-ripple structure is shown in Fig. 6.7. The smoothly varying group delay across the majority of the pump window is responsible for a region of GVD with significantly reduced oscillations in comparison with the conventional structure. Across a 25 nm band centered at 915 nm, the GVD oscillates by  $\pm 200 \text{ fs}^2$  about a mean value of  $\approx -75 \text{ fs}^2$ . This smoother GVD response results in a much lower cubic-dispersion term. Consequently, a transform-limited pulse reflected off the low-ripple structure is anticipated to return with a shorter duration and a chirp much closer to quadratic than the conventional structure. Additionally, the

negative GVD trend across the optical pumping window has the potential of compressing a quadratically upward chirped pulse.

### Group Delay in Transmittance

While the transmission in these structures is simply one minus the reflectance above the absorption cutoff of GaAs ( $\approx 870$  nm), the phase on reflection can not be related so simply to the phase on transmission. As a result, the dispersive characteristics differ significantly in transmission. The calculated transmittance spectra and group delay for the conventional and low-ripple cavities are shown in Figs. 6.8 and 6.9. The most noticeable difference in the transmission and reflection group-delay calculations is the lack of “ringing” on transmission. This lack of ringing is a result of a smoother phase dependence experienced in transmission than in reflection. Additionally, the lowest values of group delay for transmission are along the high reflector. At all other wavelengths the group delay is a larger positive value. The correlation of the transmission minima with the group delay minima suggests that resonance effects (interference) are dominant. As shown in Chapter 3, the transmission maxima are in fact resonant modes of the structure. Intuitively, the group delay in transmission for these modes can, in some sense, be pictured as the time of flight of light through a build-up cavity. For a build-up cavity with perfect reflectors (high  $Q$ ), light that enters becomes contained and never exits (an infinite delay). As the cavity  $Q$  is reduced, pulses are emitted with a spacing in time representative of the delay.<sup>4</sup> The longest delay is experienced by the mode at the center of the DBR stop band. All of the other resonant modes of the

---

<sup>4</sup>This assumes the “cavity” length is larger than the geometrical length of the pulse so as to avoid interference effects caused by overlapping pulses.

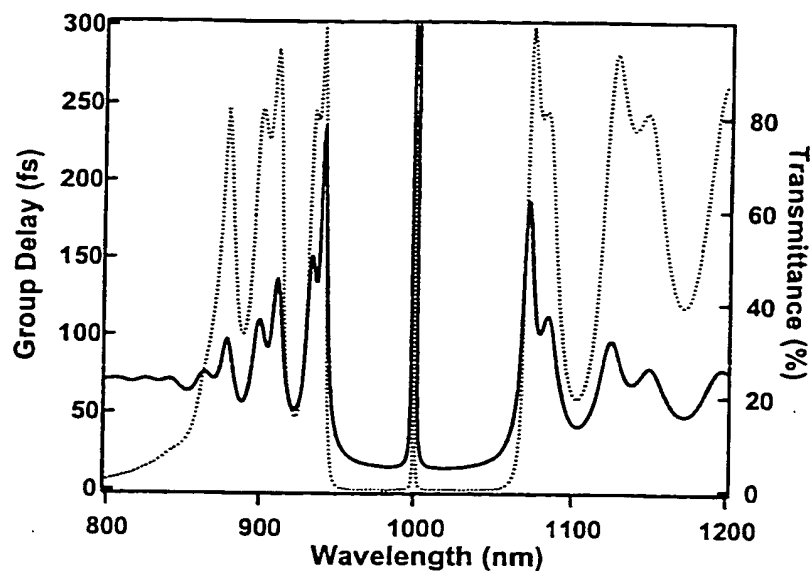


Figure 6.8: The calculated group delay (solid) for the conventional VCSEL cavity on transmittance.

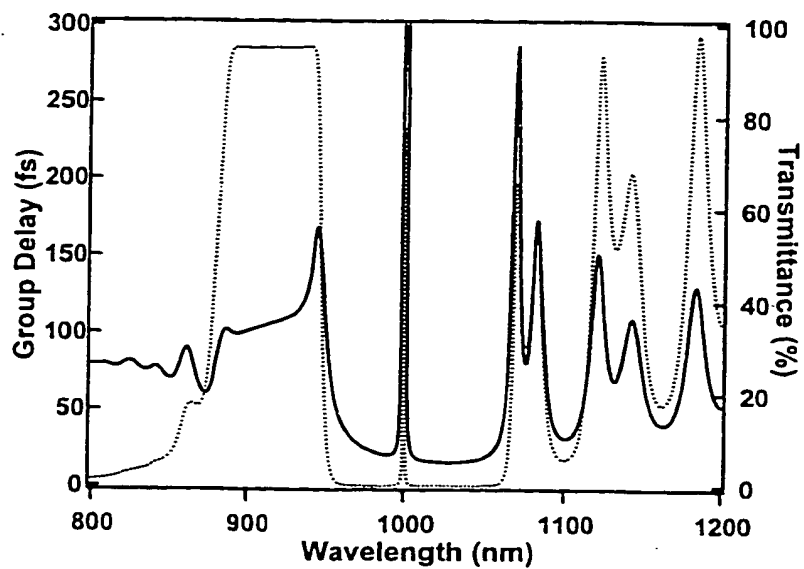


Figure 6.9: The calculated group delay (solid) for the low-ripple VCSEL cavity on transmittance.

structure have shorter delays.

The group delay on transmission for the low-ripple structure has similar traits relating to the delay on reflection as the conventional structure. Additionally, the group delay on transmission across the optical pumping window is somewhat flatter than on reflection. Lastly, the mode on the short wavelength side of the high reflector, near 945 nm, shows a single positive peak with no ringing for both transmission and reflection. This indicates a nonabrupt phase change that is consistent with an aperiodic structure. The profile of the group delay across the optical pumping window shows a similar trend as the reflectance variation of the bottom mirror of the laser structures. This observation is consistent with the build-up cavity analogy as the reflectance variation causes a change in the "cavity-Q" and thus a change in the ring-down time or equivalently the delay of the pulse.

### GVD in Transmittance

The properties of the group delay on transmission through the structures discussed above result in reduced GVD variations across the entire 800-1200 nm spectrum. The calculated GVD for the conventional and low-ripple cavities in transmission are shown in Figs 6.10 and 6.11.

Although the severity of the GVD oscillations is reduced in transmission for the conventional structure across the 915 nm wavelength region, the oscillations are still extremely large and would result in severe pulse dispersion. Comparison of the low-ripple structure in both transmission and reflection shows that a larger, flatter region of GVD is present across the pumping window. Across the same 25 nm band centered at

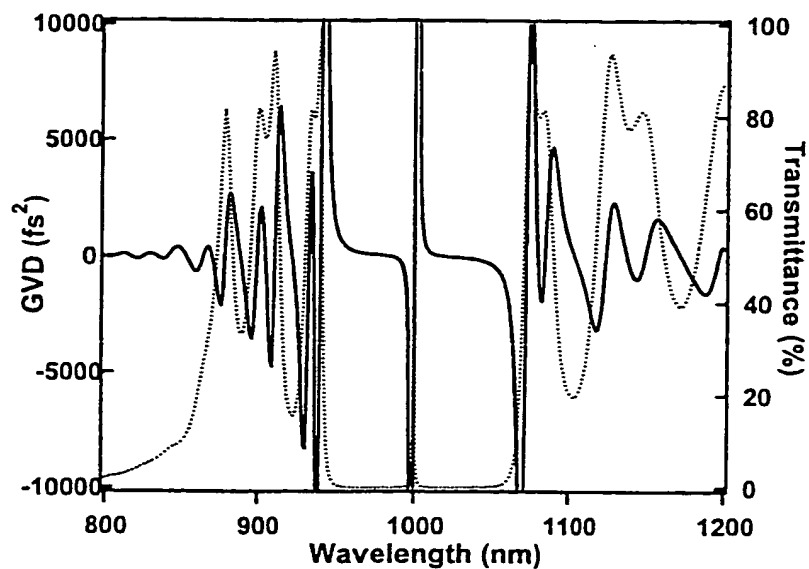


Figure 6.10: The calculated group velocity dispersion (GVD) of the conventional VCSEL cavity on transmittance. The transmittance is illustrated by the dotted curve.

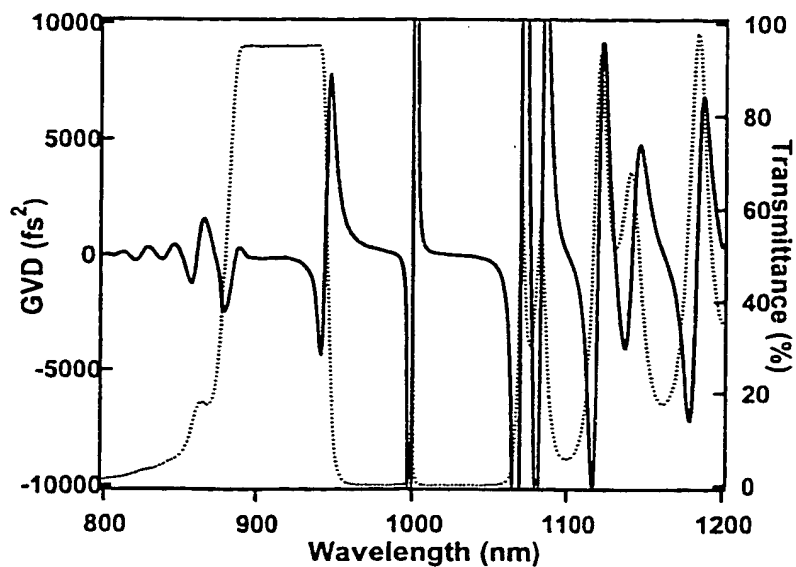


Figure 6.11: The calculated group velocity dispersion (GVD) of the low-ripple VCSEL cavity on transmittance. The transmittance is illustrated by the dotted curve.

915 nm, the GVD in transmission oscillates by  $\pm 50 \text{ fs}^2$  about a mean value of  $\approx -130 \text{ fs}^2$ . In transmission, these oscillations are about 4 times lower and the mean negative GVD value is about 1.5 times smaller. Additionally, the negative GVD dip nearest the lowest energy side of the high reflectance region is shallower. The reduced depth of this dip indicates that this type of structure could be used to more controllably chirp an incoming pulse through either tuning of the pulse's wavelength or tuning of the incident angle.

### 6.2.3 Calculated Pulse Profiles Through VCSEL Cavities

The temporal evolution of a transmitted ultrashort pulse through the conventional and low-ripple multilayer structures has been simulated using the transfer function approach discussed in section 6.2.1. A Gaussian shaped pulse with an intensity profile having a 40 fs full-width at half-maximum (FWHM) was used as the input pulse. (All spectral and temporal widths to be discussed are FWHM values.) The complex electric field describing this input pulse is,

$$\tilde{E}_{in}^+(t) = \frac{\epsilon_0}{2} e^{-(1+ia)(t/\tau_G)^2} e^{i\omega_1 t}, \quad (6.10)$$

where,

$$\tau_p = \sqrt{2 \ln(2)} \tau_G, \quad (6.11)$$

and  $\tau_p$  represents the pulse width. The linear chirp of the pulse is controlled by the parameter  $a$  related to the time dependent phase,  $\phi(t)$  by,

$$\frac{d\phi(t)}{dt} = \frac{-2at}{\tau_G^2}. \quad (6.12)$$

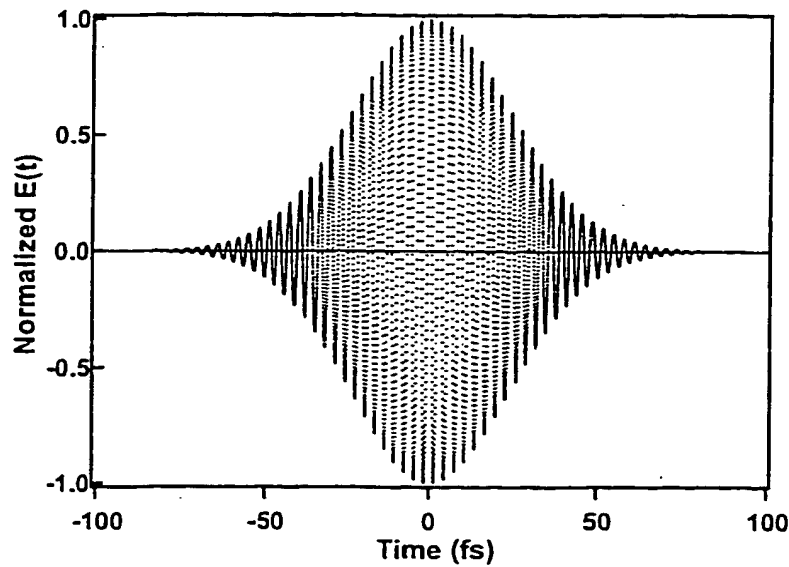


Figure 6.12: The real electric field amplitude for the unchirped ( $a = 0$ ) 40 fs Gaussian input pulse.

The amplitude function of the real electric field,  $E(t)$ , for this pulse (with  $a = 0$ ) centered at a wavelength of 915 nm is shown in Fig. 6.12. The intensity of  $\tilde{E}_{in}^+(t)$  and its time dependent carrier frequency,  $\omega(t)$ , are shown in Fig. 6.13. The spectral intensity of the pulse,  $|\tilde{E}_{in}(\Omega)|^2$ , is also a Gaussian and is centered at a wavelength of 915 nm. The overlap of the pulse's broad spectrum (31 nm) with the interference ripple of the conventional structure is apparent in Fig. 6.14. The interference ripple is modulating by over 80% across the region of the pump spectrum. The overlap of the pulse spectrum with the low-ripple optical pumping band is shown in Fig. 6.15. The optical pumping window reduces the modulation across the pulse spectrum to 0.5%, drastically reducing the amount of spectral filtering.

The transmitted temporal pulse profiles and time-dependent carrier frequency for two pulses with center wavelengths of 915 nm and 940 nm are shown in Figs. 6.16 (a)



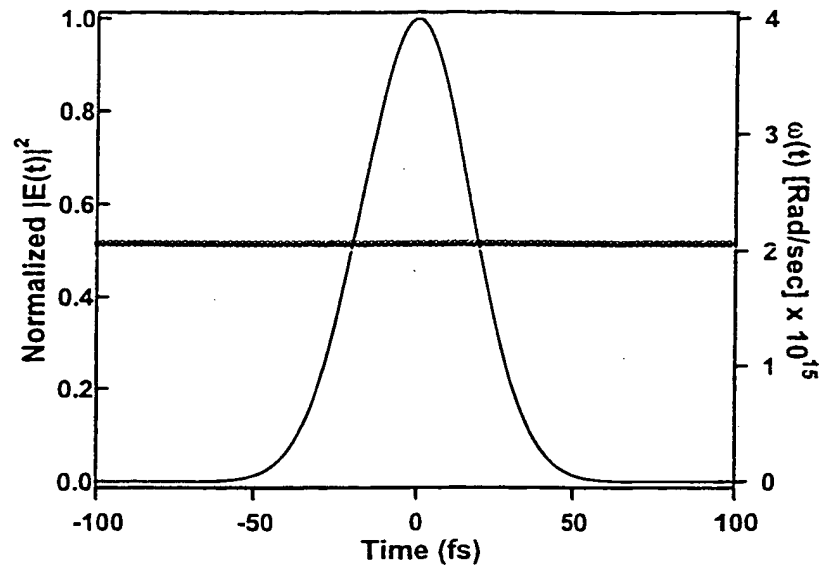


Figure 6.13: The intensity of  $\tilde{E}_{in}^+(t)$  and its time dependent carrier frequency,  $\omega(t)$ , for the 40 fs Gaussian input pulse.

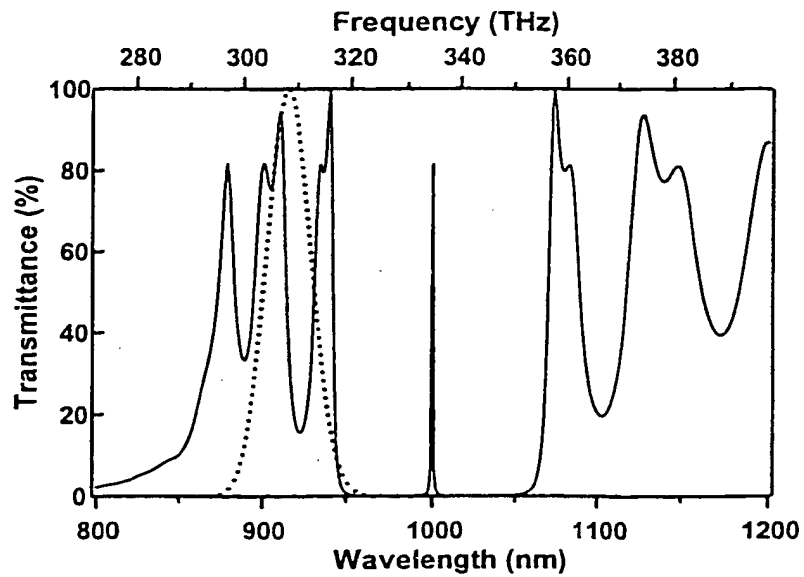


Figure 6.14: Illustration of the overlap of the spectral intensity of the 40 fs input pulse, centered at a wavelength of 915 nm, with the interference ripple of the conventional cold-cavity VCSEL structure.

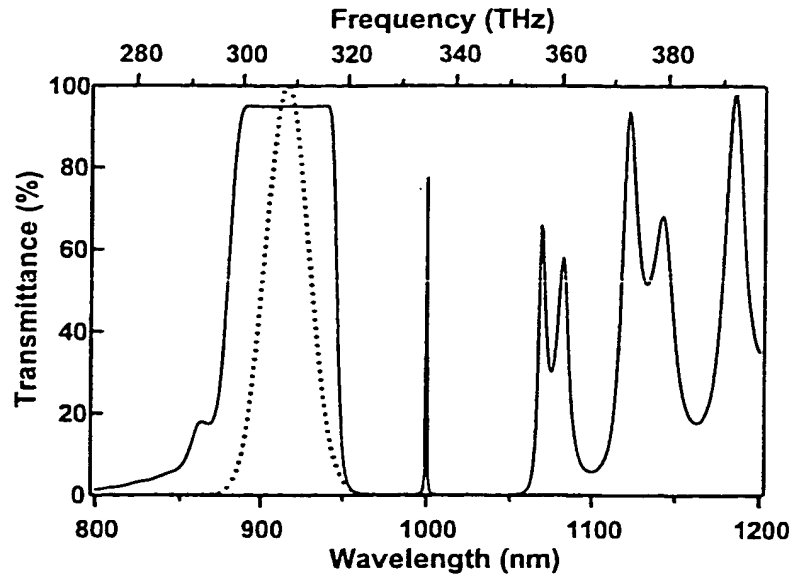


Figure 6.15: Illustration of the overlap of the spectral intensity of the 40 fs input pulse, centered at a wavelength of 915 nm, with the optical pumping window of the low-ripple cold-cavity VCSEL structure.

and (b), respectively. In the 915 nm plots of (a), the amplitude of the electric field,  $E(t)$ , is significantly reduced and broadened in comparison to the input pulse's electric field shown in Fig. 6.12. The energy of the pulse is now being distributed over more than 300 fs. The intensity envelope (dotted curve) of the transmitted pulse consists of a large central peak preceded and trailed by smaller pulses due to ringing. By fitting the central peak to a Gaussian, the broadened pulse width is determined to be 50 fs. The time-dependent carrier frequency (circles),  $\omega(t)$ , is seen to oscillate about the carrier frequency of the input pulse (x's) with maxima and minima correlated to the minima in the intensity profile. The presence of these oscillations, rather than a sloping or flat line, indicates that cubic and higher dispersion terms are appreciable as foretold by the plot of Fig. 6.10. The oscillations and spikes in  $\omega(t)$  are virtually meaningless at

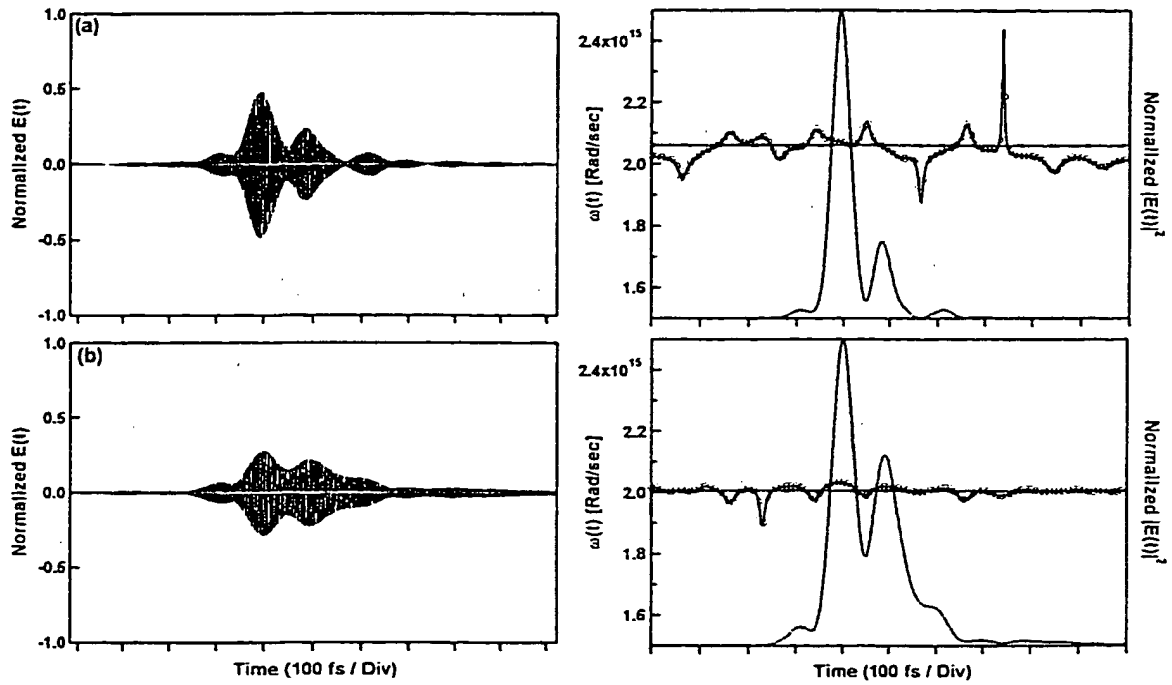


Figure 6.16: Plots of the electric field amplitude, intensity, and time dependent carrier frequency for a 40 fs pulse transmitted through the conventional structure at a center wavelength of (a) 915 nm, and (b) 940 nm. The electric field plots are normalized to an input pulse amplitude of 1. The intensity profiles are shown with dotted lines. The instantaneous frequency of the transmitted pulse is shown by circles and for the input pulse by x's. The markers are spaced by 100 calculation points.

times where the pulse intensity is not considerable. The transmitted pulse amplitude, intensity envelope, and time-dependent carrier frequency are shown in Fig. 6.16 (b) for an input pulse at 940 nm. The peak of the pulse is centered at the first propagation mode, and the longer wavelengths of the pulse are now severely clipped by the onset of the high reflectance region. This clipping results in a further increase in ringing and a broadening of the central peak to 58 fs.

The transmitted pulse profiles through the low-ripple structure and their time-dependent carrier frequencies are shown in Fig. 6.17 for input pulses centered at 915 nm with various degrees of upward chirp ( $a \leq 0$ ). The results for an unchirped ( $a = 0$ ) 40 fs input pulse are shown in (a). In comparison to Fig. 6.16 (a), the transmitted pulse through the 50 nm spectrally flat optical pumping window passes nearly unchanged. The plot of the amplitude shows that the majority of the input pulse's energy is transmitted due to the low reflectance of the pump window, and it remains contained in a single broadened 50 fs packet. A very slight amount of ringing is observed on the trailing edge of the pulse. The time-dependent carrier frequency (circles),  $\omega(t)$ , varies linearly across the pulse with a slight negative slope. The constant carrier frequency across the input pulse is shown by the solid flat line marked with x's. The linear negative sloping dependence of the transmitted pulse's carrier frequency indicates the presence of negative GVD as foretold by Fig. 6.11. Thus, by adding an upward chirp to the input pulse (as would be obtained by propagating through glass), the output pulse can be compressed to a shorter duration.<sup>5</sup> Simulation results for input chirp

<sup>5</sup>In the limit of these simulations, this is true. Nonlinear and catastrophic pulse breakdown effects, however, have not been considered.

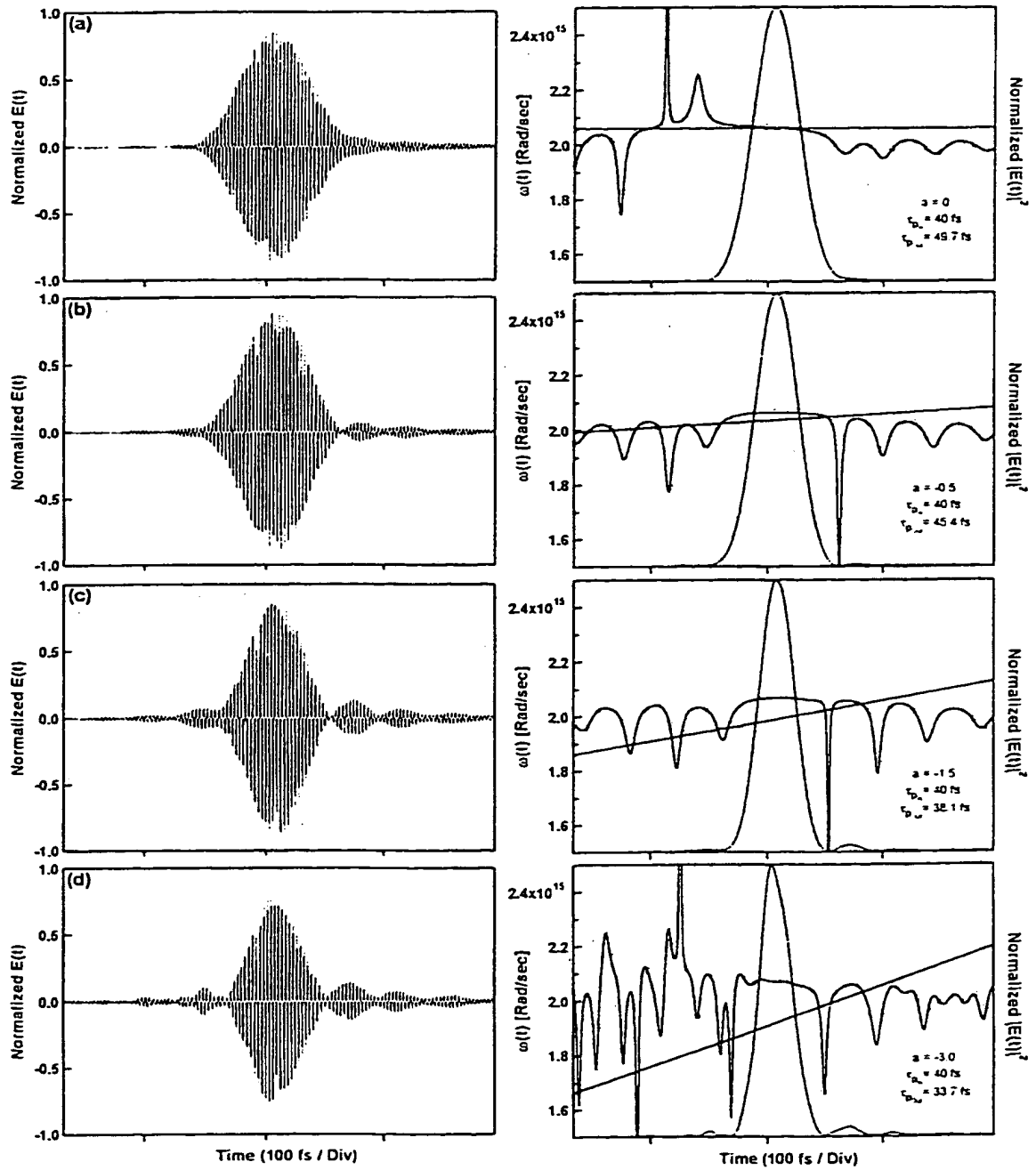


Figure 6.17: Plots of the electric field amplitude, intensity, and time dependent carrier frequency for a 40 fs pulse transmitted through the low-ripple structure at a center wavelength of 915 nm with various chirp parameters: (a)  $a=0$ , (b)  $a=-0.5$ , (c)  $a=-1.0$ , and (d)  $a=-3.0$ . The electric field plots are normalized to an input pulse amplitude of 1. The intensity profiles are shown with dotted lines. The instantaneous frequency of the transmitted pulse is shown by circles and for the input pulse by x's. The markers are spaced by 100 calculation points.

parameters of -0.5, -1.5, and -3.0 are shown in Figs. 6.17 (b-d). For an input chirp of  $a = -0.5$ , the transmitted pulse is seen to shorten to 45 fs, and the carrier frequency becomes constant across the pulse. Increased chirp further compresses the pulse width to below that of the input pulse. At a value of  $a = -0.5$  the pulse is 38 fs in width and for -3.0 the pulse width is 34 fs. In all cases, the increased chirp causes the formation of satellite peaks and ringing in the trailing edge.

### 6.3 Spectrally Resolved White-Light Interferometry

#### 6.3.1 Technique

The incoherent radiation of a white light source has been described as a "poor man's" femtosecond laser (Diels, 1996). The coherence properties of white light are remarkably similar to that of femtosecond pulses. White light can be viewed as a superposition of short light pulses whose average duration determines the spectral bandwidth (Diels, 1996). Consequently, the white-light interferometric techniques developed by Albert A. Michelson in the late 1800's can be used to measure the dispersive properties of today's femtosecond optics cheaply and easily over a broad spectral range.

Using white light as a source for a Michelson interferometer, the phase difference on reflection between a reference mirror and sample structure can be measured over a spectral bandwidth of 100's of nanometers. This is carried out by dispersing the interference pattern at the output of the interferometer in either time or space. For dispersion in time, the path length of the reference arm is varied as a photodetector monitors transitions through peaks and nulls of the interference pattern. For this tech-

nique, the sample and reference mirrors must be held flat with respect to one another over the travel of the reference mirror and the lateral extent of the detector. This method has successfully been used for the measurement of the dispersion properties of water (A.G. Van Engen, 1998), dielectric mirrors (W.H. Knox, 1988), and semiconductor devices (K. Naganuma, 1991). For dispersion in space, the sample mirror is tilted around its horizontal axis to set up a cosine-varying intensity distribution that contains all spectral components. A spectrometer then spatially disperses the pattern onto a charge coupled device (CCD) camera. This technique is known as spectrally-resolved white-light interferometry and it has been used for refractive index measurements of dye solutions (C. Sainz, 1994 ) and measurements of the group delay of dielectric laser mirrors (A.P. Kovacs, 1995).

The experimental setup for the spectrally resolved white-light interferometer built for this work is shown in Fig. 6.18. The 100  $\mu\text{m}$  horizontal slit,  $S_1$ , is used to increase the spatial coherence of the tungsten halogen lamp in the vertical direction. The cylindrical lens then collimates the white light before it enters the 50/50 beam-splitter cube. A low-dispersion gold mirror on a substrate with  $\lambda/10$  flatness serves as the reference,  $M_{ref}$ . The sample under test,  $M_s$ , is mounted in the other arm of the interferometer. Both the test and reference mirrors are held in gimbal mounts to separately allow precise rotation, both vertically and horizontally. The reference mirror mount was attached to a translation stage to initially set the path lengths of both arms equal.<sup>6</sup> The beamsplitter, as well as both mirrors, was mounted to stainless

<sup>6</sup>The short coherence length of the white-light demands that the difference in path lengths is  $\lesssim 3 \mu\text{m}$ . This alignment is the most tedious and time consuming portion of the entire experiment.

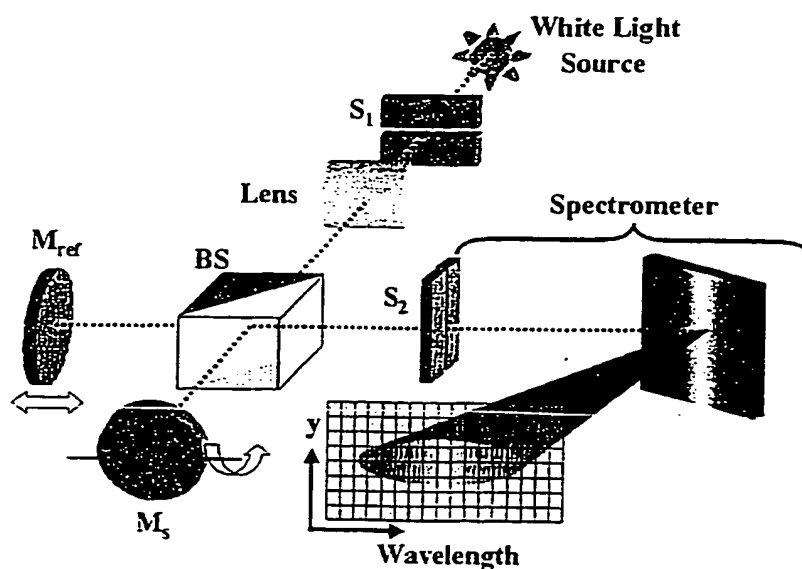


Figure 6.18: The experimental setup for the spectrally resolved white-light interferometer.

steel optical rails for stability. The interference pattern created at the output of the interferometer by slightly rotating the sample mirror about its horizontal axis is imaged and dispersed through a 0.25 m spectrometer onto a two-dimensional (800 vertical pixels by 2000 horizontal pixels) liquid-nitrogen-cooled CCD array. The slit on the input of the spectrometer,  $S_2$ , allows only a narrow vertical slice of the horizontal fringe pattern to enter. The spectral resolution of the measurement is determined by the input slit width, dispersive power of the spectrometer, and the horizontal pixel size of the CCD array. The captured image displays the variation (intensity, frequency, and phase) of the cosinusoidal intensity distribution as a function of wavelength. The dispersive properties of the sample can be determined by computer processing of this captured image.

Assuming homogeneous illumination of the interferometer by a monochro-



matic plane-wave and perfectly flat mirrors, the intensity distribution in the plane of the spectrometer entrance slit can be written as,

$$I(y, \lambda) = I_{ref}(\lambda) + I_s(\lambda) + 2\sqrt{I_{ref}(\lambda) I_s(\lambda)} \cos[\phi_{diff}(y, \lambda)], \quad (6.13)$$

where  $\lambda$  is wavelength and  $I_{ref}$  and  $I_s$  are the intensities reflected from the reference and sample mirrors, respectively. The cosine nature of the intensity distribution is a function of the phase difference between the two arms,  $\phi_{diff}$ . For the case where the two mirrors are aligned flat with respect to one another,  $\phi_{diff}$  is simply equal to the difference in the phase of the sample,  $\phi_s$ , and the phase of the reference mirror,  $\phi_{ref}$ , with no dependence on position. For the case of a small tilt around the horizontal axis of the sample mirror, as well as an inevitable slight translation,  $\phi_{diff}$  acquires two additional terms (A.P. Kovacs, 1995) dependent on position:

$$\phi_{diff}(y, \lambda) = \phi_s(\lambda) - \phi_{ref}(\lambda) + \frac{2\pi}{\lambda} 2(y - y_o)\theta, \quad (6.14)$$

where  $y$  is the vertical position along the entrance slit,  $y_o$  is the vertical offset of the sample mirror's center of rotation, and  $\theta$  is the tilt angle. In this case, the intensity varies along the  $y$  axis with a periodicity of  $\lambda/2\theta$ . The phase of the sample can not be precisely determined as  $\theta$  and  $y_o$  are not accurately known. However, to determine the group delay and GVD of the sample mirror, only the first and second derivatives of the phase with respect to angular frequency are needed (see Eq. 6.7).

The  $\phi_{diff}$  function is determined by fitting the intensity distributions along the vertical axis of the captured image, for each resolvable wavelength  $\lambda_n$ , to a cosine

function scaled with an linear dependent amplitude:

$$I_{fit}(y, \lambda_n) = \left( W_0 + W_1 \cos \left[ \frac{2\pi}{\lambda_n} y C + W_\varphi \right] \right) (W_2 y + W_3), \quad (6.15)$$

where the fitting coefficients are represented by the  $W$ 's and  $C$  is a frequency scale factor that is not permitted to vary from one wavelength slice fit to the next.<sup>7</sup> The linear dependent amplitude term  $(W_2 y + W_3)$  is needed to correct for inhomogeneities in the illumination. The phase of the fitted cosine,  $W_\varphi$ , is,

$$W_\varphi(\lambda_n) = \phi_s(\lambda_n) - \phi_{ref}(\lambda_n) - \frac{D}{\lambda_n} \quad (6.16)$$

where  $D$  is a constant phase offset experienced by all wavelengths due to  $y_o$ . A gold mirror with a nearly constant group delay is used as the reference so the  $\lambda$  dependence of  $\phi_{ref}$  can be removed from Eq. 6.16. A polynomial fit of 10 data points around  $W_\varphi(\Omega - \omega_n)$  is performed to determine the group delay and GVD via the Taylor expansion coefficients given in Eq. 6.8. This fit is performed about a shifted angular frequency  $(\Omega - \omega_n)$  where  $\omega_n$  is the angular frequency of the wavelength,  $\lambda_n$ .

The group delay and GVD of the bare interferometer can be measured by placing identical mirrors into both arms. The spectrally-resolved images recorded for the case of two gold mirrors is shown in Fig. 6.19. The intensity of the images is reduced at longer wavelengths due to the roll-off in the Si CCD's responsivity and the roll-off of the tungsten-halogen lamp in the near-infrared. The exposure time is increased for these wavelengths to enhance the signal-to-noise ratio. In the case of no dispersion, the vertical period of the interference fringes is proportional to wavelength as can be seen from Eqs. 6.13 and 6.14. Additionally, the vertical pixel position corresponding

<sup>7</sup>Allowing  $C$  to vary results in an apparent increase in the noise of the phase term  $W_\varphi$ .

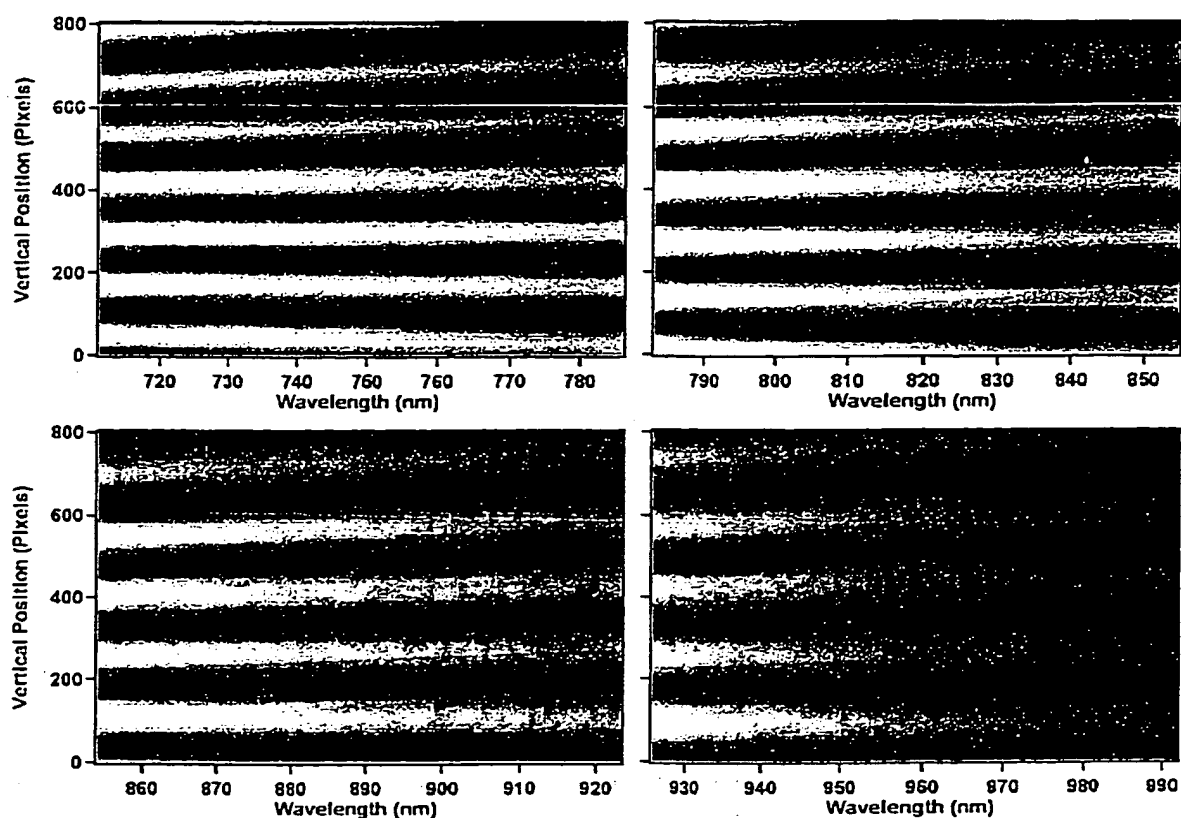


Figure 6.19: Spectrally-resolved images recorded for the bare interferometer. All scans were taken with a  $100\ \mu\text{m}$  entrance slit (1 nm res.) and the images were binned horizontally to the resolution. The top two images were recorded with exposures times of 200 ms while the bottom two were exposed for 300 ms.

Wavelength Range	Group Delay (fs)	GVD (fs <sup>2</sup> )
720-780 nm	$\pm 0.2$	$\pm 0.4$
930-990 nm	$\pm 0.3$	$\pm 1.5$

Table 6.1: Standard deviation of group delay and GVD measurements based on seven scans of the bare interferometer.

to the same phase difference is a linear function of wavelength per Eq. 6.14. This is best seen by visually tracing across in wavelength the edge of a bright fringe. The “interferograms” for the bare interferometer shows these traits as the difference in the path lengths within the beamsplitter are negligible.

The temporal resolution of the measurement is limited by the inaccuracies in the cosine function fitting. By performing seven bare interferometer runs on the gold mirrors, the standard deviation has been determined for the group delay and GVD in two wavelength ranges. The standard deviations are listed in Table 6.1. This error will be assumed for the sample measurements discussed in the next section.

### 6.3.2 Dispersion Measurements

The conventional and low-ripple cold-cavity designs discussed in section 6.2.2 were grown and their dispersion properties measured using spectrally-resolved white-light interferometry. A 2 cm square test sample was waxed to an optical flat for mounting. While MBE growth allows monolayer control of the layer thickness, the substrate on which the samples were grown have a flatness of only  $50\lambda$  across the entire 2 inch wafer.<sup>8</sup> Consequently, the sample curvature, and possibly the curvature induced by the mounting wax, result in a fringe pattern at the output of the interferometer consisting

<sup>8</sup>This was measured at a wavelength of 632.8 nm using an interferometer at the JILA laboratories by Dr. Steven Cundiff and Dr. Michael Raymer.

of nonevenly-spaced circular rings rather than evenly-spaced (in the vertical direction) horizontal lines. This observation is exactly what is used in a Twyman-Green configuration of the Michelson interferometer for the measurement of imperfections in optical elements (Fowles, 1975). To obtain group delay and GVD measurement with this fringe pattern, the horizontal alignment was adjusted so the vertical slice taken by the entrance slit of the spectrometer was directly through the middle of the circular pattern. The angle of the sample was then increased to send closely spaced fringes through the entrance slit. This allowed the higher-order nonevenly-spaced fringes to be fit with a cosine function that has a linear dependence on spatial frequency. The fitting function used is,

$$I_{fit}(y, \lambda_n) = \left( W_0 + W_1 \cos \left[ \frac{2\pi}{\lambda_n} (C_2 y^2 + C_1 y) + W_\varphi \right] \right) (W_2 y + W_3), \quad (6.17)$$

where the fitting coefficients are again represented by the  $W$ 's,  $C_1$  is now the frequency scale factor, and  $C_2$  is the added parameter which adjusts the chirp of the spatial frequency.

### Dispersion of the Conventional Cavity

The measured interferograms for the conventional cavity are shown in Fig. 6.20. Each image has been horizontally binned down to the resolution of the measurement, 1 nm. A 200 ms exposure time was used for the two shorter wavelength images and a 300 ms exposure time was used for the two longer wavelength images. The variation in the vertical spatial frequency is observable in each image. The large kinks in the fringes illustrate the variations in the reflected phase versus wavelength occurring near

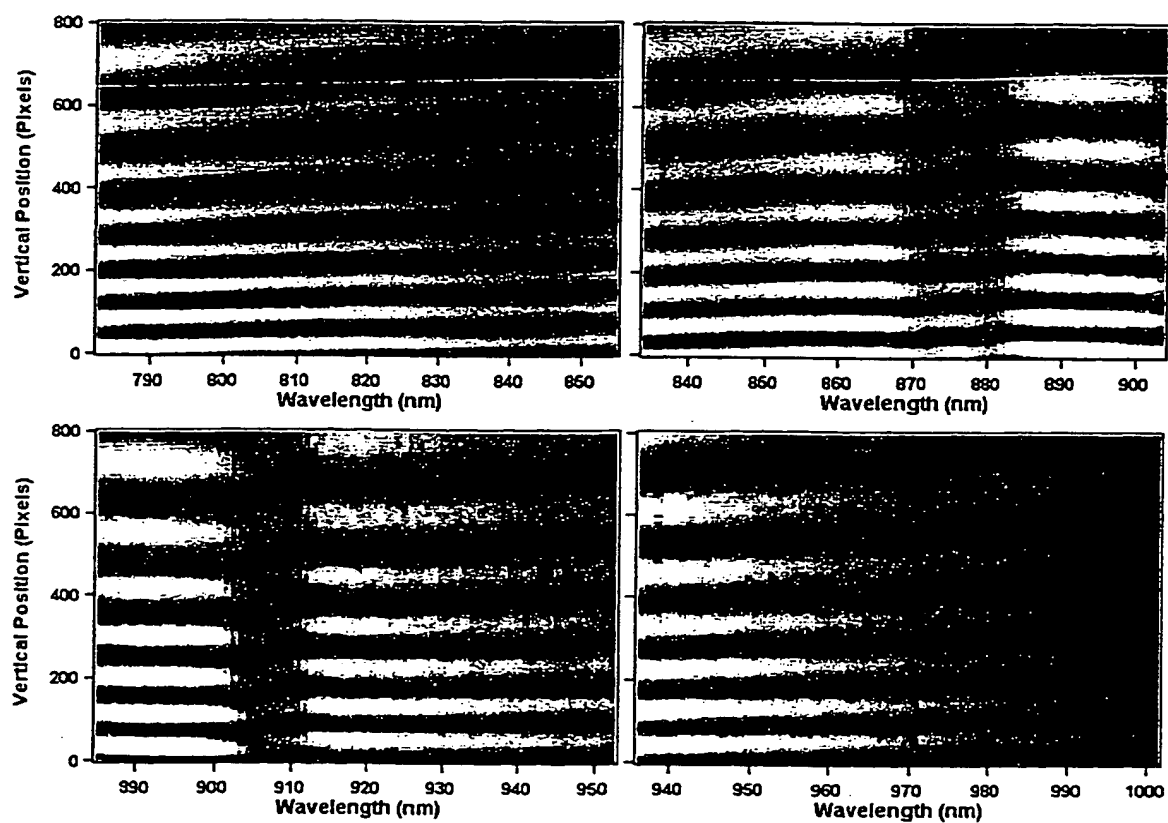


Figure 6.20: Spectrally-resolved interferogram images for the conventional cold-cavity VCSEL illustrating the variations in the reflected phase versus wavelength.

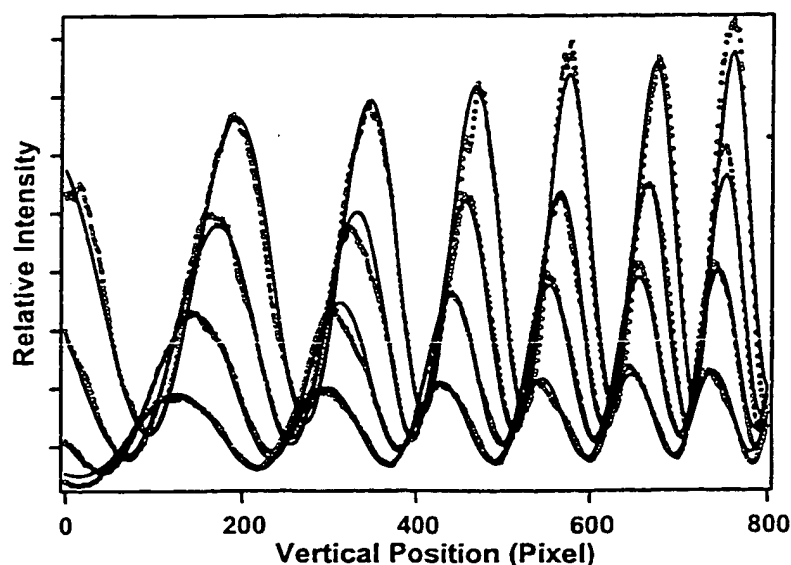


Figure 6.21: Fits to four representative vertical slices at various wavelengths across the 970 nm image of the conventional cavity. The dots represent the 800 collected data points and the solid curve is the fit to them obtained using Eq. 6.17.

the interference ripple in the sample's reflectance. The phase shift occurring at the cavity's resonance is observable near 970 nm. Fits to four representative vertical slices across the 970 nm image are shown in Fig. 6.21. The dots represent the 800 collected data points and the solid curve is the fit to them obtained using Eq. 6.17.

Through computer processing of these images as outlined in section 6.3.1, the group delay and GVD has been determined for the conventional structure. The group delay and GVD upon reflection from the sample is illustrated in Figs. 6.22 and 6.23, respectively. The measured reflectance of the structure is shown for reference in both figures by the dotted line. The cavity resonance in both plots is illustrated by the dashed line with circular markers representing points obtained for a scan with 0.5 nm resolution and a 5 point polynomial fit. The group delay in Fig. 6.22 is only the

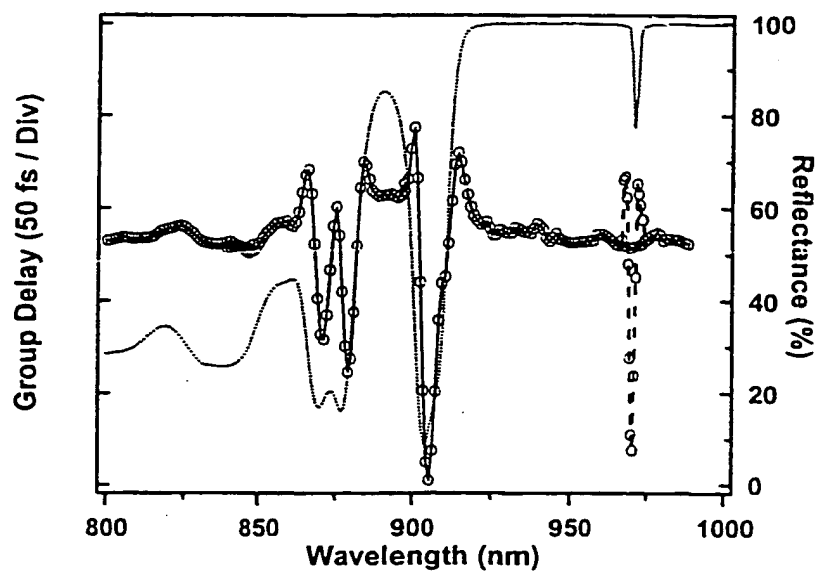


Figure 6.22: Measured group delay upon reflection from the conventional VCSEL cavity. The dotted curve represents the sample's measured reflectance.

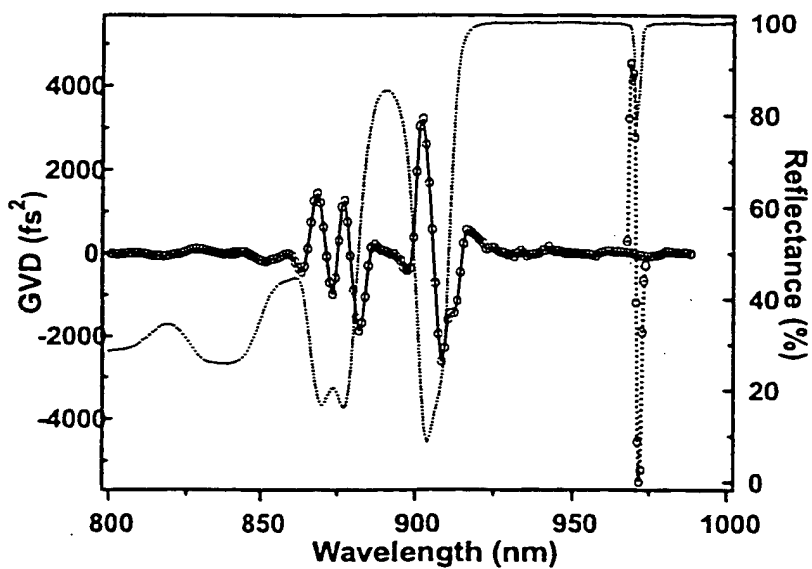


Figure 6.23: Measured GVD upon reflection from the conventional VCSEL cavity. The dotted curve represents the sample's measured reflectance.



relative group delay as the constant phase term in Eq. 6.16 adds an offset. This offset does not effect the shape of the pulse. The features of the measured group delay spectrum are very similar to the calculated results presented in Fig. 6.3. The severe oscillations present in the simulation nearest the first propagation mode, however, are not seen in the measurement. Their lack of appearance is attributed to thickness deviations throughout the growth causing a mixture of constructive and destructive interference resulting in a smoother phase function. This is confirmed by the nonzero ( $\approx 10\%$ ) reflectance minimum measured in this null. The GVD of the conventional structure also matches the features of the simulation in Fig. 6.6 with the exception of the large oscillations around the reflectance minima. The cavity resonance of the structure is somewhat resolvable in the 0.5 nm resolution scan; however, the sharp ringing surrounding it in the simulation is not. Despite the smoother phase function of the grown structure, the ultrafast optical excitation problem remains readily apparent by the  $\pm 3000 \text{ fs}^2$  variations across the desired pumping region.

### Dispersion of the Low-Ripple Cavity

The group delay and GVD upon reflection from the low-ripple sample has similarly been determined and the results are illustrated in Figs 6.24 and 6.25, respectively. The measured reflectance of the structure is shown for reference in both figures by the dotted line. The cavity resonance in both plots is again illustrated by the dashed line with circular markers representing points obtained for a scan with 0.5 nm resolution and a 5 point polynomial fit. As a result of the variations in the measured reflectance across the optical pumping window there are, as one would expect, variations in the

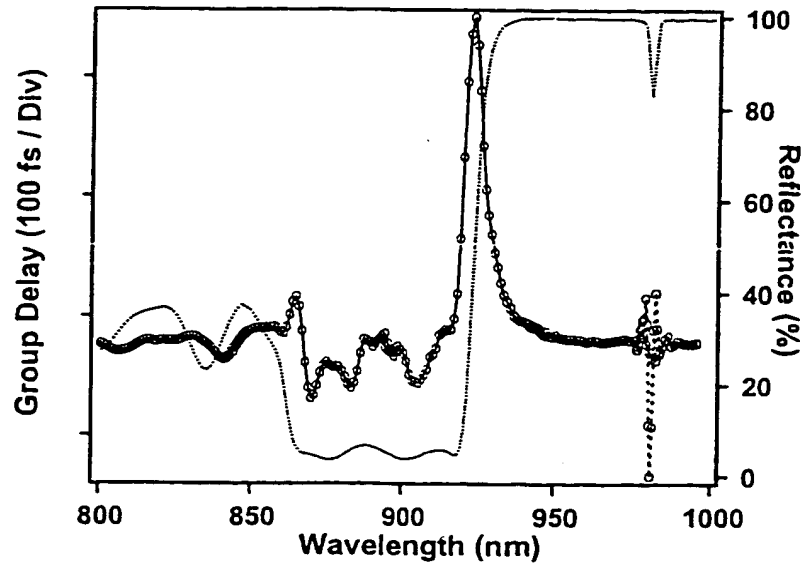


Figure 6.24: Measured group delay upon reflection from the low-ripple VCSEL cavity. The dotted curve represents the sample's measured reflectance.

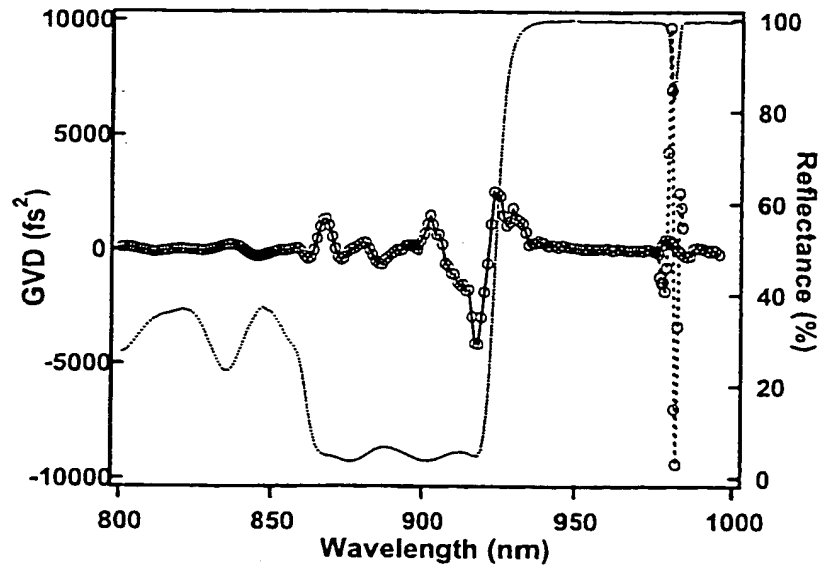


Figure 6.25: Measured GVD upon reflection from the low-ripple VCSEL cavity. The dotted curve represents the sample's measured reflectance.

measured group delay. These variations in group delay do exhibit a downward trend with decreasing wavelength as seen in the simulation of Fig. 6.4. The large  $\approx 250$  fs peak at the first mode on the short wavelength side of the high reflector is also observable and agrees well with the simulation. As a direct consequence of the variations in group delay, the measured GVD of the low-ripple structure oscillates substantially more than predicted by the simulation. The large dip ( $\gg -10,000$  fs<sup>2</sup>) of negative GVD present in the simulation is observable in the measurement but with a reduced magnitude as a result of growth errors. Despite the nonidealities of the grown structure, the GVD across a 40 nm region of the optical pumping window has been reduced by a factor of 2.5 in comparison to the conventional cavity structure.

#### 6.4 Summary

Throughout this chapter, the interaction of ultrashort pulses with semiconductor cavities has been discussed through theory, simulations, and experimental measurements. The motivation for this chapter stems out of the need for microcavities that facilitate excitation by femtosecond optical pulses. I have shown that conventional VCSEL structures severely filter the broad bandwidth of an ultrashort pulse leading to a transmitted pulse that is longer in time, chirped in frequency, and lower in intensity. By using thin-film admittance optimization techniques, microcavities can be created that have a region of nearly constant reflectivity over a 50 nm spectral band amidst the interference ripple. I have shown that this region exhibits reduced oscillations in the GVD as well as an overall negative value. Simulations of the temporal evolution of an incident pulse with a positive prechirp show that compression of the pulse's time

duration is possible. Spectrally-resolved white-light interferometry is used to measure the group delay and GVD of conventional and optimized low-ripple cavities over a spectral range of nearly 300 nm. This measurement reveals that the GVD across a 40 nm region of the optical pumping window of the low-ripple cavity is reduced by a factor of 2.5 in comparison to the conventional cavity structure. This reduced GVD will enable more accurate measurements of the carrier scattering processes in off-resonant optically pumped VCSELs through ultrafast pump-probe experiments. Furthermore, the low-ripple pump band can easily be designed with different widths and center wavelengths, providing tailored pump and probe channels in VCSELs.

## Chapter 7

### Conclusion

The work of this dissertation has been focused on enhancing the thin-film optical properties of vertical-cavity surface-emitting lasers (VCSELs). The optical admittance of VCSELs has been studied and optimized in both the longitudinal and transverse dimensions for control of incident and emitted laser radiation.

In the longitudinal dimension, I have shown that optical admittance matching in a VCSEL can be used to create a wideband window (50 nm) of constant reflectance ( $5 \pm 0.25\%$ ) in the typical interference fringe spectrum. Through this modification of the device's reflectance signature, I have improved the stability of the coupling to an optical pump source. Simultaneously, I have reduced the group velocity dispersion experienced by an incident ultrashort optical pulse. Low-ripple VCSELs are now being further pursued within industry for vertically stacked devices. It is anticipated that the reduced dispersion of these devices will impact the academic community by enabling more accurate measurement of the carrier scattering processes in off-resonant optically-pumped VCSELs.

In the transverse dimension, I have analyzed the competition of transverse modes in multimode VCSELs. I have explored the dynamic evolution of these modes

as well as their near-field spatial distributions. I have shown through experiment that spatially separated modes coexist by sharing of the available gain while spatially overlapping modes compete. The time-resolved data illustrates two dramatically different rise-times for orthogonal polarizations as the transverse mode families compete. This result has inspired industry to investigate the effects of this imposed turn-on-jitter on a system's bit-error-rate (BER). Further, this work is motivating the advancement of the state-of-the-art in VCSEL characterization through inspiring the combination of the high spectral and spatial resolution afforded by near-field scanning optical microscopy (NSOM) with time-resolved collection techniques. The spatio-spectral results presented have prompted several inquiries from industry on the construction of such a measurement system. Additionally, I have introduced a novel transverse-mode control technique and have shown through simulations that high-order transverse modes can be suppressed to a current of several times threshold in a 30  $\mu\text{m}$  diameter device using an out-of-phase reflection from an aluminum layer atop the semiconductor distributed Bragg reflector (DBR). It is possible that higher-power large-area single-mode VCSELs can be created using this admittance tailoring technique.

The native oxide technologies demonstrated in this dissertation are applicable to admittance optimization in both the longitudinal and transverse dimensions. The technologies I have discussed have impacted the mainstream optoelectronic community. I have reported the first measurements of the dispersion of the oxide's refractive index. This data is contributing to a better understanding of the oxide and will aid in the development of high-contrast DBRs, embedded microlenses, birefringent waveguides, and

photonic lattices. This report has also been important within this work for the development of native-oxide antireflection (AR) coatings for integration on vertical-cavity devices. I have shown using conventional admittance matching techniques that high-quality ( $<0.5\%$  reflectance), broad-bandwidth ( $<1\%$  over 250 nm) AR coatings can be designed and fabricated using native oxides. These coatings reduce manufacturing complexities and promote integration with oxide current apertures. Additionally, I have investigated the use of oxide apertures in the transverse dimension to form intra-cavity lenses. The lateral phase distribution of these apertures was derived and their diffraction losses were quantified through Fox and Li calculations.

The surface and buried oxide layers discussed can be incorporated into a VCSEL to provide a spatially-dependent phase shift. This phase shift can be used in the proposed method of transverse mode control. This effective lens can be equivalently viewed as adding a curvature to one of the cavity's DBRs, as introduced in the confocal VCSEL discussion. It is then clear that native-oxide confined VCSELs inherently have an adjustable method of mode control. Near-field studies using NSOM on similar devices with varying numbers and positions of oxide apertures are anticipated to reveal this control. Furthermore, the admittance optimization presented in the longitudinal dimension is not truly independent of the transverse dimension. By optimizing the layer thicknesses of the VCSEL's DBRs, the angular response of the mirror's reflectance has been altered. Thus, the higher-order modes traveling more "off-axis" are anticipated to see a different reflectance than the "on-axis" lower-order modes. A complete vectorial eigenmode calculation (D. Burak<sup>b</sup>, 1997) of the optimized structure is expected to

indicate a different transverse mode distribution from that of a conventional structure (Burak<sup>a</sup>, 1997).

The vast amount of research to date on VCSELs has been centered around the electrical aspects of the device. Now that low threshold voltages and currents are commonplace, more effort will be devoted to refining its optics. Through further studies and tailoring of a VCSEL's unique and flexible admittance structure, lower threshold devices operating at higher powers and faster modulation rates will reach fruition.



## Bibliography

- Afromovitz, M. A. (1974). "Refractive index of  $\text{Ga}(1-x)\text{Al}(x)\text{As}$ ." Solid State Commun. 15(1): 59-63.
- Agoston, G. A. (1987). Color Theory and Its Application in Art and Design. New York, Springer-Verlag.
- Ashby, C. I. H., J. P. Sullivan, K. D. Choquette, K. M. Geib and H. Q. Hou (1997). "Wet oxidation of  $\text{AlGaAs}$ : the role of hydrogen." J. Appl. Phys. 82(6): 3134-3136.
- Aspnes, D. E., J. B. Theeten and F. Hottier (1979). "Investigation of effective-medium models of microscopic surface roughness by spectroscopic ellipsometry." Phys. Rev. B. 20(8): 3292-3302.
- Babic, D. I. (1995). Double-fused long-wavelength vertical-cavity lasers. Electrical and Computer Engineering. Santa Barbara, University of California Santa Barbara.
- Babic, D. I. and S. W. Corzine (1992). "Analytic expressions for the reflection delay, penetration depth, and absorptance of quarter-wave dielectric mirrors." IEEE J. Quantum Electron. 28(2): 514-524.
- Babic, D. I., J. J. Dudley, K. Streubel, R. P. Mirin, E. L. Hu and J. E. Bowers (1994). "Optically pumped all-epitaxial wafer-fused 1.52 mm vertical-cavity lasers." Electron. Lett. 30(9): 704-705.
- Babic, D. I., R. P. Mirin, E. L. Hu and J. E. Bowers (1996). "Characterization of metal mirror on  $\text{GaAs}$ ." Electron. Lett. 32(4): 319-320.
- Bacher, K., B. Pezeshki, S. M. Lord and J. S. Harris (1992). "Molecular beam epitaxy growth of vertical cavity optical devices with in-situ corrections." Appl. Phys. Lett. 61(12): 1387-1389.
- Bardinal, V., R. Legros and C. Fontaine (1995). "Precision Bragg reflectors obtained by molecular beam epitaxy under in situ tunable dynamic reflectometry control." Appl. Phys. Lett. 67(23): 3390-3392.
- Bek, A., A. Aydinli, J. G. Champlain, R. Naone and N. Dagli (1999). "A study of wet oxidized  $\text{AlGaAs}$  for integrated optics." IEEE Photon. Technol. Lett. 11(4): 436-438.
- Bennett, H. E. and J. O. Porteus (1961). "Relation between surface roughness and specular reflectance at normal incidence." J. Opt. Soc. Am. 51(2): 123-129.
- Betzig<sup>a</sup>, E., P. L. Finn and J. S. Weiner (1992). "Combined shear force and near-field scanning optical microscopy." Appl. Phys. Lett. 60: 2484-2486.
- Betzig<sup>b</sup>, E. and J. K. Trautman (1992). "Near field optics - microscopy, spectroscopy, and surface modification beyond the diffraction limit." Science 257(5067): 189-195.

Born, M. and E. Wolf (1980). Principles of Optics. New York, Pergamon.

Buccafusca, O., J. L. A. Chilla, J. J. Rocca, P. Brusenbach and J. Martin-Regalado (1999). "Transient response of vertical-cavity surface-emitting lasers of different active-region diameters." IEEE J. Quantum. Electron. 35(4): 608-614.

Burak<sup>a</sup>, D. (1997). Personal Communication.

Burak<sup>b</sup>, D. and R. Binder (1997). "Cold-cavity vectorial eigenmodes of VCSELs." IEEE J. Quantum. Electron. 33(7): 1205-1215.

Casey, H. C., D. D. Sell and K. W. Wecht (1975). "Concentration dependence of the absorption coefficient for n- and p-type GaAs between 1.3 and 1.6 eV." J. Appl. Phys. 46(1): 250-257.

Chand, N. and R. F. Karlicek (1993). "Real-time monitoring and analysis of chemical wet etching of III-V compound semiconductors." J. Electrochemical Soc. 140(3): 703-705.

Chang-Hasnain, C. J., M. Orenstein, A. V. Lehman, L. T. Florez, J. P. Harbison and N. G. Stoffel (1990). "Transverse mode characteristics of vertical-cavity surface-emitting lasers." Appl. Phys. Lett. 57: 218-220.

Chilla, J., B. Benware, M. Watson, P. Stanko, J. Rocca, C. Wilmsen, S. Feld and R. Leibenguth (1995). "Coherence of VCSEL's for holographic interconnects." IEEE Photon. Technol. Lett. 7(5): 449-451.

Chin, A. K., G. Zydzik, S. Singh, L. G. V. Uitert and G. Minneci (1983). "Al<sub>2</sub>O<sub>3</sub> as an antireflection coating for InP/InGaAsP LEDs." J. Vac. Sci. Technol. B 1(1): 72-73.

Choquette, K. D., K. M. Geib, C. I. H. Ashby, R. D. Twisten, O. Blum, H. Q. Hou, D. M. Follstaedt, B. E. Hammons, D. Mathes and R. Hull (1997). "Advances in selective wet oxidation of AlGaAs alloys." IEEE J. Sel. Tpcs. Quantum Electron. 3(3): 916-926.

Christensen, D. H., J. G. Pelligrino, R. K. Hickernell, S. M. Crochiere, C. A. Parsons and R. S. Rai (1992). "Characterization of vertical-cavity semiconductor structures." J. Appl. Phys. 72(12): 5982-5989.

Chua, C. L., R. L. Thorton and D. W. Treat (1997). "Planar laterally oxidized vertical-cavity lasers for low-threshold high-density top-surface-emitting arrays." IEEE Photon. Technol. Lett. 9(8): 1060-1062.

Coldren, L. A. and S. W. Corzine (1995). Diode Lasers and Photonic Integrated Circuits. New York, Wiley.

Collings, B. C., K. Bergman, S. T. Cundiff, S. Tsuda, J. N. Kutz, J. E. Cunningham, W. Y. Jan, M. Koch and W. H. Knox (1997). "Short-cavity erbium/ytterbium fiber lasers mode-locked with a saturable Bragg reflector." IEEE J. Sel. Tpcs. Quantum Electron. 3(4): 1065-1075.

Corzine, S. W. (1993). Design of vertical-cavity surface-emitting lasers with strained and unstrained quantum well active regions. Electrical and Computer Engineering. Santa Barbara, University of California Santa Barbara.

Corzine, S. W., R. S. Geels, J. W. Scott, R. H. Yan and L. A. Coldren (1989). "Design of Fabry-Perot surface-emitting lasers with a periodic gain structure." IEEE J. Quantum Electron. 25(6): 1513-1523.

Corzine, S. W., R. H. Yan and L. A. Coldren (1991). "A Tanh substitution technique for the analysis of abrupt and graded interface multilayer dielectric stacks." IEEE J. Quantum Electron. Lett. 27(9): 2086-2090.

Dallesasse<sup>a</sup>, J. M., N. El-Zein, N. Holonyak and K. C. Hsieh (1990). "Environmental degradation of AlGaAs-GaAs quantum -well heterostructures." J. Appl. Phys. 68(5): 2235-2238.

Dallesasse, J. M. and N. Holonyak (1991). "Native-oxide stripe-geometry Al(x)Ga(1-x)As-GaAs quantum-well heterostructure lasers." Appl. Phys. Lett. 58(4): 394-396.

Dallesasse<sup>b</sup>, J. M., N. Holonyak, A. R. Sugg, T. A. Richard and El-Zein (1990). "Hydrolyzation oxidation of Al(x)Ga(1-x)As-AlAs-GaAs quantum-well heterostructures and superlattices." Appl. Phys. Lett. 57(26): 2844-2846.

Diels, J.-C. and W. Rudolph (1996). Ultrashort Laser Pulse Phenomena. San Diego, Academic Press, Inc.

Docter, D. P., J. P. Ibbetson, Y. Gao, U. K. Mishra, T. Liu and D. E. Grider (1998). "Analysis of V/III incorporation in nonstoichiometric GaAs and InP films using SIMS." J. Electron. Mat. 27(5): 479-483.

Dowd, P., L. Raddatz, Y. Sumaila, M. Asghari, I. H. White, P. J. Heard, G. C. Allen, R. P. Schneider, M. R. T. Tan and S. Y. Wang (1997). "Mode control in vertical-cavity surface-emitting lasers by post processing using focused ion-beam etching." IEEE Photon. Tech. Lett. 9(9): 1193-1195.

Ebeling, K. J. and T. Hackbarth (1991). "Analysis of vertical cavity surface emitting semiconductor lasers." Frequenz 45(9): 207-212.

Engen, A. G. V., S. A. Diddams and T. S. Clement (1998). "Dispersion measurements of water with white-light interferometry." Appl. Opt. 37(24): 5679-5686.

Epstein, L. I. (1952). "The design of optical filters." J. Opt. Soc. Amer. 42(11): 806-810.  
Fink, Y., J. N. Winn, S. Fan, C. Chen, J. Michel, J. D. Joannopoulos and E. L. Thomas (1998). "A dielectric omnidirectional reflector." Science 282(5394): 1679-1682.

Fisher, M. A., A. J. Dann, D. A. O. Davies, D. J. Elton, M. J. Harlow, C. B. Hatch, S. D. Perrin, J. Reed, I. Reid and M. J. Ada (1993). "High temperature photopumping of 1.55  $\mu\text{m}$  vertical cavity surface emitting lasers." Electron. Lett. 29(17): 1548-1550.

Floyd, P. D., B. J. Thibeault, L. A. Coldren and J. L. Merz (1996). "Scalable etched-pillar, AlAs-oxide defined vertical cavity lasers." Electron. Lett 32(2): 114-116.

Fowles, G. R. (1975). Introduction to Modern Optics. New York, Holt, Rinehart, and Winston, Inc.

Fox, A. G. and T. Li (1961). "Resonant modes in a maser interferometer." Bell Sys. Tech. J. 40: 453-488.

Funk, D. S., D. L. Veasey, P. M. Peters, N. A. Sanford, N. H. Fontaine, M. Young and J. S. Hayden (1999). Erbium/Ytterbium co-doped glass waveguide laser producing 170 mW of output power at 1540 nm. Proceedings of the Fourteenth OSA Topical Meeting on Advanced Solid-State Lasers.

Geels, R. S., S. W. Corzine, J. W. Scott, D. B. Young and L. A. Coldren (1990). "Low threshold planarized vertical-cavity surface-emitting lasers." IEEE Photon. Technol. Lett. 2(4): 234-236.

Gerber, D. S. and G. N. Maracas (1993). "A simple method for extraction of multiple-quantum-well absorption-coefficient from reflectance and transmittance measurements." IEEE J. Quant. Elect. 29(10): 2589-2595.

Giaretta, G., M. Y. Li, G. S. Li, W. P. Yuen and C. J. Chang-Hasnain (1997). "A novel 4x8 single-mode independently addressable oxide-isolated VCSEL array." IEEE Photon. Tech. Lett. 9(9): 1196-1198.

Goldberg, B. B., M. S. Ünlü, W. D. Herzog and E. Towe (1995). "Near field optical microscopy and spectroscopy of heterostructures and laser diodes." IEEE J. Sel. Tpcs. Quantum Electron. 1(4): 1073-1081.

Gunter, J. K., R. A. Hawthorne, D. N. Granville, M. K. Hibbs-Brenner and R. A. Morgan (1996). "Reliability of proton-implanted VCSELs for data communications." Proc. SPIE 2683: 102-113.

Gupta, S., M. Y. Frankel, J. A. Valdmanis, J. F. Whitaker, G. A. Mourou, F. W. Smith and A. T. Calawa (1991). "Subpicosecond carrier lifetime in GaAs grown by molecular beam epitaxy at low temperatures." Appl. Phys. Lett. 59(25): 3276-3278.

Hadley, G. R. (1995). "Effective-index model for vertical-cavity surface-emitting lasers." Opt. Lett. 20(13): 1483-1485.

Hadley, G. R., K. L. Lear, M. E. Warren, K. D. Choquette, J. W. Scott and S. W. Corzine (1996). "Comprehensive numerical modeling of vertical-cavity surface-emitting lasers." IEEE J. Quantum Electron 32(4): 607-661.

Hahn, K. H., M. R. Tan, Y. M. Houn and S. Y. Wang (1993). "Large area multitransverse-mode VCSELs for modal noise reduction in multimode fibre systems." Electron. Lett. 29(16): 1482-1483.

Hall, D. C. (1999). Personal Communication.

Heavens, O. S. (1954). "All-dielectric high reflecting layers." J. Opt. Soc. Amer. 44(5): 371-373.

Hegblom, E. R., D. I. Babic, B. J. Thibeault and L. A. Coldren (1996). "Estimation of scattering losses in dielectrically apertured vertical cavity lasers." Appl. Phys. Lett. 68(13): 1757-1759.

Heinzen, D. J., J. J. Childs, J. E. Thomas and M. S. Feld (1987). "Enhanced and inhibited visible spontaneous emission by atoms in a confocal resonator." Phys. Rev. Lett. 58(13): 187-190.

Heppner, J. and J. Kuhl (1985). "Intracavity chirp compensation in a colliding pulse mode-locked laser using thin-film interferometers." Appl. Phys. Lett. 47(5): 453-455.

Hill, D. E. (1964). "Infrared transmission and fluorescence of doped gallium arsenide." Phys. Rev. 133(3A): A866-A872.

Houdre, R., J. L. Gibernon, P. Pellandini, R. P. Stanley, U. Oesterle, C. Weisbuch, J. O'Gorman, B. Roycroft and M. Illegems (1995). "Saturation of the strong-coupling regime in a semiconductor microcavity: Free-carrier bleaching of cavity polaritons." Phys. Rev. B 52(11): 7810-7813.

Houng, Y. M., M. R. T. Tan, B. W. Liang, S. Y. Wang and D. E. Mars (1994). "In-situ thickness monitoring and control for highly reproducible growth of distributed Bragg reflectors." J. Vac. Sci. Technol. B 12(2): 1221-1223.

Huffaker<sup>a</sup>, D. L., D. G. Deppe, K. Kumar and T. J. Rogers (1994). "Native-oxide defined ring contact for low-threshold vertical-cavity lasers." Appl. Phys. Lett. 65(1): 97-99.

Huffaker<sup>b</sup>, D. L., J. Shin and D. G. Deppe (1994). "Low threshold half-wave vertical-cavity lasers." Electron. Lett. 30(23): 1946-1947.

Ibbetson, J. P. (1998). Personal Communication.

Jackson, J. D. (1975). Classical Electrodynamics. New York, John Wiley and Sons.

Jacobson, J., S. Pau, H. Cao, G. Bjork and Y. Yamamoto (1994). "Observation of exciton-polariton oscillating emission in a single-quantum-well semiconductor microcavity." Phys. Rev. A 51(3): 2542-2544.

Jeon, H., V. Kozlov, P. Kelkar, A. V. Nurmikko, C. C. Chu, D. C. Grillo, J. Han, G. C. Hua and R. L. Gunsh (1995). "Room-temperature optically pumped blue-green vertical cavity surface emitting laser." Appl. Phys. Lett. 67(12): 1668-1670.

Jewell, J. L., J. P. Harbison, A. Scherer, Y. H. Lee and L. T. Florez (1991). "Vertical-cavity surface-emitting lasers: design, growth, fabrication, characterization." IEEE J. Quantum Electron. 27(6): 1332-1346.

Jewell, J. L., A. Scherer, S. L. McCall, Y. H. Lee, S. Walker, J. P. Harbison and L. T. Florez (1989). "Low-threshold electrically pumped vertical-cavity surface-emitting microlasers." Electron. Lett. 25(17): 1123-1124.

John, S. (1987). "Strong localization of photons in certain disordered dielectric superlattices." Phys. Rev. Lett. 58(23): 2486-2489.

Johs, B., C. M. Herzinger, J. H. Dinan, A. Cornfeld and J. D. Benson (1998). "Development of a parametric optical constant model for  $\text{Hg}(1-x)\text{Cd}(x)\text{Te}$  for control of composition by spectroscopic ellipsometry during MBE growth." Thin Solid Films 313: 137-142.

Karrai, K. and R. D. Grober (1995). "Piezo-electric tip-sample distance control for near field optical microscopes." Appl. Phys. Lett. 66(14): 1842-1844.

Keller, U., K. J. Weingarten, F. X. Kärtner, D. Kopf, B. Braun, I. D. Jung, R. Fluck, C. Hönniger, N. Matuschek and J. A. d. Au (1996). "Semiconductor saturable absorber mirrors (SESAM's) for femtosecond to nanosecond pulse generation in solid-state lasers." IEEE J. Sel. Tpcs. Quantum Electron. 2(3): 435-451.

Knopp<sup>a</sup>, K. J., D. H. Christensen and J. R. Hill (1996). "Vertical-cavity surface-emitting lasers with low-ripple optical pump bands." Appl. Phys. Lett. 69(26): 3987-3989.

Knopp<sup>a</sup>, K. J., D. H. Christensen and J. R. Hill (1997). "Vertical-Cavity Surface-Emitting Lasers with Low-Ripple Optical Pumping Windows." IEEE J. Sel. Tpcs. Quantum. Electron. 3(2): 366-371.

Knopp<sup>b</sup>, K. J., D. H. Christensen, J. R. Hill and K. A. Bertness (1996). Vertical-cavity surface emitters with low-ripple optical pump bands. 54th IEEE Device Research Conference, University of California., Santa Barbara, CA.

Knopp<sup>a</sup>, K. J., D. H. Christensen, G. V. Rhodes, J. M. Pomeroy, B. B. Goldberg and M. S. Ünlü (1999). "Spatio-spectral mapping of multimode vertical-cavity surface-emitting lasers." to appear in IEEE J. Lightwave Tech. to appear August 1999.

Knopp<sup>b</sup>, K. J., D. H. Christensen, G. V. Rhodes, J. M. Pomeroy, B. B. Goldberg and M. S. Ünlü (1999). Spectral mapping of multimode VCSELs by near-field scanning optical microscopy. Photonics West, San Jose, CA.

Knopp<sup>a</sup>, K. J., J. R. Ketterl, D. H. Christensen, T. P. Pearsall and J. R. Hill (1997). "Simultaneous monitoring of wafer- and environment-states during molecular beam epitaxy." Mat. Res. Soc. Symp. Proc. 441: 761-766.

Knopp<sup>a</sup>, K. J., R. P. Mirin, K. A. Bertness, A. Roshko and D.H.Christensen (1998). Optical properties of native-oxide antireflection coatings on GaAs. TMC Electronics Materials Conference, University of Virginia, Charlottesville, VA.

Knopp<sup>c</sup>, K. J., R. P. Mirin, K. A. Bertness, K. L. Silverman and D. H. Christensen (1999). "Compound Semiconductor Oxide Antireflection Coatings." Submitted to IEEE J. Quantum Electron.

Knopp<sup>b</sup>, K. J., R. P. Mirin, D. H. Christensen, K. A. Bertnesss, A. Roshko and R. A. Synowicki (1998). "Optical constants of  $(\text{Al}_{0.98}\text{Ga}_{0.02})\text{xOy}$  native oxides." Appl. Phys. Lett. 73(24): 3512-3514.

Knox, W. H., N. P. Pearson, K. D. Li and C. A. Hirlimann (1988). "Interferometric measurements of femtosecond group delay in optical components." Opt. Lett. 13(7): 574-576.

Kopf, D., G. Zhang, R. Fluck, M. Moser and U. Keller (1996). "All-in-one dispersion-compensating saturable absorber mirror for compact femtosecond laser sources." Opt. Lett. 21(7): 486-488.

Kovacs, A. P., K. Osvay, Z. Bor and R. Szipocs (1995). "Group-delay measurment on laser mirrors by spectrally resolved white-light interferometry." Opt. Lett. 20(7): 788-790.

Koyama, F., S. Kinoshita and K. Iga (1988). "Room temperature CW operation of GaAs vertical-cavity surface-emitting laser." Trans. IEICE E71(11): 1089-1090.

Koyama, F., S. Kinoshita and K. Iga (1989). "Room-temperature continuous-wave lasing characteristics of a GaAs vertical-cavity surface-emitting laser." Appl. Phys. Lett. 55(3): 221-222.

Kuksenkov, D. V., H. Temkin and S. Swirhun (1995). "Polarization instability and relative intensity noise in vertical cavity surface emitting lasers." Appl. Phys. Lett. 67: 2141-2143.

Lear, K. L., K. D. Choquette, R. P. Schneider and S. P. Kilcoyne (1995). "Modal-analysis of a small surface-emitting laser with a selectively oxidized wave-guide." Appl. Phys. Lett. 66(20): 2616-2618.

Leonhardt, U., M. Munroe, T. Kiss, T. Richter and M. G. Raymer (1996). "Sampling of photon statistics and density matrix using homodyne detection." Optics Communication 127(1-3): 144-160.

Loong, W. A. and H. L. Chaung (1991). "Oxidation of GaAs surface by oxygen plasma and its application as an antireflection layer." Jpn. J. Appl. Phys. Lett. 30(7B): L1319-L1320.

MacDougal, M. H., P. D. Dapkus, A. E. Bond, C. K. Lin and J. Geske (1997). "Design and fabrication of VCSELs with  $\text{AlxOy}$ -GaAs DBR's." IEEE J. Sel. Tpcs. Quantum Electron. 3(3): 905-915.

MacDougal, M. H., H. Zhao, P. D. Dapkus, M. Ziari and W. H. Steier (1994). "Wide-bandwidth distributed Bragg reflectors using oxide GaAs multilayers." Electron. Lett. 30(14): 1147-1149.

Macleod, H. A. (1969). Thin-Film Optical Filters. New York, American Elsevier.

Matuschek, N., F. X. Kartner and U. Keller (1998). "Theory of douple chirped mirrors." IEEE J. Sel. Tpcs. Quant. Electron. 4(2): 197-208.

Melngailis, I. (1965). "Longitudinal Injection-Plasma Laser of InSb." Appl. Phys. Lett. 6(3): 49-50.

Mickelson, A. (1992). Physical Optics. New York, Van Nostrand Reinhold.

Milster, T., W. Jiang, E. Walker, D. Burak, P. Claisse, P. Kelly and R. Binder (1998). "A Single-Mode High-Power Vertical Cavity Surface Emitting Laser." Appl. Phys. Lett. 72(26): 3425-3427.

Mirin, R. P. and R. A. Synowicki (1998). Personal Communication.

Morgan, R. A., G. D. Guth, M. W. Focht, M. T. Asom, K. Kojima, L. E. Rogers and S. E. Callis (1993). "Transverse mode control of vertical-cavity top-surface-emitting lasers." IEEE Photon. Tech. Lett. 4(4): 374-377.

Morgan, R. A. and M. K. Hibbs-Brenner (1995). "Vertical-cavity surface-emitting laser arrays." Proc. SPIE 2398: 65-90.

Morozov, V. N., J. A. Neff and H. Zhou (1997). "Analysis of vertical-cavity surface-emitting laser multimode behavior." IEEE J. Quantum Electron. 33(6): 980-988.

Munroe, M., K. J. Knopp and D. H. Christensen (1997). Ultrafast Optical Excitation of Vertical-Cavity Surface-Emitting Lasers. Quantum Electronics and Laser Science Conference (QELS), Baltimore, MD.

Naganuma, K. and H. Yasaka (1991). "Group delay and alpha-parameter measurement of 1.3 $\mu$ m semiconductor traveling-wave optical amplifier using the interferometric method." IEEE J. Quantum Electron. 27(6): 1280-1287.

Naone, R. L., E. R. Hegblom, B. J. Thibeault and L. A. Coldren (1997). "Oxidation of AlGaAs layers for tapered apertures in vertical-cavity lasers." Electron. Lett. 33(4): 300-301.

Norris, T. B., J. K. Rhee, C. Y. Sung, Y. Arakawa, M. Nishioka and C. Weisbuch (1994). "Time-resolved vacuum Rabi oscillations in a semiconductor quantum microcavity." Phys. Rev. B 50(19): 14 663 - 14 666.

Ochiai, M., G. E. Giudice, H. Temkin, J. W. Scott and T. M. Cockerill (1996). "Kinetics of thermal oxidation of AlAs in water vapor." Appl. Phys. Lett. 68(14): 1898-1900.

Ogura, M., T. Hata, Naoyuki, J. Kawai and T. Yao (1983). "GaAs/Al(x)Ga(1-x)As multilayer reflector for surface emitting laser diode." Jpn. J. Appl. Phys. 22(2): L112-L114.

Ogura, M., W. Hsin, M.-C. Wu, S. Wang, J. R. Whinnery, S. C. Wang and J. J. Yang (1987). "Surface-emitting laser diode with vertical GaAs/GaAlAs quarter-wavelength multilayer and lateral buried heterostructure." Appl. Phys. Lett. 51(21): 1655-1657.

Othonos, A. (1998). "Probing ultrafast carrier and phonon dynamics in semiconductors." J. Appl. Phys. 83(4): 1789-1830.



- Palik, E. D. (1985). Handbook of Optical Constants of Solids. San Diego, Academic Press.
- Pankove, J. I. (1963). Laser Structures. RCA Patent Disclosure, Radio Corporation of America (RCA).
- Peterman, K. (1988). Laser Diode Modulation and Noise. Norwell, MA, Kluwer Academic Publishers.
- Peters, M. (1995). Molecular beam epitaxy growth of vertical-cavity lasers for optical communications. Electrical and Computer Engineering. Santa Barbara, University of California Santa Barbara.
- Press, W., S. Teukolsky, W. Vetterling and B. Flannery (1988). Numerical Recipes in C. New York, Cambridge University Press.
- Purcell, E. M. (1946). Spontaneous emission probabilities at radio frequencies. Proceedings of the American Physical Society, Hamilton, New York.
- Rhodes, G. H. V., K. J. Knopp, J. M. Pomeroy, H. Ulu, M. S. Unlu, B. B. Goldberg and D. H. Christensen (1998). "Pump intensity profiling of vertical-cavity surface-emitting lasers using near-field scanning optical microscopy." Appl. Phys. Lett. 72(15): 1811-1813.
- Rodney, W. S. and R. J. Spindler (1954). "Index of refraction of fused-quartz glass for ultraviolet, visible, and infrared wavelengths." J. Res. Nat. Bur. Stand. 53: 185-189.
- Sainz, C., P. Jourdain, R. Escalona and J. Calatroni (1994). "Real-time interferometric measurements of dispersion-curves." Opt. Commun. 110(3-4): 381-390.
- Schaafsma, D. T. and D. H. Christensen (1995). "Cross-sectional photoluminescence and its application to buried-layer semiconductor structures." J. Appl. Phys. 78(2): 694-699.
- Schubert, E. F., M. Passlack, M. Hong, J. Mannerts, R. L. Opila, L. N. Pfeiffer, K. W. West, C. G. Bethea and G. J. Zydzik (1994). "Properties of Al<sub>2</sub>O<sub>3</sub> optical coatings on GaAs produced by oxidation of epitaxial AlAs/GaAs films." Appl. Phys. Lett. 64(22): 2976-2978.
- Schuster, K. (1949). "Anwendung der vierpoltheorie auf die probleme der optischen reflexionsminderung, reflexionsverstarkung, und der interferenzfilter." Ann. Phys. 4(6): 352-356.
- Scott, J. W., R. S. Geels, S. W. Corzine and L. A. Coldren (1993). "Modeling of temperature effects and spatial hole burning to optimize vertical-cavity surface-emitting laser performance." IEEE J. Quantum. Electron. 29(5): 1295-1308.
- Shi, Z., H. Zogg and U. Keller (1998). "Thick crack-free CaF<sub>2</sub> epitaxial layer on GaAs (100) substrate by molecular beam epitaxy." J. Electron. Mat. 27(2): 55-58.
- Shiffman, B. (1999). Communication at NFOEC '98 via David L. Veasey.
- Siegman, A. E. (1977). "Quasi fast Hankel transform." Opt Lett. 1(1): 13-15.

Siegman, A. E. (1986). Lasers. Sausalito, CA, University Science Books.

Soda, H., K. Iga, C. Kitahara and Y. Suematsu (1979). "GaInAsP/InP surface emitting injection lasers." Jpn. J. Appl. Phys. 18(12): 2329-2330.

Stanley, R. P., R. Houdr'e, U. Oesterle, M. Gailhanou and M. Ilegems (1994). "Ultrahigh finesse microcavity with distributed Bragg reflectors." Appl. Phys. Lett. 65(15): 1883-1885.

Sugg, A. R., E. I. Chen, J. N. Holonyak, K. C. Hsieh, J. E. Baker and N. Finnegan (1993). "Effects of low-temperature annealing on the native-oxide of Al(x)Ga(1-x)As." J. Appl. Phys. 74: 3880-3885.

Sugimoto, M., H. Kosaka, K. Kurihara, I. Ogura, T. Numai and K. Kasahara (1992). "Very low threshold current density in vertical-cavity surface-emitting laser diodes with periodically doped distributed Bragg reflectors." Electron. Lett. 28(4): 385-387.

Sze, S. M. (1981). Physics of Semiconductor Devices. New York, Wiley.

Szipocs, R. and A. Kohazi-Kis (1997). "Theory and design of chirped dielectric laser mirrors." Appl. Phys. B 65(2): 115-135.

Takamori, T., K. Takemasa and T. Kamijoh (1996). "Interface structure of selectively oxidized AlAs/GaAs." Appl. Phys. Lett. 69(5): 659-661.

Tatum, J. A., D. Smith, J. K. Guenter and R. Johnson (1997). "High speed characteristics of VCSELs." Proc. SPIE 3004: 151-159.

Tayebati, P., P. Wang, D. Vakhshoori, C. Lu, M. Azimi and R. N. Sacks (1998). "Half-symmetric cavity tunable microelectromechanical VCSEL with single spatial mode." IEEE Photon. Technol. Lett. 10(12): 1679-1681.

Terry, F. L. (1991). "A modified harmonic oscillator approximation scheme for the dielectric constants of Al(x)Ga(1-x)As." J. Appl. Phys. 70(1): 409-417.

Theeten, J. B., D. E. Aspnes and R. P. H. Chang (1978). "A resonant ellipsometric technique for characterizing the interface between GaAs and its plasma-grown oxide." J. Appl. Phys. 49: 6097-6102.

Twستن, R. D., D. M. Follstaedt, K. D. Choquette and R. P. Schneider (1996). "Microstructure of laterally oxidized Al(x)Ga(1-x)As layers in vertical-cavity lasers." Appl. Phys. Lett. 69(1): 19-21.

Udem, T., J. Reichert, T. W. Hänsch and M. Kourogi (1998). "Accuracy of optical frequency comb generators and optical frequency interval divider chains." Opt. Lett. 23(17): 1387-1389.

Ünlü, M. S., M. Gokkavas, B. M. Onat, R. P. Mirin, K. J. Knopp, K. A. Bertness and D. H. Christensen (1998). "High bandwidth-efficiency resonant cavity-enhanced schottky photodiodes for 800-850 nm operation wavelength." Appl. Phys. Lett. 72(21): 2727-2729.

Valle, A., J. Sarma and K. A. Shore (1995). "Spatial holeburning effects on the dynamics of vertical cavity surface-emitting laser diodes." IEEE J. Quantum Electron. 31(8): 1423-1431.

Veasey, D. L., D. S. Funk, N. A. Sanford and J. S. Hayden (1999). "Arrays of distributed-Bragg-reflector waveguide lasers at 1536 nm in Yb/Er codoped phosphate glass." Appl. Phys. Lett. 74(6): 789-791.

Verdeyen, J. T. (1989). Laser Electronics. Englewood Cliffs, New Jersey, Prentice-Hall.

Weisbuch, C., M. Nishioka, A. Ishikawa and Y. Arakawa (1992). "Observation of the coupled exciton-photon mode splitting in a semiconductor quantum microcavity." Phys. Rev. Lett. 69(23): 3314-3317.

Williams, R. (1990). Modern GaAs Processing Methods. Boston, Artech House.

Woollam, J. A. and P. G. Snyder (1992). Variable Angle Spectroscopic Ellipsometry, VASE. Encyclopedia of Materials Characterization. R. C. Brundle, C. A. Evans and S. Wilson. Boston, Butterworth-Heinemann: 401.

Wu, Y. A., C. J. Chang-Hasnain and R. Nabiev (1993). "Singlemode emission from a passive-antiguide-region vertical-cavity surface-emitting laser." Electron. Lett. 29(21): 1861-1863.

Yablonovitch, E. (1987). "Inhibited spontaneous emission in solid-state physics and electronics." Phys. Rev. Lett. 58(20): 2059-2062.

Yamanishi, M. and Y. Yamamoto (1991). "An ultimately low-threshold semiconductor laser with separate quantum confinements of single field mode and single electron-hole pair." Jap. J. Appl. Phys. 30(1A): L60-L63.

Yariv, A. (1991). Optical Electronics. Philadelphia, Saunders College Publishing.

Yeh, P. (1988). Optical Waves in Layered Media. New York, Wiley.

Zhao, Y. G. and J. G. McInerney (1996). "Transverse-mode control of vertical-cavity surface-emitting lasers." IEEE J. Quantum Electron. 32(11): 1950-1958.

## Appendix A

### Electrically Pumped VCSEL Process Sheets

#### PURPOSE

This procedure is for processing the epi grown for the intracavity p-contact, backside n-contact, electrically-pumped VCSEL. (Proc. Rev. J)

#### SAMPLE IDENTIFICATION

Growth # \_\_\_\_\_  
Piece(s) # \_\_\_\_\_

#### MESA ETCH PROCEDURE

##### Sample Preparation

- ☐ Place a piece of material on the PR spinner.
- ☐ Spin and perform solvent clean (ACE, METH, ISO, & DI).
- ☐ Perform a dehydration bake for >10 min. at >110 deg. C. \_\_\_\_\_
- ☐ Photoresist Conditions:
  - Temperature \_\_\_\_\_ Humidity \_\_\_\_\_
  - Expiration Date \_\_\_\_\_ Poured Date \_\_\_\_\_
- ☐ Spin on AZ1813 at 5 kRPM for 40 sec.
- ☐ Soft-bake on a hotplate at 80 deg. C for 5 min.
- ☐ Carefully remove edge bead using ACE on swab.
- ☐ Prepare \_\_\_\_\_ samples in this fashion.

##### Sample Exposure & Development

- ☐ Clean the mask field of interest with ACE and METH.
- ☐ Use the mask aligner to expose the mesa etch pattern for 18 sec.

- [ ] Develop in straight CD30 for 25 sec.  
(Use additional dips of 5-10 sec. till clear if needed.)

- [ ] Observations:

-----  
-----

- [ ] Hard-bake the PR for 1 min. on the 125 deg. C hotplate.

## Laser Monitored In-situ Etch

### *Sample Mounting*

- [ ] Remove the bottom delron cage plate from the glass rod assembly.
- [ ] Remove the parallel window and heat it up on the 95 deg. C hotplate.
- [ ] Using low temperature ACE soluble wax (100 deg. C), fix the sample to the center of the window.
- [ ] Reattach the cage plate and window.

### *Optic Alignment*

- [ ] Turn the laser on to 17 mA drive current. Turn on the Si PIN detector.
- [ ] Using the IR viewer, verify that the beam is hitting the sample.
- [ ] Place a piece of lens tissue over the iris.
- [ ] Tweak the kinematic mount until the reflected beam is aligned collinear with the input beam.
- [ ] Remove the lens tissue and maximize the detected signal.
- [ ] Prepare a beaker of water and dunk the assembly while monitoring the signal. Take care to not to submerge the surface stabilizing window.
- [ ] Again maximize the signal.
- [ ] Start and test the Kiethley A/D Card testpoint application.

### *Enchant Preparation*

- [ ] Prepare 140 ml of 1:6:40 H<sub>2</sub>SO<sub>4</sub> (96%) / H<sub>2</sub>O<sub>2</sub> (30%) / H<sub>2</sub>O Solution  
(Time mixed: \_\_\_\_\_)

### *Etch*

- [ ] Start the A/D acquisition and set the magnetic stirrer.
- [ ] Carefully!! Dunk the assembly into the prepared etch.
- [ ] Monitor and count 22 minima and 1 maximum in the oscillations.  
Approx. (2 min 26 sec)
- [ ] Retract the sample and rinse in a beaker of DI water.

- [ ] Heat the sample plate, remove sample, and remove wax with ACE swap.
  - [ ] Soak sample in fresh ACE for 5 min.
  - [ ] Irrigate with ACE and rinse with ISO and blow dry
  - [ ] Note Surface Quality and Etch Uniformity:
- 
- 

## CURRENT CONFINEMENT MESA ETCH

### Sample Preparation

- [ ] Place a piece of material on the PR spinner. Spin and perform full solvent clean. (10 min. ACE, 10 min METH, 10 min. ISO, & rinse w/ DI)
- [ ] Perform a dehydration bake for >10 min. at >110 deg. C.
- [ ] Photoresist Conditions:
  - Temperature        \_\_\_\_\_ Humidity        \_\_\_\_\_
  - Expiration Date    \_\_\_\_\_ Poured Date    \_\_\_\_\_
- [ ] Spin on AZ1818 at 4 kRPM for 40 sec. (Yields a 2 micron thick layer)
- [ ] Spin on AZ1818 at 4 kRPM for 40 sec. (Yields a 4 micron thick layer)
- [ ] Soft-bake on a hotplate at 80 deg. C for 5 min.
- [ ] Carefully remove edge bead using ACE on swab.
- [ ] Prepare \_\_\_\_\_ samples in this fashion.

### Sample Exposure & Development

- [ ] Clean the mask field of interest with ACE and METH.
- [ ] Use mask aligner to expose the current confinement mask for 68 sec.
- [ ] Develop in straight CD30 for 25 sec.
  - (If residue, blanket expose for 2 sec. and develop for 15 sec.)
- [ ] Hard-bake the PR for 1 min. on the 125 deg. C hotplate.

### Enchant Preparation

- [ ] Prepare 165 ml of 10:1 (Citric:DI H2O):H2O2 (30%)
  - (Time mixed: \_\_\_\_\_)
- [ ] Setup in-situ laser monitoring to monitor selective nature of etch.
- [ ] Etch the sample watching for 5 min. and then constant reflectivity.
  - (42-45 sec./per half-wave) Approx. (3 min. 22 sec.)
- [ ] Rinse with DI.
- [ ] Soak sample in fresh ACE for 10 min. and rinse with ISO and blow dry.

## OXIDE APERTURE FORMATION

### Sample Preparation

- [ ] Set hotplate to 250 deg. C with a ramp rate of 200 deg./hour.
  - [ ] Set furnace to 410 deg. C with a ramp rate of 10 deg./min.
  - [ ] Set wet N2 to 1 L/min and ensure the bubbler water temperature is 75 deg. C. (Temperature \_\_\_\_\_)
  - [ ] Furnace should be in the range of 450-490 deg. C. (Temperature \_\_\_\_\_)
  - [ ] Load sample, and connect exhaust hose.
  - [ ] Allow sample to oxidize \_\_\_\_\_ minutes. (Depends on device size.)
  - [ ] Observe Oxidation Rate and Aperture Uniformity
- 
- 

## RING P-CONTACT PROCEDURE

### Sample Preparation

- [ ] Place a piece of material on the PR spinner. Spin and perform solvent clean. (ACE, METH, ISO, & rinse w/ DI)
- [ ] Perform a dehydration bake for >10 min. at >110 deg. C.
- [ ] Photoresist Conditions:
  - Temperature \_\_\_\_\_ Humidity \_\_\_\_\_
  - Expiration Date \_\_\_\_\_ Poured Date \_\_\_\_\_
- [ ] Spin on AZ1818 at 4 kRPM for 40 sec. (Yields a 2 micron thick layer)
- [ ] Spin on AZ1818 at 4 kRPM for 40 sec. (Yields a 4 micron thick layer)
- [ ] Soft-bake on a hotplate at 80 deg. C for 5 min.
- [ ] Carefully remove edge bead using ACE on swab.
- [ ] Prepare \_\_\_\_\_ samples in this fashion.

### Sample Exposure & Development

- [ ] Clean the mask field of interest with ACE and METH.
- [ ] Use mask aligner to expose the lift-off contact pattern for 70 sec. (Take extreme care to align as best as possible to the mesas.)
- [ ] Soak the sample in Toluene for 27 min.
- [ ] Blow dry with nitrogen and rinse in DI.
- [ ] Develop in straight CD30 for 25 sec. (If residue, blanket expose for 2 sec. and develop for 15 sec.)
- [ ] Perform a 30 min UV/Ozone clean.

### Metal Deposition

- [ ] Prepare a solution of Ammonium Hydroxide and DI water (1:15).
- [ ] Dip sample for 20 sec.
- [ ] Rinse and blow dry.
- [ ] Follow evaporator procedures in clean room notebook to deposit:  
60 Angstroms of Ti and 2 Kilo-Angstroms of Au. (4 pellets).
- [ ] Soak samples in ACE for 20 minutes. Use ACE flow to peel off metal.  
If not all squares have lifted out, let soak for an additional 20 min.  
If still not all lifted-off, gently scrub using a swab.  
As a last resort, use ultrasonic agitation for 5-10 sec. increments.
- [ ] Rinse in METH and blow dry with nitrogen.

### BACKSIDE N-CONTACT PROCEDURE

#### Protection of Mesas

- [ ] Spin on 2 spins of AZ1818 resist at 4 kRPM for 40 sec  
onto the epi side of the sample.
- [ ] Soft-bake on a hotplate at 95 deg. C for 1 min.

#### Metal Deposition

- [ ] Thoroughly clean the backside of the sample with an ACE soaked swab.
- [ ] Prepare a solution of Ammonium Hydroxide and DI water (1:15)
- [ ] Dip the sample for 20 sec.
- [ ] Rinse and blow dry.
- [ ] Follow evaporator procedures in clean room notebook to deposit:  
50 Angs. of Ni, 1050 Angs. of AuGe (3 plts.), 250 Angs. of Ni,  
and 1200 Angs. of Au (3 plts.).
- [ ] Soak samples in ACE for a few minutes to remove protective resist.
- [ ] Rinse in METH and blow dry with nitrogen.
- [ ] Finished !!!

#### Comments

-----  
-----  
-----  
-----



## Appendix B

### A Proposal for Further Study – Ultrafast Photonics: Semiconductor Temporal Dynamics Enabling 10 GHz Passively Mode-Locked Solid-State Waveguide Lasers

*(A proposal to the National Research Council (NRC) for a postdoctoral research associateship tenable at NIST.)*

#### B.1 Objective

The proposed work examines femtosecond carrier and phonon dynamics of novel semiconductor saturable absorbers realized in both InP and InGaAs material systems. Ultrafast dynamics of quantum well, quantum dot and low-temperature grown (LTG) materials will be investigated. Additionally, the impact of group velocity dispersion (GVD) on femtosecond pulse propagation through structures incorporating saturable absorbers and thin-film optimized mirror stacks will be studied. III-V compound semiconductor oxides will be used for dispersion control and the formation of low (optical) penetration depth, broad-band saturable absorber mirrors. This study will culminate in the demonstration of a compact passively mode-locked solid-state laser producing femtosecond optical pulsewidths at multigigahertz repetition rates.

A comprehensive understanding of the ultrafast photonics of semiconductor saturable absorber mirrors (SESAMs) is essential for this demonstration. An objective of this proposal is to address the fundamental materials-physics challenges by developing innovative SESAMs using methods of ultrafast metrology and fabrication techniques and materials originating from vertical-cavity surface-emitting laser (VCSEL) technologies. In the more general sense, the results of this work will enhance the understanding of the role of GVD and the underlying saturation mechanisms in novel material systems.

## B.2 Motivation

For many applications, optically pumped solid-state lasers offer inherent advantages over semiconductor lasers. The comparatively long upper-state and cavity lifetimes of rare-earth ions and transition metal ion lasers fundamentally results in relaxation oscillations at megahertz frequencies and thus a relative intensity noise (RIN) of  $< -160$  dB/Hz at 10 GHz. In contrast, the high gain and short cavity length of semiconductor lasers result in a RIN spectrum centered at gigahertz frequencies near the desired fundamental mode-locking frequency. Secondly, the superior phase noise of solid-state versus semiconductor lasers will produce a pulse stream with nearly quantum limited timing jitter. Furthermore, the now commonplace availability of high-power semiconductor diode lasers; for Erbium doped fiber amplifiers, makes solid-state lasers in the 1 to 1.5  $\mu\text{m}$  wavelength range extremely attractive.

Applications for these high repetition-rate mode-locked solid-state lasers are numerous with the some of the most exciting being: wavelength division multiplexing (WDM) channel synthesizers, optical analog-to-digital converters, high-speed low-jitter

clock generators, and pulse sources for terahertz radiation spectroscopy.

Within the Time and Frequency division (847) at the National Institute of Standards and Technology (NIST), the phase-locked comb of longitudinal modes generated by these novel mode-locked lasers is anticipated to facilitate a tenfold improvement in accuracy over current day cesium clocks serving as the primary standard of time. Unparalleled precision in the measurement of fundamental physical constants will result (Th. Udem, 1998).

## **B.3 Background**

### **B.3.1 Infrastructure & The State-of-the-Art**

Independently of this proposed work, NIST researchers developed and optimized cw Yb and Er/Yb doped solid-state planar wave-guide lasers. These devices routinely produce powers in upwards of 200 mW in wavelength bands centered around 1  $\mu\text{m}$  and 1.5  $\mu\text{m}$ , respectively (D.S. Funk, 1999 ; D.L. Veasey, 1999). Cleanroom fabrication facilities and MBE growth capabilities exist onsite which have produced VCSELs (K.J. Knopp, 1997), quantum dot lasers, and high-speed resonant cavity-enhanced photodiodes (M.S. Unlu, 1998). Additionally, a full array of semiconductor metrology tools and advanced ultrafast diagnostic systems (including a femtosecond mode-locked Ti:Sapphire laser with a diode-pumped solid-state pump source, a synchronously pumped optical parametric oscillator (OPO) for 1.55  $\mu\text{m}$  characterization, and a optical homodyne detection (OHD) scheme for single photon sensitivity (U. Leonhardt, 1996) ) are also available onsite for support of this work.

The proposed work will facilitate development of self-starting, passively mode-locked rare-earth doped glass waveguide lasers with fundamental mode-locked frequencies near 10 GHz. Specifically, innovative quantum dot and quantum well SESAMS will be designed and fabricated to provide the non-linear change in reflectivity needed to initiate mode-locking. It is anticipated that this work will lead to at least a 30-fold increase in the fundamental repetition rate of mode-locked lasers beyond the current state-of-the-art 290 MHz Yb/Er-doped fiber lasers (B.C. Collings, 1997). To date, there has been no reports of quantum-dot SESAMs or passively mode-locked planar waveguide lasers.

### B.3.2 Mode-Locking Mechanisms

Passive mode-locking mechanisms are categorized by three models: slow-saturable absorber with gain saturation mode-locking, fast saturable absorber mode-locking, and soliton mode-locking (U. Keller, 1996). Slow-saturable absorbers with gain saturation and fast saturable absorbers rely on opening a short net-gain window to stabilize the pulse. Soliton mode-locking relies on a careful balance of GVD and self-phase-modulation (SPM) for the formation of a femtosecond pulse while the absorber dynamics only start the pulse formation and stabilize the soliton. A slow saturable absorber in combination with pulse-to-pulse dynamic gain saturation is not suitable to these solid-state lasers with long upper-state lifetime ( $\sim 1$  ms) and small gain cross section ( $\sim 10^{-21}$  cm<sup>2</sup>). We will need to turn to the dynamics of semiconductor fast saturable absorber mode-locking and soliton mode-locking for these waveguide lasers.

The non-linear reflectivity change in a SESAM is due to bleaching of the ab-

sorption through band filling by the photo excited carriers. As the carriers are scattered out of their excited non-equilibrium states by phonon emission or carrier-carrier scattering, the absorption recovers. The recovery has a bitemporal response (A. Othonos, 1998). Thermalization processes and intraband carrier-carrier scattering take femtoseconds while interband trapping and recombination take picoseconds to nanoseconds depending on growth conditions. Mode-locking using a fast saturable absorber requires recovery of the absorber from pulse-to-pulse (i.e. within the cavity round-trip time). The pulse duration is set in part by the recovery time. By balancing GVD and SPM using intracavity prisms or other dispersion compensating elements, soliton mode-locked pulses with duration ten times less than the net-gain window's temporal width can be achieved (U. Keller, 1996). The recovery time of the absorber, however, must still be less than the cavity round-trip time. The saturation intensity can be varied by the selection of the number of quantum wells, or the density and number of quantum dot layers, and their overlap with the electric-field.

#### B.4 Problem Statement

There are several foreseen intrinsic difficulties associated with the realization of such a compact solid-state mode-locked source. The two foremost concerns are Q-switching instabilities arising in the pulse stream and self-starting. Both of these problems arise due to the desired multigigahertz repetition rate and long upper state lifetime of the solid-state medium. If the recovery time of the absorber is longer than or on the order of the round-trip time of ( $\sim 200$  ps) the laser will tend to cw Q-switch as the gain can not react fast enough to fluctuations in laser power and relaxation oscillations

grow. Through reducing the cw saturation intensity of the absorber, we can leave this regime, however, self-starting becomes increasingly difficult. Once the mode-locking build-up time has been passed, the relevant saturation parameter becomes pulse energy rather than cw intensity. Operation in a mode-locking regime under a Q-switch envelope rather than a cw Q-switching regime is then more likely by a factor of one over the cavity roundtrip normalized absorber recovery time ( $\sim 100$ ) (U. Keller, 1996). A third concern is a result of the laser's desired compactness. The laser is to consist of simply a 1 cm x 0.5 cm x 0.3 cm glass substrate with the SESAM bonded to one end and a dielectric reflector bonded to the other. To achieve the shortest duration pulse supported by the gain bandwidth ( $< 100$  fs) using soliton mode-locking, dispersion compensation is needed. There is no available space within the cavity for bulk optical elements such as a prisms. Additionally, the low absorption cross section in solid-state lasers requires the SESAM to be highly reflective at the higher energy pump wavelength (980 nm) to avoid influencing the saturation dynamics of the absorber and provide a second pass through the waveguide to increase the wall-plug efficiency. Furthermore, the fixed mode size ( $11 \mu\text{m} \times 16 \mu\text{m}$ ), low intracavity powers, and the  $1.5 \mu\text{m}$  wavelength range of the Yb/Er waveguides push on the frontiers of epitaxial growth technology and SESAM design.

## B.5 Proposed Research

During a fellowship to NIST, I plan to address the problem statement with a research plan that covers two areas. First, a systematic study of the recovery dynamics of quantum dot and quantum well absorbers and the temporal response of the mid-gap

states of low-temperature grown materials. Second, the development and measurement of dispersion compensating SESAMs using thin-film optimization and spectrally resolved white-light interferometry. This research will culminate in the demonstration of a compact passively mode-locked solid-state laser producing femtosecond optical pulsewidths at 10 GHz.

### B.5.1 Saturation Recovery Dynamics

Knowledge of the saturation intensities and recovery dynamics in SESAMs is of the utmost importance for designing cw mode-locked lasers without Q-switching instabilities. For these compact laser cavities, recovery times of tens of picoseconds or less are needed. This can be achieved using LTG grown GaAs and InGaAs which have been shown to exhibit recombination times of photoinjected carriers as short as a few hundred femtoseconds (depending on annealing conditions) due to point defects induced by the incorporation of excess arsenic (S. Gupta, 1991). The low intracavity power of these compact solid-state lasers may require lower cw saturation intensities than permissible with a single quantum well. The novel use of quantum-dots will extend the range of available saturation intensities to lower values.

The time evolution of the saturation recovery will be mapped over several nanoseconds with femtosecond resolution using the ultrafast metrology technique of excite and probe time-resolved reflectivity. The recovery dynamics of GaAs, InGaAs, and InGaAsP quantum well absorbers and InAs quantum dots will be studied. Other ultrafast metrology techniques such as time resolved luminescence spectroscopy will be explored for the measurement of cooling rates of carriers in the presence of non

equilibrium LO phonons in these LTG materials (A. Othonos, 1998). Correlation of these dynamics to the MBE growth conditions of substrate temperature (beyond the conventionally reported substrate thermocouple accuracy) and Arsenic overpressure will be performed.

For Yb waveguide lasers operating at  $1\ \mu\text{m}$ , the crystal material system of choice for the SESAM is an AlAs/GaAs DBR and an InGaAs quantum well or InAs quantum dot absorber region. The index contrast of the DBR provides a flat high reflectance region over 75 nm and a high reflector can be formed with 25 pairs. For the Yb/Er lasers operating at  $1.5\ \mu\text{m}$ , the "traditional" crystal material system is InGaAsP/InP latticed matched to an InP substrate. One problem with this material system is the small index contrast achievable in the Bragg stack. There are no epitaxial mirrors lattice matched to InP that exhibit the reflectance, ease of fabrication, or thermal characteristics matching the quality of AlAs/GaAs DBRs. This problem has plagued the development of long-wavelength VCSELs for some time. VCSEL development has turned to novel wafer-fusion bonding techniques to fuse an InGaAsP active region to a mirror stack of AlAs/GaAs. Alternatively, for SESAMs, we propose to investigate the usage of mid-gap states in LTG-GaAs as the absorbing mechanism. It has been demonstrated by spectroscopic ellipsometry that LTG-GaAs exhibits significant below bandgap absorption at  $1.5\ \mu\text{m}$  (Synowicki, 1998). Recent excite-probe experiments have shown that carriers excited high in the conduction band rapidly decayed ( $<1\ \text{ps}$ ) to the mid-gap trap states where they can then decay with a time constant of a few picoseconds (A. Othonos, 1998). Further exploration of the temporal dynamics of



this material at longer wavelengths may show that this is a promising long-wavelength technology for SESAMs.

### B.5.2 Dispersion Compensating SESAMs

Dispersion control through the use of integrated "chirped" mirrors is essential to the realization of these compact femtosecond mode-locked lasers as bulk prisms do not meet the space requirement. Nearly all reported chirped mirrors have been constructed using dielectric materials (e.g.  $\text{SiO}_2$  and  $\text{TiO}_2$ ) (R. Szipocs, 1997). A few reports of Gires-Tournois dispersion controlled SESAMs have been published in the literature (D. Kopf, 1996). These structures do not have precise control over the delay spectrum as they operate using a air-semiconductor reflection. I have shown that more complicated non-periodic layer structures can be designed with thin-film optimization techniques and grown within the limits of MBE (K.J. Knopp, 1997). These optimized structures tailor the wavelength dependant penetration depth and have been shown to have desirable ultrafast photonics properties (M. Munroe, 1997). Accurate knowledge of the dispersion characteristics of the semiconductor materials is essential for the design and optimization of chirped DBRs. My work (K.J. Knopp, 1997) and in depth studies performed at NIST (D.H. Christensen, 1992) demonstrate this knowledge. Similar optimization techniques will be utilized to create dispersion compensated chirped DBRs for SESAMS. The monolayer precision and accuracy, afforded by MBE, make integration of complex non-periodic and/or continuously graded chirped DBRs with SESAMs achievable. The group delay of the chirped SESAMs as well as the solid state medium will be measured using spectrally resolved white-light interferometry for feedback and

further optimization (A.P. Kovacs, 1995).

In previous work, I have studied the dispersion characteristics (K.J. Knopp, 1998) of III-V compound semiconductor oxides for use in broadband antireflection coatings (K.J. Knopp, 1998). Knowledge of the dispersion characteristics allows the use of this technology for chirped SESAM mirrors with a low penetration depth and a spectrally wide region of high reflectance. The low penetration depth provides a means of further reducing the saturation intensity of the absorber. With as few as 5 pairs, mirrors can be created that have a region of high reflectance that nearly spans the lasing and pump wavelengths (M.H. MacDougall, 1997). These mirrors are compatible with the material systems discussed and provide an elegant broadband solution for this and other work as compared to currently researched AlGaAs/CaF<sub>2</sub> mirrors (Z. Shi, 1998).

## B.6 Summary

The application potential for a turn-key, 1 cm long, femtosecond pulse source with gigahertz repetition rates is enormous. Such a source would revolutionize ultrafast laser optics and create a wealth of new commercial outlets.

The proposed research plan pursues such sources, at 1  $\mu\text{m}$  and 1.5  $\mu\text{m}$  wavelengths, by developing innovative semiconductor saturable absorber mirrors (SESAMs) capable of starting, stabilizing and shaping the ultrashort pulses at gigahertz repetition rates. To accomplish this I plan to systematically study the temporal dynamics and underlying saturation mechanisms in quantum dots, quantum wells and low-temperature grown (LTG) materials. To achieve the shortest pulse durations possible, I will develop dispersion compensating semiconductor and native-oxide distributed Bragg reflectors

using thin-film optimization.

Through this marriage of novel LTG low-dimensional semiconductors with VCSEL technologies, the proposed work will culminate in the demonstration of a compact passively mode-locked solid-state laser producing femtosecond optical pulsewidths at 10 GHz.

The proposed research leverages on the expertise and facilities of the semiconductor and dielectric projects within the manufacturing group of the Optoelectronics Division at NIST. Furthermore, this work will be greatly benefited by the unique opportunity of having epitaxial growth and fabrication facilities, ultrafast optical characterization facilities, and glass-waveguide fabrication facilities under one roof.

**THIS PAGE BLANK (USPTO)**